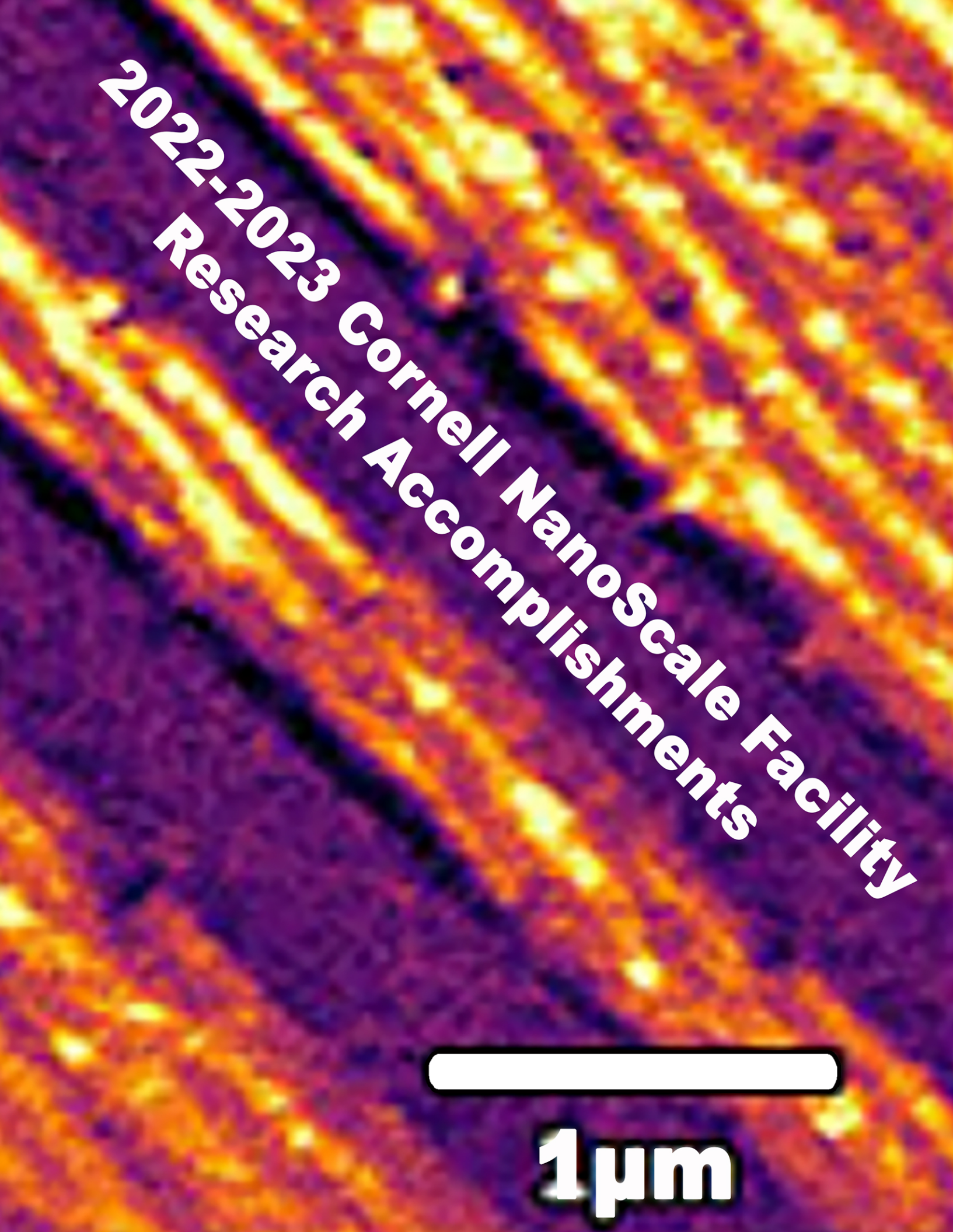
2022-2023 Cornell NanoScale Facility
Research Accomplishments
1 µm

250 Duffield Hall • 343 Campus Road • Ithaca NY 14853-2700
Phone: 607.255.2329 • Fax: 607.255.8601
Email: information@cnf.cornell.edu • Website: www.cnf.cornell.edu

Cornell NanoScale Facility 2022-2023 Research Accomplishments

CNF Lester B. Knight Director:
Jeeyoung Judy Cha

CNF Director of Operations:
Ronald Olson

Cornell NanoScale Facility (CNF) is a member of the National Nanotechnology Coordinated Infrastructure *(www.nnci.net)* and is supported by the National Science Foundation under Grant No. NNCI-2025233, the New York State Office of Science, Technology and Academic Research, Cornell University, Industry, and our Users.

The 2022-2023 CNF Research Accomplishments are also available on the web in full color: http://cnf.cornell.edu/publications/research_accomplishments

2022-2023 CNF Research Accomplishments

TABLE of CONTENTS

ELECTRONICS, 38-57

MATERIALS, 58-93

MECHANICAL DEVICES, 94-99

OPTICS & OPTO-ELECTRONICS, 100-115

PHYSICS & NANO-STRUCTURE PHYSICS, 116-159

PHOTOGRAPHY CREDITS

This year's cover image is from the report "Physics of nm-Scale Superconductors and Magnets"; CNF Project 598-96, Principal Investigator: Daniel C. Ralph; User: Xiaoxi Huang; Affiliation: Department of Physics, Cornell University — and was used with their permission. The full report starts on page 118.

Photography credits for pages vii and viii are as follows: furnace, Charles Harrington Photography; CNF REU Before, Melanie-Claire Mallison; CNF REU After, Ron Olson; Fischbach and Ober, Cornell Unversity Photography; CNF Annual Meeting Student Award Winners with CNF Directors and Funding Corporate Sponsors, Hodges Photography.

COMMENTS, FEEDBACK, AND SUGGESTIONS ARE ALWAYS WELCOME.

FEEL FREE TO USE OUR ONLINE USER COMMENT FORM AT HTTPS://WWW.CNFUSERS.CORNELL.EDU/USER_FEEDBACK

2022-2023 CNF Research Accomplishments
DIRECTORS' INTRODUCTION

The Cornell NanoScale Science and Technology Facility (CNF) takes pride in presenting the research achievements of our users and research groups who utilize the extensive array of resources provided by the CNF. We appreciate all the contributors who provided input to this publication. The Research Accomplishments showcases excellence in research while underscoring the diverse array of cutting-edge advancements spanning various fields of science and technology. Together with the spotlight on 87 featured research reports, CNF-related patents, presentations, and publications (totaling nearly 391 in 2022) have been included.

NNCI

The CNF is excited to maintain its membership within the National Nanotechnology Coordinated Infrastructure (NNCI), supported by the National Science Foundation (NSF) and the New York State NYSTAR/ESD Matching Grant Program. This ongoing relationship plays a pivotal role in sustaining CNF's position as a leader in nanofabrication. Cornell proudly stands as one of 16 collaborative sites within this national user consortium, dedicated to delivering cutting-edge fabrication and characterization tools to a diverse range of users from both academia and industry. Earlier this year the CNF submitted "The Year 8 Annual Report" and actively engaged in a successful virtual, reverse site visit: reaffirming our commitment to our cooperative agreement with the NNCI.

CNF continues to take the lead in establishing the NYS Nanotechnology Network (NNN). Building on the success of our 1st student showcase in May of 2022, the 2nd Annual NNN Student Showcase/Career Fair highlighting "Advances in the Semiconductor Industry" was held at the University at Albany on April 15, 2023. Binghamton University hosted the 3rd NNN symposium at the Albany Nanotech Complex in conjunction with the 34th Annual Electronics Packaging Symposium at the beginning of September 2023. With the CHIPS and Science Act, the pending Micron fabrication complex in Syracuse, and associated NYS initiatives, workforce development has assumed a stronger impactful presence in the region, further emphasizing the role of the NNN in uniting regional industry and universities.

NNCI STAFF AWARDS

Congratulations to Karlis Musa who was recently honored with a national award from the NNCI. Annually, the NNCI acknowledges the efforts of NNCI staff who provide exceptional service and support to network users in the categories of Technical Staff, Education and Outreach, and User Support. Karlis was recognized by the NNCI in the User Support category. This award is given to site staff who provide excellent service and support to all network users. Karlis will receive a plaque, acknowledgement at the NNCI Annual Conference and will be recognized on the NNCI website and in the NNCI yearly report to the NSF. We are proud of Karlis' efforts and his contributions.

The exceptional staff at the CNF have been consistently recognized with NNCI Outstanding Staff Member Awards. Past award recipients include Chris Alpha – Technical Staff (2018), Tom Pennell – Education and Outreach (2020), Phil infante – Technical staff (2021) and Mike Skvarla – User Support (2021), Melanie -Claire Mallison – Education and Outreach (2022) and Aaron Windsor (2022) – User Support.

NEW TOOLS AND CAPABILITIES

New, more advanced capabilities are constantly being added at CNF to improve the user experience. Acquisition of new tools is guided by discussions with the advisory committees and Cornell faculty. CNF is in the process of replacing its 20-year-old lab management software with NEMO, an intuitive and easy to use laboratory logistics software suite designed by NIST. NEMO manages tool reservations, enables and disables tools, tracks usage, and provides billing of user charges.

A cutting-edge superconducting film deposition system has been ordered. This specialized AJA system is

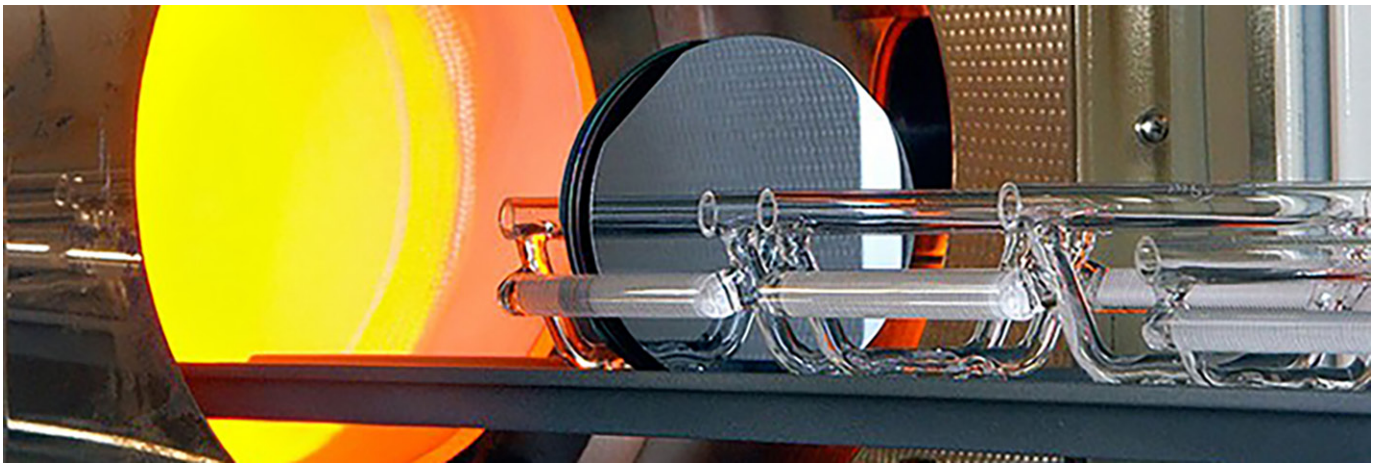

designed specifically for quantum technology. We remain optimistic the delays presented by persistent supply chain issues will be resolved and the scheduled delivery date in spring of 2024 will be met.

Furnace tube A4 and A3 have been meticulously reconfigured to deposit LPCVD silicon carbide and high temperature LPCVD silicon nitride respectively. These upgrades are pivotal steps toward enhancing our capabilities and positioning ourselves at the forefront of groundbreaking research and innovation.

ME COMMONS NORDTECH

This past month Deputy Secretary of Defense Kathleen Hicks announced funding for the establishment of eight Microelectronics Commons regional innovation hubs. Cornell proudly stands as a founding member of The Northeast Regional Defense Technology Hub (NORDTECH). NORDTECH represents a regional coalition comprised of public and private sector experts in the Microelectronics Commons region in and around New York State. Within this alliance the CNF serves a pivotal role supporting a wide range of research and development activities. In addition, the CNF takes pride in its dedication to training and empowering the next generation workforce. This collaborative program will facilitate the integration of Department of Defense (DoD)-selected research and development projects. Harnessing the collective expertise provided by diverse stakeholders committed to fostering innovation is vital to the successful advancements of the field of nanotechnology. This initiative is expected to significantly expand the CNF's state-of-the-art micro-nanotechnology equipment as well as its user base while propelling the facility into the forefront of cutting-edge advancements in microelectronics and nanotechnology.

FUTURE OF NNCI

Given the conclusion of the current National Nanotechnology Coordinated Infrastructure (NNCI) award cycle in 2025, the nanotechnology community is looking ahead to the future and the next nanotechnology infrastructure. In September the CNF actively participated in the 2023 Workshop on Nanotechnology Infrastructure of the Future. The workshop was held in Washington, D.C., as well as online. Stanford led this interactive workshop. The breakout sessions helped capture input from attendees on various topics to prepare for the future. The input from everyone will assist with the development of a public-facing white paper including recommendations for a path forward for presentation to US government agencies.

EDUCATION AND OUTREACH

The CNF supports a broad range of educational and outreach (E&O) activities at all levels including K-12, higher education, professional and public. Last year we had over 2,600 participants in workforce and outreach activities in addition to the distribution of 100,000 copies of Nanooze. We have been working with Tompkins Cortland Community College (TC3) to establish a Micro-Credential in the semiconductor field and collaborating on a few NY State Workforce Development proposals.

We continue to collaborate with Micron on various Workforce Development activities including the Northeast University Semiconductor Network and Micron "Chip Camps". The "chip camps" are designed to introduce middle school students to the concept of microtechnology, and possible careers in the field. In 2023 we held three separate camps with > 300 students from Syracuse regional school districts. Tom

Pennell piloted ATLAS (Accelerated Training for Labor Advancement in Semiconductors), a program in cooperation with the Tompkins-Seneca-Tioga Board of Cooperative Educational Services (TST BOCES) New Visions Engineering to further workforce development educational opportunities. This program provided students with a comprehensive in person/hands on training in the key areas of the cleanroom semiconductor environment.

Since 1991, CNF has hosted an NSF-funded Research Experiences for Undergraduates (REU) Program — an informative ten-week summer research experience for a diverse group of talented undergraduates. We've since added two 2nd-year programs in collaboration with the National Institute for Materials Science (NIMS) in Japan — the CNF International Research Experiences for Undergraduates (CNF iREU) Program and the CNF International Research Experiences for Graduates (CNF iREG) Program. For the CNF iREU, we send 8-10 NNCI REU interns to Japan for a summer of international research and in return, for the CNF iREG, NIMS sends several Japanese graduate students to the NNCI sites. In 2023, the CNF hosted seven CNF REU interns, plus one CNF iREG. And eight NNCI REU participated in the CNF iREU Program. All their final reports can be found online at https://cnf.cornell.edu/education — along with websites for all the education and outreach activities mentioned above!

Above, the 2023 CNF REU Interns BEFORE the program.

Below, the 2023 CNF REU Interns AFTER the program!

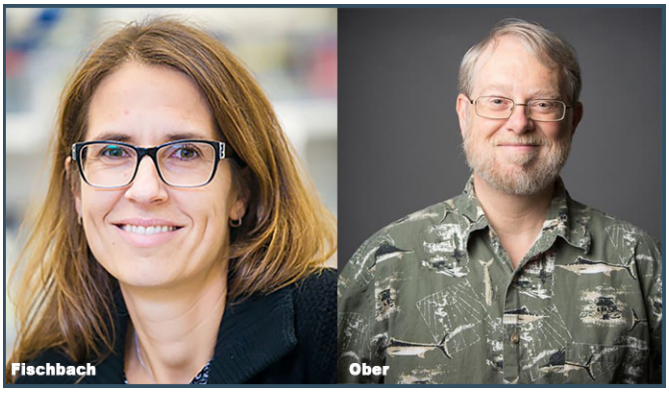

LEADERSHIP LEGACIES

The Directors extend their genuine gratitude to Prof. Christopher Ober, the 8th Lester B. Knight Director of the CNF (2016 -2023) for his exceptional leadership in support of the CNF. Chris' unwavering commitment to excellence, visionary guidance, and exceptional ability to strategically position the CNF for the future has left an indelible mark on both the NNCI and the CNF itself. His dedication and innovation has not only elevated the CNF to new heights but has contributed significantly to the advancement of nanoscience and technology on a broader scale. Chris is leaving a legacy for future generations. We wish Chris the best and look forward to seeing him around campus.

We would also like to thank Prof. Claudia Fischbach-Teschl, Associate Director (2020-2023), for her support and guidance during her tenure. Claudia's insight and expertise further enhanced the CNF's support of Life Sciences. Her collaborative nature paired with her dedication and leadership greatly enhanced the CNF mission.

Thank you, Chris, and Claudia, we wish you both the best in your future endeavors. Your daily presence will be missed by all at the CNF!

Judy Cha, Lester B. Knight Director, and Ron Olson, Director of Operations (seated), with the award winning students at the 2023 CNF Annual Meeting and the award-funding sponsors. Hodges Photography.

2022-2023 CNF Research Accomplishments

A SELECTION OF 2022 CNF-RESEARCH-RELATED PATENTS, PRESENTATIONS, AND PUBLICATIONS

"A biofabricated conduit structure to reconstitute lymphatic valve formation in 3D"; Lu, R., Lee, E., Biomedical Engineering Society (BMES), San Antonio, TX (Oral presentation), 2022 (2022, Cornell University).

"A Differential SPAD Array"; Bhaskar, A., M. Walth, R.H. Rand, A.T. Zehnder, arXiv:2207.09376 [Submitted on 19 Jul 2022] https://doi.org/10.48550/arXiv.2207.09376 (2022, Cornell University).

"A Differential SPAD Array Architecture in 0.18 μm CMOS for HDR Imaging"; White, M., S. Ghajari, T. Zhang, A. Dave, A. Veeraraghavan, A. Molnar, 2022 IEEE International Symposium on Circuits and Systems (ISCAS), 27 May 2022 - 01 June 2022, DOI: 10.1109/ISCAS48785.2022.9937558 (2022, Cornell University).

"A guide to the organ-on-a-chip"; Leung, C. M., de Haan, P., Ronaldson-Bouchard, K., Kim, G-A., Ko, J., Rho, H. S., Chen, Z., Habibovic, P., Jeon, N. L., Takayama, S., Shuler, M. L., Vunjak-Novakovic, G., Frey, O., Verpoorte, E., Toh, Y-C., Nature Reviews Methods Primers, 2(1), [33]. https://doi.org/10.1038/s43586-022-00118-6 (2022, Cornell University).

"A high-throughput integrated biofilm-on-a-chip platform for the investigation of combinatory physicochemical responses to chemical and fluid shear stress"; Nguyen, A.V., A.Y. Shourabi, M. Yaghoobi, S. Zhang, K.W. Simpson, A. Abbaspourrad, PloS One, Published: August 12, 2022, https://doi.org/10.1371/journal.pone.0272294 (2022, Cornell University).

"A high-voltage p-channel FET based on III-Nitride heterostructures"; Bader, S., R. Chaudhuri, D. Jena, H.G. Xing, Patent Issued, Docket # 8358-02-US, United States, Filed 11/6/19, 16/676,083, Issued 12/6/22, Patent 11,522,080 (2022, Cornell University).

"A hybrid bio-electrical device used to power Shewanella oneidensis metabolism using electricity and formate"; Barstow, B., F. Salimijazi, D. Specht, Invention, Docket 10492, Status: Unfiled, Disclosure Date 9/26/22 (2022, Cornell University).

"A lymphatic tissue engineered model to reconstitute lymphatic drainage and lymphedema"; Lee, E., 9th World Congress of Biomechanics (WCB), Session: Biomechanics of Vascular and Lymphatic Tissue Engineering, Taiwan (Oral presentation), JULY 14, 2022 (2022, Cornell University).

"A Microfluidic Model of AQP4 Polarization Dynamics and Fluid Transport in the Healthy and Inflamed Human Brain: The First Step Towards Glymphatics-on-a-Chip"; Soden, P.A.; Henderson, A.R.; Lee, E., Advanced Biology, 2022 Aug 4; doi: adbi.202200027 (Cover Article) (2022, Cornell University).

"A modular and autonomous bioreactor for tissue-engineered meniscus "; Bonassar, L., B. Kim, C. Lee, Patent Application, Docket # 10469-01-US, United States, Filed 10/12/22, 63/415,605 (2022, Cornell University).

"A puzzling insensitivity of magnon spin diffusion to the presence of 180° domain walls in a ferrimagnetic insulator"; Li, R.; Riddiford, L.J.; Chai, Y.; Dai, M.; Zhong, H.; Li, B.; Li, P.; Yi, D.; Broadway, D.A.; Dubois, A.E.E., arXiv preprint arXiv:2204.12377 (2022, Cornell University).

"A puzzling insensitivity of magnon spin diffusion to the presence of 180° domain walls in a ferrimagnetic insulator"; Li, R.; Riddiford, L.J.; Chai, Y.; Dai, M.; Zhong, H.; Li, B.; Li, P.; Yi, D.; Broadway, D.A.; Dubois, A.E.E., Research Square, 11 May 2022 DOI: 10.21203/rs.3.rs-1571984/v1 PPR: PPR491105 (2022, Cornell).

"A tunable bilayer Hubbard model in twisted WSe2"; Xu, Y.; Kang, K.F.; Watanabe, K.; Taniguchi, T.; Mak, K.F.; Shan, J., Nature Nanotechnology, SEP, Vol 17, Issue 9, 934-939, http://dx.doi.org/10.1038/s41565-022-01180-7 (2022, Cornell University).

"Acoustic Sensing Systems, Devices and Methods"; Abdelmejeed, M., J. Kuo, A. Lal, Patent Issued, Docket # 7683-04-US, United States, Filed 7/31/20, 15/733,459, Issued 10/18/22, Patent 11,474,077 (2022, Cornell University).

"Acoustic Sensing Systems, Devices and Methods"; Abdelmejeed, M., J. Kuo, A. Lal, Patent Application, Docket # 7683-06-US, United States, Filed 9/21/22, 17/933,988 (2022, Cornell University).

"Acoustically-driven Quantum Spin Sensor"; Chen, H., G. Fuchs, Patent Application, Docket # 9329-03-US, United States, Filed 7/15/22, 17/7493,357 (2022, Cornell University).

"Additively manufactured porous ceramic electrospray emitters"; Chamieh. S., E. Petro, S. Sobhani, Invention, Docket 10526, Status: Filed - by Cornell, Disclosure Date 10/25/22 (2022, Cornell).

"All Perovskite MESO using Spin-orbit Mott Material for readout"; Gosavi, T., M. Holtz, C.-c. Lin, S. Manipatruni, D. Nikonov, R. Ramesh, D. Schlom, R. Steinhardt, I. Young, Invention, Docket 10229, Status: Filed - by Joint Owner, Disclosure Date 2/1/22 (2022, Cornell University).

"All-dry free radical polymerization inside nanopores: Ion-milling-enabled coating thickness profiling revealed necking phenomena"; Cheng, Y.F.; Khlyustova, A.; Yang, R., Journal of Vacuum Science & Technology A, MAY, Vol 40, Issue 3, 33406, http://dx.doi.org/10.1116/6.0001718 (2022, Cornell University).

"All-Optical Tunability of Metalenses Permeated with Liquid Crystals"; Palermo, G.; Lininger, A.; Guglielmelli, A.; Ricciardi, L.; Nicoletta, G.; De Luca, A.; Park, J.S.; Lim, S.W.D.; Meretska, M.L.; Capasso, F., arXiv preprint arXiv:2206.02235 (2022, Harvard University).

"All-Optical Tunability of Metalenses Permeated with Liquid Crystals"; Palermo, G.; Lininger, A.; Guglielmelli, A.; Ricciardi, L.; Nicoletta, G.; De Luca, A.; Park, J.S.; Lim, S.W.D.; Meretska, M.L.; Capasso, F.; Strangi, G., ACS Nano, 10-Oct-22, Vol 16, Issue 10, 16539-16548, http://dx.doi.org/10.1021/acsnano.2c05887 (2022, Harvard University).

"AlN quasi-vertical Schottky barrier diode on AlN bulk substrate using Al0.9Ga0.1N current spreading layer"; Maeda, T.; Page, R.; Nomoto, K.; Toita, M.; Xing, H.G.; Jena, D., Applied Physics Express, 1-Jun, Vol 15, Issue 6, 61007, http://dx.doi.org/10.35848/1882-0786/ac702e (2022, Cornell University).

"An Adaptive Learning Platform for STEM Instruction"; Shen, K., Invention, Docket 10326, Status: Unfiled - Ownership Determination - TBD, Disclosure Date 4/13/22 (2022, Cornell University).

"An Image-Correlated Genomics Approach for Characterizing Changes in Chromatin-Lamina Association in Breast Cancer"; Crowley, J.C., Roberts, T.C., Woodhouse, M.V., Ozer, A., Lis, J.T., Fischbach-Teschl, C., Zipfel, W.R., 3rd Annual Cornell Intercampus Cancer Symposium Poster Session. 2022 May 19 (2022, Cornell).

"An optical sensor patch for the measurement of water activity"; Huber, A., P. Jain, S. Sen, A. Stroock, I-F. Wu, Invention, Docket 10581, Status: Unfiled, Disclosure Date 12/15/22 (2022, Cornell).

"Angular Optical Trapping to Directly Measure DNA Torsional Mechanics"; Gao, X.; Inman, J.T.; Wang, M.D., Optical Tweezers, Springer, Page(s) 37-73 (2022, Cornell University).

"Anisotropic Gigahertz Antiferromagnetic Resonances of the Easy-Axis van der Waals Antiferromagnet CrSBr"; Cham, T.M.; Karimeddiny, S.; Dismukes, A.H.; Roy, X.; Ralph, D.C.; Luo, Y.K., Nano Letters, August 24, Vol 22, Issue 16, 6716-6723, http://dx.doi.org/10.1021/acs.nanolett.2c02124 (2022, Cornell University).

"Anisotropic Magnon Spin Transport in Ultrathin Spinel Ferrite Thin Films—Evidence for Anisotropy in Exchange Stiffness"; Li, R., P. Li, D. Yi, L.J. Riddiford, Y. Chai, Y. Suzuki, D.C. Ralph, T. Nan, Nano Letters 2022, 22, 3, 1167–1173, January 25, 2022, https://doi.org/10.1021/acs.nanolett.1c04332 (2022, Cornell University).

"Anisotropic spin-current source layers for generating out-of-plane anti-damping spin-orbit torques"; Ralph, D.C., D. Schlom, Invention, Docket 10271, Status: Closed - In Process, Disclosure Date 3/6/22 (2022, Cornell University)

"Aperture Restoration of Single Axis Reflective Optical Scanners"; Hebert, E., C. Xu, Invention, Docket 10360, Status: Filed - by Cornell, Disclosure Date 5/5/22 (2022, Cornell University).

"Apparatus and Methods for Detecting a Vibratory Signal"; Davaji, B., S. Gupta, A. Lal, S. Nadig, Patent Issued, Docket # 7431-03-US, United States, Filed 11/7/18, 16/099,584, Issued 5/10/22, Patent 11,326,937 (2022, Cornell University).

"Artificial Cilium And Arrays Thereof"; Liu, Q., Wang, W., Cohen, I., McEuen, P., Molnar, A., Patent submitted (2022) (2022, Cornell).

"Assembly and use of a microfluidic device to study nuclear mechanobiology during confined migration"; Agrawal, R., Windsor, A., Lammerding, J., The Nuclear Pore Complex. Methods in Molecular Biology, vol 2502. Humana, New York, NY. https://doi.org/10.1007/978-1-0716-2337-4_22, Goldberg, M.W. (eds) (2022, Cornell University).

"Assembly and use of a microfluidic device to study nuclear mechanobiology during confined migration"; Agrawal, R., Windsor, A., Lammerding, J., Methods in Molecular Biology 2022. 2502: 329-349, DOI: 10.1007/978-1-0716-2337-4_22 PMID: 35412249 PMCID: PMC9862508 (2022, Cornell University).

"Assessing Lewis Acidity and Confinement for Zeotype-Catalyzed Aldol Condensation between Lower Aldehydes"; He, W.; Zhang, Z.; Flaherty, D.W.; Cybulskis V.J., 27th North American Meeting of the Catalysis Society, New York, NY (5/2022) (2022, Syracuse University).

"ATM modulates nuclear mechanics by regulating lamin A levels"; Shah, P.; McGuigan, C.W.; Cheng, S.; Vanpouille-Box, C.; Demaria, S.; Weiss, R.S.; Lammerding, J., bioRxiv, Posted April 29, 2022, doi: https://doi.org/10.1101/2022.02.28.482418 (2022, Cornell University).

"ATM modulates nuclear mechanics by regulating lamin A levels"; Shah, P.; McGuigan, C.W.; Cheng, S.; Vanpouille-Box, C.; Demaria, S.; Weiss, R.S.; Lammerding, J., Frontiers Cell Dev Biol. 2022. 10: 875132 (2022, Cornell University).

"Autonomous self-healing optical sensors for damage intelligent soft-bodied systems"; Bai, H.; Kim, Y. S.; Shepherd, R. F., Science Advances, Vol 8, Issue 49, Page(s) eabq2104 (2022, Cornell University).

"Band repulsion in periodically modulated lattice models and electromagnetic systems"; Yu, Y.; Shvets, G., Physical Review B, 10-May, Vol 105, Issue 19, 195116, http://dx.doi.org/10.1103/PhysRevB.105.195116 (2022, Cornell University).

"Bioelectronic Platform to Investigate Charge Transfer between Photoexcited Quantum Dots and Microbial Outer Membranes"; Suri, M.; Mohamed, Z.; Bint E Naser, S.F.; Mao, X.; Chen, P.; Daniel, S.; Hanrath, T., ACS Applied Materials & Interfaces, Vol 14, Issue 13, Page(s) 15799-15810 (2022, Cornell University).

"Bioengineering enucleated human cells for in vivo homing and delivery of therapeutic cargos"; Wang, H., Alarcon, C.N., Liu, B., Watson, F., Searles, S., Lee, C.K., Keys, J., Pi, W., Allen, D., Lammerding, J., Bui, J., Klemke, R.L., Nature Biomedical Engineering. 2022. 6(7): 882–897 (2022, Cornell University).

"Biofunctional matrix models reveal mineral-dependent mechanoregulation of bone metastatic breast cancer"; Choi, S.; Whitman, M.A.; Shimpi, A.A.; Chiou, A.; Druso, J.E.; Verma, A.; Lux, S.C.; Cheng, Z.; Paszek, M.; Elemento, O., bioRxiv, Posted July 02, 2022, doi: https://doi.org/10.1101/2022.06.29.498001 (2022, Cornell University).

"Bistability and irregular oscillations in pairs of opto-thermal micro-oscillators"; Bhaskar, A., M. Walth, R.H. Rand, A.T. Zehnder, SEM Annual Conference and Exposition on Experimental and Applied Mechanics, 2022, Omni William Penn Hotel, Pittsburgh, PA USA. (2022, Cornell University).

"Bistability in Coupled Opto-Thermal Micro-Oscillators"; Bhaskar, A.; Walth, M.; Rand, R.H.; Zehnder, A.T., Journal of Microelectromechanical Systems, AUG, Vol 31, Issue 4, 580-588, http://dx.doi.org/10.1109/JMEMS.2022.3169430 (2022, Cornell).

"Blazed reflection gratings with electron-beam lithography and ion-beam etching"; Miles, D.M.; McEntaffer, R.L.; Grise, F., Proceedings of SPIE, Space Telescopes and Instrumentation 2022: Ultraviolet To Gamma Ray, July 17-22, 2022, Montreal, CANADA, Vol 12181, 1218153, http://dx.doi.org/10.1117/12.2637880 (2022, The Pennsylvania State University).

"Body-on-a-Chip: The Potential to Transform Drug Development"; Shuler, M.L., MPS World Summit, New Orleans, LA, May 30-June 3, 2022 (2022, Cornell University).

"Bone demineralization alters breast cancer growth and tumor microenvironment"; Whitman, M.A., M. Mantri, S. Choi, L.A. Estroff, I. De Vlaminck, C. Fischbach, Gordon Research Conference for Metabolism and Local Environments in Development, Disease and Regeneration of the Skeleton, September 2022 (2022, Cornell University).

"Bubble dynamics in a subcooled flow boiling of near-critical carbon dioxide"; Parahovnik, A., Y. Peles, International Journal of Heat and Mass Transfer, Volume 183, Part C, February 2022, 122191, https://doi.org/10.1016/j.ijheatmasstransfer.2021.122191 (2022, University of Central Florida).

"Building a Human Body on a Chip – a 33 Year Odyssey"; Shuler, M.L., Organoids & Microphysiological Systems, Long Beach, CA Dec 12-14, 2022 (2022, Cornell University).

"Building a Human Body on a Chip: An Ongoing Journey 1989-20?? – A 33 Year Odyssey"; Shuler, M.L., Bioengineering for Building Microphysiological Systems 2022. Select Bio. Rotterdam, Netherlands, Oct 24-25, 2022 (2022, Cornell University).

"Disentangling types of lattice disorder impacting superconductivity in Sr2RuO4 by quantitative local probes"; Goodge, B.H.; Nair, H.P.; Baek, D.J.; Schreiber, N.J.; Miao, L.; Ruf, J.P.; Waite, E.N.; Carubia, P.M.; Shen, K.M.; Schlom, D.G., APL Materials, April 1, Vol 10, Issue 4, 41114, http://dx.doi.org/10.1063/5.0085279 (2022, Cornell).

"Distributed polarization-doped GaN p–n diodes with near-unity ideality factor and avalanche breakdown voltage of 1.25 kV"; Nomoto, K., W. Li, B. Song, Z. Hu, M. Zhu, M. Qi, V. Protasenko, Z. Zhang, M. Pan, X. Gao, H. Marchand, W. Johnson, D. Jena, H.G. Xing, Appl. Phys. Lett. 120, 122111 (2022); https://doi.org/10.1063/5.0083302 (2022, Cornell University).

"Doxorubicin alters mesenchymal stromal cells phenotype and bone matrix remodeling"; Onissema Karimu, S., A. Shimpi, N. Sempertegui, C. Fischbach, 3rd Cornell Intercampus Cancer Research Symposium, May 2022 (2022, Cornell University).

"Doxorubicin Reduces Bone Matrix Formation by Altering Mesenchymal Stromal Cell Phenotype"; Onissema Karimu, S., A. Shimpi, N. Sempertegui, C. Fischbach, Biomedical Engineering Society Annual Meeting 2022, October 2022 (2022, Cornell University).

"Durable and Regenerative Superhydrophobic Surface using Porous Nanochannels"; Ranjan, D.; Zou, A.; Maroo, S.C., Chemical Engineering Journal, Page(s) 140527 (2022, Syracuse University).

"Effects of Lewis Acidity and Confinement on Aldol Reactions of Aldehydes in Zeotypes"; He, W.; Potts, D.S.; Flaherty, D.W.; Cybulskis V.J, 2022 AIChE Annual Meeting, Phoenix, AZ (11/2022) (2022, Syracuse University).

"Effects of light and nutrients on the growth of algal cells revealed by a microfluidic platform"; Liu, F., L. Gaul, M. Yazdani, B.A. Ahner, M. Wu, Bulletin of the American Physical Society, APS March Meeting 2022, Vol 67, # 3, March 14–18, 2022; Chicago, https://meetings.aps.org/Meeting/MAR22/Session/W05.10 (2022, Cornell University).

"Efficient large scale synthesis of Î´-MnO2 for aqueous batteries"; Archer, L., S. Hong, S. Jin, Invention, Docket 10359, Status: Unfiled, Disclosure Date 5/5/22 (2022, Cornell University).

"Electrically induced adiabatic wavelength conversion in an integrated lithium niobate ring resonator"; He, X.; Cortes-Herrera, L.; Opong-Mensah, K.; Zhang, Y.; Song, M.; Agrawal, G.P.; Cardenas, J., CLEO: Science and Innovations, Optica Publishing Group, Page(s) SM4O-4 (2022, University of Rochester).

"Electrochemical recovery of Ca- and Mg-carbonates and high value metals from siliceous substrates "; Gadikota, G., P. Lu, P. Ochonma, Invention, Docket 10528, Status: Unfiled, Disclosure Date 10/27/22 (2022, Cornell University).

"Electronic and optical characterization of bulk single crystals of cubic boron nitride (cBN)"; Milas, P.; Mathab, S.; Abraham, S.; Bishoy, J.; Alam, J.; Chandrashekar, M.V.S.; Robinson, A.J.; Vora, P.M.; Ozturk, B.; Spencer, M.G., AIP Advances, Vol 12, Issue 9, Page(s) 95303 (2022, Morgan State University).

"Electronically Integrated Microscopic Robots"; Cohen, I.; Keynote speaker, MicroTAS 2022 (2022) (2022, Cornell University).

"Elevated Plasmonic Optical Nanostructures for Infared Spectroscopy"; Huang, S., A. Mahalanabish, G. Shvets, Invention, Docket 10541, Status: Filed - by Cornell, Disclosure Date 11/7/22 (2022, Cornell University)

"Engineered Extracellular Matrix (ECM) Models"; Fischbach, C., Wolff Lecture, Berlin Center for Regenerative Therapies, April 14 2022 (2022, Cornell University).

"Engineered Extracellular Matrix (ECM) Models"; Fischbach, C., UT Dallas, Biomedical Engineering September 9, 2022 (2022, Cornell University).

"Engineered Extracellular Matrix (ECM) Models"; Fischbach, C., Aachen University or Rheinisch-Westfälische Technische Hochschule (RWTH) Aachen, Germany, May 4, 2022 (2022, Cornell University).

"Engineered Extracellular Matrix (ECM) Models"; Fischbach, C., Annual Meeting of the Americal Association for Cancer Research (AACR), Physical Aspects of Cancer and Physical Sciences of Oncology, April 2022 (2022, Cornell University).

"Engineered Extracellular Matrix (ECM) Models"; Fischbach, C., Biomedical Engineering Department at the National University of Singapore, June 7, 2022 (2022, Cornell University).

"Engineered Extracellular Matrix (ECM) Models"; Fischbach, C., Biomedical Engineering Society, CMBE Meeting, Keynote speaker, Indian Wells, CA January 2-6 2023 (2022, Cornell University).

"Engineered Extracellular Matrix (ECM) Models"; Fischbach, C., GRC Physical Science of Oncology, Galveston, TX, February 2023 (2022, Cornell University).

"Engineered Extracellular Matrix (ECM) Models"; Fischbach, C., IFATS, Fort Lauderdale, FL, November 4-6 2022 (2022, Cornell University).

"Engineered Extracellular Matrix (ECM) Models"; Fischbach, C., Max Planck Institute for the Science of Light, Erlangen, Germany July 20, 2022 (2022, Cornell University).

"Engineered Extracellular Matrix (ECM) Models"; Fischbach, C., Summer School, Mechanics and Cancer, La Cerdanya, Spain, 28-30 September 2022 (2022, Cornell University).

"Engineered second-order nonlinearity in silicon nitride"; Zhang, Y.; Nauriyal, J.; Song, M.; Baez, M.G.; He, X.; MacDonald, T.; Cardenas, J., arXiv preprint arXiv:2210.09374 (2022, University of Rochester).

"Enucleated human mesenchymal stromal cells for the homing and the delivery of therapeutic cargos in vivo"; Wang, H.; Alarcón, C.N.; Liu, B.; Watson, F.; Searles, S.; Lee, C.K.; Keys, J.; Pi, W.; Allen, D.; Lammerding, J., Nature Biomedical Engineering, Vol 6, Issue 7, Page(s) 882 (2022, Cornell University).

"Epitaxial growth of the first two members of the Ban+1InnO2.5n+1 Ruddlesden–Popper homologous series"; Hensling, F.V.E.; Smeaton, M.A.; Show, V.; Azizie, K.; Barone, M.R.; Kourkoutis, L.F.; Schlom, D.G., Journal of Vacuum Science & Technology A, DEC, Vol 40, Issue 6, 62707, http://dx.doi.org/10.1116/6.0002205 (2022, Cornell University).

"Epitaxial ScxAI1-xN Semiconductor Devices"; Casamento, J., B. Davaji, V. Gund, D. Jena, A. Lal, H. Lee, T. Maeda, H.G. Xing, Patent Application, Docket # 9924-01-US, United States, Filed 5/20/22, 63/344,270 (2022, Cornell University).

"Epitaxial ScxAl1−xN on GaN exhibits attractive high-K dielectric properties"; Casamento, J., H. Lee, T. Maeda, V. Gund, K. Nomoto, L. van Deurzen, W. Turner, P. Fay, S. Mu, C.G. Van de Walle, A. Lal, H.G. Xing, D. Jena, Appl. Phys. Lett. 120, 152901 (2022); https://doi.org/10.1063/5.0075636 (2022, Cornell University).

"Epitaxial Synthesis of a Vertically Aligned Two-Dimensional van der Waals Crystal:(110)-Oriented SnO"; Barone, M.R.; Du, C.; Radosavljevic, L.; Werder, D.; Pan, X.; Schlom, D.G., Crystal Growth & Design, 2022, 22, 12, 7248–7254, November 23, 2022, https://doi.org/10.1021/acs.cgd.2c00905 (2022, Cornell University).

"Excited-state spin-resonance spectroscopy of VB– defect centers in hexagonal boron nitride"; Mathur, N.; Mukherjee, A.; Gao, X.Y.; Luo, J.L.; McCullian, B.A.; Li, T.C.; Vamivakas, A.N.; Fuchs, G.D., Nature Communications, June 9, Vol 13, Issue 1, 3233, http://dx.doi.org/10.1038/s41467-022-30772-z (2022, Cornell University).

"Exciton density waves in Coulomb-coupled dual moiré lattices"; Zeng, Y., Z. Xia, R. Dery, K. Watanabe, T. Taniguchi, J. Shan, K.F. Mak, arXiv:2205.07354 (2022, Cornell University).

"Exploration of microfluidic technologies and eukaryotic oligosaccharyltransferases to improve Escherichia coli-based glycoprotein production"; Aquino, A.K., Cornell University, 2022 Ph.D.Thesis (2022, Cornell University).

"Exploring No Man's Land—Arrhenius Crystallization of Thin-Film Phase Change Material at 1 000 000 K s−1 via Nanocalorimetry"; Zhao, J., J. Hui, Z. Ye, T. Lai, M.Y. Efremov, H. Wang, L.H. Allen, Advanced Materials, Interfaces, Vol 9, Issue 23, August 11, 2022, 2200429, https://doi.org/10.1002/admi.202200429 (2022, University of Illinois at Urbana-Champaign).

"Extending the Kinetic and Thermodynamic Limits of Molecular-Beam Epitaxy Utilizing Suboxide Sources or Metal-Oxide-Catalyzed Epitaxy"; Vogt, P.; Hensling, F.V.E.; Azizie, K.; McCandless, J.P.; Park, J.; DeLello, K.; Muller, D.A.; Xing, H.G.; Jena, D.; Schlom, D.G., Physical Review Applied, MAR 8, Vol 17, Issue 3, 34021, http://dx.doi.org/10.1103/PhysRevApplied.17.034021 (2022, Cornell University).

"Externally Driven Nonlinear Time-Variant Metasurfaces"; Zubyuk, V.V.; Shafirin, P.A.; Shcherbakov, M.R.; Shvets, G.; Fedyanin, A.A., ACS Photonics, Feb 16, Vol 9, Issue 2, 493-502, http://dx.doi.org/10.1021/acsphotonics.1c01222 (2022, Cornell University).

"Extracting Mural and Volumetric Growth Patterns of Platelet Aggregates on Engineered Surfaces by Use of an Entity Tracking Algorithm"; Kang, J.; Jayaraman, A.; Antaki, J.; Kirby, B., ASAIO Journal, 10.1097/MAT.0000000000001841, October 28, 2022. | DOI: 10.1097/MAT.0000000000001841 (2022, Cornell University).

"Extremely fast-charge lithium batteries using improved InLi anode"; Archer, L., S. Jin, Invention, Docket 10454, Status: Filed - Attorney Instructed to File, Disclosure Date 8/22/22 (2022, Cornell).

"Ferroelectric Modulation of Surface Electronic States in BaTiO3 for Enhanced Hydrogen Evolution Activity"; Abbasi, P.; Barone, M.R.; Cruz-Jauregui, M.D.; Valdespino-Padilla, D.; Paik, H.; Kim, T.; Kornblum, L.; Schlom, D.G.; Pascal, T.A.; Fenning, D.P., Nano Letters, May 25, Vol 22, Issue 10, 4276-4284, http://dx.doi.org/10.1021/acs.nanolett.2c00047 (2022, Cornell University).

"First demonstration of N-polar GaN/AlGaN/AlN HEMT on Single Crystal AlN Substrates"; Kim, E.; Zhang, Z.; Singhal, J.; Nomoto, K.; Hickman, A.; Toita, M.; Jena, D.; Xing, H.G., 2022 IEEE Device Research Conference (DRC), 26-29 June 2022, DOI: 10.1109/DRC55272.2022.9855776 (2022, Cornell University).

"Flow boiling of carbon dioxide with a micro impinging jet"; Adeoye, S., Y. Peles, International Journal of Heat and Mass Transfer, Volume 187, 15 May 2022, 122495, https://doi.org/10.1016/j.ijheatmasstransfer.2021.122495 (2022, University of Central Florida).

"Frustrated magnetic interactions in a Wigner-Mott insulator"; Tang,Y., K.Su, L.Li, Y.Xu, S.Liu, K.Watanabe, T.Taniguchi, J.Hone, C.Jian, C.Xu, K.Mak, J.Shan, arXiv:2204.08148 (2022, Cornell).

"Gallium oxide photonics and nonlinear optics"; Jena, D., G. Khalsa, B. Liu, H. Nair, V. Protasenko, Y. Zhang, Invention, Docket 10253, Status: Filed - by Cornell, Disclosure Date 2/17/22 (2022, Cornell University)

"Gate-Tunable Anomalous Hall Effect in a 3D Topological Insulator/2D Magnet van der Waals Heterostructure"; Gupta, V.; Jain, R.; Ren, Y.F.; Zhang, X.S.; Alnaser, H.F.; Vashist, A.; Deshpande, V.V.; Muller, D.A.; Xiao, D.; Sparks, T.D.; Ralph, D.C., Nano Letters, September 14, Vol 22, Issue 17, 7166-7172, http://dx.doi.org/10.1021/acs.nanolett.2c02440 (2022, Cornell University).

"Gate-tunable anomalous Hall effect in a 3D topological insulator/2D magnet van der Waals heterostructure"; Gupta, V.; Jain, R.; Ren, Y.; Zhang, X.S.; Alnaser, H.F.; Vashist, A.; Deshpande, V.V.; Muller, D.A.; Xiao, D.; Sparks, T.D., arXiv preprint arXiv:2206.02537 (2022, Cornell University).

"Gate-tunable heavy fermions in a moiré Kondo lattice"; Zhao, W., B. Shen, Z. Tao, Z. Han, K. Kang, K. Watanabe, T. Taniguchi, K. F. Mak, J. Shan, arXiv:2211.00263 (2022, Cornell University).

"Genetically engineered and enucleated human mesenchymal stromal cells for the targeted delivery of therapeutics to diseased tissue"; Wang, H.; Alarcón, C.N.; Liu, B.; Watson, F.; Searles, S.; Lee, C.K.; Keys, J.; Pi, W.; Allen, D.; Lammerding, J., Nature Biomedical Engineering, Vol 6, Issue 7, Page(s) 882-897 (2022, Cornell University).

"Giant anisotropic magnetoresistance in Ising superconductor-magnetic insulator tunnel junctions"; Kang, K., S. Jiang, H. Berger, K. Watanabe, T. Taniguchi, L. Forró, J. Shan, K.F. Mak, arXiv:2101.01327 (2022, Cornell University).

"Giant bulk spin-orbit torque and efficient electrical switching in single ferrimagnetic FeTb layers with strong perpendicular magnetic anisotropy"; Liu, Q.B.; Zhu, L.J.; Zhang, X.Y.S.; Muller, D.A.; Ralph, D.C., Applied Physics Reviews, June, Vol 9, Issue 2, 21402, http://dx.doi.org/10.1063/5.0087260 (2022, Cornell University).

"Gigahertz Metamaterial Ultrasonic Lens Characterization Using GHz CMOS Integrated Ultrasonic Micro Imager"; Hwang, J., A. Baskota, B. Davaji, J. Kuo, A. Lal, 2022 IEEE International Ultrasonics Symposium (IUS), Venice, Italy, 2022, pp. 1-4, doi: 10.1109/IUS54386.2022.9958496 (2022, Cornell University).

"Gigahertz Ultrasonic Multi-Imaging of Soil Temperature, Morphology, Moisture, and Nematodes"; Baskota, A.; Kuo, J.; Lal, A., 2022 IEEE 35th International Conference on Micro Electro Mechanical Systems Conference (MEMS), IEEE, Page(s) 519-522 (2022, Cornell University).

"Group III Oxide Devices with Select Iron Doped Areas"; Cromer, B., D. Dryden, D. Jena, H.G. Xing, Patent Application, Docket # 10396-01-US, United States, Filed 8/6/22, 63/395,809 (2022, Cornell University).

"Growth of PdCoO2 films with controlled termination by molecular-beam epitaxy and determination of their electronic structure by angle-resolved photoemission spectroscopy"; Song, Q.; Sun, J.; Parzyck, C.T.; Miao, L.; Xu, Q.; Hensling, F.V.E.; Barone, M.R.; Hu, C.; Kim, J.; Faeth, B.D., APL Materials, September 1, Vol 10, Issue 9, 91113, http://dx.doi.org/10.1063/5.0101837 (2022, Cornell).

"Growth of Ta2SnO6 Films, a Candidate Wide-Band-Gap p-Type Oxide"; Barone, M.; Foody, M.; Hu, Y.Q.; Sun, J.X.; Frye, B.; Perera, S.S.; Subedi, B.; Paik, H.; Hollin, J.; Jeong, M.; Lee, K.; Winter, C.H.; Podraza, N.J.; Cho, K.; Hock, A.; Schlom, D.G., Journal of Physical Chemistry C, Feb 24, Vol 126, Issue 7, 3764-3775, http://dx.doi.org/10.1021/acs.jpcc.1c10382 (2022, Cornell).

"Haptic perception using optoelectronic robotic flesh for embodied artificially intelligent agents"; Barreiros, J.A., A. Xu, S. Pugach, N. Iyengar, G. Troxell, A. Cornwell, S. Hong, B. Selman, R.F. Shepherd, Science Robotics, 8 Jun 2022, Vol 7, Issue 67, DOI: 10.1126/scirobotics.abi6745 (2022, Cornell University).

"Heat Transfer Characteristics of Turbulent Flow of Supercritical Carbon Dioxide (Sco2) in a Microchannel"; Manda, U., A. Parahovnik, Y. Peles, Posted: 20 Apr 2022, SSRN: https://ssrn.com/abstract=4087972 or http://dx.doi.org/10.2139/ssrn.4087972 (2022, University of Central Florida).

"Heat Transfer Characterization of Carbon Dioxide in Micro Impinging Jet(s) Near Critical Conditions"; Adeoye, S., University of Central Florida, 2022 Ph.D.Thesis (2022, University of Central Florida).

"Heat transfer mode shift to adiabatic thermalization in near-critical carbon dioxide with flow boiling in a microchannel"; Parahovnik, A., U. Manda., Y. Peles, International Journal of Heat and Mass Transfer, Volume 188, 1 June 2022, 122629, https://doi.org/10.1016/j.ijheatmasstransfer.2022.122629 (2022, University of Central Florida).

"High pressure saturated flow boiling of CO2 at the micro scale"; Parahovnik, A., Y. Peles, International Journal of Heat and Mass Transfer, Volume 186, 1 May 2022, 122449, https://doi.org/10.1016/j.ijheatmasstransfer.2021.122449 (2022, University of Central Florida).

"High thermal conductivity and ultrahigh thermal boundary conductance of homoepitaxial AlN thin films"; Alvarez-Escalante, G.; Page, R.; Hu, R.; Xing, H.G.; Jena, D.; Tian, Z., APL Materials, January 1, Vol 10, Issue 1, 11115, http://dx.doi.org/10.1063/5.0078155 (2022, Cornell University).

"High Voltage Schottky Barrier Diode"; Jena, D., T. Maeda, K. Nomoto, R. Page, M. Toita, H.G. Xing, Invention, Docket 10215, Status: Unfiled, Disclosure Date 1/7/22 (2022, Cornell University).

"High-Efficiency Al (Ga) N Ultraviolet Optoelectronics and Integrated Photonics"; Shin, W.J., University of Michigan, 2022 Ph.D.Thesis (2022, University of Michigan).

"High-efficiency, 80-mm aperture metalens telescope"; Zhang, L.; Chang, S.; Chen, X.; Ding, Y.; Rahman, M.T.; Duan, Y.; Stephen, M.; Ni, X., arXiv preprint arXiv:2205.12739 (2022, The Pennsylvania State University).

"High-Performance Chain Scissionable Resists for Extreme Ultraviolet Lithography: Discovery of the Photoacid Generator Structure and Mechanism"; Deng, J.; Bailey, S.; Jiang, S.; Ober, C.K., Chemistry of Materials, July 12, Vol 34, Issue 13, 6170-6181, http://dx.doi.org/10.1021/acs.chemmater.2c01444 (2022, Cornell University).

"High-speed tunable microwave-rate soliton microcomb"; He. Y., R. Lopez-Rios, U.A. Javid, J. Ling, M. Li, S. Xue, K. Vahala, Q. Lin, arXiv:2208.08046 [physics.optics, Submitted on 17 Aug 2022] (2022, University of Rochester).

"High-Throughput Biofilm Assay to Investigate Bacterial Interactions with Surface Topographies"; Lee, S.W.; Johnson, E.L.; Chediak, J.A.; Shin, H.; Wang, Y.; Phillips, K.S.; Ren, D., ACS Applied Bio Materials, Vol 5, Issue 8, Page(s) 3816-3825 (2022, Syracuse University).

"How to Unleash Power of Ga2O3?"; Xing, H.G., CS MANTECH Conference, May 9 -12, 2022; Invited Speaker (2022, Cornell University).

"Human mesenchymal stromal cells release functional mitochondria in extracellular vesicles"; Thomas, M.A.; Fahey, M.J.; Pugliese, B.J.; Irwin, R.M.; Antonyak, M.A.; Delco, M.L., Frontiers in Bioengineering and Biotechnology, 10:870193. doi: 10.3389/fbioe.2022.870193 (2022, Cornell University).

"Hyaluronic acid biosynthesis promotes an invasive, stem-like cancer cell phenotype by broadly altering metabolism"; Shimpi, A.A., M.L. Tan, M. Vilkhovoy, D. Dai, L. M. Roberts, J. Kuo, L. Huang, J. D. Varner, M. Paszek, C. Fischbach, bioRxiv preprint PPR: PPR504129 doi: https://doi.org/10.1101/2022.06.08.495338; posted June 9, 2022 (2022, Cornell University).

"Hybrid quantum devices using a superconducting resonator and low-damping magnons in an integrated platform"; Fuchs, G., 68th meeting of the American Vacuum Society, 2022 (2022, Cornell University).

"HZO-based FerroNEMS MAC for in-memory computing"; Jadhav, S.; Gund, V.; Davaji, B.; Jena, D.; Xing, H.G.; Lal, A., Applied Physics Letters, Nov 7, Vol 121, Issue 19, 193503, http://dx.doi.org/10.1063/5.0120629 (2022, Cornell University).

"IGF2BP2 Promotes Cancer Progression by Degrading the RNA Transcript Encoding a v-ATPase Subunit"; Latifkar, A.; Wang, F.; Mullmann, J.; Panizza, E.; Fernandez, I.; Ling, L.; Miller, A.; Fischbach, C.; Weiss, R.; Lin, H., Proceedings of the National Academy of Sciences, Vol 119, Issue 45, Page(s) e2200477119 (2022, Cornell University)

"IGF2BP2 Promotes Cancer Progression by Degrading the RNA Transcript Encoding a v-ATPase Subunit"; Wang, F., A.Latifkar, J.Mullmann, E.Panizza, I.Fernandez, L.Ling, A.Miller, C.Fischbach, R.Weiss, H.Lin, R.Cerione, M.Antonyak, FASEB Journal, Biochemistry and Molecular Biology, Volume 36, Issue S1, May 2022, https://doi.org/10.1096/fasebj.2022.36.S1.L7433 (2022, Cornell University).

"Imaging complex magnetic materials using single spins and heat"; Fuchs, G., Petaspin seminar, IEEE Magnetics society Italy chapter (virtual) 2022 (2022, Cornell University).

"Impedance sensing of antibiotic interactions with a pathogenic E. coli outer membrane supported bilayer"; Ghosh, S.; Mohamed, Z.; Shin, J.; Naser, S.; Bali, K.; Dörr, T.; Owens, R.; Salleo, A.; Daniel, S., Biosensors & Bioelectronics, May 15, Vol 204, 114045, http://dx.doi.org/10.1016/j.bios.2022.114045 (2022, Cornell University).

"Improving Low-Temperature CH4 Oxidation Performance with High-Silica Pd/CHA Zeolite Catalysts"; Liu, J.; Mon, T.; Kyriakidou, E.; Cybulskis, V.J., 2022 AIChE Annual Meeting, Phoenix, AZ (11/2022) (2022, Syracuse University).

"In situ Crystalline AlN Passivation for Reduced RF Dispersion in Strained-Channel AlN/GaN/AlN High-Electron-Mobility Transistors"; Chaudhuri, R.; Hickman, A.; Singhal, J.; Casamento, J.; Xing, H.G.; Jena, D., physica status solidi (a), Volume 219, Issue 4, Special Issue: Compound Semiconductors, February 2022, 2100452 (2022, Cornell University).

"In situ imaging of CDW phase transition in two-dimensional rare-earth tellurides using 4D-STEM"; Siddique, S. (contributed talk), MRS Fall Meeting in Boston (11/2022) (2022, Cornell University).

"In situ Sensing of Water Potential"; Gore, M., P. Jain, D. Pauli, A. Stroock, O. Vincent, Patent Issued, Docket # 7532-03-US, United States, Filed 1/28/20, 16/634,665, Issued 12/27/22, Patent 11,536,660 (2022, Cornell University).

"In vivo Capsid Engineering of Bacteriophages for Oriented Surface Conjugation"; Hufziger, K.A.; Farquharson, E.L.; Werner, B.G.; Chen, Q.; Goddard, J.M.; Nugen, S.R., ACS Applied Bio Materials, Vol 5, Issue 11, Page(s) 5104-5112 (2022, Cornell University).

"In-situ Ultrasonic Imaging of Printed Electronics Ink Deposition and Curing"; Baskota, A.; Ivy, L.; Ospina, C.; Kuo, J.; Hwang, J.; Gund, V.; Davaji, B.; Doerschuk, P.; Lal, A., https://www.researchgate.net/, publication 362242467 (2022, Cornell University).

"Initial nucleation of metastable γ-Ga2O3 during sub-millisecond thermal anneals of amorphous Ga2O3"; Gann, K.; Chang, C.; Chang, M.; Sutherland, D.; Connolly, A.; Muller, D.; van Dover, R.B.; Thompson, M., Applied Physics Letters, Vol 121, Issue 6, Page(s) 62102 (2022, Cornell University).

"Inkjet printing of epitaxially connected nanocrystal superlattices"; Balazs, D.M.; Erkan, N. D.; Quien, M.; Hanrath, T., Nano Research, Vol 15, Issue 5, Page(s) 4536-4543 (2022, Cornell University).

"Integrated Chip-Scale GHz Ultrasound Transducer and Micro-Electrode Arrays for Biological Interface Applications"; Balasubramanian, P., A. Lal, Invention, Docket 10315, Status: Filed - by Cornell, Disclosure Date 4/8/22 (2022, Cornell University).

"Integrated electronics on the aluminum nitride platform"; Hickman, A., Xing, H.G., Jena, D., patent application filed (2022, Cornell University).

"Integrated Photonic Devices with Inverse Weak Value Amplification for Precision Metrology"; Song, M., University of Rochester, 2022 Ph.D.Thesis (2022, University of Rochester).

"Integrated Pockels Laser"; Li, M., L. Chang, L. Wu, J. Staffa, J. Ling, U.A. Javid, S. Xue, Y. He, R. Lopez-rios, T.J. Morin, H. Wang, B. Shen, S. Zeng, L. Zhu, K.J. Vahala, J.E. Bowers, Q. Lin, Nature Communications volume 13, Article number: 5344 (2022) (2022, University of Rochester).

"Integrated Quantum Computing with Epitaxial Materials"; Dang, P., D. Jena, G. Khalsa, J. Wright, H.G. Xing, Patent Application, Docket # 9762-02-PC, Not Applicable (PCT App), Filed 2/17/22, PCT/US22/70708 (2022, Cornell University).

"Interfacial charge transfer and persistent metallicity of ultrathin SrIrO3/SrRuO3 heterostructures"; Nelson, J.; Schreiber, N.; Georgescu, A.; Goodge, B.; Faeth, B.; Parzyck, C.; Zeledon, C.; Kourkoutis, L.; Millis, A.; Georges, A., Science Advances, Feb 4, Vol 8, Issue 5, eabj0481, http://dx.doi.org/10.1126/sciadv.abj0481 (2022, Cornell University).

"Interstitial fluid flow-dependent AQP4 expression dictates endogenous protein aggregation in microfluidic glymphatics system in vitro"; Henderson, A.R., Brunkhorst, C., Eom, C.Y., Nishimura, N., Lee, E., Biomedical Engineering Society (BMES), San Antonio, TX (Oral presentation), 2022 (2022, Cornell University).

"Intracellular Forces and Nuclear Mechanobiology during Confined Cell Migration in 3-Dimensions"; Keys, J.T., Cornell University, 2022 Ph.D.Thesis (2022, Cornell University).

"Intrinsic spin Hall torque in a moiré Chern magnet"; Tschirhart, C. L., E. Redekop, L. Li, T. Li, S. Jiang, T. Arp, O. Sheekey, T. Taniguchi, K. Watanabe, K.F. Mak, J. Shan, A.F. Young, arXiv:2205.02823 (2022, Cornell University).

"Intrinsically Switchable GHz Ferroelectric ScAlN SAW Resonators"; Gund, V.; Nomoto, K.; Xing, H.G.; Jena, D.; Lal, A., 2022 IEEE International Symposium on Applications of Ferroelectrics (ISAF), IEEE, Page(s) 1-4 (2022, Cornell University).

"Investigating lymphatic vessel remodeling in pancreatic cancer and its implications for anti-tumor immunity using tumor-on-chip and mouse models"; Kolarzyk, A.M., Fowell, D., Lee, E., Gordon Research Conference (GRC) Lymphatics, Lucca, Italy, 2022 (2022, Cornell University).

"Investigating sarcomere length non-uniformity and repeatability in immunofluorescent labelled skeletal rabbit psoas muscles"; Desai, D., Sekhon, A., Leonard, T., Herzog, W., 23rd Annual Alberta Biomedical Engineering Conference, Banff AB, Oct 21-22, 2022 (2022, University of Calgary).

"Investigating the effects of confined cell migration on chromatin organization"; McAllister, J., Hsia, J., Hasan, O., Judd, J., Lee, S., Agrawal, R., Change, C.-Y., Soloway, P., Lammerding, J., American Society for Cell Biology CellBio 2022 conference. Washington, DC (Dec 4-7, 2022). Poster presentation selected from submitted abstract. (2022, Cornell University).

"Investigation of perpendicular magnetic anisotropy in Pt/Co20Fe60B20/Pt multi-layer structures"; Cestarollo, L.; Srinivasan, K.; El-Ghazaly, A., Journal of Magnetism and Magnetic Materials, Nov 15, Vol 562, 169825, http://dx.doi.org/10.1016/j.jmmm.2022.169825 (2022, Cornell University).

"It's good to have Lamins: nuclear mechanobiology in confined migration and muscle disease"; Lammerding, J.; Invited seminar, Connecting Intermediate Filaments international seminar series. Virtual Seminar (February 9, 2022) (2022, Cornell University).

"Ladder shaped microfluidic system enabling rapid antibiotic susceptibility testing with standardized concentration panel"; Nguyen, A.V.; Yaghoobi, M.; Azizi, M.; Davaritouchaee, M.; Abbaspourrad, A., bioRxiv, Posted August 26, 2022, doi: https://doi.org/10.1101/2022.08.26.505478 (2022, Cornell University).

"Large Signal Performance of AlN/GaN/AlN HEMTs at 94 GHz"; Hickman, A., International Conference of Nitride Semiconductors in Berlin, Germany (2022, Cornell University)

"Laser-Induced Graphene Pressure Sensors Manufactured via Inkjet PCB Printer : Locally Producing Super-Sensitive and Cost-Effective Circular Diaphragm Pressure Gauges"; Ivy, L., V. Gund, B. Davaji, C. Ospina, D. Ni, P. Doerschuk, A. Lal, 2022 IEEE International Conference on Flexible and Printable Sensors and Systems (FLEPS), Vienna, Austria, 2022, pp. 1-4, doi: 10.1109/FLEPS53764.2022.9781522 (2022, Cornell University).

"Liberating a hidden antiferroelectric phase with interfacial electrostatic engineering"; Mundy, J., B. Grosso, C. Heikes, D. Ferenc Segedin, Z. Wang, Y. Shao, C. Dai, B. Goodge, Q. Meier, C Nelson, B. Prasad, F. Xue, S. Ganschow, D. Muller, L. Kourkoutis, L. Chen, W. Ratcliff, N. Spaldin, R. Ramesh, D. Schlom, Science Advances, Vol 8, Issue 5, Page(s) eabg5860 (2022, Cornell University).

"Lorentz electron ptychography for imaging magnetic textures beyond the diffraction limit"; Chen, Z., E. Turgut, Y. Jiang, K.X. Nguyen, M.J. Stolt, S. Jin, D.C. Ralph, G.D. Fuchs, D.A. Muller, Nat. Nanotech. 17, 1165 (2022) (2022, Cornell University).

"Low lamin A levels enhance confined cell migration and metastatic capacity in breast cancer"; Bell, E.S.; Shah, P.; Zuela-Sopilniak, N.; Kim, D.; Varlet, A.A.; Morival, J.L.P.; McGregor, A.L.; Isermann, P.; Davidson, P.M.; Elacqua, J.J.; Lakins, J.N.; Vahdat, L.; Weaver, V.M.; Smolka, M.B.; Span, P.N.; Lammerding, J., Oncogene, September 2, Vol 41, Issue 36, 4211-4230, http://dx.doi.org/10.1038/s41388-022-02420-9 (2022, Cornell University).

"Low SWaP Hyperspectral Imaging Sensor for CubeSat Applications"; Bendoym, I.; Lepak, L.; Leitch, J.; Applegate, J.; Crouse, D., Proceedings of SPIE, Metamaterials, Metadevices, and Metasystems 2022, August 21-23, 2022, San Diego, CA, Vol 12195, 121950J, http://dx.doi.org/10.1117/12.2633886 (2022, Clarkson University).

"Low SWaP Hyperspectral Imaging Sensor for CubeSat Applications"; Bendoym, I.; Lepak, L.; Leitch, J.; Applegate, J.; Crouse, D., SPIE, Metamaterials, Metadevices, and Metasystems 2022, August 21-23, 2022, San Diego, CA, POSTER (2022, Clarkson University).

"Low SWaP-C Hyperspectral Metamaterial Spectrometer (MMS) for Narrow-Band, Wide Angle-of-Incidence MWIR Atmospheric Sensing"; Bendoym, I.; Lepak, L.; Leitch, J.; Applegate, J.; Crouse, D., Proceedings of SPIE, Image Sensing Technologies: Materials, Devices, Systems, and Applications Ix, April 03-JUN 12, 2022, ELECTR NETWORK, POSTER (2022, Clarkson University).

"Low SWaP-C Hyperspectral Metamaterial Spectrometer (MMS) for Narrow-Band, Wide Angle-of-Incidence MWIR Atmospheric Sensing"; Bendoym, I.; Lepak, L.; Leitch, J.; Applegate, J.; Crouse, D., Proceedings of SPIE, Image Sensing Technologies: Materials, Devices, Systems, and Applications Ix, April 03-JUN 12, 2022, ELECTR NETWORK, Vol 12091, 120910J, http://dx.doi.org/10.1117/12.2632794 (2022, Clarkson University).

"Low voltage FE-FET device for ultra low voltage high density and high-speed back end compatible 1T memory"; Avci, U., T. Gosavi, R. Kim, H. Li, C.-c. Lin, D. Nikonov, A. Penumatcha, R. Ramesh, D. Schlom, R. Steinhardt, I. Young, Invention, Docket 10230, Status: Filed - by Joint Owner, Disclosure Date 2/1/22 (2022, Cornell University).

"Low-power multilevel resistive switching in β-Ga2O3 based RRAM devices"; Velpula, R.T., B. Jain, H.P.T. Nguyen, Nanotechnology, Volume 34, Number 7, Published 2 December 2022 DOI 10.1088/1361-6528/aca418 (2022, New Jersey Institute of Technology).

"Magneto-thermal Microscopy and Single-spin Microscopy of Complex Magnetic Materials"; Fuchs, G., Spin Caloritronics, UIUC, 2022 (2022, Cornell University).

"Magnon Transport in Insulating Magnetic Thin Films"; Li, R., Cornell University, 2022 Ph.D.Thesis (2022, Cornell University).

"Measurements and Modeling of Atomic-Scale Sidewall Roughness and Losses in Integrated Photonic Devices"; Roberts, S.; Ji, X.C.; Cardenas, J.; Corato-Zanarella, M.; Lipson, M., Advanced Optical Materials, SEP, Vol 10, Issue 18, 2102073, http://dx.doi.org/10.1002/adom.202102073 (2022, Columbia University).

"Measuring sarcomere dynamics following fluorescent labelling of a a-actinin and myomesin structural proteins"; Sekhon, A., Desai, D., Leonard, T., Herzog, W., 23rd Annual Alberta Biomedical Engineering Conference, Banff AB, Oct 21-22, 2022 (2022, University of Calgary).

"Measuring sarcomere dynamics following immunofluorescent labelling of alpha-actinin and myomesin structural proteins"; Sekhon, A., Herzog, W., North American Congress on Biomechanics (NACOB), Ottawa ON, Aug 21-25, 2022. (2022, University of Calgary).

"Mechanical stimuli activate gene expression via a cell envelope stress sensing pathway"; Harper, C.E.; Zhang, W.; Shin, J.-H.; van Wijngaarden, E.; Chou, E.; Lee, J.; Wang, Z.; Dörr, T.; Chen, P.; Hernandez, C.J., bioRxiv, Posted September 25, 2022, doi: https://doi.org/10.1101/2022.09.25.509347 (2022, Cornell University).

"Mechanically induced nuclear damage as a driver of muscle disease and therapeutic target in laminopathies"; Lammerding, J.; Invited talk, LMNA Related Cardiac Disease Network Meeting. Virtual conference (April 13, 2022) (2022, Cornell University).

"Metabolic Regulation of Breast Cancer Cell Invasion in the Perivascular Niche"; Tan, M.L., N. Jenkins-Johnston, P. Shah, J. Lammerding, W.R. Zipfel, C. Fischbach, Gordon Research Conference for Signal Transduction by Engineered Extracellular Matrices, Manchester NH, August 2022 (2022, Cornell University).

"Metal Etchant Compositions and Methods of Fabricating a Semiconductor Device Using the Same"; Jeong, J., K. Kim, Y. Ko, K. Lee, H. Lee, C. Lin, C. Ober, Patent Issued, Docket # 6614-03-KR, South Korea, Filed 10/6/21, 10-2014-0103753, Issued 4/7/22, Patent 10-2385915 (2022, Cornell University).

"Methods for improving rate capability of lithium sulfur batteries"; Joo, Y., Invention, Docket 10535, Status: Unfiled, Disclosure Date 11/1/22 (2022, Cornell University).

"Micro-triboelectric generator for zero-power shock detection"; Alzgool, M.; Mousavi, M.; Davaji, B.; Towfighian, S., Nano Energy, Vol 103, Page(s) 107758 (2022, Binghamton University).

"Micrometer-sized, electrically morphing metamaterial-robots (MetaBots)"; Liu, Q., W. Wang, H. Sinhmar, I. Griniasty, M.F. Reynolds, H. Kress-Gazit, P.L. McEuen, I. Cohen, Bulletin of the American Physical Society, APS March Meeting 2022 Bulletin, Vol 67, # 3, March 14–18, 2022; Chicago, Abstract: B21.00007 (2022, Cornell University).

"Micron-scale biophysical dynamics of reovirus nonstructural protein μNS inclusion bodies"; Crowley, J.C., Brodrick, A.J., Parker, J.S.L., Zipfel, W.R., Biophysical Journal. 2022 February 11; 121(3):472a (2022, Cornell University).

"Micropatterned Ligand Arrays to Investigate Spatial Regulation of Cellular Signaling Initiated by Clustered Fc Receptors"; Mohr, J.D., M. Ramezani, D. Holowka, B.A. Baird, Methods in Molecular Biology 2421 (Immune Receptors), pp. 1-19 (2022), https://link.springer.com/protocol/10.1007/978-1-0716-1944-5_1 (2022, Cornell University).

"Microscope-based light gradient generation for quantitative growth studies of photosynthetic micro-organisms"; Liu, F.; Gaul, L.; Shu, F.; Vitenson, D.; Wu, M., Lab on a Chip, Vol 22, Issue 17, Page(s) 3138-3146 (2022, Cornell University).

"Microscopic robots with onboard digital control"; Reynolds, M.F.; Cortese, A.J.; Liu, Q.; Zheng, Z.; Wang, W.; Norris, S.L.; Lee, S.; Miskin, M.Z.; Molnar, A.C.; Cohen, I., Science Robotics, Vol 7, Issue 70, Page(s) eabq2296 (Featured on cover) (2022, Cornell University).

"Miniature optical system for wide-range spectrofluorometry"; DeNapoli, J., J. Horwitz, L. Huang, P. Jain, C. Luo, Y. Peng, A. Stroock, Invention, Docket 10584, Status: Unfiled, Disclosure Date 12/20/22 (2022, Cornell University).

"Mitigation of quasiparticle poisoning in superconducting qubits using normal metal backside metallization"; Iaia, V., et al. – Contributed talk, American Physical Society March Meeting (virtual due to COVID), March 16, 2022 (2022, Syracuse University).

"Modular Synthesis of Phthalaldehyde Derivatives Enabling Access to Photoacid Generator-Bound Self-Immolative Polymer Resists with Next-Generation Photolithographic Properties"; Deng, J.; Bailey, S.; Jiang, S.; Ober, C.K., Journal of the American Chemical Society, Vol 144, Issue 42, Page(s) 19508-19520 (2022, Cornell University)

"Molecular beam homoepitaxy of N-polar AlN on bulk AlN substrates"; Singhal, J., J. Encomendero, Y. Cho, L. van Deurzen, Z. Zhang, K. Nomoto, M. Toita, H.G. Xing, D. Jena, AIP Advances 12, 095314 (2022); https://doi.org/10.1063/5.0100225, editors-pick (2022, Cornell University).

"Mucins form a nanoscale material barrier against immune cell attack"; Park, S.; Colville, M.J.; Shurer, C.R.; Huang, L.-T.; Kuo, J.C.-H.; Paek, J.H.; Goudge, M.C.; Su, J.; DeLisa, M.P.; Lammerding, J., bioRxiv, Posted January 29, 2022, doi: https://doi.org/10.1101/2022.01.28.478211 (2022, Cornell University).

"Multi-level Analog Programmable Graphene Resistive Memory with Fractional Channel Ferroelectric Switching in Hafnium Zirconium Oxide"; Gund, V.; Davaji, B.; Jadhav, S.; Lee, H.; Jena, D.; Xing, H.G.; Lal, A., 2022 Joint Conference of the European Frequency and Time Forum and IEEE International Frequency Control Symposium (EFTF/IFCS), IEEE, Page(s) 1-4 (2022, Cornell University).

"Multi-modal in situ characterizations for phase transformations of nanomaterials"; Cha, J. (Invited Talk), MRS Fall Meeting in Boston (11/2022) (2022, Cornell University).

"N-polar GaN p-n junction diodes with low ideality factors"; Nomoto, K.; Xing, H.G.; Jena, D.; Cho, Y.J., Applied Physics Express, Vol 15, Issue 6, Page(s) 64004 (2022, Cornell University).

"Nano-Filamented Textile Sensor Platform with High Structure Sensitivity"; Yan. S., D.K. Dinh, G. Shang, S. Wang, W. Zhao, X. Liu, R. Robinson, J.P. Lombardi III, N. He, S. Lu, M. Poliks, B.S. Hsiao, I. Gitsov, C.-J. Zhong, ACS Appl. Mater. Interfaces 2022, 14, 13, 15391–15400, March 25, 2022, https://doi.org/10.1021/acsami.2c00021 (2022, Binghamton University).

"Nanocalorimetry using microscopic optical wireless integrated circuits"; Smart, C.L.; Cortese, A.J.; Ramshaw, B.J.; McEuen, P.L., Proceedings of the National Academy of Sciences, Vol 119, Issue 45, Page(s) e2205322119 (2022, Cornell University).

"Nanomolding of Copper Interconnects"; Cha, J.J., M. Kiani, Invention, Docket 10518, Status: Filed - by Cornell, Disclosure Date 10/19/22 (2022, Cornell University).

"Nanomolding of electrical interconnects"; Cha, J., Filed provisional patent (U.S. Serial No. 63/428,280), November 28, 2022 (2022, Cornell University).

"Nanomolding of Electrical Interconnects"; Cha, J.J., M. Kiani, Patent Application, Docket # 10518-01-US, United States, Filed 11/28/22, 63/428,280 (2022, Cornell University).

"Nanomolding of metastable Mo4P3"; Kiani, M.T.; Sam, Q.P.; Jin, G.; Pamuk, B.; Han, H.J.; Hart, J.L.; Stauff, J.R.; Cha, J.J., arXiv preprint arXiv:2210.13392 (2022, Cornell University).

"Nematode Species Differentiation Using GHz Ultrasonic Micro Imager"; Baskota, A.; Kuo, J.; Ardanuç, S.; Lal, A., 2022 IEEE International Ultrasonics Symposium (IUS), IEEE, Page(s) 1-4 (2022, Cornell University).

"Ni3Si2 nanowires for efficient electron field emission and limitations of the Fowler-Nordheim model"; Belkadi, A.; Zeng, E.M.; Isakovic, A.F., Journal of Vacuum Science & Technology B, JAN, Vol 40, Issue 1, 13202, http://dx.doi.org/10.1116/6.0001248 (2022, Colgate University).

"Niobium-tantalum oxide as a material platform for linear and nonlinear integrated photonics"; MacFarlane, N.; Schreyer-Miller, A.; Foster, M.A.; Houck, W.D.; Foster, A.C., Optics Express, Vol 30, Issue 23, Page(s) 42155-42167 (2022, VIAVI Solutions).

"Non-contact ultrasound oocyte denudation"; Mokhtare, A.; Davaji, B.; Xie, P.; Yaghoobi, M.; Rosenwaks, Z.; Lal, A.; Palermo, G.; Abbaspourrad, A., Lab on a Chip, Vol 22, Issue 4, Page(s) 777-792 (2022, Cornell University).

"Nonlinear electrophoretic velocity of DNA in slitlike confinement"; Lamontagne, M.; Levy, S., Physical Review E, Vol 105, Issue 5, Page(s) 54503 (2022, Binghamton University).

"Nonreciprocity in Photon Pair Correlations of Classically Reciprocal Systems"; Graf, A.; Rogers, S.D.; Staffa, J.; Javid, U.A.; Griffith, D.H.; Lin, Q., Physical Review Letters, Vol 128, Issue 21, Page(s) 213605 (2022, University of Rochester).

"Nuclear actin polymerization promotes DNA damage response"; Varlet, A.A., Wolfson, H.A., Lammerding, J., Biomedical Engineering Society (BMES) Annual Meeting. San Antonio, TX (Oct 13-15, 2022). Poster presentation selected from submitted abstract. (2022, Cornell University).

"Nuclear mechanobiology during confined migration"; Lammerding, J.; Invited platform presentation, Biophysical Society Annual Meeting. San Francisco, CA (February 19, 2022) (2022, Cornell University).

"Nuclear mechanobiology during confined migration"; Lammerding, J.; Invited platform presentation, World Congress of Biomechanics, Taipei, Taiwan. Virtual attendance (July 12, 2022) (2022, Cornell University).

"Nuclear mechanobiology in confined cancer cell migration"; Lammerding, J.; Keynote talk, Biomedical Engineering Society (BMES) Annual Meeting. San Antonio, TX (October 14, 2022). 'Mechanisms of cancer cell migration and invasion' session, along with platform presentation selected from submitted abstract. (2022, Cornell University).

"Nuclear mechanobiology in confined migration"; Lammerding, J.; Invited seminar, University of Pennsylvania NSF funded Science and Technology Center for Engineering Mechanobiology. Virtual Seminar (February 25, 2022) (2022, Cornell University).

"Nuclear mechanobiology in confined migration and cancer metastasis"; Lammerding, J., National Cancer Institute Cancer Systems Biology Consortium (CSBC) / Physical Science Oncology Network (PS-ON) Cell & Tissue Mechanics Working Group seminar series. Virtual Seminar (September 8, 2022) (2022, Cornell).

"Optically pumped deep-UV multimode lasing in AlGaN double heterostructure grown by molecular beam homoepitaxy"; van Deurzen, L.; Page, R.; Protasenko, V.; Nomoto, K.; Xing, H.G.; Jena, D., AIP Advances, Vol 12, Issue 3, Page(s) 35023 (2022, Cornell University).

"Optimized Solid-Phase Mesh-Enhanced Sorption from Headspace (SPMESH) for Rapid Sub-ng/kg Measurements of 3-Isobutyl-2-methoxypyrazine (IBMP) in Grapes"; Bates, T.L., J. Rafson, H. Feng, B.S. Pan, B.R.J. Mueller, B. Yancey, W. Fatigante, G.L. Sacks, Molecules 2022, 27(19), 6195; https://doi.org/10.3390/molecules27196195 (2022, Cornell University).

"Ordered, cubic ZrNb alloys with high critical temperature in the theoretical limit, method of making same, and use for superconducting applications"; Liepe, M., T. Oseroff, Z. Sun, Patent Application, Docket # 10502-01-US, United States, Filed 11/11/22, 63/383,387 (2022, Cornell University).

"Ordered, cubic ZrNb alloys with high critical temperature in the theoretical limit, method of making same, and use for superconducting applications"; Liepe, M., T. Oseroff, Z. Sun, Invention, Docket 10502, Status: Filed - by Cornell, Disclosure Date 10/5/22 (2022, Cornell University).

"Ordering Transitions of Liquid Crystals Triggered by Metal Oxide-catalyzed Reactions of Sulfur Oxide Species"; Bao, N.; Gold, J.I.; Sheavly, J.K.; Schauer, J.J.; Zavala, V.M.; Van Lehn, R.C.; Mavrikakis, M.; Abbott, N.L., Journal of the American Chemical Society, Vol 144, Issue 36, Page(s) 16378-16388 (2022, Cornell University).

"Origin of transverse voltages generated by thermal gradients and electric fields in ferrimagnetic-insulator/heavy-metal bilayers"; Bose, A.; Jain, R.; Bauer, J.J.; Buhrman, R.A.; Ross, C.A.; Ralph, D.C., Physical Review B, Vol 105, Issue 10, Page(s) L100408 (2022, Cornell University)

"Rapid Identification of DNA Fragments through Direct Sequencing with Electro-Optical Zero-Mode Waveguides"; Farhangdoust, F., M. Amin Alibakshi, F. Cheng, W. Liang, Y. Liu, M. Wanunu, Advanced Materials, Vol 34, Issue 9, March 3, 2022, https://doi.org/10.1002/adma.202108479 (2022, Northeastern University).

"Re-entrant transition as a bridge of broken ergodicity in confined monolayers of hexagonal prisms and cylinders"; Prajwal, B.P.; Huang, J.-Y.; Ramaswamy, M.; Stroock, A.D.; Hanrath, T.; Cohen, I.; Escobedo, F.A., Journal of Colloid and Interface Science, Vol 607, Page(s) 1478-1490 (2022, Cornell University).

"Realization of the Haldane Chern insulator in a moiré lattice"; Zhao, W., K. Kang, L. Li, C. Tschirhart, E. Redekop, K. Watanabe, T. Taniguchi, A. Young, J. Shan, K.F. Mak, arXiv:2207.02312 (2022, Cornell University)

"Rear cortex contraction aids in nuclear transit during confined migration by increasing pressure in the cell posterior"; Keys, J.T.; Cheung, B.C.H.; Wu, M.; Lammerding, J., bioRxiv, Posted September 21, 2022, doi: https://doi.org/10.1101/2022.09.10.507419 (2022, Cornell University).

"Recent advance in phase transition of vanadium oxide based solar reflectors and the fabrication progress"; Mirbagheri, G.; Crouse, D.T.; Tan, C.K., Proceedings of SPIE, Physics and Simulation of Optoelectronic Devices Xxx, January22-FEB 28, 2022, ELECTR NETWORK, Vol 11995, 119950O, http://dx.doi.org/10.1117/12.2626406 (2022, Clarkson University).

"Recovery of energy critical high value metals using functionalized materials"; Asgar, H., G. Gadikota, S. Mohammed, P. Ochonma, T. Yin, R. Zheng, Patent Application, Docket # 10453-01-US, United States, Filed 11/3/22, 63/382,203 (2022, Cornell University).

"Recovery of energy critical high value metals using functionalized materials"; Asgar, H., G. Gadikota, S. Mohammed, P. Ochonma, T. Yin, R. Zheng, Invention, Docket 10453, Status: Filed - by Cornell, Disclosure Date 8/19/22 (2022, Cornell University).

"Reducing phonon-mediated quasiparticle poisoning of qubits with normal metal reservoirs"; Iaia, V., et al. – Poster presentation, Applied Superconductivity Conference, Honolulu, HI, Oct. 24-28, 2022 (2022, Syracuse University).

"Reduction of surface oxidation in molecular beam epitaxy sources"; Cho, Y., D. Jena, J. McCandless, V. Protasenko, H.G. Xing, Patent Application, Docket # 9803-01-US, United States, Filed 6/28/22, 63/356,445 (2022, Cornell University).

"Regulation of Tumor Invasion by the Physical Microenvironment: Lessons from Breast and Brain Cancer"; Beeghly, G.F.; Amofa, K.Y.; Fischbach, C.; Kumar, S., Annual Review of Biomedical Engineering, Vol 24, Page(s) 29-59 (2022, Cornell University).

"Resistive Electrodes on Ferroelectric Devices for Linear Piezoelectric Programming"; Davaji, B., V. Gund, S. Jadhav, D. Jena, A. Lal, H.G. Xing, Patent Application, Docket # 10038-02-US, United States, Filed 8/23/22, 17/821,789 (2022, Cornell University).

"Resonator nanophotonic standing-wave array trap for single-molecule manipulation and measurement"; Ye, F.; Inman, J.T.; Hong, Y.; Hall, P.M.; Wang, M.D., Nature Communications, Vol 13, Issue 1, Page(s) 1-10 (2022, Cornell University).

"Reversible Computing: Adiabatic Capacitive Logic"; Cordova, R.C., University of Notre Dame, 2022 Ph.D.Thesis (2022, University of Notre Dame).

"Review of essential use of fluorochemicals in lithographic patterning and semiconductor processing"; Ober, C.K., F. Kafer, J. Deng, Journal of Micro/Nanopatterning, Materials, and Metrology, Vol. 21, Issue 1, 010901 (March 2022). https://doi.org/10.1117/1.JMM.21.1.010901 (2022, Cornell University).

"RF Reflectometry of NEMS Motional Capacitance with Micromanipulator Probe"; Celis-Cordova, R.; Williams, E.M.; Cayaspo, G.J.Q.; Gose, J.J.; Brown, A.F.; Chisum, J.D.; Orlov, A.O.; Snider, G.L., 2022 IEEE Silicon Nanoelectronics Workshop (SNW), IEEE, Page(s) 1-2 (2022, University of Notre Dame).

"Rheotaxis quality index: a new parameter that reveals male mammalian in vivo fertility and low sperm DNA fragmentation"; Yaghoobi, M.; Azizi, M.; Mokhtare, A.; Javi, F.; Abbaspourrad, A., Lab on a Chip, Vol 22, Issue 8, Page(s) 1486-1497 (2022, Cornell).

"Rheotaxis-Basis Separation of Motile Sperms and Bacteria Using a Microfluidic Corral System"; Abbaspourrad, A., S. Cheong, M. Zaferani, Patent Issued, Docket # 8071-02-US, United States, Filed 4/3/19, 16/374,529, Issued 11/8/22, Patent 11,491,485 (2022, Cornell University).

"Rheotaxis-Basis Separation of Motile Sperms and Bacteria Using a Microfluidic Corral System"; Abbaspourrad, A., S. Cheong, M. Zaferani, Patent Application, Docket # 8071-03-US, United States, Filed 11/7/22, 17/981,711 (2022, Cornell University).

"Sagnac interferometry for high-sensitivity optical measurements of spin-orbit torque"; Luo, Y.K.; Karimeddiny, S.; Cham, T.M.J.; Mak, K.F.; Shan, J.; Ralph, D.C., APS Bulletin, APS March Meeting, abstract id.G52.001, 2022APS.MARG52001L (2022, Cornell).

"Sagnac interferometry for high-sensitivity optical measurements of spin-orbit torque"; Luo, Y.K.; Karimeddiny, S.; Cham, T.M.J.; Mak, K.F.; Shan, J.; Ralph, D.C., Spintronics XV; PC122050R (2022) Proceedings Volume PC12205, https://doi.org/10.1117/12.2633424, SPIE Nanoscience + Engineering, 2022, San Diego, CA (2022, Cornell University).

"Scissionable polymer photoresist for EUV lithography"; Deng, J.; Bailey, S.; Ober, C.K., SPIE Advances in Patterning Materials and Processes XXXIX, Vol 12055, Page(s) 132-138 (2022, Cornell University).

"Select area semi-insulating gallium oxide by iron implantation"; Cromer, B., D. Dryden, D. Jena, H. G. Xing, Invention, Docket 10396, Status: Filed - by Cornell, Disclosure Date 6/10/22 (2022, Cornell University).

"Self-injection-locked second-harmonic integrated source"; Ling, J., J. Staffa, H. Wang, B. Shen, L. Chang, U.A. Javid, L. Wu, Z. Yuan, R. Lopez-Rios, M. Li, Y. He, B. Li, J.E. Bowers, K.J. Vahala, Q. Lin, arXiv:2207.03071 [physics.optics] [Submitted on 7 Jul 2022] (2022, University of Rochester).

"Self-Organization under Confinement (part 2)"; Cohen, I., Lorentz Center Workshop (2022) (2022, Cornell University).

"Separation of Artifacts from Spin-Torque Ferromagnetic Resonance Measurements of Spin-Orbit Torque for the Low-Symmetry Van der Waals Semi-Metal ZrTe3"; Cham, T.M.; Karimeddiny, S.; Gupta, V.; Mittelstaedt, J.A.; Ralph, D.C., Advanced Quantum Technologies, Vol 5, Issue 2, Page(s) 2100111 (2022, Cornell University).

"Sheathless inertial microfluidic cell separation via a serpentine–contraction–expansion device coupled with a combinatorial extraction regulator"; Javi, F.; Zaferani, M.; Lopez-Barbosa, N.; DeLisa, M.P.; Abbaspourrad, A., Microfluidics and Nanofluidics, Vol 26, Issue 7, Page(s) 1-10 (2022, Cornell University).

"Single Cell Whole Genome Amplification Via Micropillar Arrays Under Flow Conditions"; Craighead, H., H. Tian, Patent Issued, Docket # 7443-03-US, United States, Filed 11/20/18, 16/303,659, Issued 7/12/22, Patent 11,383,240 (2022, Cornell University).

"Single Cell Whole Genome Amplification Via Micropillar Arrays Under Flow Conditions"; Craighead, H., H. Tian, Patent Application, Docket # 7443-04-US, United States, Filed 6/4/22, 17/832,628 (2022, Cornell University).

"Skeletal muscle titin IG domain refolding after passive lengthening"; Leonard, T., Faridi, W., Ramrattan, D., Schappacher-Tilp, G., Moo, E.K., Herzog, W., 66th Biophysical Society Annual Meeting, San Francisco, CA, Feb 19-23, 2022 (2022, University of Calgary).

"Smart Microscopic Robots"; McEuen, P., Bulletin of the American Physical Society, APS March Meeting 2022, March 14-18, 2022, Chicago; (2022, Cornell University).

"Smooth and homogenous Nb3Sn superconductors, method of making same, and use for superconducting radio-frequency accelerators"; Liepe, M., Z. Sun, Invention, Docket 10495, Status: Closed - In Process, Disclosure Date 9/27/22 (2022, Cornell University)

"Soft, strong, tough and durable gelatin fiber hydrogels"; Butcher, J., M. Wang, Patent Application, Docket # 10373-01-US, United States, Filed 11/11/22, 63/424,772 (2022, Cornell University).

"Soft, strong, tough and durable gelatin fiber hydrogels"; Butcher, J., M. Wang, Invention, Docket 10373, Status: Filed - by Cornell, Disclosure Date 5/19/22 (2022, Cornell University).

"Solution deposition of silanes films on thermoplastic polyurethane blend optical fibers for enhancing silicone cladding adhesion in wearable stretchable optical waveguide strain sensors."; Miller, R., R. Shepherd, Invention, Docket 10223, Status: Filed - Attorney Instructed to File, Disclosure Date 1/26/22 (2022, Cornell University).

"Spatial and temporal dynamics of RhoA activities of single breast tumor cells in a 3D environment revealed by a machine learning-assisted FRET technique"; Cheung, B.C.H., L. Hodgson, J.E. Segall, M. Wu, Experimental Cell Research, Volume 410, Issue 2, 15 January 2022, 112939, https://doi.org/10.1016/j.yexcr.2021.112939 (2022, Cornell University).

"Spatial Total RNA-Sequencing (spTotal)"; Cosgrove, B., I. De Vlaminck, M. Mantri, D. McKellar, H. Shi, Invention, Docket 10252, Status: Filed - by Cornell, Disclosure Date 2/17/22 (2022, Cornell University).

"Sperm Separation Devices and Uses Thereof"; Abbaspourrad, A., M. Yaghoobi, Patent Application, Docket # 10436-01-US, United States, Filed 11/4/22, 63/422,803 (2022, Cornell University).

"Spin-Polarized Fractional Corner Charges and Their Photonic Realization"; Gladstone, R.G.; Jung, M.; Shvets, G., Physical Review Letters, Vol 128, Issue 2, Page(s) 26801 (2022, Cornell University).

"Squish and squeeze – Nuclear mechanobiology in cell migration and muscle disease"; Lammerding, J.; Invited seminar, Cellular, and Developmental Biology (MCDB) Program, Student selected speaker. The Ohio State University. Columbus, OH (October 25, 2022) (2022, Cornell University).

"Squish and squeeze – Nuclear mechanobiology in cell migration and muscle disease"; Lammerding, J.; Invited seminar, Max Planck Institute for Molecular Biomedicine. Münster, Germany (November 10, 2022) (2022, Cornell University).

"Squish and squeeze – Nuclear mechanobiology in cell migration and muscle disease"; Lammerding, J.; Invited seminar, Radboud University Medical Center. Nijmegen, The Netherlands (November 8, 2022) (2022, Cornell University).

"Squish and squeeze – Nuclear mechanobiology in cell migration and muscle disease"; Lammerding, J.; Invited seminar, University of Technology Delft. Delft, The Netherlands (November 14, 2022) (2022, Cornell University).

"Stochastic induction dynamics of the lac operon"; Cortes, L.B., Bulletin of the American Physical Society, APS March Meeting 2022, Vol 67, Number 3, Monday–Friday, March 14–18, 2022; Chicago (2022, Cornell University).

"Strategies to Realize Never-Before-Synthesized Epitaxial Films"; Barone, M.R., Cornell University, 2022 Ph.D.Thesis (2022, Cornell University).

"Strong photon-magnon coupling using a lithographically defined organic ferrimagnet"; Xu, Q.; Cheung, H.F.H.; Cormode, D.S.; Puel, T.O.; Yusuf, H.; Chilcote, M.; Flatté, M.E.; Johnston-Halperin, E.; Fuchs, G.D., arXiv preprint arXiv:2212.04423 (2022, Cornell University).

"Strong variation of spin-orbit torques with relative spin relaxation rates in ferrimagnets"; Zhu, L.; Ralph, D.C., arXiv preprint arXiv:2210.11042 (2022, Cornell University).

"Superconducting metamaterials for quantum simulations and qubit addressability in quantum processors"; Plourde, B.L.T., US Patent Application, 17/545,592, 2022 (2022, Syracuse University).

"Superconducting Qubit Control with Single Flux Quantum Pulses in a Multi-chip Module"; Ballard, A., et al. – Contributed talk, American Physical Society March Meeting (virtual due to COVID), March 14, 2022 (2022, Syracuse University).

"Supercooling of the A phase of 3He"; Tian, Y.; Lotnyk, D.; Eyal, A.; Zhang, K.; Zhelev, N.; Abhilash, T.S.; Chavez, A.; Smith, E.; Hindmarsh, M.; Saunders, J.; Mueller, E.; Parpia, J., arXiv preprint arXiv:2208.14981 (2022, Cornell University).

"Supercritical carbon dioxide in an array of micro impinging jets"; Adeoye, S., P. Ahmed, Y. Peles, International Journal of Heat and Mass Transfer, Volume 196, 1 November 2022, 123215, https://doi.org/10.1016/j.ijheatmasstransfer.2022.12321 (2022, University of Central Florida).

"Superfluid response of an atomically thin, gate-tuned van der Waals superconductor"; Jarjour, A.; Ferguson, G.M.; Schaefer, B.T.; Lee, M.; Loh, Y.L.; Trivedi, N.; Nowack, K.C., arXiv preprint arXiv:2209.11800 (2022, Cornell University).

"Suppressing Correlated Errors in Superconducting Qubits through Phonon Downconversion"; Plourde, B.L.T. (Invited talk), Workshop on Quantum Coherence, Information, and Computing, Stevens Institute of Technology, Hoboken, NJ, Oct. 13, 2022 (2022, Syracuse University).

"Surface Acoustic Wave (SAW)-based Inertial Sensor Methods and Applications"; Ardanuc, S., A. Lal, Patent Issued, Docket # 7370-03-US, United States, Filed 8/31/18, 16/081,559, Issued 2/15/22, Patent 11,249,105 (2022, Cornell University).

"Surviving under pressure: adaptation to mechanical forces as a key step in the evolution of multicellular life "; Lammerding, J., Status Symposium of the Volkswagen Foundation. "Life? – A fresh scientific approach to the basic principles of life". Hannover, Germany (Nov. 30, 2022) (2022, Cornell University).

"Switchable moiré potentials in ferroelectric WTe2/WSe2 superlattices"; Kang, K., W. Zhao, Y. Zeng, K. Watanabe, T. Taniguchi, J. Shan, K.F. Mak, arXiv:2209.04981 (2022, Cornell).

"Synchronization in Coupled Opto-thermal Silicon MEMS Limit Cycle Oscillators"; Bhaskar, A., Cornell University, 2022 Ph.D.Thesis (2022, Cornell University).

"Synchronization in pairs of opto-thermally driven mechanically coupled micro-oscillators"; Bhaskar, A., M. Walth, R.H. Rand, A.T. Zehnder, arXiv:2207.09376, July 2022, DOI: 10.48550/arXiv.2207.09376 (2022, Cornell University).

"Synchronization in pairs of opto-thermally driven mechanically coupled micro-oscillators"; Bhaskar, A., M. Walth, R.H. Rand, A.T. Zehnder, Journal of Microelectromechanical Systems, 2022. https://doi.org/10.1109/JMEMS.2022.3229957 (2022, Cornell University).

"Synthesis of End-Cap Enabled Self-Immolative Photoresists For Extreme Ultraviolet Lithography"; Deng, Ji.; Bailey, S.; Ai, R.; Delmonico, A.; Denbeaux, G.; Jiang, S.; Ober, C.K., ACS Macro Letters, Vol 11, Issue 9, Page(s) 1049-1054 (2022, Cornell).

"Synthesis of metastable Ruddlesden–Popper titanates, (ATiO3) nAO, with n ≥ 20 by molecular-beam epitaxy"; Barone, M.R.; Jeong, M.; Parker, N.; Sun, J.; Tenne, D.A.; Lee, K.; Schlom, D.G., APL Materials, Vol 10, Issue 9, Page(s) 91106 (2022, Cornell)

"Synthesis of N-Substituted Maleimides and Poly (styrene-co-N-maleimide) Copolymers and Their Potential Application as Photoresists"; Eken, G.; Käfer, F.; Yuan, C.; Andrade, I.; Ober, C.K., Macromolecular Chemistry & Physics, 12 August 2022, Page(s) 2200256, https://doi.org/10.1002/macp.202200256 (2022, Cornell).

"System and method for enabling highly reversible, long-duration, cost-effective Al batteries"; Archer, L., M.G. Mendez, J. Zheng, Invention, Docket 10280, Status: Filed - by Cornell, Disclosure Date 3/15/22 (2022, Cornell University).

"Systems and Methods for On-Chip Analysis of Nucleic Acids and for Multiplexed Analysis of Cells"; Bisogni, A., H.Craighead, D.Lin, H.Tian, Patent Application, United States 20220016629, 01/20/2022 (2022, Cornell University).

"Systems and Methods for On-Chip Analysis of Nucleic Acids and for Multiplexed Analysis of Cells"; Craighead, H.; Tian, H., Patent Application, Europe, 01/20/2022 (2022, Cornell University).

"Temperature Dependence of the Emission Spectrum of GaN Defect Single-Photon Emitters"; Geng, Y., J. Luo, L. van Deurzen, H.G. Xing, D. Jena, G.D. Fuchs, F. Rana, arXiv:2206.12636 (2022) (2022, Cornell University).

"Textured Electrodes: Manipulating Built-In Crystallographic Heterogeneity of Metal Electrodes via Severe Plastic Deformation"; Archer, L., J. Zheng, Invention, Docket 10364, Status: Filed - by Cornell, Disclosure Date 5/3/22 (2022, Cornell University).

"The dynamics of sarcomere length non-uniformity from passive to active states in skeletal muscles"; Li, M., W. Herzog, North American Congress on Biomechanics (NACOB), Ottawa ON, Aug 21-25, 2022 (2022, University of Calgary).

"The effect of hold time on mechanical properties of myofibrils stretched passively due to immunoglobulin domain unfolding and refolding"; Tiessen, C., Leonard, T., Herzog, W., 23rd Annual Alberta Biomedical Engineering Conference, Banff AB, Oct 21-22, 2022 (2022, University of Calgary).

"The Lamin A/C Ig-fold undergoes cell density-dependent changes that alter epitope accessibility"; Wallace, M.; Fedorchak, G.R.; Agrawal, R.; Gilbert, R.M.; Patel, J.; Park, S.; Paszek, M.; Lammerding, J., bioRxiv, Posted November 22, 2022., doi: https://doi.org/10.1101/2022.11.22.517482 (2022, Cornell University).

"The Roles of Sub-Micron and Microscale Roughness on Shear-Driven Thrombosis on Titanium Alloy Surfaces"; Jayaraman, A., J. Kang, J.F. Antaki, B.J. Kirby, Artifical Organs, Wiley Online Library, First published: 24 November 2022 https://doi.org/10.1111/aor.14467 (2022, Cornell University).

"The Squares: US Physical and Engineering Scientists in the Long 1970s"; Mody, Cyrus C. M., MIT Press, Jul 12, 2022 (2022, Maastricht University).

"Theory of Nb-Zr Alloy Superconductivity and First Experimental Demonstration for Superconducting Radio-Frequency Cavity Applications"; Sitaraman, N.S.; Sun, Z.; Francis, B.; Hire, A.C.; Oseroff, T.; Baraissov, Z.; Arias, T.A.; Hennig, R.; Liepe, M.U.; Muller, D.A., arXiv preprint arXiv:2208.10678 (2022, Cornell University).

"Thermally-generated spin current in the topological insulator Bi2Se3"; Jain, R.; Stanley, M.; Bose, A.; Richardella, A.R.; Zhang, X.S.; Pillsbury, T.; Muller, D.A.; Samarth, N.; Ralph, D.C., arXiv preprint arXiv:2210.05636 (2022, Cornell University).

"Thermomechanical Nanomolding in 2D"; Kiani, M.T. (contributed talk), MRS Fall Meeting in Boston (11/2022) (2022, Cornell).

"Thermomechanical nanomolding of topological materials"; Sam, Q. (contributed talk), MRS Fall Meeting in Boston (11/2022) (2022, Cornell University).

"Threshold switching stabilization of NbO2 films via nanoscale devices"; Sullivan, M.C.; Robinson, Z.R.; Beckmann, K.; Powell, A.; Mburu, T.; Pittman, K.; Cady, N., Journal of Vacuum Science & Technology B, DEC, Vol 40, Issue 6, 63202, http://dx.doi.org/10.1116/6.0002129 (2022, Ithaca College).

"Tilted spin current generated by the collinear antiferromagnet ruthenium dioxide"; Bose, A.; Schreiber, N.J.; Jain, R.; Shao, D.-F.; Nair, H.P.; Sun, J.; Zhang, X.S.; Muller, D.A.; Tsymbal, E.Y.; Schlom, D.G., Nature Electronics, Vol 5, Issue 5, Page(s) 267-274 (2022, Cornell University).

"Tissue Engineered Models of Metastasis: Focus on Bone Metastasis"; Sempertegui, N.; Fischbach, C., Biomaterial Based Approaches to Study the Tumour Microenvironment, Royal Society of Chemistry, Page(s) 384-414 (2022, Cornell University).

"Topological metal MoP nanowire for interconnect"; Han, H.J., S. Kumar, X. Ji, J.L. Hart, G. Jin, D.J. Hynek, Q.P. Sam, V. Hasse, C. Felser, D.G. Cahill, R. Sundararaman, J.J. Cha, arXiv:2208.02784 (2022), accepted in Advanced Materials (2022, Cornell University).

"Topological metal nanowires for interconnect"; Jin, G. (contributed talk), MRS Fall Meeting in Boston (11/2022) (2022, Cornell University).

"Toward AlGaN channel HEMTs on AlN: Polarization-induced 2DEGs in AlN/AlGaN/AlN heterostructures"; Singhal, J., R. Chaudhuri, A. Hickman, V. Protasenko, H.G. Xing, D. Jena, APL Materials 10, 111120 (2022); https://doi.org/10.1063/5.0121195 (2022, Cornell University).

"Toward CMOS-Compatible Triboelectric Generator to Operate MEMS"; Alzgool, M.; Mousavi, M.; Davaji, B.; Towfighian, S., 2022 IEEE Sensors, IEEE, Page(s) 1-4, 30 October 2022 - 02 November 2022, DOI: 10.1109/SENSORS52175.2022.9967076 (2022, Binghamton University).

"Transport properties of polarization-induced 2D electron gases in epitaxial AlScN/GaN heterojunctions"; Casamento, J.; Nguyen, T.-S.; Cho, Y.; Savant, C.; Vasen, T.; Afroz, S.; Hannan, D.; Xing, H.G.; Jena, D., Applied Physics Letters, Vol 121, Issue 19, Page(s) 192101 (2022, Cornell University).

"Triblock Terpolymer Thin Film Nanocomposites Enabling Two-Color Optical Super-Resolution Microscopy"; Lee, W.Y.; Chapman, D.V.; Yu, F.; Tait, W.R.T.; Thedford, R.P.; Freychet, G.; Zhernenkov, M.; Estroff, L.A.; Wiesner, U.B., Macromolecules, Vol 55, Issue 21, Page(s) 9452-9464, ACS Publications (2022, Cornell University).

"Tumor spheroid invasion in epidermal growth factor gradients revealed by a 3D microfluidic device"; Suh, Y.J., M. Pandey, J. E Segall, M. Wu, Physical Biology, Volume 19, Number 3, 036002, DOI 10.1088/1478-3975/ac54c7 (2022, Cornell University).

"Tuning assembly structures of hard shapes in confinement via interface curvature"; Skye, R.S., E.G. Teich, J. Dshemuchadse, Soft Matter, 2022, 18, 6782-6790, DOI: 10.1039/D2SM00545J (2022, Cornell University).

"Tuning nanosecond switching of spin-orbit torque driven magnetic tunnel junctions"; Shi, S., R.A. Buhrman, arXiv:2204.07113 [cond-mat.mes-hall] [Submitted on 14 Apr 2022] (2022, Cornell).

"Two-phase flow, pressure drop, and Joule-Thomson effect in a micro-orifice with trans critical carbon dioxide flow"; Parahovnik, A., P. Ahmed, Y. Peles, The Journal of Supercritical Fluids, Volume 188, September 2022, 105649, https://doi.org/10.1016/j.supflu.2022.105649 (2022, University of Central Florida).

"Ultrasonic Characterization of Rat Vagus Nerves using 25 MHz Pulse Reflectometry"; Ivy, L., B. Davaji, K. Lett, C. Schaffer, B. Johnson. A. Lal, 2022 IEEE International Ultrasonics Symposium (IUS), Venice, Italy, 2022, pp. 1-4, doi: 10.1109/IUS54386.2022.9957300 (2022, Cornell University)

"Understanding How Metal-Ligand Coordination Enables Solvent Free Ionic Conductivity in PDMS"; Zhang, X.; Dai, J.; Tepermeister, M.; Yeo, J.; Silberstein, M., ChemRxiv. Cambridge: Cambridge Open Engage; 2022; Dec 08, 2022 Version 1 (2022, Cornell).

"Using dc SQUID Resonances to Characterize Geometric and Electronic Capacitances of Small Josephson Junctions"; Cole, B., et al. – Poster presentation, Applied Superconductivity Conference, Honolulu, HI, Oct. 24-28, 2022 (2022, Syracuse University).

"Valley-coherent quantum anomalous Hall state in AB-stacked MoTe2/WSe2 bilayers"; Tao, Z., B. Shen, S. Jiang, T. Li, L. Ma, W. Zhao, J. Hu, K. Pistunova, K. Watanabe, T. Taniguchi, T.F. Heinz, K.F. Mak, J. Shan, arXiv:2208.07452 (2022, Cornell University).

"van der Waals π Josephson Junctions"; Kang, K.F.; Berger, H.; Watanabe, K.; Taniguchi, T.; Forro, L.; Shan, J.; Mak, K.F., Nano Letters, 22, 5510–5515 (2022) http://dx.doi.org/10.1021/acs.nanolett.2c01640 (2022, Cornell University).

"Vapor generation via porous nanochannel wicks"; Ranjan, D.; Zou, A.; Maroo, S.C., Cell Reports Physical Science, Vol 3, Issue 2, Page(s) 100738 (2022, Syracuse University).

"Vapor phase synthesis of topological semimetal MoP2 nanowires and their resistivity"; Jin, G., H. J. Han, J. L. Hart, Q. P. Sam, M. Kiani, D. J. Hynek, V. Hasse, C. Felser, J. J. Cha, Applied Physics Letters 121, 113105 (2022) (2022, Cornell University).

"Very High Density (> 10(14) cm(-2)) Polarization-Induced 2D Hole Gases Observed in Undoped Pseudomorphic InGaN/AlN Heterostructures"; Chaudhuri, R.; Zhang, Z.X.; Xing, H.G.; Jena, D., Advanced Electronic Materials, MAY, Vol 8, Issue 5, 2101120, http://dx.doi.org/10.1002/aelm.202101120 (2022, Cornell).

"VxrAB signaling in Vibrio cholerae is activated by diverse mechanical stimuli"; Harper, C.E., Zhang, W., Shin, J-H., Lee, J., Chou E., Chen, P., Dörr, T., Hernandez, C.J., Biophysical Society Annual Meeting. San Francisco, CA, USA. (2022) (2022, Cornell).

"Watchful System to keep track of Hazardous waste during COVID'19 epidemic"; Karunakaran, K., R. Amirtharajan, P. Praveenkumar, 2022 International Conference on Computer Communication and Informatics (ICCCI), 25-27 January 2022, DOI: 10.1109/ICCCI54379.2022.9740950 (2022, SASTRA Deemed University, India).

"Waveguides for Use in Sensors or Displays"; Bai, H., R. Huang, S. Li, R. Shepherd, H. Zhao, Patent Issued, Docket # 7179-03-US, United States, Filed 8/24/18, 16/079,798, Issued 10/20/22, Patent 11,473,942 (2022, Cornell University).

"Waveguides for Use in Sensors or Displays"; Bai, H., R. Huang, S. Li, R. Shepherd, H. Zhao, Patent Application, Docket # 7179-07-US, United States, Filed 8/31/22, 17/900,475 (2022, Cornell University).

"Waveguides for Use in Sensors or Displays"; Bai, H., R. Huang, S. Li, R. Shepherd, H. Zhao, Patent Application, Docket # 7179-08-HK, Hong Kong, Filed 8/31/22, 42022059320 (2022, Cornell University).

"Widely-Tunable RF Receiver Employing Synthetic Diversity for Interference Mitigation"; Sadeghi, S.; Soni, S.; Molnar, A., 2022 IEEE International Symposium on Circuits and Systems (ISCAS), IEEE, Page(s) 1858-1862 (2022, Cornell University).

"X-band epi-BAW resonators"; Zhao, W.; Asadi, M.Ja.; Li, L.; Chaudhuri, R.; Nomoto, K.; Xing, H.G.; Hwang, J.C.M.; Jena, D., Journal of Applied Physics, Vol 132, Issue 2, Page(s) 24503 (2022, Cornell University).

"X-ray Nano-Imaging of Defects in Thin-Film Catalysts via Cluster Analysis"; Luo, A., Materials Research Society (MRS) Fall Meeting in 2022 (Conference presentation) (2022, Cornell University).

"X-ray Nano-Imaging of Defects in Thin-Film Catalysts via Cluster Analysis"; Luo, A., O.Y. Gorobtsov, J.N. Nelson, D.-Y. Kuo, T. Zhou, Z. Shao, R. Bouck, M.J. Cherukara, M.V. Holt, K.M. Shen, D.G. Schlom, J. Suntivich, A. Singer, Applied Physics Letters 121, 153904 (2022); https://doi.org/10.1063/5.0125268 (2022, Cornell University).

2022-2023

Cornell NanoScale Facility (CNF)

Research Accomplishments

Silicon Nitride Cantilevers for Muscle Myofibril Force Measurements

CNF Project Number: 1255-04
Principal Investigator(s): Walter Herzog
User(s): Timothy Leonard, Andrew Sawatsky

Affiliation(s): Faculty of Kinesiology, University of Calgary, Calgary, Canada

Primary Source(s) of Research Funding: Canadian Institutes of Health Research

Contact: wherzog@ucalgary.ca, leonard@ucalgary.ca, ajsawats@ucalgary.ca
Website(s): https://kinesiology.ucalgary.ca/research/labs-and-centres/human-performance-lab

Primary CNF Tools Used: GCA 5X Stepper, SÜSS MA6-BA6 Contact Aligner, Photolith spinners, Oxford 81 ion etcher

Abstract:

To measure muscle forces in the nano-Newton range, silicon nitride cantilever pairs were manufactured and used. Measuring sarcomere length (SL) variation across a myofibril with 20-30 sarcomeres in-series in skeletal muscle myofibrils provides useful information about variation in individual SLs and indirectly, the isoform mass, extensibility, and quantity of the structural protein titin [2]. Myofibril imaging has traditionally been done using phase-contrast (PC) microscopy, but this technique has limited resolution. Promising and reliable fluorescent epitope labelling can be done on sarcomeric structural proteins α-actinin (Z-line) and myomesin (M-line).

The purpose of this study was to 1: Test if antibody labelling techniques affect SL non-uniformities and SL repeatability following a stretch-shortening protocol, and 2: Measure passive stress at matched SL to determine if labelling affects passive force development at long SL. Myofibrils from rabbit psoas muscle were used and labelled with anti-α-actinin, anti-myomesin primary antibodies, and polyclonal IgG (H+L) AlexaFluor488 secondary antibodies and observed using both PC and Fluorescein isothiocyanate (FITC) microscopy.

Myofibrils (Labelled, n=7 and Control, n=7) were attached to force-measuring cantilevers and stretched passively from a mean SL of 2.6 μm (short position; SP) to 3.2 μm (long position; LP). Fluorescently labelled myofibrils showed no change in the range of SL non-uniformities after stretch compared to non-labelled myofibrils, but labelling contributed to a decrease in individual SL repeatability (as seen in the greater variation around the "perfect" identity line for each sarcomere). Passive force was not affected by the presence of the labels. In conclusion, antibody labeling made SL measurements easier by clearly defining the Z- and M-zones, and while they do not affect the passive force, they do alter the time-history of titin extension during stretch, resulting in poor repeatability of individual SL after stretch-shortening.

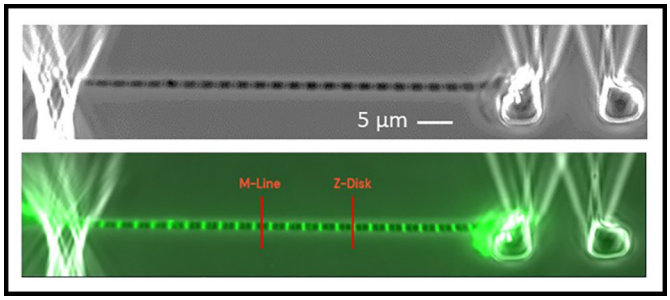

Figure 1: Myofibril attached to a glass needle for stretch-shortening and nano-cantilevers for force measurement. Top panel is a phase-contrast image and lower panel is the same myofibril, when fluorescently labelled.

Summary of Research:

Video images were collected using an Olympus IX83 microscope and analyzed to determine SL in the CellSens® Dimensions software. The maximum number of sarcomeres accurately measurable in each myofibril were chosen, and sarcomeres were pooled together from the seven control and seven antibody-labelled myofibrils, resulting in n=141 control sarcomeres and n=150 antibody-labelled sarcomeres. Individual SL was measured from adjacent M-line centroids throughout the myofibril. SL non-uniformity and individual SL

repeatability were measured after passive stretches, in both control and antibody-labelled myofibrils. An identity line was used for displaying whether each individual sarcomere was the same length, before (x-axis) and after a stretch-shortening test (y-axis). All sarcomeres with perfect repeatability would reside on the identity line. Figure 2 shows the decrease in repeatability in the labelled samples because fewer sarcomeres were close or on, the identity line (x=y).

Force was determined using a microfabricated pair of cantilevers [1], where one end of the myofibril was attached using a mixture of silicon-based adhesive to one of the cantilevers, while the other end of the myofibril was pierced using a glass needle. As passive stretches occurred, the relative movement of the cantilever relative to the stationary cantilever was measured and force calculated based on the known stiffness of the cantilevers. The cross-sectional area of the myofibril was determined and used to determine the stress in the myofibril (nN/μm^2). Figure 3 box plot shows no difference in passive stress at SL of 3.2 μm.

Overall, the introduction of antibodies did not affect the passive force produced by the myofibril at long SL. It did, however, cause a decrease in the repeatability of the length for each sarcomere following the stretch-shortening cycle. This is possibly due to some "internal drag" caused by the label antibodies or by the fluorophores, on the extension/unfolding of titin during stretch. These findings help support further use of protein labeling in myofibril research.

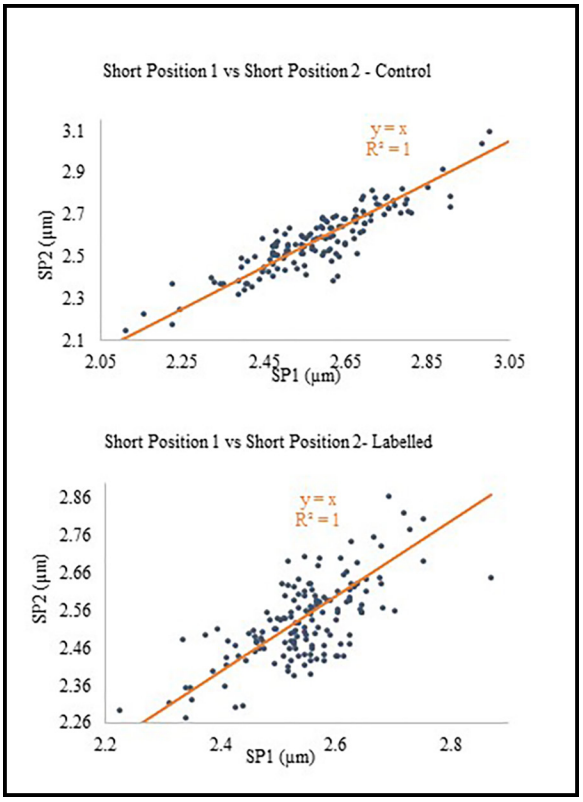

Figure 2: Sarcomere length for control (top) and labelled (bottom) myofibrils. Each sarcomere was measured prior to stretch (SL on x-axis) and then plotted after stretch-shortening (SL on y-axis). If a sarcomere had the identical length following stretch and return to initial length, then each sarcomere length was perfectly repeatable, and the data point would reside on the "perfect identity line".

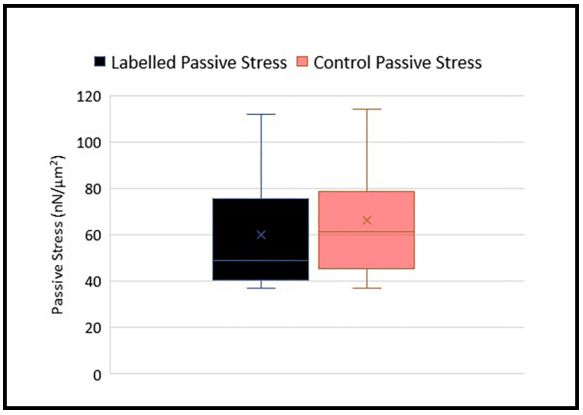

Figure 3: Boxplots comparing passive stress for control and antibody-labelled myofibrils at long sarcomere length (SL 3.2 µm).

References:

[1] M. E. Fauver, et al. IEEE Trans Biomed Eng 45(7):891-898, 1998.
[2] Granzier and Labeit. Muscle Nerve. 36:740-755, 2007.

High Throughput RF Bio Sensors

CNF Project Number: 1606-07
Principal Investigator(s): Pingshan Wang
User(s): Md Saiful Islam

Affiliation(s): Electrical & Computer Engineering, Clemson University

Primary Source(s) of Research Funding: Army

Contact: pwang@clemson.edu, mdsaifi@clemson.edu

Primary CNF Tools Used: ABM Contact Aligner, SÜSS MA6-BA6 Contact Aligner, CHA Mark 50 E-beam Evaporator, Heidelberg Mask Writer - DWL2000, Glen 1000 Resist Strip

Abstract:

The aim of this research is to build a microstrip based sensor that has integrated microfluidics to transport biological cells. The sensor will be able propagate low power microwave (100MHz to 15GHz) microwave signals. Biological Cells transported to the sensor will generate electrical signal which will correspond to the dielectric material change. This sensor will be a non-invasive method to analyze biological cells. The sensors are designed to analyze Chinese Hamster Ovarian Cells (CHO) for a comprehensive study of the cell life cycle, different drug effects, conditions effecting the production of protein by the CHO cells, identifying sub-populations that has higher protein yield. Apart from that another set of sensors were built to do similar analysis on candida yeast cells. These investigations will also include SF9 line of cells for cell apoptosis and different virus infection state identification.

Summary of Research:

The work we did in June 2023 at CNF was to build new devices based on the results obtained earlier this year. In Figure 1, we achieved to demonstrate scattering parameter signals differentiate two different variants of Chinese Hamster Ovarian (CHO) cells. Namely VRC01 and PF variants. In that experiment about 50 individual CHO cells of each type were measured by the sensor (one at a time). Their corresponding scattering parameter scatter plot showed a noticeable difference. However, the sensor had inherent design flaws as in the metal used for the microwave circuit used copper, which would corrode over time and render the sensor unusable. Apart from that the idea of having multiple channel passes with the microfluidic system did not offer any benefits. To remedy this, we came up with some modifications in the microfluidics and planned on changing the metal deposition to Ti-Au-Ti. Some delay line fluidic channel and cell trapping mechanisms were introduced in the microfluidics. The new design has been fabricated over June. We are preparing to run experiments with it on biological cells like CHO, SF9, and candida yeast cells.

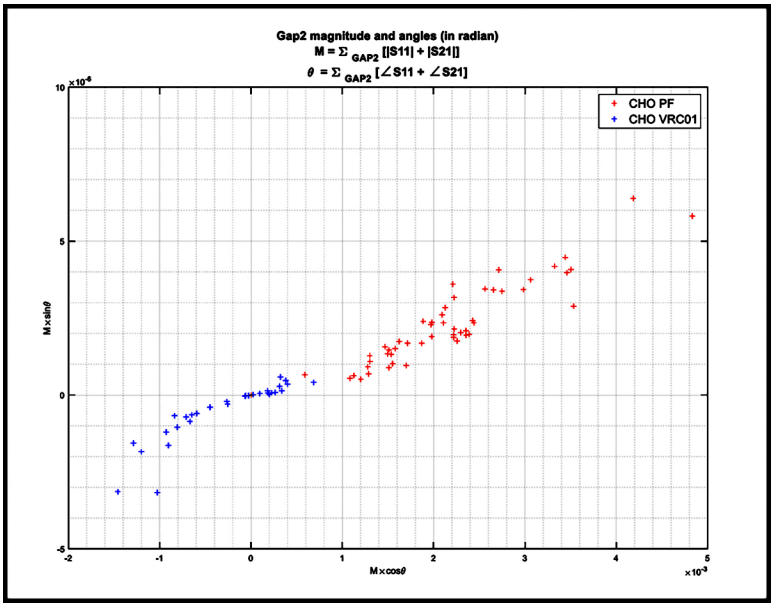

Figure 1: Scattering parameter scatter plot of CHO VRC01 and CHO PF cells.

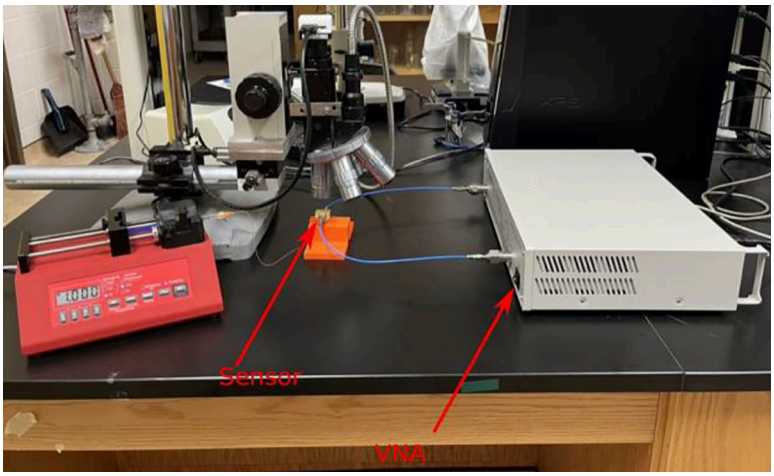

Figure 2: Experimental setup for the results obtained in Figure 1.

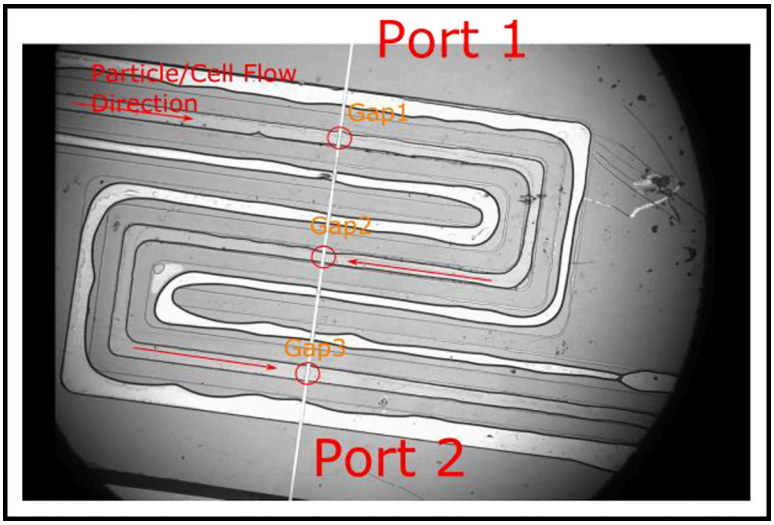

Figure 3: Microscopic view of microfluidics of the sensor used in Figs 1 and 2.

Quartz Cylinder Fabrication for Torque Measurement in the Single-Molecule Level

CNF Project Number: 1738-08
Principal Investigator(s): Michelle D. Wang
User(s): Yifeng Hong

Affiliation(s): a) Department of Electrical and Computer Engineering, Cornell University; b) Department of Physics, Cornell University; c) Howard Hughes Medical Institute

Primary Source(s) of Research Funding: Howard Hughes Medical Institute

Contact: mdw17@cornell.edu, yh874@cornell.edu

Website(s): http://wanglab.lassp.cornell.edu/

Primary CNF Tools Used: ASML Deep Ultraviolet Stepper, Oxford 81 Etcher, Oxford 82 Etcher, Oxford PECVD, SC4500 Odd-Hour Evaporator, SC4500 Even-Hour Evaporator, Zeiss Supra SEM, Zeiss Ultra SEM

Abstract:

To facilitate single-molecule torque measurements with the angular optical tweezer (AOT), we designed and fabricated quartz cylinders that can specifically attach DNA molecules to achieve a true angular trap. These cylinders have been widely used to investigate single-molecule torsional properties and they are currently uses in multiple research projects.

Summary of Research:

Torsional stress plays an important role in fundamental biological processes such as transcription and replication. During these processes, torsion can accumulate both upstream and downstream of the transcription complex or the replisome. We are specifically interested in how the DNA responds to these topological changes. To quantitatively investigate this, our lab developed a tool, the angular optical trap (AOT), to measure torque at the single-molecule level [1-3]. In our approach, a linearly polarized light is used to trap and rotate a birefringent particle anchored with a torsionally constrained DNA molecule for manipulations and measurements [1]. To achieve a true angular trap, we designed the birefringent particle to have a cylindrical geometry (with an aspect-ratio ~ 2) [2, 3] (Figure 1). In this way, the cylindrical axis tends to align to the laser propagation direction, which ensures the extraordinary axis is always perpendicular to the laser propagation direction even when attached to a biomolecule. The cylinder top surface is specifically functionalized with (3-Aminopropyl)triethoxysilane to be covalently coupled with protein for DNA molecule anchoring. These quartz cylinders have been broadly used in the single-molecule torsional mechanics study in our lab [3-8].

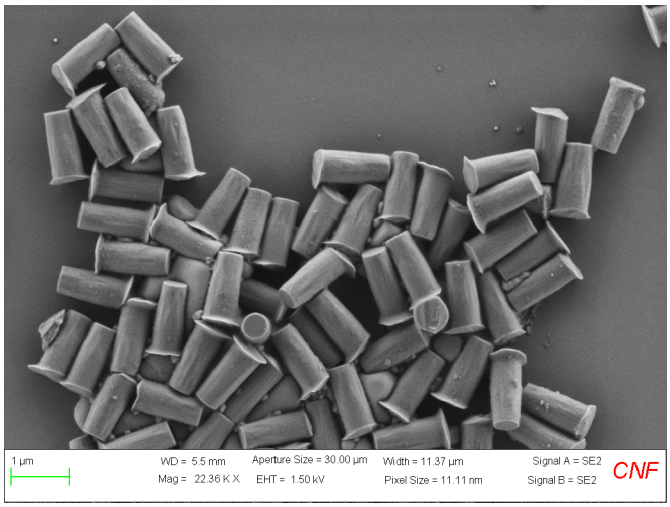

Figure 1: An SEM image of the cleaved quartz cylinders.

Conclusions and Future Steps:

We are now applying the quartz cylinders to extend our previous work on the torsional stiffness of the braided DNA molecules [6].

References:

[1] La Porta, A. and M.D. Wang, Optical Torque Wrench: Angular Trapping, Rotation, and Torque Detection of Quartz Microparticles. Physical Review Letters, 2004. 92(19): p. 190801.

[2] Deufel, C., et al., Nanofabricated quartz cylinders for angular trapping: DNA supercoiling torque detection. Nature Methods, 2007. 4(3): p. 223-225.

[3] Gao, X., et al., Torsional Stiffness of Extended and Plectonemic DNA. Physical Review Letters, 2021. 127(2): p. 028101.

[4] Forth, S., et al., Abrupt Buckling Transition Observed during the Plectoneme Formation of Individual DNA Molecules. Physical Review Letters, 2008. 100(14): p. 148301.

[5] Ma, J., L. Bai, and M.D. Wang, Transcription under torsion. Science, 2013. 340(6140): p. 1580-3.

[6] Le, T.T., et al., Synergistic Coordination of Chromatin Torsional Mechanics and Topoisomerase Activity. Cell, 2019. 179(3): p. 619-631.e15.

[7] Ma, J., et al., Transcription factor regulation of RNA polymerase's torque generation capacity. Proceedings of the National Academy of Sciences, 2019. 116(7): p. 2583-2588.

[8] Sheinin, M.Y., et al., Torque modulates nucleosome stability and facilitates H2A/H2B dimer loss. Nature Communications, 2013. 4(1): p. 2579.

Building Microfluidics Devices to Study Zinc Metal Homeostasis in *E. coli* Communities

CNF Project Number: 1844-09
Principal Investigator(s): Peng Chen
User(s): Felix Alfonso

Affiliation(s): Department of Chemistry and Chemical Biology, Cornell University

Primary Source(s) of Research Funding: National Institutes of Health, National Institute of General Medical Sciences

Contact: pc252@cornelll.edu, fsa33@cornell.edu

Website(s): http://chen.chem.cornell.edu/

Primary CNF Tools Used: Heidelberg Mask Writer DWL2000, SÜSS MA6-BA6 Contact Aligner, Oxford Cobra ICP Etcher, Plasma-Therm Deep Silicon Etcher, P7 Profilometer

Abstract:

Microbial life has evolved a set of molecular tools designed to import essential nutrients from the surrounding environment while simultaneously effluxing the excess to prevent harmful toxicity. The aim of this study is to elucidate the role individual bacterial cells play in achieving metal homeostasis at the community level. With this in mind, we engineered a custom microfluidic device that facilitates the controlled growth of *Escherichia coli* (*E. coli*) colonies within well-defined microchambers. These chambers' dimensions are carefully matched to the diameter of *E. coli* cells, thereby allowing for strategic cellular confinement — a critical aspect of our investigative method. The microfluidic devices we employed exhibit dynamic environmental control features, giving us unprecedented power to study and understand the microbial world. Leveraging this, we were able to probe deeper into the nuances of how this miniature bacterial community strikes a balance in their zinc metal homeostasis.

We employed advanced molecular biology techniques to engineer *E. coli* strains equipped with fluorescent protein reporters. This unique genetic modification allowed us to visualize and quantify gene expressions linked to the intricate influx and efflux ion channels, with particular emphasis on those specific to zinc. The insights derived from this study could have profound implications for our understanding of microbial ecosystems and their interactions with the environment.

Summary of Research:

Zinc, a fundamental micronutrient, is indispensable for all living organisms [1]. It serves vital functions in protein folding, catalysis, and gene regulation [2,3]. An imbalance in zinc levels, either a deficiency or an excess, can trigger substantial alterations in the gut microbiome, thereby resulting in adverse health conditions [4,5]. Microbial life, over time, has developed a specialized suite of molecular mechanisms to efficiently import nutrients from the environment while effluxing excesses, thus preventing toxicity. To regulate these efflux pumps, bacteria modulate the transcription of protein pumps using metal-responsive transcription regulators. These regulators monitor the cellular concentration of metal ions, guiding cells towards achieving an optimal state of metal homeostasis.

Our project is designed to explore and quantify the management of Zn^{2+} within a microbiome, shedding light on the role individual cells assume in establishing community-wide metal homeostasis. We have chosen *Escherichia coli* (*E. coli*) as our model organism to investigate the complexities of community-derived zinc metal regulation. *E. coli*'s natural motility and poor adherence to substrates present challenges for long-duration imaging studies. However, microfluidics technology offers an effective solution, providing a controlled environment conducive to studying bacterial communities [6]. A microfluidic platform permits tight control of the nutrients influx and has been successfully used for long-timescale imaging studies [7].

The microfluidic device employed in our study is engineered with three key components: a gradient generator, channels, and microchambers. The microchambers' depth is tailored to match the diameter of an *E. coli* cell (~1μm), thereby facilitating the efficient confinement of colonies. The gradient generator was designed with the goals of creating a stable concentration gradient and minimization of convection inside the chambers. The design presented by E. Bernson, and A. Shamloo provided an optimal method to create a stable

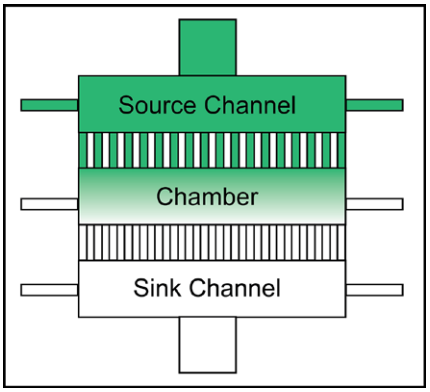

Figure 1: Schematic of gradient generating microfluidic device showing the source and sink channels and the chamber.

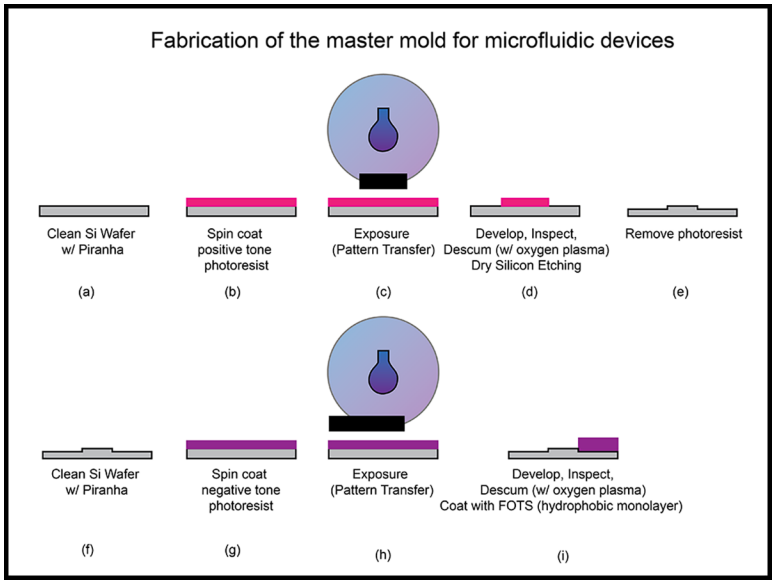

Figure 2: Fabrication of microfluidic devices combining dry etching to construct the chambers and SU-8 lithography to construct the channels.

gradient inside the chamber (Figure 1, 8-9). This is accomplished by having a source chamber and a sink chamber. The molecule of interest diffuses through the micro capillaries that connect the source and sink to the main culture chamber.

The construction of these microfluidic devices relies on established silicon nanofabrication technology. The fabrication scheme is summarized in Figure 2. The fabrication process begins with silicon wafers being cleaned with piranha solution. They are then coated with photoresists, which are removed 2 mm from the wafer's edge using an edge bead removal system. The substrate is patterned using a pre-designed photomask created with the Heidelberg Mask Writer DWL2000. The Karl SUSS MA6-BA6 contact aligner provides UV light exposure for the wafer, which is developed and cleaned with a brief oxygen plasma treatment. Chambers are created by etching approximately ~ 1 μm of silicon using the Oxford Cobra ICP Etcher, and then the photoresist is removed with a stripper bath. The chamber's height is measured using a profilometer. Channel construction involves the use of SU-8 lithography, where SU-8 is spin-coated onto the substrate and patterned with the Karl SUSS MA6-BA6 contact aligner. After a curing phase on a hot plate at 95°C, the unpolymerized SU-8 is removed with the developer. The resulting structure is then hard baked for 10 minutes at 200°C. The final step entails coating the silicon mold with a hydrophobic molecular monolayer such as tridecafluoro-1,1,2,2-tetrahydrooctyl trichlorosilane (FOTS) to facilitate PDMS removal. After casting PDMS on the silicon mold, the microfluidic devices are bonded to coverslips and inspected under a microscope. Cells are loaded into the chambers and imaged with a microscope equipped with the appropriate laser line and filters.

References:

[1] R. R. Robert B. Saper, Zinc: An Essential Micronutrient. Am. Fam. Physician. 79, 768 (2009).

[2] S. Tan, D. Guschin, A. Davalos, Y.-L. Lee, A. W. Snowden, Y. Jouvenot, H. S. Zhang, K. Howes, A. R. McNamara, A. Lai, C. Ullman, L. Reynolds, M. Moore, M. Isalan, L.-P. Berg, B. Campos, H. Qi, S. K. Spratt, C. C. Case, C. O. Pabo, J. Campisi, P. D. Gregory, Zinc-finger protein-targeted gene regulation: genomewide single-gene specificity. Proc. Natl. Acad. Sci. U. S. A. 100, 11997-12002 (2003).

[3] C. Andreini, I. Bertini, in Encyclopedia of Metalloproteins (Springer, New York, NY, 2013), pp. 2549-2554.

[4] S. R. Gordon, S. Vaishnava, Zinc supplementation modulates T helper 17 cells via its effect on gut microbiome. The Journal of Immunology. 204, 83.18-83.18 (2020).

[5] O. Koren, E. Tako, Chronic Dietary Zinc Deficiency Alters Gut Microbiota Composition and Function. Proc.AMIA Annu. Fall Symp. 61, 16 (2020).

[6] F. Wu, C. Dekker, Nanofabricated structures and microfluidic devices for bacteria: from techniques to biology. Chem. Soc. Rev. 45, 268-280 (2016).

[7] D. Binder, C. Probst, A. Grünberger, F. Hilgers, A. Loeschcke, K.-E. Jaeger, D. Kohlheyer, T. Drepper, Comparative Single-Cell Analysis of Different *E. coli* Expression Systems during Microfluidic Cultivation. PLoS One. 11, e0160711 (2016).

[8] E. Bernson, Development of a Microfluidic Platform for Cell migration Studies along Gradients (2012) (available at https://odr.chalmers.se/items/8199a5e9-f3f0-4824-9056-51f603dcfd7d).

[9] A. Shamloo, N. Ma, M.-M. Poo, L. L. Sohn, S. C. Heilshorn, Endothelial cell polarization and chemotaxis in a microfluidic device. Lab Chip. 8, 1292-1299 (2008).

Development of 3D Microfluidic Platform for Dynamic Compression of Tumor Spheroids

CNF Project Number: 2068-11
Principal Investigator(s): Dr. Mingming Wu
User(s): Young Joon Suh

Affiliation(s): Department of Biological and Environmental Engineering, Cornell University

Primary Source(s) of Research Funding: NIH Grant R01CA22136,
Cornell Center on the Microenvironment and Metastasis (National Center Institute Grant U54CA143876)

Contact: mw272@cornell.edu, ys668@cornell.edu

Website(s): biofluidics.bee.cornell.edu

Primary CNF Tools Used: Heidelberg Mask Writer - DWL2000, ABM Contact Aligner, P7 Profilometer, MVD100, SUEX Laminator, Dicing Saw - DISCO, YES EcoClean Asher, Unaxis 770 Deep Si Etcher, PT Deep Si Etcher, Oxford 81 Etcher, Oxford PECVD, YES Polyimide Oven, Hamatech Hot Piranha

Abstract:

Solid tumor stress caused by rapid growth of tumor cells and abnormality of vascular vessels has long been associated with a poor prognosis of cancer. However, understanding of tumor mechanics has been limited largely to single cells under static compressive loads. In this study, we have developed a high throughput microfluidic platform providing well-controlled dynamic compression to tumor spheroids.

Summary of Research:

A 6 × 2 array microfluidic compression device for tumor mechanics studies was designed (See Figure 1). The device consists of three layers: (1) cell culture layer, where the tumor spheroids embedded in extracellular matrices (ECM) are loaded; (2) PDMS piston layer, which is a PDMS membrane that has a top hat shape; and (3) a pressure control layer, which can push the PDMS piston down to apply compressive forces on the tumor spheroids. The three-layers are then sandwiched between a Plexiglass® top cover and a stainless-steel frame to provide a good seal. A COMSOL modeling has been used to calculate the displacement of the PDMS piston and the force applied on the tumor spheroids at pressure ranging from 0 to 7000 Pa (Figure 2). When pressure is applied in the pressure control chamber, the PDMS piston moves down a distance of Δh, applying a force on the tumor spheroids underneath, and leads to a well-controlled compressive strain, Δh /h, on the spheroids. This device can accommodate tumor spheroids of Young's modulus of about 1250 Pa, that are 100-200 μm in diameter for up to compressive strain (Δh/h) of 0.5.

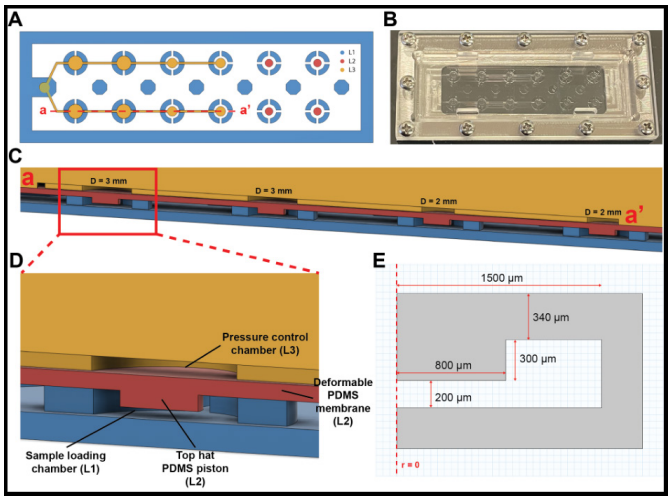

Figure 1: Design of the Microrheometer. A. Schematic of the three layers L1, L2, and L3. B. Picture of the assembled device. C. Cross-section of the device from a to a'. D. A closeup of the cross-section of one device unit with Sample loading layer (L1), Piston layer (L2), and Pressure control layer (L3). E. Dimensions of an axisymmetric compression unit. A critical dimension is the distance between the bottom of the sample loading well and the PDMS piston, which is 200 µm. The piston layer (L2) has a PDMS membrane thickness of 340 µm, and the piston is 1600 µm in diameter and 300 µm in height. The Sample loading well diameter is 3 mm and 500 µm in height.

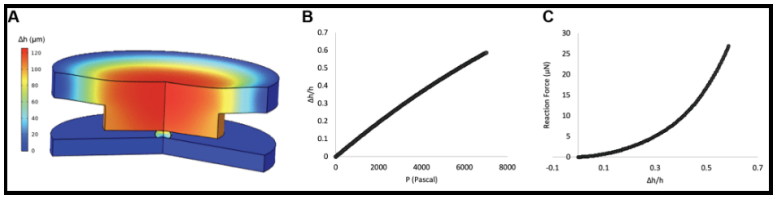

Figure 2: Computation of a microfluidic compression unit. A. Computed Δh under a pressure of 7000 Pa with spheroid. The spheroid modulus is assumed to be 1250 Pa. B. Relationship between the compression strain and applied pressure. C. Compression force on spheroid versus compression strain, Δh/h.

Fabrication:

Three layers of the device were fabricated separately. The cell culture layer consists of SU-8 wells 600 μm in depth on a 500 μm thick glass (Borofloat®). To fabricate this layer, SU-8 100 was spun on a Borofloat wafer at 475 rpm and soft baked at 95°C for 30 hours. The SU-8 was then exposed to 2310 mJ/cm^2 of UV light through a 365 nm filter using an ABM contact aligner. The resist was then postexposure-baked and developed in the SU-8 developer, followed by a hard bake at 200°C. The main challenge was to fabricate the height of the wells uniform at 600 μm across the wafer. Keeping the wafer leveled at all steps was found to be crucial. The piston layer consists of PDMS pistons that are 300 μm in height and 1600 μm in diameter and the PDMS membrane is 300 μm thick.

To fabricate the master for this layer, 300 μm wells were etched into a Si wafer. Briefly, 4.5 μm of SPR-220-4.5 was spun on a Si wafer. The resist was then baked at 115°C for 2 mins on a proximity hot plate. Then, it was exposed to the pattern of the pistons at 120 mJ/cm^2 on the ABM contact aligner. After leaving it in room temperature for 30 mins for the post exposure reaction, it was baked at 115°C for 2 mins on a proximity hot plate for the post exposure bake. It was then developed in 726MIF for 120 sec. Then, a mild descum procedure was completed using the Oxford 81 for 90 sec. Finally, the Si wafer was loaded on the Unaxis 770 Deep Si etcher and a total of 567 loops (200 + 200 + 167) of Bosch process were performed to etch 300 μm into the Si wafer.

To remove any excess resist, the wafer was exposed to a strong plasma in a EcoClean Asher. The wafer was then coated with FOTS using the MVD-100 to make the surface hydrophobic. The depth of the piston wells was then measured using the P-7 profilometer. The pressure control layer is a PDMS membrane with five parallel channels of 200 μm depth. The master is fabricated in a similar way as that for cell culture layer, except that a Si wafer is used instead of a Borofloat wafer.

A 10:1 PDMS was poured and cured on the master molds of the piston and the pressure control layer. After curing the PDMS in a 65°C oven overnight, these two layers were bonded together after plasma treatment and placed in a 90°C oven for 20 mins. Then, these two layers were placed on top of the cell culture layer and sandwiched between a metal frame and a Plexiglass top and connected to a pressure controller.

The compression (Δh) was measured using the defocused particle imaging velocimetry, which was originally developed in our lab [1]. Tumor spheroids were embedded in collagen, which was then introduced into the cell culture chamber. The pressure control chamber is pressurized with a pressure controller. We were able to precisely control the tumor compression with a precision of 1 μm.

References:

[1] Wu, et al, Three-dimensional fluorescent particle tracking at micron-scale using a single camera, Experiments in Fluids, 38, 461(2005).

Microfabrication of Sample Holders for Cryogenic Small Angle X-Ray Scattering and Flow Cells for Fluorescence Measurements of Ligand Diffusion in Protein Crystals

CNF Project Number: 2157-12
Principal Investigator(s): Robert Thorne
User(s): John Indergaard, Christopher Biloski, Myeonghak Lee, Ash Mahmood

Affiliation(s): Departments of Physics, Mechanical and Aerospace Engineering, Cornell University

Primary Source(s) of Research Funding: NIH, NSF

Contact: ret6@cornell.edu, jai55@cornell.edu, cjb358@cornell.edu, ml2564@cornell.edu, km929@cornell.edu

Website(s): https://www.lassp.cornell.edu/Thorne/

Primary CNF Tools Used: Heidelberg DWL 2000 Laser Writer, Hamatech Wafer Processor, Filmetrics Reflectometer, SÜSS MA6 Contact Aligner, Oxford PlasmaLab 80+, SUEX Laminator, Harrick Plasma Generator, PDMS Casting Station, DISCO Dicing Saw, KOH Hood and Bath

Abstract:

Small angle X-ray scattering (SAXS) and X-ray crystallography are key tools used to study the structure and function of biomolecules. We have been developing microfabricated sample cell arrays for collection of SAXS data from biomolecular samples cooled to cryogenic temperatures, which could simplify SAXS sample handling and increase data collection throughput. We have also been developing microfluidic flow cells for quantitative fluorescence measurements of diffusion of small molecules into biomolecular crystals. These measurements inform choice of crystal sizes in time-resolved crystallography of biomolecules in action.

Summary of Research:

Sample cell arrays for cryo-SAXS. Small-angle X-ray scattering (SAXS) probes the shape and size of biomolecules (e.g., proteins) in solution. SAXS is currently performed using biomolecule samples at or near room temperature. Samples are rapidly damaged by X-rays and may undergo degradation during transport to the X-ray source. If samples are cooled to cryogenic temperature, the rate of X-ray damage decreases by orders of magnitude and samples can be stored indefinitely without degradation. Our goal is to develop sample cell arrays and methods to enable routine high-throughput SAXS sample handling and measurements at cryogenic temperature. Major challenges in achieving this goal include finding a combination of materials, structures, and protocols that allow easy loading of nanoliter sample volumes, sample cooling into a vitrified state without formation of crystalline ice, bubbles, anisotropic stresses, or fractures, and that allow quantitatively and qualitatively identical data to be collected from any cell in the array.

Our sample cell arrays are constructed from two 3 mm × 12 mm pieces of 300 μm thick, <100> oriented, double-side polished Si wafer, coated via LPCVD with 500 nm of SiN. The wafer is photolithographically patterned, SiN is removed from one side, and Si is removed using an anisotropic KOH etch, leaving arrays of 500 μm square, X-ray transparent SiN windows. A sheet of SUEX is bonded to the window side of the wafer and patterned to define cell alignment and liquid trapping features. The wafer is diced into rectangles containing eight windows, each forming half of a sample cell array. On one half, segments of thin-walled polyimide tubing are bonded over each nitride window and quartz spacers are attached. The spacers fix the distance between nitride windows in the two halves of the device, fixing the X-ray path length through each cell.

We have evaluated our cryoSAXS sample cell arrays at synchrotron beamlines at CHESS (Cornell) and NSLS-II (Brookhaven National Lab). The cells allow rapid cooling to a vitrified sample state. The critical challenge has been to eliminate all sources of cell-to-cell variability/irreproducibility in SAXS scatter, as differences as small as 1% can have a major impact on data quality. We have been addressing this challenge via changes in device geometry and assembly, changes in X-ray beamline configuration, and changes in device cleaning protocols.

Our current design — involving both microfabrication and precision manual assembly — presents obstacles to both reproducible data collection and routine, high-volume production and use. We will continue optimization of the current design and exploring alternative designs, including all-microfabrication designs made possible using two-photon polymerization.

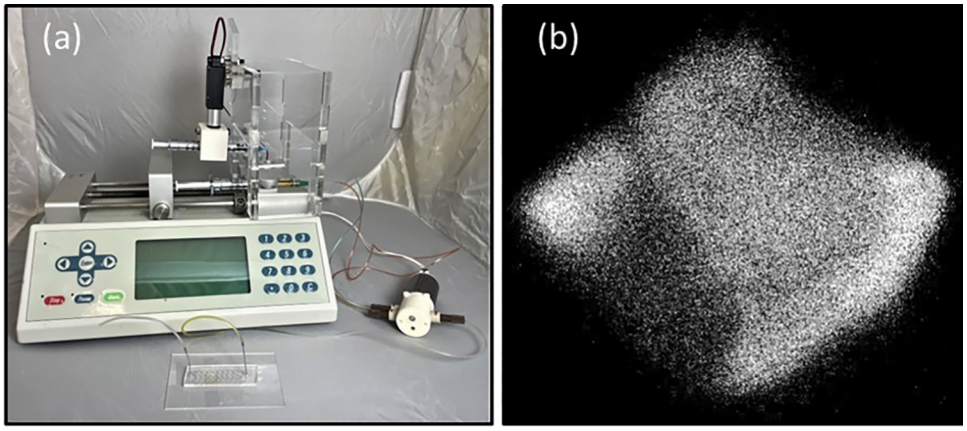

Figure 1: (a) Experimental setup including microfluidic crystal trap array for measuring diffusion of fluorescent small molecules into biomolecular crystals. (b) Two-photon fluorescence image of a fluorophore (lysotracker blue DND-22) diffused into a ~ 50 µm lysozyme crystal.

Microfluidic traps for *in crystallo* diffusion measurements. A long-term project in structural biology has been to develop methods for making atomic-resolution "movies" of biomolecules in action. This typically involves mixing small crystals with a ligand that diffuses into the crystal and binds to the biomolecule, reacting with it and/or triggering a change in its structure. X-ray diffraction patterns are recorded at different times after the start of mixing and are used to generate "snapshots" versus time.

We demonstrated a mix-and-quench method [1] where biomolecular crystals on a support are translated through a film containing reactant. After a delay, the crystals are plunged into liquid nitrogen, stopping the reaction and trapping the structural state for subsequent X-ray examination. We achieved a nominal time resolution of 40 ms, and with hardware improvements sub-5 ms time resolution should be feasible.

However, a key unknown is the time required for a given ligand/reactant to diffuse into a given biomolecular crystal. Time-resolved experiments have so far assumed that diffusion constants within crystals are the same as in free solution. However, biomolecular crystals are nanoporous solids with complex internal pore geometries. Diffusion constants could be one to two orders-of-magnitude smaller, causing uncertainty in reaction "time points" due to inhomogeneous ligand distribution within the crystal, limiting achievable time resolution, and/or requiring use of much smaller crystals.

To examine diffusion within crystals, we are fabricating microfluidic flow cells for use in multiphoton imaging (Figure 1). Crystals in carrier solution flow into the cells and are trapped at an array of locations, and then a solution containing a small-molecule fluorophore flows into the cell and diffuses into the crystals. To create these crystal traps, we fabricate a master mold by bonding a SUEX sheet to a silicon wafer and photolithographically patterning it. Trap arrays are fabricated by casting a 2 mm layer of PDMS on top of the wafer. Once the crystal traps are filled by a flow of crystal-containing solution, fluorophore is abruptly introduced using an electronically controlled syringe-holding manifold and a switching valve.

We have demonstrated successful trapping of 50 μm crystals and obtained fluorescence data yielding a plausible initial diffusion coefficient estimate. We are improving the design to allow study of larger crystals (which should give more accurate estimates) and faster flow switching to improve time resolution.

References:

[1] Clinger, J. A., Moreau, D. W., McLeod, M. J., Holyoak, T., and Thorne, R.E. Millisecond mix-and-quench crystallography (MMQX) enables time-resolved studies of PEPCK with remote data collection. IUCrJ 8, 784-792 (2021).

Nanoscribe 3D Printing of Versatile Microfluidic Mixers for Experiments with Biomolecules

CNF Project Number: 2158-12
Principal Investigator(s): Lois Pollack
User(s): Scout Fronhofer, Kara Zielinski

Affiliation(s): Applied and Engineering Physics, Cornell University
Primary Source(s) of Research Funding: National Science Foundation
Contact: lp26@cornell.edu, shf56@cornell.edu, kaz42@cornell.edu
Website(s): https://pollack.research.engineering.cornell.edu/
Primary CNF Tools Used: Nanoscribe 3D Printer

Abstract:

We report the fabrication and implementation of a 3D printed microfluidic mixer for studying biological macromolecules. The device mixes fluids by chaotic advection, enabling time-resolved structural measurements of large molecules and offers advantages over turbulent mixers in terms of sample consumption. Previous versions of the mixer have been used for time-resolved measurements for multiple biological systems and techniques, and there are many avenues for future work.

Summary of Research:

Microfluidic mixers have enabled time-resolved structural studies of biological macromolecules [1,2]. Snapshots of the reaction can be captured by different structural techniques, such as X-ray crystallography [3], Small Angle X-ray Scattering (SAXS) [4], and various spectroscopies [5]. Many time-resolved experiments have utilized flow-focused diffusive mixers [2], which rely on an outer sheath flow to thin the central sample stream so small molecules can rapidly diffuse into the stream for reaction initiation. Timescales ranging from single milliseconds to seconds are reachable. One reactant, however, must be relatively small and highly soluble for efficient diffusion. Thus, diffusive mixers are suited for reactions involving one large biological macromolecule, such as a protein or nucleic acid, and one small ligand.

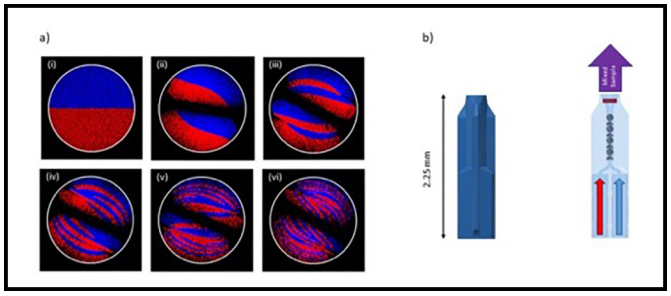

Figure 1: (a) Cross section of simulated flows after each mixing element inside the Kenics (b) CAD rendering of the exterior and cross section of the Kenics.

Reactions between two biological macromolecules, such as two proteins or a protein and a nucleic acid, are essential so there is interest in studying these interactions via time-resolved measurements. Turbulent mixers can achieve this, but high sample consumption is often prohibitive for lab-purified biological molecules. Mixing by chaotic advection is a strong alternative to diffusive and turbulent mixers, as the mixing is efficient enough for reactions between large macromolecules, and sample consumption is lower than turbulent mixers. The Kenics is a type of chaotic advection mixer that consists of a channel containing several helical mixing elements (Chemineer, Dayton, Ohio). As two fluids flow through, these mixing elements cause the fluids to undergo baker's transformations (Figure 1a); the two fluids are repeatedly stretched, split, and stacked on top of one another [6], and increasingly thin layers are produced, facilitating the diffusion of molecules between the two fluids. This design has efficient mixing for large molecules and can reach timepoints from 10 ms and beyond.

Kenics mixers can be fabricated using the Nanoscribe 3D printer at CNF. The Nanoscribe uses two-photon polymerization to print with submicron resolution, which is the level of precision required for our design (Figure 1b). The mixer was designed using Autodesk Inventor and the print settings were programmed in Describe. The inserts were printed with IP-S resin and 70% laser power. After printing, the inserts were placed in propylene glycol monomethyl ether acetate (PGMEA) for development for at least four days. Next, the inserts were submerged in IPA and sonicated for five minutes before UV curing for 60 minutes.

Previous versions of this mixer have been used for time-resolved SAXS (TR-SAXS) measurements [7]. Mixers of this design can also be coupled to other measurements. Absorbance spectroscopy was used to track the binding of myoglobin and azide, which caused a shift in the absorbance that was captured over time (Figure 2). The k value of the binding was accurately extracted from this data, demonstrating that kinetics experiments are possible [7]. Recent, CNF fabricated versions of this device are being used for x-ray spectroscopy measurements, with encouraging preliminary results.

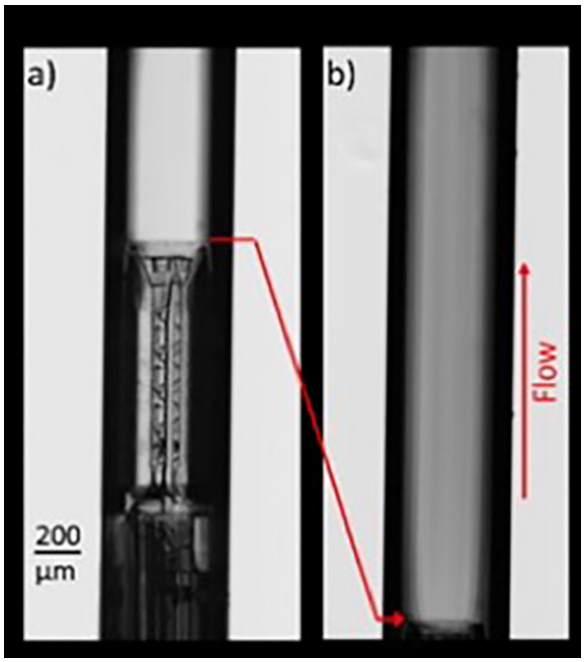

Figure 2: (a) Kenics mixer inside glass capillary absorbance spectroscopy measurements. (b) Fully mixed myoglobin and azide exiting the Kenics (tip of the mixer moved to the bottom of the field of view).

Conclusion and Future Steps:

Due to the high precision of the NanoScribe 3D Printer, we can fabricate a Kenics mixer for time-resolved experiments of a wide range of biological systems and a variety of techniques. Past work demonstrates the utility of this design for probing protein-protein, protein-nucleic acid, protein-ligand, and nucleic-acid ligand reactions with SAXS and absorbance spectroscopy. Future experiments will explore additional biological systems and use other techniques to capture the dynamics of biological reactions.

References:

[1] Calvey, G. D., Katz, A. M. & Pollack, L. (2019). Anal. Chem. 91, 7139-7144.

[2] Calvey, G. D., Katz, A. M., Schaffer, C. B., and Pollack, L. (2016). Struct. Dyn. 3, 054301.

[3] Olmos, J. L., Pandey, S., Martin-Garcia, J. M., Calvey, G., Katz, A., Knoska, J., Kupitz, C., Hunter, M. S., Liang, M., Oberthuer, D., Yefanov, O., Wiedorn, M., Heyman, M., Holl, M., Pande, K., Barty, A., Miller, M. D., Stern, S., Roy-Chowdhury, S., Coe, J., Nagaratnam, N., Zook, J., Verburgt, J., Norwood, T., Poudyal, I., Xu, D., Koglin, J., Seaberg, M. H., Zhao, Y., Bajt, S., Grant, T., Mariani, V., Nelson, G., Subramanian, G., Bae, E., Fromme, R., Fung, R., Schwander, P., Frank, M., White, T. A., Weierstall, U., Zatsepin, N., Spence, J., Fromme, P., Chapman, H. N., Pollack, L., Tremblay, L., Ourmazd, A., Phillips, G. N., and Schmidt, M. (2018). BMC Biology 16, 59.

[4] Plumridge, A., Katz, A. M., Calvey, G. D., Elber, R., Kirmizialtin, S., and Pollack, L. (2018). Nucleic Acids Research 46, 7354-7365.

[5] Calvey, G. D., Katz, A. M., Zielinski, K. A., Dzikovski, B., and Pollack, L. (2020). Anal. Chem. 92, 13864-13870.

[6] Saatdjian, E., Rodrigo, A. J. S., and Mota, J. P. B. (2012). Chemical Engineering Journal 187, 289-298.

[7] Zielinski, K. A., Katz, A. M., Calvey, G. D., Pabit, S. A., Milano, S. K., Aplin, C., San Emeterio, J., Cerione, R. A. & Pollack, L. (2023). IUCrJ 10, 363-375.

Metasurface-Enhanced Infrared Spectroscopy for the Measurement of Live Cells

CNF Project Number: 2472-16
Principal Investigator(s): Gennady Shvets
User(s): Steven He Huang, Po-Ting Shen, Aditya Mahalanabish

Affiliation(s): Applied and Engineering Physics, Cornell University

Primary Source(s) of Research Funding: National Cancer Institute of the National Institutes of Health award number R21 CA251052. National Institute of General Medical Sciences of the National Institutes of Health award number R21 GM138947

Contact: gs656@cornell.edu, hh623@cornell.edu, ps944@cornell.edu, am2952@cornell.edu

Website(s): http://shvets.aep.cornell.edu

Primary CNF Tools Used: JEOL 9500, SC4500 evaporator, Zeiss Supra SEM, PDMS Casting Station, Anatech Resist Strip, Glen 1000, Oxford PECVD, Oxford ALD FlexAL, Plasma-Therm 720/740, DISCO dicing saw

Abstract:

We have developed Metasurface-Enhanced Infrared Spectroscopy (MEIRS) as a novel tool to perform spectral analysis and chemical imaging of live cells. In MEIRS, cells are cultured on an array of plasmonic nanoantennas (metasurface), which enhances infrared vibrational signal through the coupling of molecular vibrations to plasmonic resonances. Various cellular responses can be observed from the infrared spectra collected in real-time. Our current work focuses on expanding the application of MEIRS to the chemical imaging of live cells as well as combining plasmonic metasurfaces with nano-topography to study cell-nanostructure interactions.

Summary of Research:

Infrared (IR) spectroscopy is widely used to identify chemical compounds through their molecular vibration fingerprints and has recently found many applications in biological analysis. We have developed a novel technique called Metasurface-Enhanced Infrared Spectroscopy (MEIRS) to measure live cells in physiological conditions. In MEIRS, cells are grown on an array of plasmonic nanoantennas called metasurfaces. These resonant nano-antennas support plasmonic hot spots, enhancing the light-matter interaction and IR absorption. We have used MEIRS to detect spectroscopic changes related to cell adhesion and dissociation, cholesterol depletion, response to chemotherapeutics, and activation of intracellular signaling pathways [1-3]. Our current work focuses on expanding the application of MEIRS to mid-infrared chemical imaging, as well as combining plasmonic metasurfaces with nano-topography to study cell-nanostructure interactions. Figure 1 shows a schematic drawing of the MEIRS measurement setup for live cells.

Our mid-IR metasurface is fabricated as an array of gold nanoantennas on IR transparent CaF_2 substrates. The substrate is first cleaned using oxygen plasma etcher (Anatech or Glen 1000 Resist Strip) and optionally coated with 20 nm of SiO_2 using plasma enhanced chemical vapor deposition (Oxford PECVD) as a protection layer. Metasurface patterns are defined using electron beam lithography with the JEOL 9500 system and poly(methyl methacrylate) (PMMA) as the resist. 5 nm Cr and 70 nm Au are deposited using SC4500 evaporator. If needed, metasurfaces fabricated on large substrates (up to 4" diameter) are diced to smaller pieces using DISCO dicing saw. As the final step, oxygen plasma etcher (Anatech or Glen 1000 Resist Strip) is used to clean the metasurface sample. The metasurface is then attached to superstructures for cell culture chambers and cells are grown on top of the metasurface for analysis. Figure 2 shows a scanning electron microscope image of a cell on the metasurface.

We are currently investigating the mid-IR chemical imaging of cells on the metasurface using a quantum cascade laser (QCL). An inverted laser point-scanning confocal microscope operating in the mid-IR is designed and built, providing a spatial resolution around 5 μm in the protein absorption bands (amide I and II, 1500 cm^{-1} to 1700 cm^{-1}). A hyperspectral image of formalin-fixed cells on the metasurface, with contrast from protein vibrational absorption, is presented in Figure 3. Although the spatial resolution of mid-IR microscopy is lower than visible microscopy, MEIRS microscopy provides chemical contrast in a label-free manner and is suitable for the long-term monitoring of live cells. We plan to apply this MEIRS microscopy to study the localization of different chemical species in live cells and the variation in spectral signature from a heterogeneous population of cancer cells.

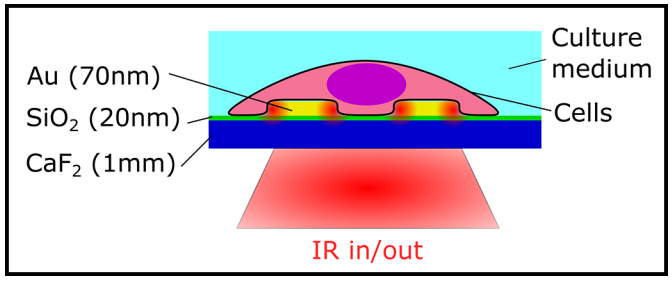

Figure 1: Schematic drawing of the metasurface-enhanced infrared spectroscopy setup for live cell measurement.

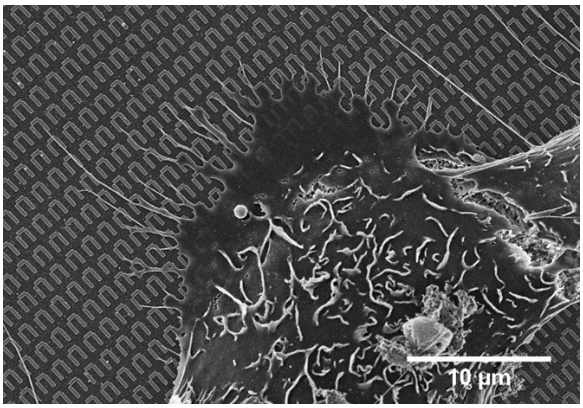

Figure 2: Scanning electron microscope image of a human skin cancer cell on the metasurface. Scale bar: 10 µm.

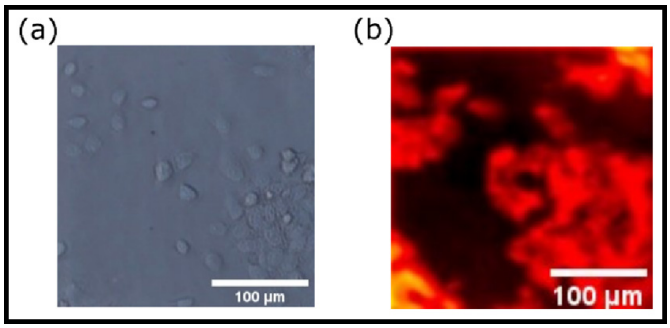

Figure 3: Formalin-fixed human skin cancer cells on the metasurface. (a) Phase contrast image. (b) MEIRS microscopy image with contrast from protein absorption. Scale bar: 100 µm.

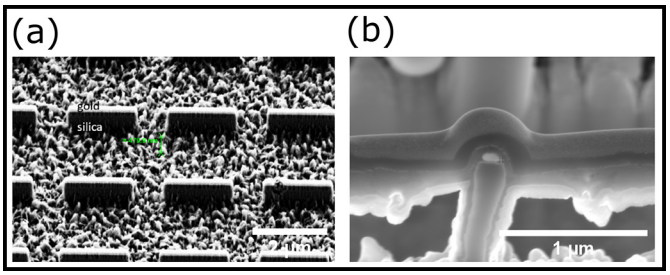

Figure 4: Nanoantenna-on-nanopillar structure. (a) SEM image of the nanoantenna-on-nanopillar structure without cells. Scale bar: 2 µm. (b) Cross section SEM image of one nanoantenna, with a cell adhered on top. Cell membrane can be seen curved around the nanoantenna-on-nanopillar. Scale bar: 1 µm.

Another direction in this project is the combination of metasurfaces with nano-topography to study cell-nanostructure interactions. Current research in surface nano-projections has shown that they can be used as effective tools to manipulate cellular attachment. We use nanopillars to incite physical and chemical responses in cells, which are then monitored through MEIRS. We have fabricated gold nanoantennas on top of silica nanopillars (Figure 4(a)). The fabrication process starts with growing a layer of silica (~1μm) on top of CaF_2 substrate using the Oxford PECVD. Next, metasurface patterns are defined using electron beam lithography (JEOL 9500). Gold is deposited in the patterned region using the CVC SC4500 Even/Odd Hour evaporator. We also deposit a thin layer of chromium above the gold nanoantenna and use it as a mask to chemically etch the silica using the Plasma-Therm 740. When cells attach to such nanopillar structures, cell membrane curves around these nanopillars (Figure 4(b)), increasing the overlap between the metasurface hotspots and the cells and also increasing the concentration of certain proteins (actin, clathrin) in the metasurface hotspots. Spectroscopically, we have observed that IR absorption from these cells on the nano-contoured metasurfaces is enhanced and shows different spectral features compared with cells on flat metasurfaces, likely related to protein secondary structures.

References:

[1] Huang, S. H., et al. Monitoring the effects of chemical stimuli on live cells with metasurface-enhanced infrared reflection spectroscopy. Lab Chip 21, 3991-4004 (2021).

[2] Shen, P.-T., et al. Probing the Drug Dynamics of Chemotherapeutics Using Metasurface-Enhanced Infrared Reflection Spectroscopy of Live Cells. Cells 11, (2022).

[3] Huang, S. H., et al. Metasurface-enhanced infrared spectroscopy in multiwell format for real-time assaying of live cells. Lab Chip 23, 2228-2240 (2023).

Ultra-Wideband Impedance Spectroscopy of a Live Cell

CNF Project Number: 2827-19
Principal Investigator(s): Alireza Abbaspourrad
User(s): Amirhossein Favakeh, Amir Mokhtare

Affiliation(s): Food Science & Technology, Cornell University

Primary Source(s) of Research Funding: US Army Research, Development and Engineering Command

Contact: alireza@cornell.edu, af446@cornell.edu, am2964@cornell.edu

Primary CNF Tools Used: ABM Contact Aligner, Heidelberg Mask Writer - DWL2000, SC4500 Even-Hour Evaporator

Abstract:

Accurate measurement of single-cell biophysical properties can represent helpful information on its physiological state. Electrical impedance spectroscopy (EIS) of single cells is a method for quantifying the phenotypic heterogeneity of cells. Compared to conventional optical or biochemical methods, EIS is a fast, compact, label-free, and non-invasive method. Therefore, a single cell can be trapped, characterized, and released using broad microwave frequency, by vector network analyzer (VNA). Hence, the frequency from low (kHz) up to high (GHz) can be swept through the cell to measure the subcellular features of the cell. This data will provide useful information about cell size, membrane properties, cytoplasm, and intracellular properties.

Summary of Research:

We fabricated a coplanar waveguide (CPW) electrode (Figure 1) that can be set up in a standard microscopy environment [1]. The CPW enables trapping, characterizing, and releasing a single cell and particle. Cells in an isotonic solution are moved through a microchannel equipped with electrodes in an impedance-based microfluidic channel. For this purpose, we fabricated microfluidic channels on these electrodes to guide cells through them at the minimum fluid flow and monitor the cell manipulation inside the channels which only requires one alignment step [2] (Figure 2).

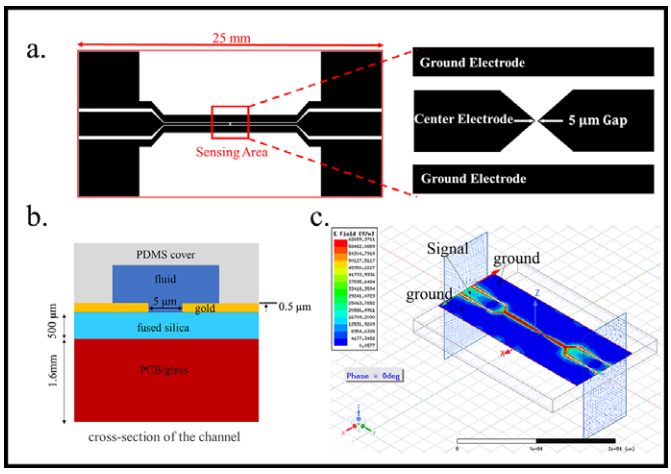

Figure 1: Coplanar waveguide (CPW) design, that includes a. a gold CPW, 2.5 cm long and 0.5 µm thick, which is deposited on a 500 µm thick fused silica substrate by an e-beam evaporator on a 1.6 mm PCB sheet. The gold CPW was covered with a 5 mm layer of PDMS. A microfluidic channel is molded onto the bottom side of the PDMS cover, intersecting the CPW. There is a 16 µm gap between the center and ground electrodes in the CPW. Besides the electrodes under the microfluidic channel, the center electrode is 200 µm wide. b. CPW cross-sectional dimensions in the channel region. c. The image shows a frequency sweeping pattern between two ports of the electrodes simulated by high-frequency structure simulator (HFSS) software.

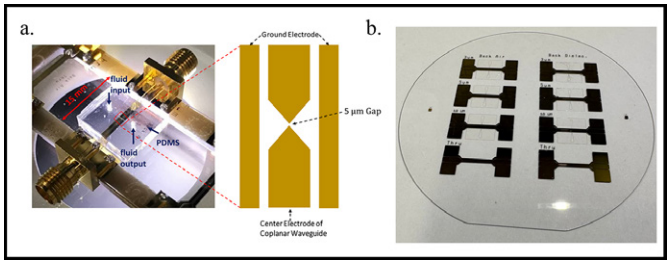

Figure 2: Microwave microfluidic device, a. The system includes a gold coplanar waveguide covered by PDMS microfluidic channel. b. Shows CPW with a different signal gap.

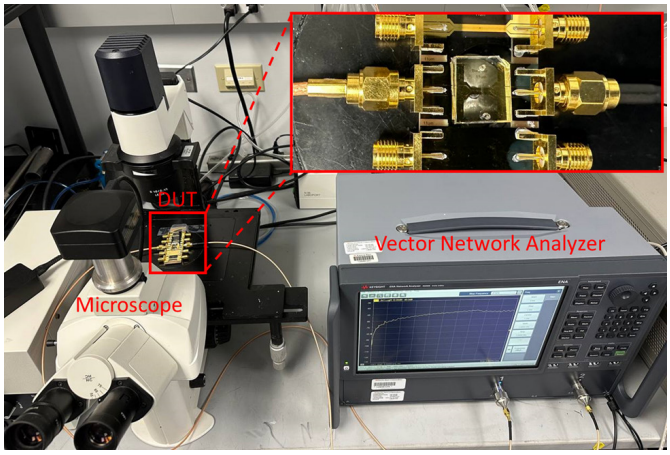

Figure 3: Shows the experimental setup. The device is placed on the microscope stage and connected to the VNA.

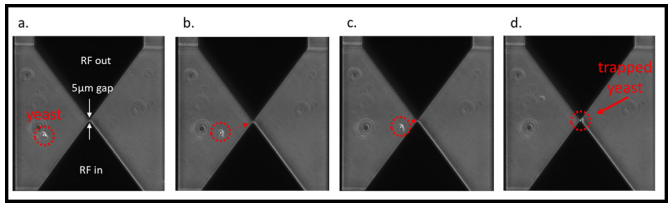

Figure 4: a-d. Shows single yeast trapped process by DEP micrograph. Yeast can be trapped and released by adjusting the frequency and power of the DEP signal from 5 MHz at 0 dBm to 30 kHz at 3 dBm.

The experimental setup is shown in Figure 3. We captured the cell using a dielectrophoresis (DEP) signal at 4 MHz and 0 dBm by VNA. The benefits of using this method are that the cells can be captured and released quickly between the two electrodes and the DEP focuses the electric field inside the cell. A yeast cell was trapped in the CPW gap by DEP and visually confirmed using a microscope. A yeast cell moves randomly in solution in the absence of DEP (Figure 4a). When DEP is applied to the solution the yeast is captured and moved toward the electrodes and immobilized by the CPW (Figures 4 b to d). When the cell is trapped between the two sharp electrode points, the majority of the radio frequency (RF) passes through the cell by way of the nucleolus. After trapping the yeast, the VNA was switched from the hold-frequency (4 MHz) to the sweep-frequency mode (30 kHz to 9 GHz) to measure the yeast's biophysical characteristics. The changes in S parameters were calculated and used to derive yeast biophysical characteristics using rapidly successive scattering parameters recorded with and without a trapped yeast.

Conclusions and Future Steps:

Impedance measurements are frequency dependent such that dispersion of a frequency spectrum can be allocated to different subcellular parts. We developed an ultra-wideband EIS device which is a non-invasive, and label-free method to characterize living single-cells. It can provide helpful information on its physiological state within the radio frequency (RF) range. This enables researchers to analyze the characterization of the cell more efficiently, instead of having to master complex tools.

For future steps, we will test the initially developed CPW electrode for validation and streamlining the sensing measurements. However, coplanar waveguides electrodes, despite having fewer fabrication complications, suffer from electric field non-uniformity with a strong electric field near the electrodes that fades away when moving away electrodes in the vertical direction. We will fabricate vertical electrodes. In this configuration, however, electric field linearity between electrodes is significantly more homogeneous with uniform electric field distribution in the entire testing region. This configuration of electrodes despite having more complexity and fabrication steps, significantly improves measurements' accuracy and signal-to-noise ratio.

References:

[1] Du, Xiaotian, Caroline Ferguson, Xiao Ma, Xuanhong Cheng, and James C. M. Hwang. 2022. "Ultra-Wideband Impedance Spectroscopy of the Nucleus in a Live Cell." IEEE Journal of Electromagnetics, RF and Microwaves in Medicine and Biology 6 (2): 267-72.

[2] Li, Hang, Caroline Multari, Cristiano Palego, Xiao Ma, Xiaotian Du, Yaqing Ning, Javier Buceta, James C. M. Hwang, and Xuanhong Cheng. 2018. "Differentiation of Live and Heat-Killed E. Coli by Microwave Impedance Spectroscopy." Sensors and Actuators. B, Chemical 255 (February): 1614-22.

Microfluidic Devices for High-Throughput Directed Evolution of Microbes for Rare Earth Element Purifications

CNF Project Number: 2852-19
Principal Investigator(s): Buz Barstow, Mingming Wu
User(s): Sean Medin, Young Joon Suh

Affiliation(s): Department of Biological and Environmental Engineering, CALS; Cornell University

Primary Source(s) of Research Funding: Air Force Research Labs

Contact: bmb35@cornell.edu, mw272@cornell.edu, sm2769@cornell.edu, ys668@cornell.edu

Primary CNF Tools Used: Heidelberg Mask Writer - DWL2000, ABM Contact Aligner, MVD100, Hamatech Hot Piranha, Class II Photolithography Room

Abstract:

Rare earth elements (REE), consisting of the lanthanides (elements from lanthanum to lutetium) as well as scandium and yttrium, are important ingredients to many sustainable energy technologies such as magnets — found in hard drives, electric vehicles, and cell phones — room temperature superconductors, and high-efficiency lighting [1]. Current methods for extraction and purification of these elements, however, utilize environmentally harmful chemicals and have a substantial carbon footprint [2]. We aim to use biology to create a cleaner, environmentally sustainable REE purification process. It has been found that bacteria contain numerous sites on their membrane that have specificity for both REE over other elements and for certain REE over other REE [3,4]. We plan on mutagenizing the genome of *V. natriegens* and then doing high-throughput screening to find strains with changes to preference for certain REE over others. We are utilizing the CNF to build a microfluidic droplet generation and sorting device in order to carry out this high-throughput screening.

Summary of Research:

At the CNF, we used the Heidelberg Mask Writer - DWL2000 to create masks (see Figure 1 for the designs) of our droplet generator and droplet sorter based on the generator and sorter created by Mazutis, et al. [5]. Utilizing the Class II Photoresist room, the Hamatech Hot Piranha, the ABM Contact Aligner, and the MVD100, we used this mask to create a SU-8 mold that we could use to create PDMS devices.

After the creation of these PDMS devices, we bonded them to a glass slide and treated the channels with Aquapel to make them hydrophobic. We then verified that droplets could be formed with this device (Figure 2). We also verified that our bacteria could survive inside these droplets.

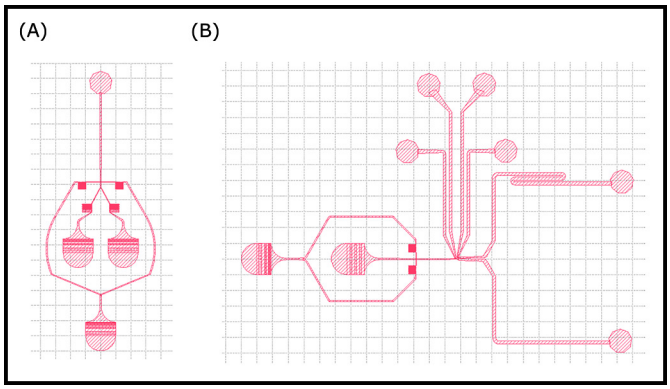

Figure 1: (A) Droplet generator design. (B) Droplet sorter design.

While we have yet to fully manufacture the sorting device we created at the CNF — which sorts via electrophoresis and requires the insertion of electrodes into two of the channels — we do have a sample of it created by a company that we were able to test. We verified that we could use this device to sort droplets generated by our device and that the bacteria were able to survive this sorting process that involves applying a square wave with an amplitude of 600-800 volts.

Conclusions and Future Steps:

Next steps involve integrating the device with an optical system so that we can sort the droplets based on the number of rare earth elements stuck to the bacterial membrane (we have a fluorescent protein that can help us with this). We also need to add electrodes to the sorting device we made at the CNF. Once these steps are done, we will be ready to use our device to select for mutagenized bacteria with membranes that have a preference for particular rare earth elements over others.

Figure 2: Droplets from droplet generator.

References:

[1] Lucas, J., Lucas, P., Le Mercier, T., Rollat, A., and Davenport, W. Rare Earths: Science, Technology, Production and Use. (Elsevier Inc., 2014).

[2] Voncken, J. H. L. The Rare Earth Elements, An Introduction. (2016).

[3] Takahashi, Y., Châtellier, X., Hattori, K. H., Kato, K., and Fortin, D. Adsorption of rare earth elements onto bacterial cell walls and its implication for REE sorption onto natural microbial mats. Chemical Geology 219, 53-67 (2005). https://doi.org:10.1016/j.chemgeo.2005.02.009.

[4] Bonificio, W. D., and Clarke, D. R. Rare-Earth Separation Using Bacteria. Environmental Science & Technology Letters 3, 180-184 (2016). https://doi.org:10.1021/acs.estlett.6b00064.

[5] Mazutis, L., Gilbert, J., Ung, W. et al. Single-cell analysis and sorting using droplet-based microfluidics. Nat Protoc 8, 870-891 (2013). https://doi.org/10.1038/nprot.2013.046.

Scalable Continuous Flow Electroporation Platform

CNF Project Number: 2900-20
Principal Investigator(s): Thomas Corso
User(s): Jacob VanderBurgh

Affiliation(s): CyteQuest
Primary Source(s) of Research Funding: Investor funding, NIH SBIR Phase I
Contact: tcorso@cytequest.com, jvanderburgh@cytequest.com
Website(s): https://cytequest.com/
Primary CNF Tools Used: Odd-hour evaporator, VersaLaser Engraver/Cutter

Abstract:

Viral vectors are a bottleneck in the manufacturing of cell therapies. To bypass viral vectors, electroporation has emerged as a non-viral transfection method for primary cells. However, standard cuvette-style approaches are limited by difficult optimization and incompatibility with large-scale cell manufacturing. Here, we present and fabricate a novel electroporation platform that can efficiently transfect small volumes of cells for research and process optimization and scale to volumes required for applications in cellular therapy. We demonstrate delivery of messenger ribonucleic acid (mRNA) to primary human T cells with high efficiency and viability at research scale and we demonstrate seamless scaling of delivery by increasing experimental throughput by a factor of five.

Summary of Research:

To address limitations associated with cuvette-style electroporation, CyteQuest has developed a scalable electroporation platform to optimize transfection parameters and deliver cargo efficiently and reproducibly at high throughput. Our approach incorporates a single use, continuous-flow fluidic system designed to integrate with automated cell processing approaches. The prototype electroporation flow cell consists of a planar flow chip with a thin slab geometry. It contains a single fluid inlet/outlet that receives cells suspended in electroporation buffer containing the cargo to be delivered. Electrodes are patterned on the top and bottom flow cell surfaces in order to apply a uniform electric field perpendicular to the flow direction (Figure 1A). The thin slab geometry of the device ensures that each cell is subject to the same electric field and the same chemical environment enabling reproducible electroporation. The shallow height (80 μm) also means that we can achieve the necessary electric field strength to open pores in the cellular and nuclear membranes by applying relatively low voltages (~15 V) compared to the high voltage of traditional commercial systems. The width (2 or 10 mm) of the device is much larger than its depth to allow for rapid and continuous flow of the cells through the chip (Figure 1B). Importantly, the width of the device can be varied to match the desired experimental throughput without changing the electric field experienced by the cells. As such, our planar geometry enables us to seamlessly scale from small volumes of precious sample to determine optimal transfection parameters to large volumes for delivery at clinical scales.

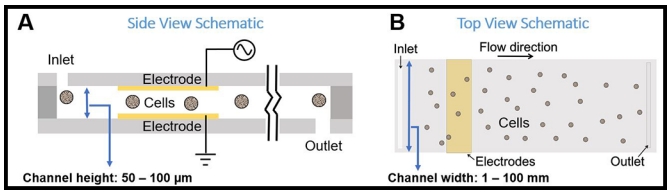

Figure 1: (A) Side view schematic of the flow cell (not to scale). (B) Top view schematic of the flow cell (not to scale).

Electroporation flow chips are constructed from a three-layer stack of polymer substrates. All three layers are laser cut with a small beam spot, high resolution carbon dioxide laser produced by the VersaLaser Engraver/Cutter. The top and bottom layers, cut from 1 mm thick acrylic slabs, create the floor and sealing channel surfaces. The middle layer is a spacer that defines the channel depth and width and is composed of a thin pressure sensitive adhesive tape. To fabricate the chip, the bottom and top acrylic layers are laser-cut into 1" × 2" pieces. The pieces are then laser-cut to add fluid inlet/outlet ports and alignment holes for use during the assembly process. Afterwards, a thin film electrode of gold is deposited by physical vapor deposition on the inside surface of each acrylic piece at the Cornell NanoScale Facility (CNF) using the odd-hour evaporator. The middle layer is cut to shape and also receives the corresponding alignment holes via the laser cutting process. The three-piece (acrylic, spacer, acrylic) sandwich assembly is then compression bonded in a press.

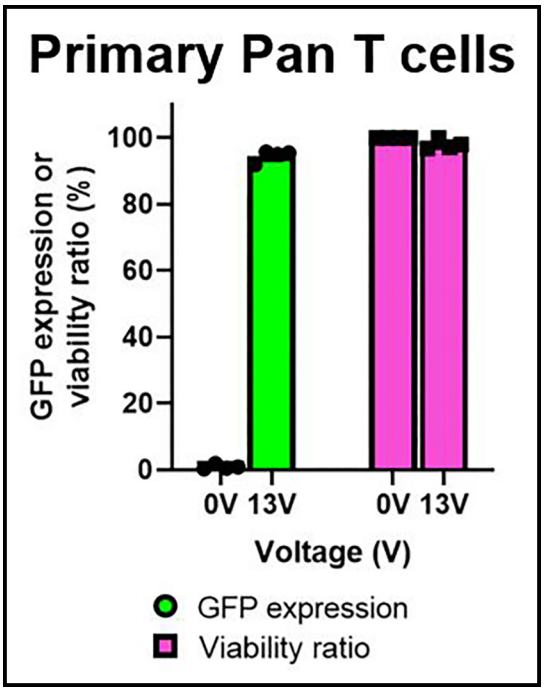

Figure 2: Delivery of mRNA to primary human T cells. Data from primary T cells from four healthy donors (n = 4). Data shown as mean ± standard deviation.

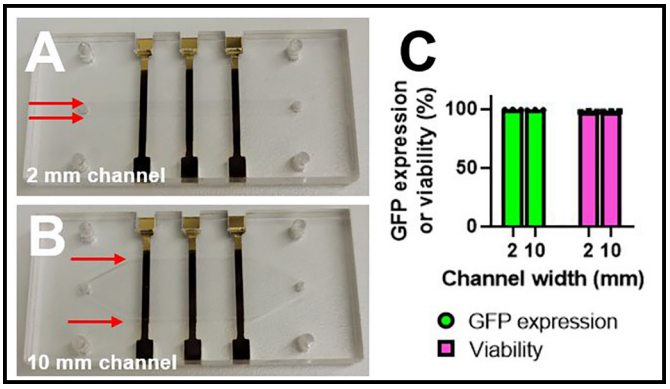

Figure 3: Scaled-up delivery of mRNA to Jurkat cells. (A) Photograph of a 2 mm and (B) 10 mm electroporation flow cell. Red arrows highlight the channel width. (C) Plot of GFP expression and viability values from Jurkat cells transfected with mRNA encoding GFP in either the 2- or 10-mm channels (n = 3). Data shown as mean ± standard deviation.

Cells with the cargo to be transfected are loaded into a syringe and injected through tubing into the flow cell by a syringe pump. As cells flow through the electrode pair, they experience a spatially uniform electrical field produced by a computer-controlled function generator and amplifier. The applied voltage waveform and resultant current are monitored via an oscilloscope. The electroporated cells then exit the flow cell and are dispensed into wells of a well-plate by a robotic fraction collector. Computer-controlled waveform selection and robotic sampling enable rapid sweeping of waveform parameters such as the voltage amplitude or waveform shape.

Using this system, CyteQuest has delivered mRNA encoding green fluorescent protein (GFP) to primary human T cells with high efficiency and high viability, observing > 95% transfection efficiency with < 2% loss of cell viability compared to control cells (Figure 2). To demonstrate the ability of our device to scale experimental throughput, we increased the width of the device from 2 to 10 mm and the volumetric flow rate from 320 μL/min to 1.6 mL/min (Figure 3A-B). Scaling both the channel width and flow rate by a factor of five produced identical GFP expression and viability values in both channel widths for Jurkat cells transfected with mRNA encoding GFP (Figure 3B). Overall, these data demonstrate the ability of our platform to efficiently deliver mRNA to cells and seamlessly scale-up delivery without changing delivery performance.

Investigating the Effect of the Tumor Microenvironment on Metastatic Progression Using Micro and Nano-Scale Tools

CNF Project Number: 2912-20
Principal Investigator(s): Claudia Fischbach
User(s): Matthew Tan, Nicole Sempertegui

Affiliation(s): Biomedical Engineering, Cornell University

Primary Source(s) of Research Funding: Stem Cell Research Training Fellowship, Stem Cell Program of Cornell; Center on the Physics of Cancer Metabolism Award Number 1U54CA210184-01, National Cancer Institute

Contact: cf99@cornell.edu, mlt239@cornell.edu, nds68@cornell.edu

Primary CNF Tools Used: ABM Contact Aligner, Heidelberg DWL2000, Hamatech 9000, Malvern NS300 NanoSight

Abstract:

Breast cancer mortality is driven by metastasis, where cancer cells disseminate from the primary tumor to seed distant tissues. During the metastatic cascade, cancer cells interact with their microenvironment consisting of extracellular matrix including collagen and other cell types such as endothelial cells in blood vessels and macrophages in the bone. Cancer cells may interact locally with these cells in the primary tumor microenvironment or from distant sites in the body through soluble factor signaling. In this study, CNF tools were used to investigate the two stages in metastasis: early invasion of tumor cells towards blood vessels and tumor cell invasion into the bone to form a pre-metastatic niche. For the former, we developed a microfluidic model of the perivascular niche and found that ECs stimulate breast cancer invasion into collagen, and that an EC-coated microchannel exhibits a distinct diffusion profile from a channel without ECs. For the latter, the same microfluidic model was modified to incorporate collagen mineralization to mimic bone ECM. Using this model, we have shown that tumor cell invasion is inhibited when co-cultured with macrophages seeded in a mineralized microchannel. Future work will continue to use the microfluidic model to investigate the mechanisms by which ECs influence cancer invasion and how mineralized collagen affects cancer cells and the formation of a pre-metastatic niche.

Summary of Research:

Introduction. Breast cancer is the second leading cause of cancer-related death for women in the United States [1]. Mortality in breast cancer is driven by metastasis, where tumor cells disseminate from the primary tumor and spread to distant tissues. During this process, tumor cells become invasive and move towards blood vessels, where they will enter the circulation and seed onto distance sites such as the bone. Tumor cells that proceed through the metastatic cascade encounter a changing microenvironment consisting of extracellular matrix (ECM) such as collagen and other cell types, including endothelial cells (ECs) and macrophages [2]. These cells are known to participate in reciprocal signaling with tumor cells to influence tumorigenesis through the exchange of soluble factors [2,3]. However, the mechanisms by which soluble factor signaling influence tumor cell invasion and the development of a pro-tumorigenic microenvironment remain unclear due to the lack of models that enable systematic study. To this end, we have used the expertise at the CNF to investigate two key steps in the metastatic cascade: initial invasion towards ECs in blood vessels, and later stage invasion into the bone pre-metastatic niche.

Regulation of Breast Cancer Invasion Using a Microfluidic Model of the Perivascular Niche. In early invasion, tumor cells initially invade towards blood vessels, responding to metabolic gradients from the vessels and signaling gradients from ECs. Using SU-8 photolithography in conjunction with the ABM Contact Aligner and a photomask generated by the Heidelberg DWL2000, we have created a dual channel microfluidic devices that enables co-culture of breast cancer cells and ECs encapsulated in a 3D collagen matrix. In this system, we found that the presence of ECs stimulated cancer invasion into a collagen hydrogel (Figure 1). Additionally, using fluorescent molecule diffusion studies, we found that an EC-coated channel restricted diffusion of molecules within in the channel compared to a channel without ECs (Figure 2).

Effects of Mineralized Collagen on Breast Cancer Cell Invasion Using a Microfluidic Model of the Bone Pre-Metastatic Niche. To colonize bone, disseminated tumor cells extravasate from the vessel and invade through the bone marrow to seed osteogenic niches [4]. Tumor cell invasion during this process is controlled by host cells including macrophages. Macrophages are particularly relevant as they not only exert immunomodulatory effects, but also have the potential to differentiate into

osteoclasts, the primary cell type driving osteolysis in bone metastasis patients. To model these interactions within a bone-like microenvironment, the microfluidic device described above was modified using the polymer-induced liquid precursor (PILP) method to include a mineralized collagen microchannel [5]. In this model, the mineralization of collagen, the primary component of bone matrix, as well as tumor cell and macrophage seeding can be selectively controlled. We have shown that macrophages promote the invasion of breast cancer cells regardless of collagen mineralization and that this effect occurs without cell-cell contact, suggesting that it was caused by soluble factors secreted from macrophages. It was also determined that collagen mineralization inhibits the ability of macrophages to promote tumor cell invasion (Figure 3).

Conclusions and Future Steps:

In this project we were able to develop tools and pipelines to study the breast cancer metastatic cascade. We were able to successfully fabricate and culture a 3D microfluidic tumor-perivascular niche model. Future work using this device will uncover the metabolic and mechanical mechanisms by which ECs influence breast cancer invasion. We were also able to isolate and characterize breast cancer derived ECs. Additionally, the 3D microfluidic device was modified to recapitulate key microenvironmental features of the bone pre-metastatic niche. These studies have shown that this model system is highly adaptable and can be modified by introducing additional cell types and/or soluble factors to probe other aspects of bone and tumor cell interactions. Future work includes will characterize the mineralized collagen and validate findings with primary murine bone marrow-derived macrophages.

Funding Acknowledgements:

Stem Cell Research Training Fellowship, by the Stem Cell Program of Cornell(NS). The work described was supported by the Center on the Physics of Cancer Metabolism through Award Number 1U54CA210184-01 from the National Cancer Institute. The content is solely the responsibility of the authors and does not necessarily represent the official views of the NCI or the NIH.

References:

[1] Siegel, R. L., Miller, K. D., Fuchs, H. E., and Jemal, A. Cancer Statistics, 2021. CA. Cancer J. Clin. 71, 7-33 (2021).

[2] Tan, M. L., Ling, L., and Fischbach, C. Engineering strategies to capture the biological and biophysical tumor microenvironment *in vitro*. Adv. Drug Deliv. Rev. 176, 113852 (2021).

[3] Zheng, P., and Li, W. Crosstalk Between Mesenchymal Stromal Cells and Tumor Associated Macrophages in Gastric Cancer. Front. Oncol. 10, 1-9 (2020).

[4] Peinado, H., et al. Pre-metastatic niches: organ-specific homes for metastases. Nat. Rev. Cancer 17, 302-317 (2017).

[5] Choi, S., et al. Intrafibrillar, bone-mimetic collagen mineralization regulates breast cancer cell adhesion and migration. Biomaterials. 198, 95-106 (2019).

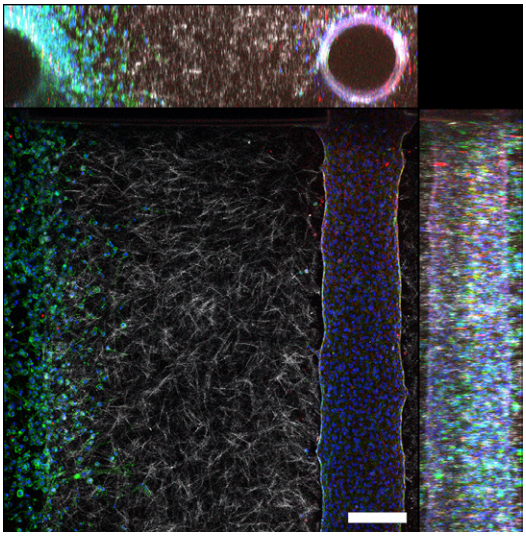

Figure 1: Confocal microscopy projection of breast cancer cells invading towards an endothelial cell channel stained with CD31 (red). DAPI was used to stain nuclei (blue), phalloidin was used to stain f-actin (green), and confocal reflectance was used to visualize collagen fibers (white). Scale bar: 200 µm.

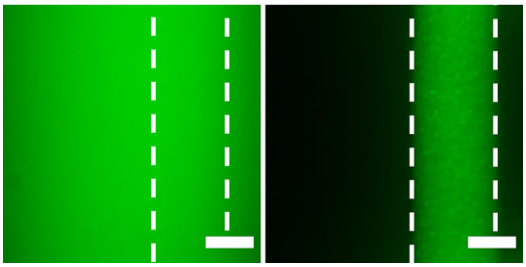

Figure 2: Diffusion of fluorescein (FITC) from a non-human umbilical vein endothelial cell (HUVEC) channel and a HUVEC coated channel. Scale bar: 200 µm.

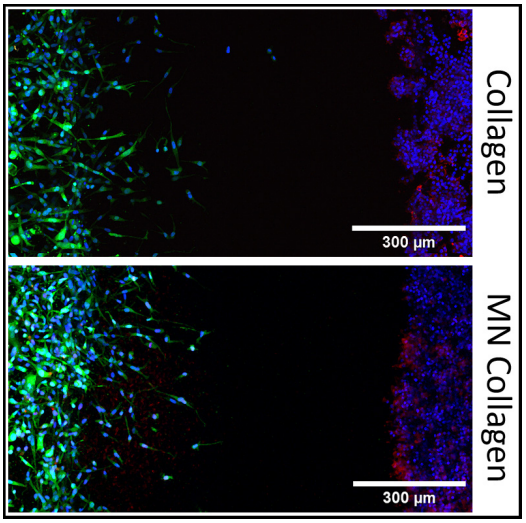

Figure 3: Fluorescent max intensity projection of non-mineralized collagen device (top) and mineralized (MN) collagen device (bottom) seeded with MDA-MB-231 breast cancer cells (green) and RAW264.7 macrophage cells (red). DAPI was used to stain nuclei (blue) Scale bar: 300 µm.

Fabrication of a Nanofluidic Fabry-Perot Cavity

CNF Project Number: 3069-23
Principal Investigator(s): Ronald Koder
User(s): Paul Molinaro

Affiliation(s): Department of Physics, City College of New York
Primary Source(s) of Research Funding: NSF MCB-2025200, NYSERDA NYS115213
Contact: rkoder@ccny.cuny.edu, pmolinaro@ccny.cuny.edu
Website(s): https://www.koderlab.org/
Primary CNF Tools Used: Mask Aligner, Substrate Bonder

Abstract:

Nanofluidic Fabry-Pérot cavities allow well understood experimental techniques from condensed matter physics to be applied to photoactive proteins under biological conditions [1]. Previous attempts to probe photoactive proteins with these techniques required the encapsulation of the system into a polymer [2] or the creation of a dehydrated thin film [3], significantly altering the proteins from their natural form. Recently, a method for measuring the reorganization energy via strong coupling to a Fabry-Pérot cavity has been proposed [4]. Due to the wavelengths involved in photo excitation, the height of these cavities must be on the order of 100 nm. These cavities can only be loaded nanofluidicly. Bahsoun and collaborators have recently fabricated a nanofluidic Fabry-Pérot cavity suitable for this experiment [1]. Our fabrication strategy borrows heavily from their approach. We are using the resources provided by the Cornell NanoScale Science and Technology Facility (CNF) to fabricate a nanofluidic Fabry-Perot Cavity.

Summary of Research:

Our lab is engaged in the design and engineering of new photosynthetic proteins [4]. Electron transfer in biological systems is well described by Marcus Theory [5]. The reorganization energy (λ) is crucial to predicting the rate of electron transfer for a given process. The parameter is most easily measured by measuring the rate of transfer as a function of the driving force of the reaction. Within a Fabry-Perot cavity, the energy of the donor state, and by extension the free energy of electron transfer, can be controlled by the number of molecules in the cavity. This observation suggests measuring the transfer rate as a function of concentration is equivalent to measuring a Marcus curve, from which λ can be extracted. The electron transfer rate can be measured by fabricating two cavities with an equal number of coupled molecules. In one cavity, the electron acceptor is absent. The reduction in transmission intensity in the presence of an electron acceptor is due to electron transfer.

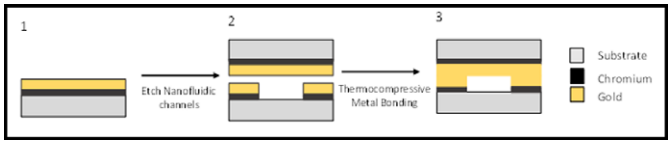

Figure 1: The nanofluidic cavity fabrication strategy. First metal is deposited on a substrate, then channels are etched into the metal via a lithographic process and two chips are bonded together by thermocompressive gold bonding.

An outline of our fabrication strategy is shown in Figure 1. A 100 mm glass wafer is coated with a 5 nm layer of chromium and between 250-500 nm of gold. A roughly 2 μm layer of AZ1512 photoresist is deposited via spin coating and baked at 110°C for 1 minute. The channels are patterned into the photoresist by exposing the resist to 150 mJ of UV light and baked for an additional minute. Development takes place by submerging the wafer in AZ 300 MIF developer for ~ 35 seconds. The exposed gold and chromium are etched away by submersion in Transene gold TFA etchant and chromium 1020 etchant for an amount of time dictated by the thickness of each metal layer. The remaining photoresist is stripped by soaking the wafer in acetone for two minutes with constant agitation. The wafers are then washed twice with methanol, isopropanol and deionized water before being blown dry with nitrogen. The wafer is then diced

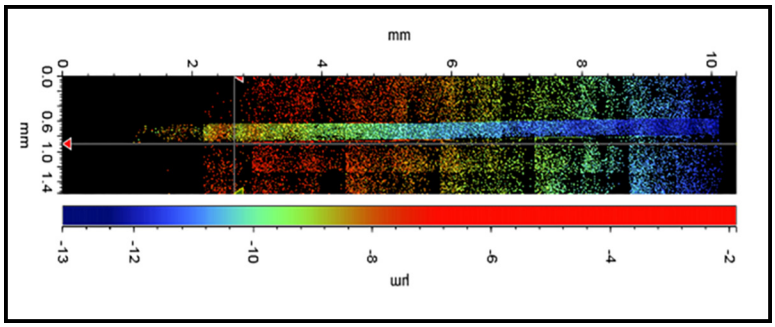

Figure 2: The depth of the cavity across the length of the channel, showing significant depth changes from one end of the channel to the other.

into 10 mm × 10 mm chips. Immediately before bonding, the washing step is repeated followed by a 2-minute 200-watt oxygen plasma ashing. One patterned chip and an unpatterned chip are aligned in a custom machined stainless-steel plate and another plate is hand screwed on top to apply pressure. The entire set-up is heated to 350°C for 30 minutes under a vacuum. Once the apparatus is cooled, the finished chip is removed.

So far, none of the finished chips have been wettable. This is due to the uneven application of pressure applied by the two steel plates. A depth profile of the resulting cavity can be seen in Figure 2. The cavity is of non-unform depth, a quality that is known for impeding nanofluidic flow.

Conclusion and Future Steps:

Currently, thermocompressive gold bonding is carried out using a custom, home built apparatus. We have been unable to produce a smooth enough surface to apply uniform pressure and thus create cavities of uniform depth. The thermocompressive gold bonding will no longer be performed using a hand screwed apparatus. Instead, a SUSS SB8e substrate bonder will be used to carry out the bonding. The tool allows for controlled, uniform application of pressure as well as temperature and pressure ramping. Once the bonding process is optimized, the cavities will be loaded with the photoactive substrate of interest and the reorganization energy will be measured.

References:

[1] Bahsoun, H., Chervy, T., Thomas, A., Börjesson, K., Hertzog, M., George, J., Devaux, E., Genet, C., Hutchison, J.A., Ebbesen, T.W., 2018. Electronic Light-Matter Strong Coupling in Nanofluidic Fabry-Pérot Cavities. ACS Photonics 5, 225-232. doi:10.1021/acsphotonics.7b00679

[2] Wu, F., Finkelstein-Shapiro, D., Wang, M., Rosenkampff, I., Yartsev, A., Pascher, T., Nguyen- Phan, T.C., Cogdell, R., Börjesson, K., Pullerits, T., 2022. Optical cavity-mediated exciton dynamics in photosynthetic light harvesting 2 complexes. Nature Communications 13. doi:10.1038/s41467-022-34613

[3] Satapathy, S., Liu, B., Deshmukh, P., Molinaro, P.M., Dirnberger, F., Khatoniar, M., Koder, R.L., Menon, V.M., 2022. Thermalization of Fluorescent Protein Exciton-Polaritons at Room Temperature. Advanced Materials 34, 2109107. doi:10.1002/adma.202109107

[4] Mauro, L., et al. "Charge-transfer chemical reactions in nanofluidic Fabry-Pérot cavities." Physical Review B 103.16 (2021): 165412.

[5] Mutter, A. C.; Norman, J. A.; Tiedemann, M. T.; Singh, S.; Sha, S.; Morsi, S.; Ahmed, I.; Stillman, M. J.; Koder, R. L., Rational Design of a Zinc Phthalocyanine Binding Protein Journal of Structural Biology 2014, 185 (2), 178-185.

[6] Punnoose, A.; McConnell, L. A.; Liu, W.; Mutter, A. C.; Koder, R. L., Fundamental Limits on Wavelength, Efficiency and Yield of the Charge Separation Triad. PLoS One 2012, 7(6).

Manipulation of Surface-Tethered Helical Polypeptide-Based Nanostructures with Localized Chemical Functionalities

CNF Project Number: 1757-09
Principal Investigator(s): Christopher Kemper Ober
User(s): Yuming Huang

Affiliation(s): Department of Materials Science and Engineering, Cornell University

Primary Source(s) of Research Funding: National Science Foundation

Contact: cko3@cornell.edu, yh839@cornell.edu
Website(s): https://ober.mse.cornell.edu/index.html

Primary CNF Tools Used: E-beam Resist Spinners, JEOL 9500, FilMetrics F50-EXR, Oxford 81 Etcher, Zeiss Ultra SEM, Veeco Icon AFM, Optical Microscope, Oxford 81

Abstract:

Polymer brushes are polymer chains with one end covalently anchored to a surface. Due to the unusual molecular arrangements and surface attachments, these densely grafted polymer brushes have exhibited unique mechanochemical properties and thus have gained wide interest from the polymer science community. Potential applications of such thin film could be biosensors, photovoltaic devices, organic electronics, and biomimicry surfaces. It was previously reported that the arrangement of polymer brushes could be organized via an integrated process of electron beam lithography, surface-initiated synthesis, and post-processing treatments. In this work, the customizability of such polymer nanostructure was further enhanced by end-point functionalization and vapor annealing process.

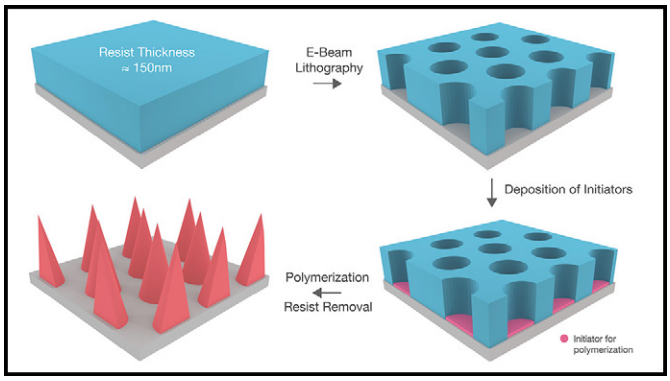

Figure 1: Schematic illustration of the fabrication process of nanopatterned brushes.

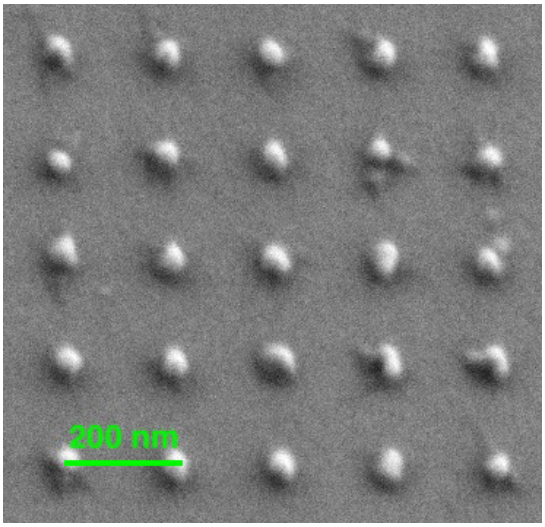

Figure 2: SEM image of the patterned PBLG rod brushes.

Summary of Research:

Polymer brushes have demonstrated various responsive behaviors towards external stimuli such as solvents [1], pH [2], temperature [3], and ionic strength [4]. It has been found that polymer brushes can display novel behaviors when subjected to nanoconfinement [5]. Previously, we reported a nanopatterning process of making "spiky" nanoarrays of polypeptide rod brushes on silicon substrates which have resulted in interesting "bridging" morphology governed by the localized chain-chain interactions (Figure 1 and 2) [6]. However, the characterization and manipulation of the chain arrangement in these nanostructured brushes can be challenging due to the extremely small feature sizes (less than 100nm) and highly confined structure.

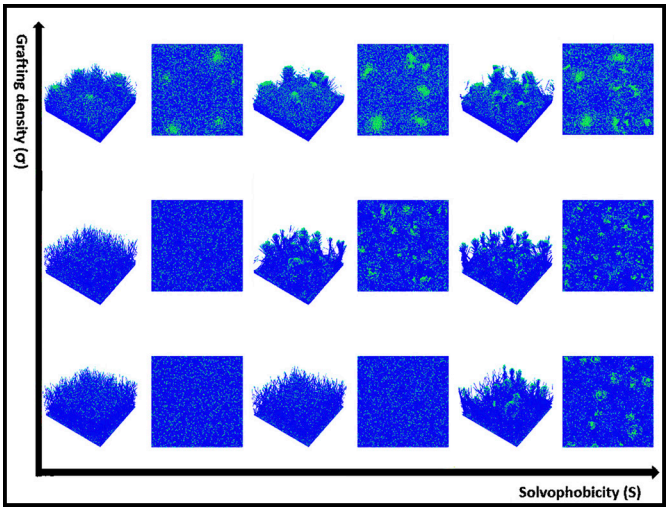

Figure 3: Computational simulation of rod brushes in various conditions.

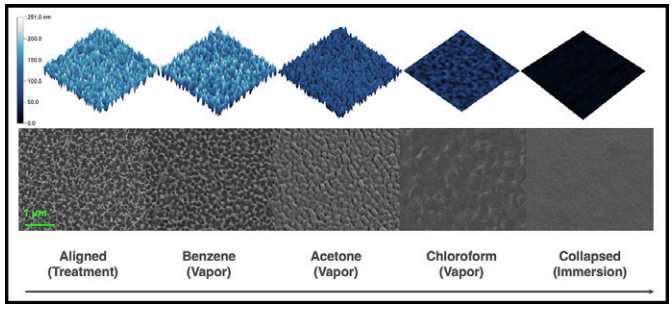

Figure 4: The SEM and AFM characterizations of PBLG brushes undergoing different treatments.

In this study, the organization of polypeptide rod brushes was examined via an integrated study of computational simulations and fluorescent dye-functionalized rod brushes. Chain-end functionalization of the brush tip was realized by chemically modifying the end groups with fluorescent probes — the fluorescence properties of the resulting brush film were found to be sensitive to the chain arrangement due to the aggregation-induced mechanism of the fluorophores. Coarse-grained rod polymer models, in conjunction with a density field-based energy function, were built to analyze the influence of various factors on the chain orientation, end-point density, and overall brush morphology (Figure 3).

Moreover, the potential of polypeptide rod brushes to serve as recognition elements in sensing devices for volatile organic compounds (VOCs) has been explored. The film's response to different VOCs, including benzene, chloroform, and acetone, was analyzed using an *in-situ* monitoring system based on reflectometry for real-time monitoring of vapor responses. It has been found that the brush exhibited reversible swelling-collapsing behavior when exposed to different VOCs such as benzene, chloroform, and acetone. Subsequently, a vapor treatment technique was developed to fine-tune the morphology of PBLG brushes, which has the potential to produce customizable nanostructured surfaces in combination with nanolithography (Figure 4).

In addition to nanolithography, we have demonstrated that polymer nanostructures can be further customized by chemical modification of the chain-ends and vapor-phase annealing process. The distribution and molecular arrangements of these active chain-ends can be examined by the behavior of the attached fluorescence molecules and controlled by vapor-phase treatment. In the future, we plan to explore the possibility of functionalizing these nanostructures with bioactive compounds for biomimicry surface and modeling study. We also plan to introduce mixed rod-coil brushes in the same system for binary and stimuli-responsive surface functionalities.

References:

[1] C.-T. Yang, Y. Wang, C. W. Frank, and Y.-C. Chang, "Chemoresponsive surface-tethered polypeptide brushes based on switchable secondary conformations," Rsc Adv, vol. 5, no. 105, pp. 86113-86119, 2015, doi: 10.1039/c5ra15839g.

[2] G. A. Eken, Y. Huang, Y. Guo, and C. Ober, "Visualization of the pH Response through Autofluorescent Poly(styrene-alt-Nmaleimide) Polyelectrolyte Brushes," Acs Appl Polym Mater, vol. 5, no. 2, pp. 1613-1623, 2023, doi: 10.1021/acsapm.2c02066.

[3] X. Wang, et al., "Temperature-Responsive Hierarchical Polymer Brushes Switching from Bactericidal to Cell Repellency," ACS Appl. Mater. Interfaces, vol. 9, no. 46, pp. 40930-40939, 2017, doi: 10.1021/acsami.7b09968.

[4] C.-H. Lin and S.-C. Luo, "Combination of AFM and Electrochemical QCMD for Probing Zwitterionic Polymer Brushes in Water: Visualization of Ionic Strength and Surface Potential Effects," Langmuir, vol. 37, no. 42, pp. 12476-12486, 2021, doi: 10.1021/acs.langmuir.1c02230.

[5] W.-L. Chen, M. Menzel, O. Prucker, E. Wang, C. K. Ober, and J. Rühe, "Morphology of Nanostructured Polymer Brushes Dependent on Production and Treatment," Macromolecules, vol. 50, no. 12, pp. 4715-4724, 2017, doi: 10.1021/acs.macromol.7b00714.

[6] Y. Huang, H. Tran, and C. K. Ober, "High-Resolution Nanopatterning of Free-Standing, Self-Supported Helical Polypeptide Rod Brushes via Electron Beam Lithography," Acs Macro Lett, vol. 10, no. 6, pp. 755-759, 2021, doi: 10.1021/acsmacrolett.1c00187.

Sequence-Defined Polypeptoid CARs for Electron-Beam and EUV Lithography

CNF Project Number: 1757-09
Principal Investigator(s): Christopher Kemper Ober
User(s): Florian Hermann Ulrich Kaefer, Chaoqiuyu Wang

Affiliation(s): Department of Material Science and Engineering, Cornell University

Primary Source(s) of Research Funding: Intel

Contact: cko3@cornell.edu, fhk28@cornell.edu, cw867@cornell.edu
Website(s): https://ober.mse.cornell.edu/

Primary CNF Tools Used: ASML 300C DUV Stepper, AFM Bruker Icon, JEOL 6300 E-Beam, Woollam RC2, Zeiss Ultra SEM, YES HMDS prime oven

Abstract:

Polymeric photoresists are limited in sensitivity, resolution, and line-edge roughness largely due to their various molar mass distributions and polymer chain compositions. Polypeptoids are, however, characterized by low stochastics. In this work we describe the synthesis of ten repeating-unit polypeptoids designed as photopolymers and demonstrate their potential as chemically amplified resists (CARs) evaluated by electron-beam (E-Beam), deep ultraviolet (DUV) and extreme-ultraviolet lithography (EUVL), obtaining well-defined line-space patterns of less than 30 nm half-pitch.

Summary of Research:

While in the last decade there has been significant progress on the design and synthesis of resists for EUVL, shortcomings of these resists still exist [1-3]. Despite the novel inorganic and metal-organic systems with good lithographic performance, their design is limited by their molecular structure [4]. For polymeric resist, their intrinsic defects always limit their lithographic performance [5]. In this work, we demonstrate the synthesis of polypeptoids whose structure, molecular weight, composition, and microstructure can be precisely controlled via a sequence-defined synthetic method [6-8] and investigate their potential as resists for EUVL.

Several libraries of polypeptoid with ten repeating units were synthesized. In particular we focus on four polypeptoids of which the sequences were altered, see Figure 1. After synthesis the polypeptoids were characterized by differential scanning calorimetry (DSC) to determine the glass transition temperature, and matrix assisted laser desorption ionization time-of-flight mass spectrometry (MALDI-TOF) was applied to confirm the polypeptoid structure, as previously reported [7]. Di-*tert*-butyl decarbonate (tBOC) was used to protect the hydroxy groups to introduce solubility-switch ability. By introducing short aliphatic and bulky sidechains, we were able to further tailor the solubility and contrast and obtained a resist which is developable in dilute aqueous base. Furthermore, polypeptoids with chain-end hydrophobic sidechains presented a better lithographic. This is attributed to microstructure and the increasing chain-mobility.

The lithographic performance of the synthesized polypeptoids was evaluated by E-Beam lithography. The best performing scanning electron microscope (SEM) micrographs represent the polypeptoid with a block-like structure where the short aliphatic and bulky aromatic sidechains are placed at the termini of the polypeptoid chain, see Figure 2.

Figure 3 shows the EUVL contrast curve taken from Paul-Scherrer Institute (PSI) in Switzerland, which presents a clearing dose at around 10 mJ/cm^2 indicating a positive tone, sensitive resist, while the change in sequence did not significantly affect the dosage to clear. It is worth noting that our first experiments indicated that a change of tone occurs by aging the resist solution. This might be attributed to the stability of the carbonate protecting group, which is reduced by terminal carboxylic acids of the polypeptoid chain. However, further studies are required to better understand the effect of the end-groups of the polypeptoids on solution stability and lithographic performance.

Conclusions and Future Work:

In this work we demonstrate the synthesis of short polypeptoids and show their potential as resists for EUVL. By introducing hydrophobic-aliphatic and aromatic bulky sidechains the solubility change could be tailored to obtain an aqueous-base developable resist. While the compositions of the synthesized polypeptoids were the same, the sequence was varied, affecting the lithographic performance. However, the best performance was observed placing the hydrophobic moieties closer to the chain ends, forming a symmetrical segmented structure, obtaining line: space patterns of 36 nm half-pitch by E-Beam lithography. The clear dosage of the best performing EUV resist was determined to be about 10 mJ/cm^2 showing a sharp change in solubility with increasing dosage. While we could successfully show the potential application of these materials as EUV resist, further research is required to optimize the lithographic performance, improve the stability in solution and identify the effect of sequence on lithographic patterning.

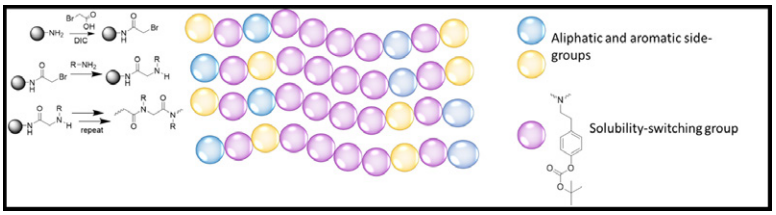

Figure 1: Solid phase supported synthesis of four different sequences of polypeptoid with short hydrophobic aliphatic and bulky aromatic side chains.

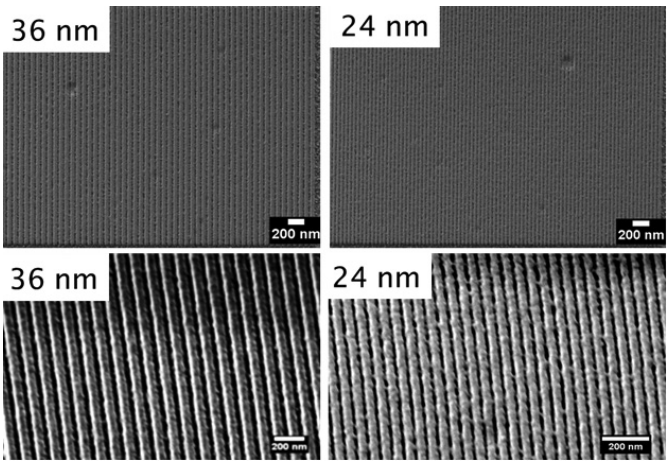

Figure 2: Electron-beam 1:1 line: space micrographs of the best performing polypeptoid developed in dilute 0.1 TMAH aqueous solution for 20s. PAG: TPS-PFBS (20 wt.%), Dosage: 216μC/cm^2.

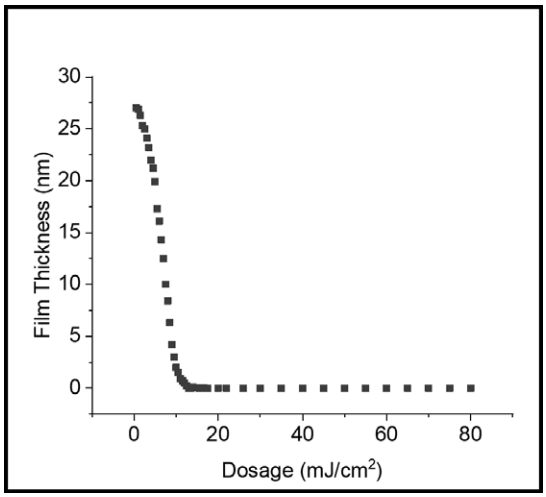

Figure 3: EUV contrast curve of a block-like polypeptoid with a short aliphatic and bulky aromatic sidechain at both termini.

References:

[1] Lio, A., "EUV Photoresists: A Progress Report and Future Prospects," Synchrotron Radiation News, 32(4): p. 9-14 (2019).

[2] Li, L., et al., "Extreme ultraviolet resist materials for sub-7 nm patterning," Chemical Society Reviews, 46(16): p. 4855-4866, (2017).

[3] Manouras, T. and P. Argitis, "High Sensitivity Resists for EUV Lithography: A Review of Material Design Strategies and Performance Results," Nanomaterials (Basel), 10(8) (2020).

[4] Luo, C., et al., "Review of recent advances in inorganic photoresists," RSC Advances, 10(14): p. 8385-8395, (2020).

[5] Anna, L. "EUV resists: What's next?," in Proc.SPIE, (2016).

[6] Deng, J., et al., "New Approaches to EUV Photoresists: Studies of Polyacetals and Polypeptoids to Expand the Photopolymer Toolbox," Journal of Photopolymer Science and Technology, 34(1): p. 71-74, (2021).

[7] Meng, X.Z., et al. "Controlled sequence peptoids as photoresist platforms for high-resolution DUV/EUV photoresists, "Proc. SPIE, (2022).

[8] Florian Kaefer, Z.M., Rachel Segalman, Christopher Ober. "Controlled Sequence Photoresists from Polypeptoids," The 39th International Conference of Photopolymer Science and Technology, (2022).

Micro-Etched Sorbent SPMESH Sheets for High Throughput, Trace-Level Analysis of "Smoke Taint" Compounds in Grapes and Wines

CNF Project Number: 2513-16
Principal Investigator(s): Gavin Sacks
User(s): Terry Bates, Austin Montgomery, Heather Scott, Andy Kalenak

Affiliation(s): Department of Food Science, Cornell University
Primary Source(s) of Research Funding: New York Wine and Grape Foundation
Contact: gls9@cornell.edu, tlb247@cornell.edu, am3253@cornell.edu, has224@cornell.edu, apk66@cornell.edu
Website(s): http://blogs.cornell.edu/winechemistry/
Primary CNF Tools Used: VersaLaser Engraver/Cutter Tool

Abstract:

Exposure of grapes to the smoke of forest or brush fires may result in "smoky" off-aromas ("smoke taint") in resulting wines due to several odorants, including volatile phenols like cresol and guaiacol. These volatile phenols are detectable at low ppb (ng/g) concentrations, and their analysis typically requires lengthy analyses (20-40 min) by gas chromatography - mass spectrometry (GC-MS). The slow analytical throughput of GC-MS creates bottlenecks during smoke exposure events during harvests, and limits the ability of vineyards and wineries to make data-driven decisions. Using tools available through the Cornell NanoScale Facility (CNF), we have prepared etched sorbents sheets ("SPMESH") designed for selective extraction of volatile phenols. The sheets are designed to fit over multiwell plates and allow for parallel extraction of odorants prior to rapid mass spectrometric analysis. The optimized method can analyze 24 samples in < 10 min, or nearly a 100-fold improvement in throughput over the gold standard method.

Summary of Research:

SPMESH sheets were prepared by etching a grid pattern in thin silicone sheets using the VersaLaser Cutter/Engraver at CNF, using a previously described protocol (Figure 1, left) [1]. SPMESH sheets were positioned over multiwell plates containing wine or grape samples to extract volatile phenols from the sample headspace. Extracted sample sheets were then analyzed by direct analysis in real time mass spectrometry (DART-MS) (Figure 1, right). Poor signal response and detection limits (>1 mg/L) were initially observed. This was determined to be due to the high polarity of the analytes. This problem was addressed by derivatization with deuterated acetic anhydride (Figure 2). The full workflow is shown in Figure 3.

Following optimization, figures of merit were determined in juice and wine. Detection limits for target compounds were ~ 1 μg/L for the three target VPs, below sensory threshold. Good linearity and reproducibility were also achieved. The DART-MS analysis requires < 10 min to analyze 24 samples, or about 50-100 faster than gas chromatography-mass spectrometry (GC-MS), the current gold standard. Including derivatization and extraction time, the entire approach requires ~ 60 min for 24 samples. For validation, juice and wine samples were sourced from an industry cooperator. Samples were analyzed by both the new SPMESH-DART-MS method and the gold standard GC-MS method. Good agreement was observed between the two methods for all analytes (r2 = 0.7-0.9). Results of the work have been published ([2] Bates and Sacks, 2023) and the approach is being shared with commercial fee-for-service analytical labs.

References:

[1] Bee, Madeleine Y., Jillian A. Jastrzembski, and Gavin L. Sacks. "Parallel headspace extraction onto etched sorbent sheets prior to ambient-ionization mass spectrometry for automated, trace-level volatile analyses." Analytical chemistry 90.22 (2018): 13806-13813.

[2] Bates, Terry L., and Gavin L. Sacks. "Rapid headspace solid-phase microextraction sheets with direct analysis in real time mass spectrometry (SPMESH-DART-MS) of derivatized volatile phenols in grape juices and wines." Analytica Chimica Acta (2023): 341577. https://www.sciencedirect.com/science/article/pii/S0003267023007985.

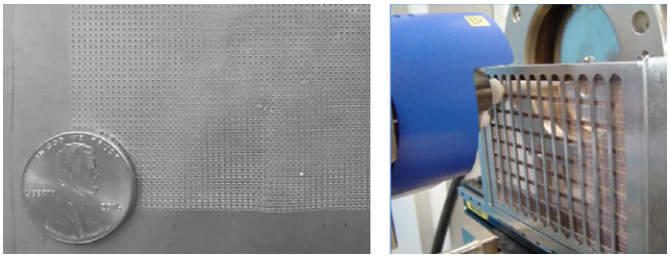

Figure 1: (left) Etched silicone SPMESH sheet produced at the CNF. The grid size is 0.5 mm × 0.5 mm, and (right) SPMESH sheet positioned during DART-MS analysis.

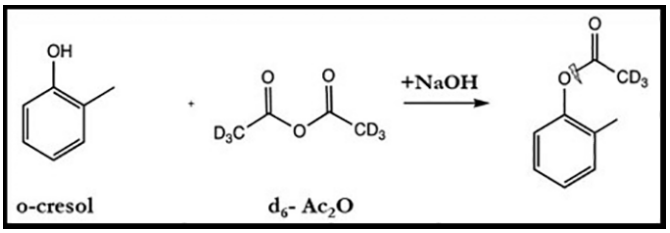

Figure 2: Acetylation scheme used to increase hydrophobicity and extractability of targeted phenols.

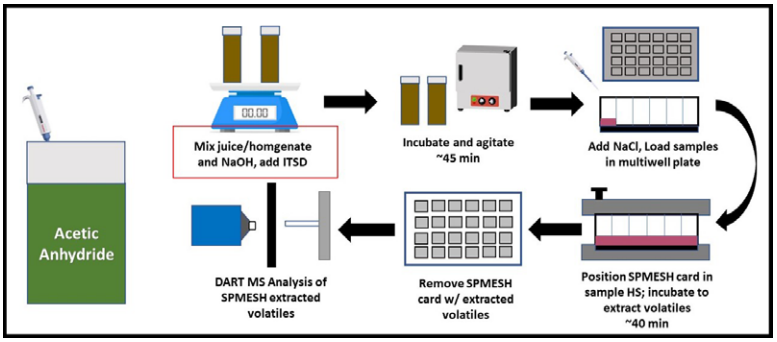

Figure 3: Workflow for rapid analyses of "smoke taint" odorants (volatile phenols) in grapes and wines.

Identifying the Occurrence and Sources of Per- and Polyfluoroalkyl Substances in Photolithography Wastewater

CNF Project Number: 2938-21
Principal Investigator(s): Damian Helbling[1], Christopher Kemper Ober[2]
User(s): Paige Jacob[1]

Affiliation(s): 1. Civil and Environmental Engineering, 2. Materials Science & Engineering; Cornell University
Primary Source(s) of Research Funding: Semiconductor Research Corporation and National Science Foundation
Contact: deh262@cornell.edu, cko3@cornell.edu, pvj7@cornell.edu
Website(s): https://helbling.research.engineering.cornell.edu/
Primary CNF Tools Used: DISCO Dicing Saw, Jelight 144AX UVO-Cleaner, FilMetrics F40

Abstract:

Per- and polyfluoroalkyl substances (PFASs) are contaminants of concern to environmental and human health [1]. PFASs are present in photolithography materials [2] and might undergo transformation reactions during photolithography. We acquired five photolithography materials and characterized the occurrence of organic fluorine and PFASs in the materials. We performed photolithography experiments, collected the wastewater samples for subsequent analyses, and used a mass balance approach to assess the extent of transformations. The goal of the project was to evaluate the evolution of fluorinated materials during photolithography to gain an improved understanding of whether photolithography is a major source PFASs in fabrication (fab) wastewater.

Chemical	Measured TF	Measured AOF	% of Solid Components as TF	% TF captured by AOF
Photoresist A	1.65±0.14	0.37±0.04	1.65±0.14	22.3±1.93
Photoresist B	0.36±0.03	0.18±0.00	0.55±0.04	51.8±3.67
Photoresist C	1.31±0.04	0.68±0.08	0.65±0.02	52.0±7.25
TARC A	18.1±0.35	2.38±0.27	60.2±1.12	13.2±1.70
TARC B	4.62±0.08	0.62±0.06	15.4±0.27	13.4±1.19

Table 1: Average and standard deviation of total fluorine (TF) and adsorbable organic fluorine (AOF) concentrations (g L-1) conducted by means of combustion ion chromatography (CIC) in the five photolithography materials prior to photolithography.

Summary of Research:

A variety of PFASs and fluoropolymers are used in photolithography materials and a recent study demonstrated that fab wastewater contains PFASs [4]. Although it is known that perfluorobutane sulfonate (PFBS) is a widely used constituent of photoacid generators (PAGs) [2], the sources of nearly all other PFASs in fab wastewater remain unknown.

Constituents of photolithography materials are also subject to transformation reactions induced by the conditions of photolithography, which expose the materials to UV radiation and highly basic conditions [5]. We hypothesize that a major source of PFASs in fab wastewater are PFASs used or generated during photolithography. We acquired five photolithography materials and designed experiments to: (1) characterize the organic fluorine and PFAS in the materials; and (2) assess the formation or destruction of PFASs during photolithography.

We acquired three photoresists (Photoresists A, B, and C) and two top antireflective coatings (TARCs A and B). We measured the total fluorine (TF) of the materials, which ranged between 0.36 - 18.1 g L-1 (Table 1). We also measured the adsorbable organic fluorine (AOF) of the materials, which ranged from 0.18 - 2.38 g L-1 (Table 1), confirming that the materials have organofluorine-containing constituents.

We performed a target analysis for 39 PFASs in the materials. In Photoresist A and Photoresist C, we identified PFBS at 581±50 mg L-1 and 470±104 mg L-1, respectively, and the fluorine from PFBS accounts for 20% of the TF in both materials. PFBS was the only target PFAS that can explain a significant portion of the TF in these two materials. In an effort to identify other PFASs that could contribute to the TF, we performed suspect and nontarget analyses. We identified 20 suspect PFASs in TARC A and found that these PFASs explained 17.0±13.8% of the TF in TARC A. No other suspect or nontarget PFASs were found in the other materials. After applying target, suspect, and nontarget screenings, 80% of the TF in Photoresist A and C, 92% of the TF in TARC A, and approximately 99% of the TF in Photoresist B and TARC B remains uncharacterized. We suspect that the remaining TF can be attributed to fluorine present in polymeric form.

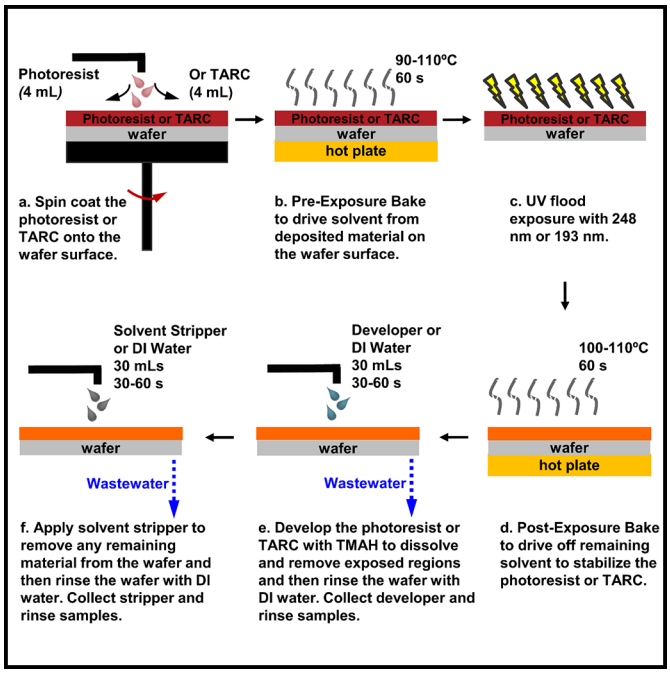

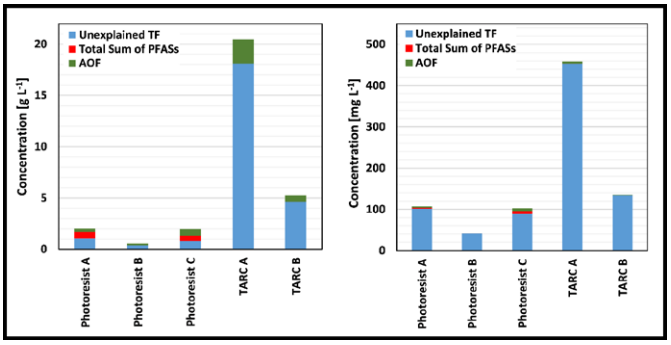

Figure 1, top: Photolithography process diagram detailing specific experimental parameters of each step. The exact parameters applied at different steps (i.e., spin coating and baking) were adjusted for each material according to the specifications provided by the manufacturers.

Figure 2, below: (a) Concentrations in g L-1 of unexplained total fluorine (TF), measured adsorbable organic fluorine (AOF), and the amount of TF that is attributed to the total sum of target PFASs measured in the materials. (b) Concentrations in mg L-1 of unexplained total fluorine (TF), measured adsorbable organic fluorine (AOF), and the amount of TF that is attributed to the total sum of target PFASs measured in the 248 nm wastewater samples. We note the different units used on the y-axis in (a) and (b) that reflect dilution of each material during the photolithography experiments.

We performed photolithography experiments and collected the wastewater from each material after development and stripping (Figure 1). We performed TF and AOF analyses and target, suspect, and nontarget screenings on the wastewater samples to identify the PFASs present post-photolithography. These measurements allowed us to track the mass of the materials throughout photolithography.

The wastewater samples generated contained no measurable TF. We surmise that a combination of TF loss during spin coating and subsequent dilution in the wastewater samples resulted in concentrations that were below the method limit of quantification. Next, we measured the AOF of the wastewater samples which ranged from 126.7 - 6976.7 ug L-1.

We performed a target screening on the wastewater samples and determined the extent of formation or destruction of the target PFASs by implementing a mass balance approach. These mass balance analyses indicate that target PFASs were being created or destroyed to some extent during photolithography, but that the changes in masses fail to explain more than 1% of the TF of each material. Over 75% of the TF of each material remains unexplained after these mass balance analyses indicating the stability of the organofluorine-containing constituents (e.g., fluoropolymers) of these materials during photolithography [2]. We also applied the suspect and nontarget screening workflows on the samples.

We discovered 13 suspect or nontarget PFASs unique to the wastewater of each material and exposure but expect that none of these compounds would contribute greater than 1% to the measured TF.

Conclusions and Future Steps:

We conclude that: (1) the selected photoresists and TARCs have organofluorine-containing compounds at similar levels of other industrial and commercial products and formulations; (2) target PFASs present in these materials can only explain up to 20% of the TF in a material; and (3) the simulated photolithography experiments did not induce significant transformations. This study highlights the complexity of tracking the source of PFASs in a fab, as the simulated photolithography experiments did not yield the expected results.

Future steps will focus on evaluating the fate and transformation of fluoropolymers during photolithography and wastewater treatment.

References:

[1] Z. Wang, et al.; 10.1021/acs.est.6b04806.
[2] C. K. Ober, et al.; 10.1117/1.JMM.21.1.010901.
[3] C. A. McDonough, et al.; 10.1016/j.coesh.2018.08.005
[4] P. Jacob, et al.; 10.1021/acs.est.0c06690.
[5] D. Bratton, et al.; 10.1002/pat.662.

Scalable Defect Engineering in Metal-Organic Frameworks via High-Concentration Self-Assembly Utilizing Pre-Assembled Cluster Precursors

CNF Project Number: 2996-21
Principal Investigator(s): Phillip J. Milner
User(s): Ronald T. Jerozal

Affiliation(s): Department of Chemistry and Chemical Biology, Cornell University

Primary Source(s) of Research Funding: National Institute of General Medical Sciences of the National Institutes of Health under award number R35GM138165

Contact: pjm347@cornell.edu, rtj32@cornell.edu

Website(s): https://blogs.cornell.edu/milner/

Primary CNF Tools Used: Rame-Hart 500 Goniometer

Abstract:

Metal-organic frameworks (MOFs) are a class of porous, crystalline materials that can have tailored properties based on the incorporation of defects and are promising for applications in gas storage, catalysis, and separations. Syntheses of MOFs on large scale, however, remain a major roadblock to their further implementation, as many are synthesized using solvothermal methods under highly dilute (≤0.01 M) conditions. Additionally, a large excess (>50 equiv.) of competing acid modulators is often used to enhance the crystallinity of and the number of defects in the resulting MOF, further amplifying the associated waste of MOF synthesis. We demonstrated that zirconium and hafnium MOFs are generally able to be synthesized at much higher reaction concentrations (up to 1.0 M). Additionally, the use of pivalate-capped metal cluster precursors — as opposed to a standard metal chloride salt — led to the inclusion of pivalate defects at missing-linker sites, which increased the hydrophobicity of the resulting MOF. Our findings provide a user-friendly approach to the scalable synthesis of defect engineered MOFs by drastically reducing solvent and acid modulator waste.

Summary of Research:

Metal-organic frameworks (MOFs) are crystalline, porous solids constructed from inorganic nodes bridged by organic linkers [1]. MOFs are promising for a variety of applications, including heterogeneous catalysis, gas storage, and chemical separations, due to their highly tunable pores that can resist collapse upon desolvation [1]. The controlled incorporation of defects in MOFs, such as missing-linker defects, can be utilized to tune the resulting framework properties by further modifying the size and chemical functionality of the pores [2]. Despite their potential, a major challenge to the further development of MOFs is their synthesis on bench top scales (1-100g). This is mostly due to the excessive waste generated during synthesis as many use very dilute (~0.01M) solvothermal conditions in hazardous solvents such as dimethylformamide (DMF) [3]. Additionally, many syntheses use a staggering excess (>50 equiv.) of competing acid modulators to enhance the crystallinity of and to increase the number of defects in the resulting MOFs [1]. These synthetic challenges are exemplified by frameworks composed of zirconium (Zr) and hafnium (Hf) cluster nodes, such as UiO-66 (UiO = Universitetet i Oslo) (Figure 1). Zr-and Hf-MOFs display exceptional tunability, hydrolytic stability, and robust structures that can accommodate large amounts of defects but often require dilute synthesis conditions and large amounts of modulators to yield crystalline products [1].

Recently, we reported that Zr-and Hf-MOFs can generally be self-assembled at much higher reaction concentrations (up to 1.0 M) than traditionally utilized [4]. By simply combining stoichiometric amounts of terephthalic acid (H_2bdc) linker and $ZrCl_4$ in DMF at concentrations up to 1.0 M, crystalline UiO-66 (labeled UiO-66-1.0M ($ZrCl_4$)) was obtained (Figure 2). Likewise, a pivalate-capped Zr_6 cluster (ZrPiv) could be combined with stoichiometric H_2bdc and hydrochloric acid (HCl) — to promote ligand exchange of pivalates for linkers — to yield crystalline MOF labeled UiO-66-1.0M (ZrPiv) (Figure 2). These high-concentration samples displayed similar crystallinity to a dilute prepared sample and had Brunauer-Emmett-Teller (BET) surface areas comparable to literature values [4]. A key difference, however, was that UiO-66-1.0M (ZrPiv) contained pivalate ligands as linker substitution defects. Proton nuclear magnetic resonance (1H NMR) analysis was used to determine a pivalate:linker ratio of 0.11:1, which is comparable to reported dilute syntheses of UiO-66 that use a slight excess of competing carboxylic acid modulators. Additionally, this ratio was higher than for a

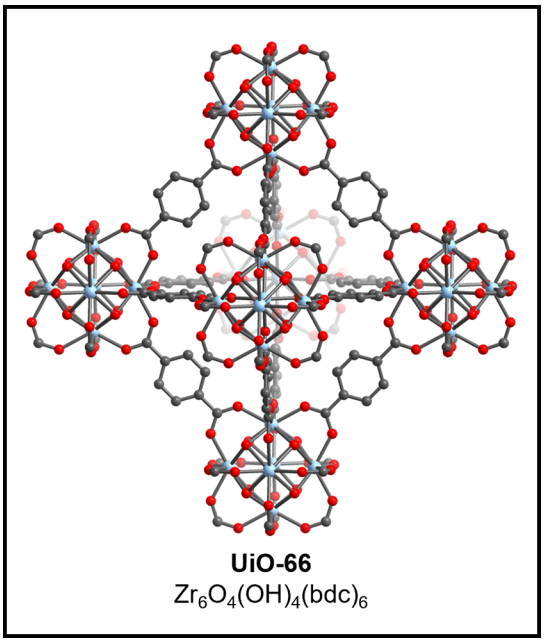

Figure 1: The structure of UiO-66. Gray, red, and light blue spheres represent carbon, oxygen, and zirconium, respectively. Hydrogens are omitted for clarity.

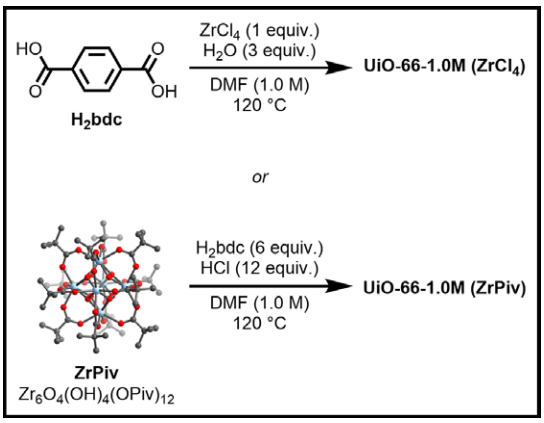

Figure 2: High-concentration synthesis of UiO-66 from either $ZrCl_4$ or ZrPiv. Adapted with permission from ref [4]. Copyright 2023 American Chemical Society.

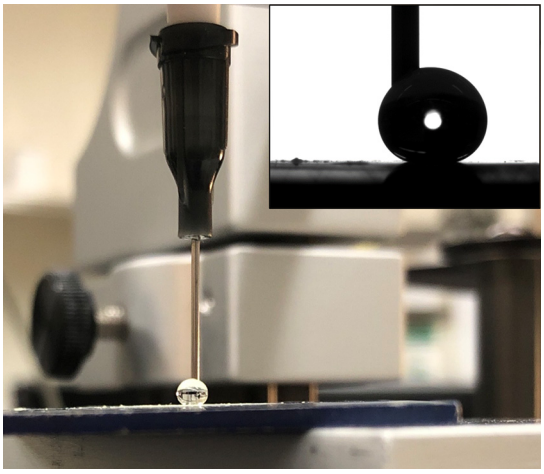

Figure 3: Photo of a water drop on UiO-66-1.0M (ZrPiv) powder. Inset: water contact angle of UiO-66-1.0M (ZrPiv). Adapted with permission from ref [4]. Copyright 2023 American Chemical Society.

sample prepared at high concentrations using $ZrCl_4$ and the same amount of pivalic acid present in ZrPiv [4]. Thus, using ZrPiv as a precursor is more effective at carboxylate defect incorporation than traditional acid modulation in high-concentration syntheses.

We hypothesized that UiO-66-1.0M (ZrPiv) should have enhanced hydrophobicity due to the inclusion of nonpolar pivalate defects. When water is added to the pivalate containing MOF, it beads up indicating that the material has a hydrophobic surface (Figure 3). Water contact angle measurements determined that UiO-66-1.0M (ZrPiv) had a large contact angle of 162° (Figure 3 inset), which indicates this as a super-hydrophobic surface [4].

Additionally, UiO-66-1.0M (ZrPiv) floats on water whereas UiO-66-1.0M ($ZrCl_4$) is rapidly wetted and sinks (Figure 4 inset). Water vapor adsorption isotherms were also measured to further probe if the interior pore surface of the pivalate containing MOF showed enhanced hydrophobicity (Figure 4). The relative pressure at which half of the total water capacity is reached (α) is larger for UiO-66-1.0M (ZrPiv) ($\alpha = 0.30$) indicating that its pore surface has weaker interactions with adsorbed water than UiO-66-1.0M ($ZrCl_4$) ($\alpha = 0.24$) [4]. Overall, these results demonstrate that preformed cluster precursors can effectively install property altering defects and thus enable defect engineering in user-friendly high-concentration MOF synthesis.

References:

[1] Bai, Y.; Dou, Y.; Xie, L.-H.; Rutledge, W.; Li, J.-R.; Zhou, H.-C. Zr-Based Metal-Organic Frameworks: Design, Synthesis, Structure, and Applications. Chem. Soc. Rev. 2016, 45 (8), 2327-2367. https://doi.org/10.1039/C5CS00837A.

[2] Feng, Y.; Chen, Q.; Jiang, M.; Yao, J. Tailoring the Properties of UiO-66 through Defect Engineering: A Review. Ind. Eng. Chem. Res. 2019, 58 (38), 17646-17659. https://doi.org/10.1021/acs.iecr.9b03188.

[3] Julien, P. A.; Mottillo, C.; Fri..i., T. Metal-Organic Frameworks Meet Scalable and Sustainable Synthesis. Green Chem. 2017, 19 (12), 2729-2747. https://doi.org/10.1039/C7GC01078H.

[4] Jerozal, R. T.; Pitt, T. A.; MacMillan, S. N.; Milner, P. J. High-Concentration Self-Assembly of Zirconium-and Hafnium-Based Metal-Organic Materials. J. Am. Chem. Soc. 2023, 145 (24), 13273-13283. https://doi.org/10.1021/jacs.3c02787.

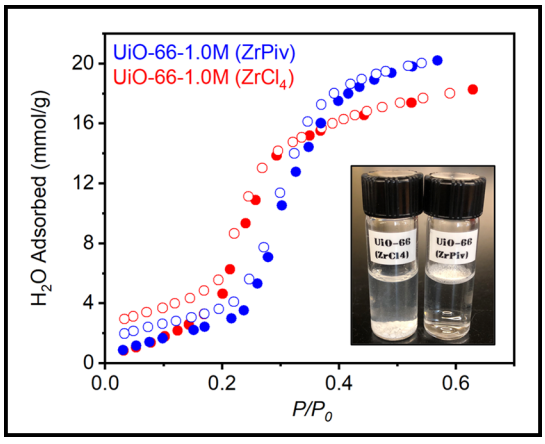

Figure 4: Water vapor adsorption isotherms of high-concentration UiO-66 samples. Inset: UiO.66-1.0M (ZrPiv) (right) floating on water vs. UiO-66-1.0M ($ZrCl_4$) (left) sinking in water. Adapted with permission from ref [4]. Copyright 2023 ACS.

A Systematic Study of How Different Phases of Niobium Nitride (Nb_xN) React to Xenon Difluoride (XeF_2) Undercut Etch

2023 CNF REU Intern: Daniel Joel Harrison
Intern Affiliation: Electrical and Computer Engineering, Morgan State University

2023 CNF REU Principal Investigator: Professor Debdeep Jena, Electrical and Computer Engineering, Cornell
2023 CNF REU Mentor: Wenwen Zhao, Applied and Engineering Physics, Cornell University
Program & Primary Source of Research Funding: 2023 Cornell NanoScale Facility Research Experiences for Undergraduates (CNF REU) Program via the National Science Foundation under Grant No. NNCI-2025233
Contact: dahar73@morgan.edu, djena@cornell.edu, wz344@cornell.edu
Website(s): https://cnf.cornell.edu/education/reu/2023
Primary CNF Tools Used: ABM Contact Aligner, Glen 1000 Resist Strip, SC4500 Electron Beam Evaporator, Xactix Xenon Difluoride Etcher, Bruker Energy-dispersive X-ray Spectrometer (EDS), Zygo 3D Optical Profilometer

Abstract:

The superconducting niobium nitride (NbN) was successfully integrated epitaxially with the III-nitride heterostructures (AlN, GaN, etc.) recently [1]. This new technology opens the possibilities for epitaxial metal/semiconductor Schottky diodes, epitaxial gate junctions for III-nitride transistors as well as all-epitaxial bulk acoustic wave resonators. The metallic epitaxial NbN also offers a way to be selectively etched chemically, which allows the lift-off of the epilayers or devices.

The NbN system is complex and presents various phases (i.e., beta, delta, epsilon, and gamma) [2]. Here in this work, by taking advantage of the high crystalline quality niobium nitride (Nb_xN) films grown by molecular-beam epitaxy (MBE), we propose to do a conclusive study to understand the xenon difluoride (XeF_2) undercut etch characteristics of different phases of Nb_xN. This study identifies the prerequisite conditions for the epilayer lift-off with a sacrificial layer of Nb_xN.

Summary of Research:

The Nb_xN films were epitaxially grown on 2-inch sapphire wafers. The Nb_xN phases used in this study are Delta phase grown at 600°C, Epsilon phase grown at 700°C, Gamma phase grown at 800°C, and Beta phase grown at 1000°C.

The Nb_xN samples were cut into 1 cm × 1 cm pieces. A total number of 12 samples were used for this research. Photolithography was done to develop a pattern of different sized circular pads ranging from 12.5 μm to 200 μm in diameter. To have a better visualization of the etch process, a transparent silicon dioxide (SiO_2) mask was deposited on the samples using an electron beam evaporator.

A XeF_2 etcher was used for the undercut etch process. Reference [3] indicates that the XeF_2 undercut etch rate

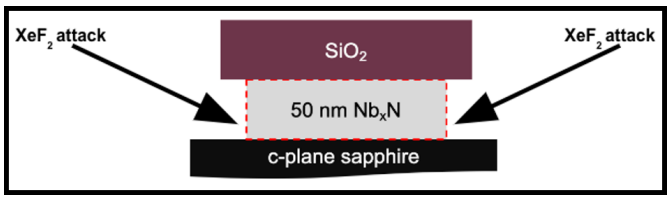

Figure 1: Cross-sectional representation of undercut process.

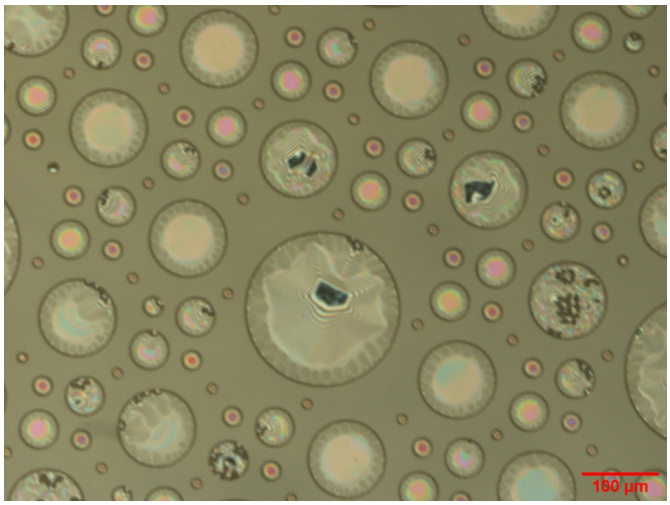

Figure 2: Delta phase niobium nitride after full undercutting at 4 Torr XeF_2 pressure.

increases with the increase of chamber temperature. The chamber temperature in this work was accordingly set at 100°C, which is the highest temperature the current etcher can achieve. Each sample for each phase was etched at a different XeF_2 pressure (4 Torr, 3 Torr and 2 Torr) for understanding the impact of the XeF_2 partial gas pressure on the undercut etch rate. It was observed that the vertical etching of Nb_xN by XeF_2 was done effortlessly, i.e., the Nb_xN not covered by SiO_2 would be etched away after the first etch cycle. The difficulty then was for the XeF_2 to go under the SiO_2 membranes

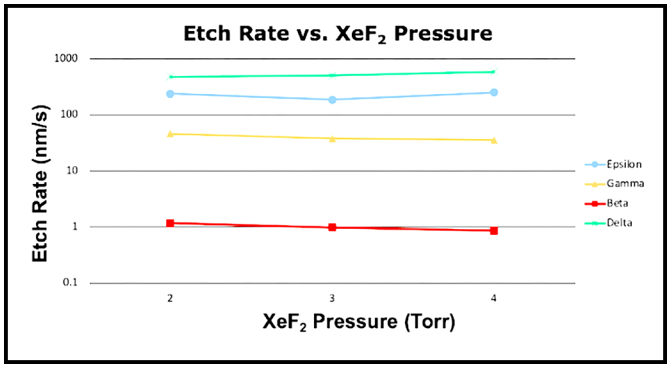

Figure 3: Average etch rates as a function of XeF_2 pressure for all four phases of Nb_xN.

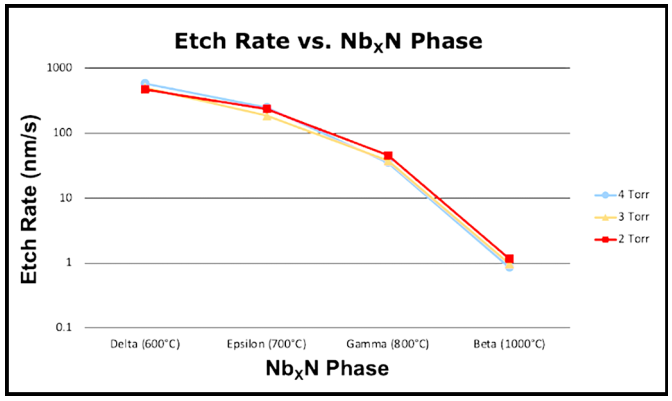

Figure 4: Average etch rates as a function of Nb_xN phase.

as seen in Figure 1 to attack the Nb_xN. This undercut etch will result in the release of the SiO_2 membranes. All the samples in this study experienced vertical etching of Nb_xN, but not all experienced a complete undercut of Nb_xN.

The samples of Delta phase were fully undercut after 70 seconds as seen in Figure 2. A change in the average etch rate was observed, which was proportional to the change of the XeF_2 pressure. Similarly, the samples of Epsilon phase were fully undercut after 3-4 minutes. There was no direct correlation of etch rates and XeF_2 pressure observed for Epsilon phase, but it was noticed that the average etch rates increased overtime.

The undercut etch of Gamma phase Nb_4N_3 at 4 Torr and 3 Torr XeF_2 pressure were not completely released after 12 minutes. Differently, a duality was seen at 2 Torr XeF_2 pressure, in which case some membranes became close to being fully undercut after 12 minutes. Unfortunately, most membranes became darker over time, implying that the reaction between XeF_2 and Gamma phase Nb_xN is unstable and unpredictable. The initial average etch rates for Gamma phase Nb_4N_3 decreased as the XeF_2 pressure increase, but overtime the etch rates went to zero, as none of the samples were fully undercut.

No full undercut for any of the samples for Beta phase Nb_2N was seen even after 14 minutes. Similar to Gamma phase, the initial average etch rates for Beta phase Nb_2N decreased as the XeF_2 pressure increased, but overtime the etch rates went to zero, as none of the samples were fully undercut.

Figure 3 shows how the average etch rate for each phase changes as the XeF_2 pressure increases. Figure 4 shows how the average etch rates changes as we move through the different Nb_xN phases. It was noticed that Nb_xN films grown at higher MBE temperatures are more difficult to be fully undercut by XeF_2.

Conclusions and Future Steps:

Results from the research show that Delta and Epsilon phase Nb_xN can be fully undercut by XeF_2; Gamma phase Nb_xN does exhibit some XeF_2 undercut capabilities, but the reaction is unstable and unpredictable; Beta phase Nb_xN cannot be fully undercut by XeF_2. In general, Nb_xN phases grown at higher MBE temperatures are more difficult to be fully undercut by XeF_2.

This research is a preliminary step to help us understand the required conditions for doing an epitaxial lift-off of high-quality aluminum nitride (AlN) membranes. The next step is a research project titled: "Monolithic integration of acoustic resonators and high electron mobility transistors (HEMTs) utilizing aluminum nitride platform." For this project, we will fabricate acoustic resonators from AlN using Delta or Epsilon phase Nb_xN as a sacrificial layer.

Acknowledgements:

This work was performed in part at the Cornell NanoScale Facility, an NNCI member supported by NSF Grant NNCI-2025233. Special thanks to Professor Debdeep Jena, Professor Huili (Grace) Xing, Wenwen Zhao, Melanie-Claire Mallison, Aaron Windsor, and Professor Michael Spencer. This work would not have been successful without their guidance.

References:

[1] Yan, R., Khalsa, G., Vishwanath, S. et al. GaN/NbN epitaxial semiconductor/superconductor heterostructures. Nature 555, 183-189 (2018). https://doi.org/10.1038/nature25768.

[2] Wright, J., Xing, H., Jena, D. Growth windows of epitaxial Nb_xN films on c-plane sapphire and their structural and superconducting properties. (2022) https://arxiv.org/pdf/2203.14083.pdf.

[3] Brian P. Downey, et al., XeF_2 etching of epitaxial Nb_2N for lift-off or micromachining of III-N materials and devices. Journal of VS&T A 1 September 2017; 35 (5): 05C312. https://doi.org/10.1116/1.4994400.

Design and Implementation of an AlScN-Based FeMEMS Multiplier for In-Memory Computing Applications

CNF Project Number: 1121-03
Principal Investigator(s): Amit Lal
User(s): Shubham Jadhav

Affiliation(s): School of Electrical and Computer Engineering, Cornell University

Primary Source(s) of Research Funding: Defense Advanced Research Projects Agency (DARPA), Tunable Ferroelectric Nitrides (TUFEN)

Contact: amit.lal@cornell.edu, saj96@cornell.edu

Website(s): http://www.sonicmems.ece.cornell.edu/

Primary Tools Used: SUS MA-6 contact aligner, CVC SC-4500 Odd-hour evaporator, Zeiss SEM, OEM Endeavor M1, Plasma-Therm Takachi HDP-CVD, Arradiance ALD, AJA sputter deposition, Oxford PECVD, Oxford 81/82, Primaxx Vapour HF Etcher, PT770 Etcher, YES EcoClean Asher, Xactix Xenon Difluoride Etcher, AJA ionmill, Heidelberg Mask Writer-DWL2000, P7 Profilometer, Zygo Optical Profilometer, Flexus Film Stress Measurement

Abstract:

This paper reports on the design, fabrication, and experimental validation of an aluminum scandium nitride (AlScN) based Ferroelectric Micro-Electro-Mechanical Systems (FeMEMS) Multiplier — a core component for multiply-accumulate (MAC) operations in next-generation in-memory computing applications. The FeMEMS multiplier leverages ferroelectric polarization switching in AlScN to change the piezoelectric coefficient (d_{31}), facilitating non-volatile, analog memory storage for weights in a neural network. The piezoelectric parameters of the films are then used to change a capacitive gap for readout. The ferroelectric thin films could be partially polarized and reached a peak remnant polarization of 216 μC/cm^2 at a voltage of 100V V_P (5MV/cm). Experimental results on optically measured displacements confirmed the AlScN unimorph multiplier's operation. The maximum resonance mode displacement was linearly dependent on the polarization and input voltages. This work provides foundational insights into the utilization of AlScN in in-memory computing, opening new avenues for high-speed, low-power, and high-accuracy computing applications.

Summary of Research:

To address the computational limitations of traditional von-Neumann architectures, researchers are exploring in-memory computing. A fundamental building block of this approach is the MAC unit, which is capable of performing matrix multiplication and summative operations [1]. The research highlights the potential of micro and nanoelectromechanical systems (M/NEMS) to provide zero standby leakage power and offer efficient computation [2,3].

The recently discovered ferroelectricity in scandium-alloyed aluminum nitride (AlScN) has enabled the implementation of MEMS MAC units in III-V systems [4,5]. This research presents the design, fabrication, and characterization of a ferroelectric aluminum scandium nitride (AlScN) based programmable nano-electromechanical system (NEMS) multiply and accumulate (MAC) unit.

A 500 μm Si substrate wafer was used to fabricate the ferroelectric unimorph. A 1 μm thermal SiO_2 layer serves as the elastic layer. Next, a continuous layer of sputtered 200 nm Pt was deposited as the bottom electrode. A ferroelectric AlScN film, with a thickness of 200 nm and 22% Sc content, was deposited on this Pt electrode. This film stack was achieved through reactive co-sputtering of scandium (Sc) and aluminum (Al) in a nitrogen environment. Next, a lift.off process was employed to evaporate 10nm/100nm Cr/Au metal top electrodes. Reactive ion-etching and ion-milling were then used to etch through the thin-film stack to fabricate etch-holes for releasing the unimorph. This step was followed by a vapor-phase bulk isotropic etching of the underlying silicon substrate using XeF_2 to release the unimorph. This process flow resulted in the successful creation of released cantilevers, clamped-clamped beams, and membranes, all on the same wafer (Figure 1).

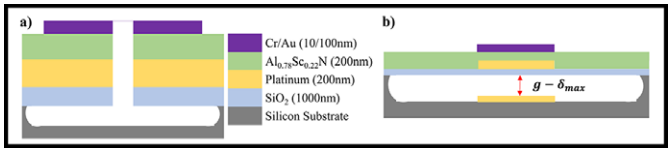

Figure 1: Schematic cross-section view of the FeNEMS.

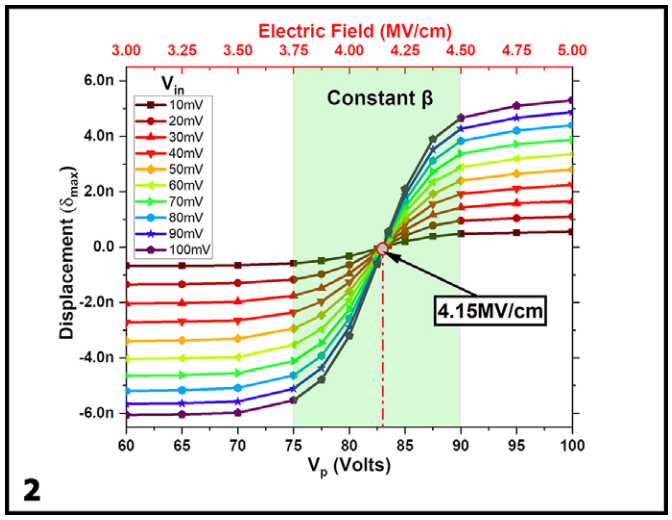

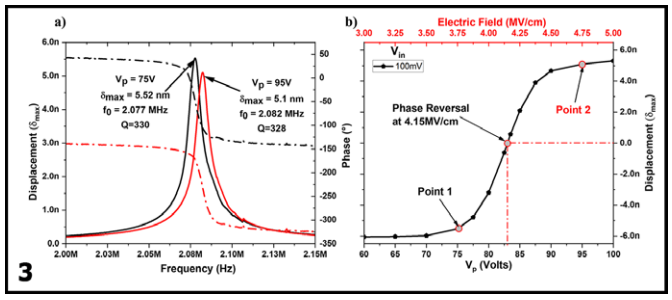

Figure 2, left: The transfer characteristics of the FeMEMS multiplier device. Figure 3, above: Magnitude and phase plot of state 1 (depicted in black) and state 2 (in red) versus frequency, illustrating the characteristic ferroelectric domain reversal phenomenon.

The device operation is based on the principle of partial polarization switching in AlScN. The polarization-switching voltage (V_p) is used to define the weights of the MAC operation. The piezoelectric coefficient (d_{31}) can be tuned by applying varying V_P voltages. The polarization switching was studied using a Radiant Technologies Precision Premier II Ferroelectric Tester. An increase in VP resulted in a gradual increase in the remnant polarization (P_r) until a maximum of $2P_r$ = 216 μC/cm^2 at V_P = 100V (5 MV/cm).

Once the weights are programmed by applying V_P voltages, the input voltage (V_{in}) is fed to the device to generate an output. The device behaves as a multiplier, where the maximum out-of-plane displacement (δ_{max}) of the unimorph actuator is a scaled product of the V_P and V_{in}. This displacement was measured using a Polytec MSA-400 Laser Doppler Vibrometer (LDV). The device functionality was verified by measuring δ_{max} as a function of V_P and V_{in}. The measurements showed a linear relationship between δ_{max} and the product of V_P and V_{in} for V_P and V_{in} in the range of 75V to 90V, confirming the multiplication operation (Figure 2).

For V_P values greater than the threshold, the polarity of δ_{max} changed, which indicates a reversal in the polarization of the AlScN. This causes a phase change in the unimorph response. This was verified by recording a phase reversal around the V_P = 83.5V, resulting in a zero displacement at this point with a complete phase inversion on either side (Figure 3).

Conclusions:

This research presents an innovative design of a Ferroelectric AlScN-based NEMS MAC unit, leveraging partial polarization switching in AlScN for in-memory computing. This approach enhances latency, power consumption, and operational efficiency in wideband gap III-V platforms, demonstrating the unit's ability to effectively store multi-level computational weights. The device's function as a multiplier was validated through a correlation between maximum displacement, polarization, and applied voltages. Notably, phase reversal was observed at V_P = 83.5V (4.15MV/cm), indicating the device's versatility. The FeMEMS multiplier's minimal standby leakage power and compatibility with III-V platforms enhance its overall efficiency. This study paves the way for future exploration of AlScN in high-speed, low-power, and high-accuracy computing applications, as well as advancements in zero standby power computing.

References:

[1] C. Mead, "Neuromorphic Electronic Systems," Proc. IEEE, vol. 78, no. 10, pp. 1629-1636, 1990.

[2] S. Jadhav, V. Gund, B. Davaji, D. Jena, H. (grace) Xing, and A. Lal, "HZO-based FerroNEMS MAC for in-memory computing," Appl. Phys. Lett., vol. 121, no. 19, p. 193503, Nov. 2022.

[3] S. Jadhav, V. Gund, and A. Lal, "Programmable Ferroelectric HZO NEMS Mechanical Multiplier for in-Memory Computing," 2023 IEEE 36th Int. Conf. Micro Electro Mech. Syst., pp. 519-521, Jan. 2023.

[4] S. Fichtner, N. Wolff, F. Lofink, L. Kienle, and B. Wagner, "AlScN: A III-V semiconductor based ferroelectric," J. Appl. Phys., vol. 125, no. 11, p. 114103, Mar. 2019, [Online]. Available: http://aip.scitation.org/doi/10.1063/1.5084945.

[5] D. Jena, et al., "The new nitrides: layered, ferroelectric, magnetic, metallic and superconducting nitrides to boost the GaN photonics and electronics eco-system," Jpn. J. Appl. Phys., vol. 58, no. SC, p. SC0801, May 2019.

Fabrication and Manipulation of Micro-Scale Opto-Electrically Transduced Electrodes (MOTEs) for Electrochemical and Neural Activity Measurements

CNF Project Number: 2658-18, 2836-19
Principal Investigator(s): Prof. Alyosha C. Molnar
User(s): Shahaboddin Ghajari, Sanaz Sadeghi, Devesh Khilwani

Affiliation(s): Electrical and Computer Engineering, Cornell University

Primary Source(s) of Research Funding: National Institute of Health

Contact: am699@cornell.edu, sg2367@cornell.edu, ss3842@cornell.edu, dk842@cornell.edu
Website(s): https://molnargroup.ece.cornell.edu/

Primary CNF Tools Used: ABM Contact Aligner, AJA Sputter, Westbond 7400A Ultrasonic Wire Bonder, Oxford 100, Oxford 81, Oxford 82, Unaxis Deep Si Etcher, Oxford PECVD, Oxford ALD, Anatech, P7 Profilometer, ZEISS Ultra and Supra SEMs

Abstract:

Microscale wireless sensors are beneficial in many applications such as electrochemical measurements and neural recordings. Recording neural activity in live animals *in vivo* is critical in elucidating how the brain functions. However, such recording poses several challenges. Electrical techniques typically require electrodes to be tethered to the outside world directly via a wire, or indirectly via an RF Coil [1], which is much larger than the electrodes themselves. Tethered implants suffer from the residual motions between electrodes and neurons as the brain moves, limiting our ability to measure peripheral nerves in moving animals. On the other hand, optical techniques, which are becoming increasingly potent [2], are often limited to subsets of neurons in any given organism, impeded by scattering of the excitation light and emitted fluorescence, and limited to low temporal resolution [3]. Here we present an untethered opto-electrical system on chip (SoC), Micro-scale Opto-electrically Transduced Electrodes (MOTEs), which are powered by, and communicating through a microscale optical interface, combining many benefits of optical techniques with high temporal-resolution of electrical recording. We also introduce an electrochemical platform similar to MOTE which is called Redox Enabled Micro-scale Opto-electrically Transduced Electrodes (ReMOTEs), which we used for pH measurements.

Summary of Research:

Our fabrication starts with a conventional 180 nm CMOS die, which contains the electronics for signal amplification, encoding, and transmission. The CMOS die is then integrated with AlGaAs diode, which acts as a photo-voltaic (PV) as well as light emitting diode (LED), hence the diode is abbreviated as PVLED. The PVLED provides an optical link which powers the electronics and transmits encoded signals in optical pulses. The MOTE utilizes Pulse Position Modulation (PPM) for signal encoding for its high information-per-photon efficiency, where the spacing between the output pulses is proportional to the measured electric field of neuronal or electrochemical signals across the measurement electrodes. Figure 1 depicts a conceptual deployment and system description of such MOTE [4,5]. It should be noted that preliminary electrochemical pH measurement results for ReMOTE are presented in [5]; however, the release process is not performed on it.

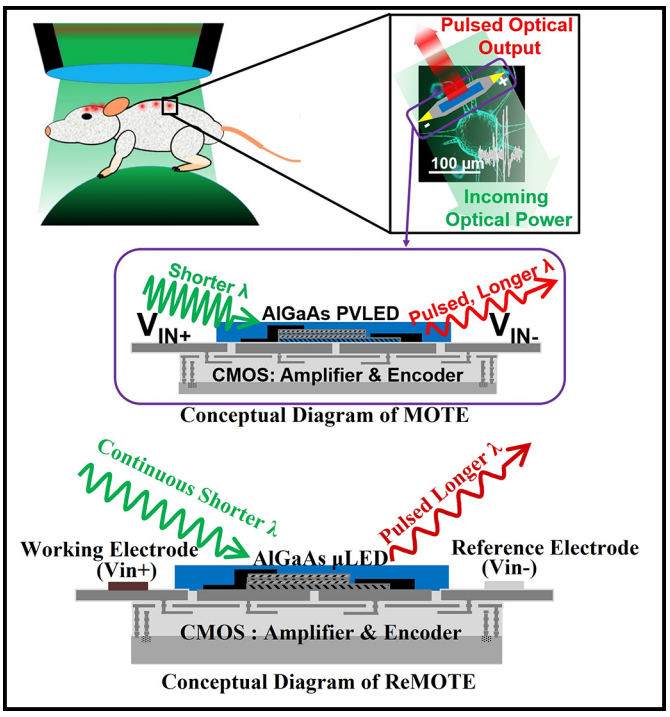

Figure 1: An exemplary implementation and system level description of the MOTEs and ReMTOEs [4,5].

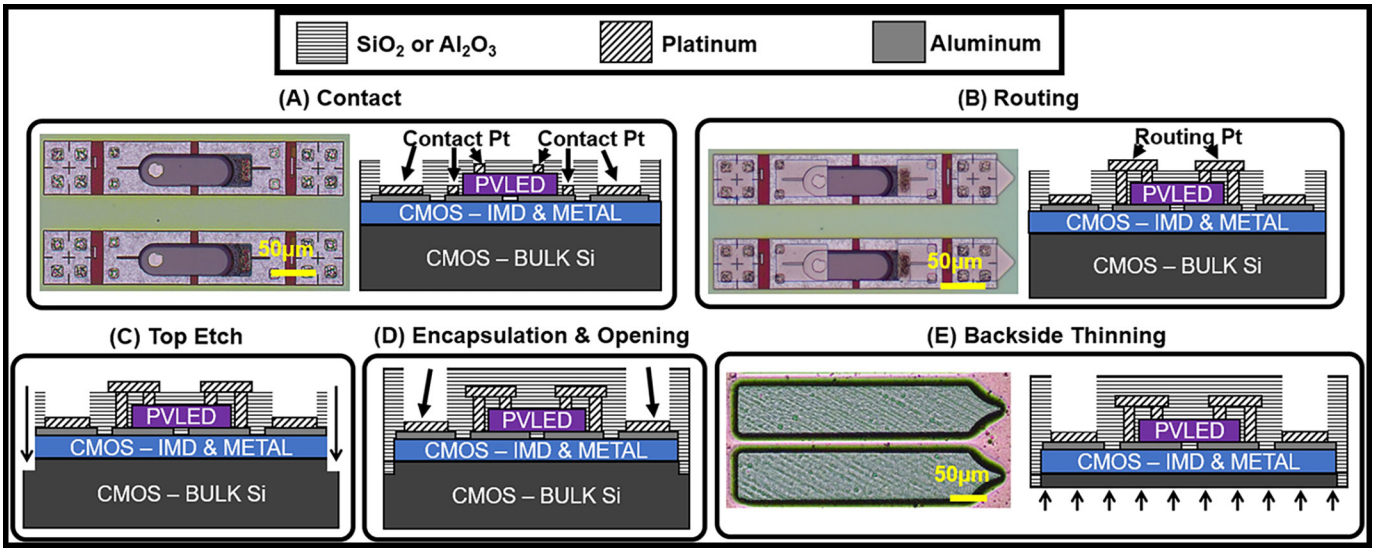

Figure 2: MOTE Fabrication Process. (A) An AlGaAs µLED (bullet-shaped) array is transferred on top of a CMOS chip containing an array of unit MOTE circuitry, and Pt is deposited over contact areas. (B) Routing Pt electrically connects each µLED with an underlying CMOS. (C) Each MOTE is segregated and (D) encapsulated with SiO_2 and Al_2O_3 except for the measurement electrodes area. (E) The backside Si is thinned so that total thickness is < 30 µm. Adapted from [6].

The AlGaAs diodes are first fabricated on a sapphire wafer, to be later released from the sapphire substrate with a sacrificial Poly (methyl methacrylate) (PMMA) polymer. Once the PMMA-coated AlGaAs diodes are transferred onto the CMOS die, Oxford 81 plasma etcher is used to remove the sacrificial PMMA, leaving only the diodes array intact on the CMOS die. To establish the electrical contact between the PVLED and CMOS, we have used CNF ABM Contact Aligner for photolithography with AZ nLof2020 UV photoresist for efficient lift-off process that ensues after metal deposition. After the contact fabrication, the contacts of CMOS and PVLED are connected via similar photo-lithography process, and to maximize the conformality of the metal routing, we employ AJA Sputter. Following the routing step, each MOTE is encapsulated using OXFORD ALD and PECVD for SiO_2 and Si_3N_4 deposition, followed by dielectric etching using OXFORD 100 and UNAXIS Deep Reactive Ion Etch (DRIE) for release. Figure 2 describes the fabrication sequence described herein.

It should be noted that before embarking on the nano/micro-fabrication flow, to confirm the functionality of each module (CMOS and the diode), we use the Westbond 7400A Ultrasonic Wire Bonder for board-level test. ZEISS Ultra and Supra Scanning Electron Microscopes (SEMs) are also used to inspect the fabricated MOTE for debugging purposes.

Conclusions and Future Steps:

MOTEs are the smallest electrophysiological sensor of its kind, and we are currently testing the MOTEs *in vivo* in mouse animal models. As we accumulate more data on our ongoing *in vivo* efforts, we plan to improve fabrication processes as well as surgical procedures for inserting the MOTEs into the mouse cortex. We also presented preliminary results for electrochemical measurements, and we plan to combine the sensors with micro-robots.

References:

[1] Harrison RR, Watkins PT, Kier RJ, Lovejoy RO, Black DJ, Greger B, and Solzbacher F. A Low-Power Integrated Circuit for a Wireless 100-Electrode Neural Recording System. IEEE J. Solid-State Circuits. 2006 Dec 26;42(1): 123-133.

[2] A. C. Molnar, S. Lee, A. Cortese, P. McEuen, S. Sadeghi and S. Ghajari, "Nanoliter-Scale Autonomous Electronics: Advances, Challenges, and Opportunities," 2021 IEEE Custom Integrated Circuits Conference (CICC), Austin, TX, USA, 2021, pp. 1-6, doi: 10.1109/CICC51472.2021.9431529.

[3] Yang W and Yuste R. *In vivo* Imaging of Neural Activity. Nature Methods. 2017 Mar 31;14(4):349-359.

[4] Lee S, Cortese AJ, Trexel P, Agger ER, McEuen PL, and Molnar AC. A 330 μm × 90 μm Opto-Electronically Integrated Wireless System-on-chip for Recording of Neural Activities. IEEE ISSCC. 2018 Feb.

[5] S. Ghajari, S. Lee, S. Norris, P. McEuen, A. Molnar, "Redox-Enabled Microscale Opto-Electronically Transduced Electrodes (ReMOTEs)", 2023 IEEE International Symposium on Circuits and Systems (ISCAS), Monterey, CA, USA, 2023.

[6] Lee S, Cortese AJ, Mok A, Wu C, Wang T, Park JU, Smart C, Ghajari S, Khilwani D, Sadeghi S, Ji Y, Goldberg JH, Xu C, McEuen PL, and Molnar AC. Fabrication of Injectable Micro-Scale Optoelectronically Transduced Electrodes (MOTEs) for Physiological Monitoring. IEEE JMEMS. 2020 June 12;29(5):720-726.

Cross-Plane Thermal Conductivity of *h*-BN Thin Films Grown by Pulsed Laser Deposition

CNF Project Number: 2758-19
Principal Investigator(s): Zhiting Tian
User(s): Gustavo A. Alvarez, Jinha Kwon

Affiliation(s): Sibley School of Mechanical and Aerospace Engineering, Cornell University
Primary Source(s): Department of the Navy, Office of Naval Research
Contact: zt223@cornell.edu, gaa78@cornell.edu
Website(s): https://ztgroup.org/
Primary CNF Tools Used: SC4500 Odd-Hour Evaporator, P7 Profilometer, AFM-Veeco Icon

Abstract:

The distinguished properties of *h*-BN, specifically its atomically smooth surface, large critical electric field, and large electronic band gap, make it ideal for thin film microelectronics and as an ultrawide bandgap (UWBG) semiconductor. Owing to weak van der Waals interactions between layers, *h*-BN exhibits a significant degree of anisotropic thermal conductivity (κ). Exfoliation from bulk crystals is not a sustainable method for mass production of *h*-BN due to its low repeatability, low yield, poor control of sample thickness, and limitation to small areas. Thus, it is necessary to investigate the thickness-dependence of $\kappa_{\perp}$ for thin films grown by a practical growth method, such as pulsed laser deposition (PLD), which enables the production of reliable and large-area *h*-BN films with control of film thickness. We grew *h*-BN using PLD at 750°C and observed a non-monotonic trend of $\kappa_{\perp}$ as thickness increased from 30 nm to 300 nm, varying from ~ 1.47 to ~ 0.19 W/(mK). We observed a high $\kappa_{\perp}$ value for *h*-BN at a thickness of 30 nm, providing insights into the $\kappa_{\perp}$ of PLD-grown films suitable for electronics applications.

Summary of Research:

The continued scaling down of device dimensions [1] and operation in high-voltage or high-frequency regimes aggravates thermal loads, and effective heat dissipation has become one of the most critical challenges in device performance and reliability [2]. Hexagonal boron nitride (*h*-BN) is a two-dimensional (2D) material with excellent properties for the thermal management of next-generation electronics. Existing literature regarding the thermal conductivity (κ) of *h*-BN films typically focuses on the in-plane thermal conductivity ($\kappa_{\parallel}$) and samples produced by the exfoliation from bulk *h*-BN. The $\kappa_{\parallel}$ of few-layer *h*-BN nanosheets falls in the range of 100 -360 W/(mK) at room temperature [3].

Owing to weak van der Waals interactions between layers, *h*-BN has a highly anisotropic κ. The only measured data of the cross-plane thermal conductivity ($\kappa_{\perp}$) of *h*-BN is 0.2 to 8.1 W/(mK) between 7 nm to 585 nm, respectively, for *h*-BN flakes exfoliated at room temperature [4]. Exfoliation from bulk crystals is not a sustainable method for mass production, thus there is a need to investigate the thickness-dependent $\kappa_{\perp}$ for a scalable growth method, which provides reliable and large-area *h*-BN with control of film thickness.

We utilized pulsed laser deposition (PLD), which offers several benefits compared to other growth methodologies. PLD involves the deposition of thin films from a single polycrystalline target directed upon the substrate, therefore ensuring the preservation of stoichiometry throughout the deposition process. We measured $\kappa_{\perp}$ of *h*-BN thin films ranging from 30 nm to 300 nm implementing the optical pump-probe method, frequency-domain thermoreflectance (FDTR), depicted in Figure 1a. The samples were modeled as a three-layer system, with each layer defined by the layer thickness, volumetric heat capacity c_p, the thermal boundary conductances G1 and G2, the $\kappa_{\perp}$ and in-plane thermal conductivity ($\kappa_{\parallel}$). To maximize the coefficient of thermoreflectance of the 532 nm probe, Au was chosen as the transducer layer and the SC4500 Odd-Hour Evaporator at CNF was utilized to deposit a 100 nm layer of Au (thickness determined by the P7 profilometer).

Two curves are plotted in Figure 2a, assuming lower and higher bounds of $\kappa_{\parallel}$. Despite the slight increase of $\kappa_{\perp}$ for the isotropic case and for film thicknesses ≤ 50 nm, the $\kappa_{\perp}$ of the *h*-BN thin films decrease from 1.47 to 0.19 W/(mK) with an increase in film thickness from 30 nm to 300 nm. Previous experiments observed long phonon mean free path > 100 nm for $\kappa_{\perp}$ of exfoliated *h*-BN flakes; predictions by first-principles calculations indicated ~ 80% of the heat is transported by phonons of MFPs ranging from 3 nm to 90 nm [4].

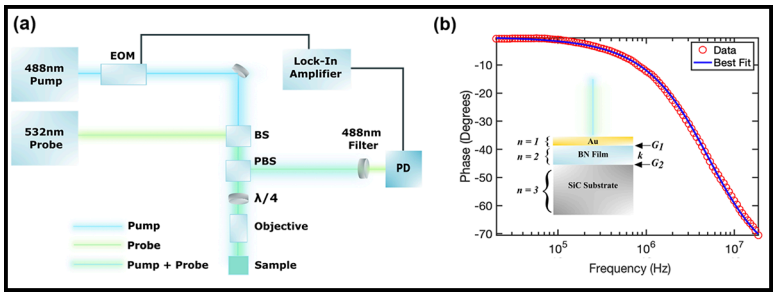

Figure 1: FDTR experimental setup and fitted data. (a) Simplified schematic of the FDTR system. (b) Phase vs. frequency data obtained from FDTR measurements for the 50 nm epitaxial h-*BN layer on bulk SiC substrate.*

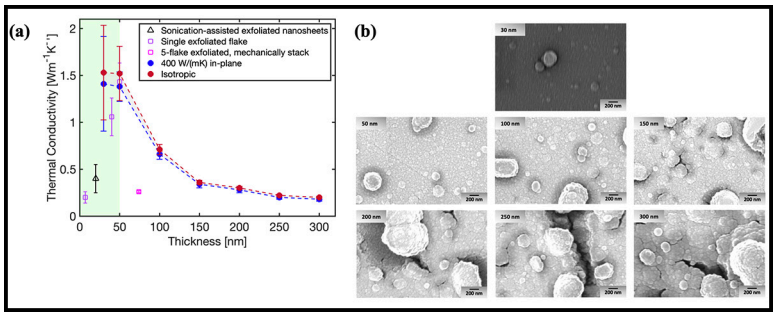

Figure 2: Thickness-dependent thermal conductivity and SEM of h-*BN films. (a) As the thickness of the thin film increases there is a decrease in sample quality, thus, reducing* $\kappa_{\perp}$ *(b) Crack propagation is evident as the thickness increases leading to an increase in phonon defect scattering.*

If the film quality of PLD-grown h-BN was consistent across the thickness range, we should expect the $\kappa_{\perp}$ increases, at least up to 100 nm, with thickness due to the size effect. However, our findings indicate the opposite trend, implying that as the thickness of the film increases, there is a significant decrease in the film quality.

To investigate the quality of the thin films, a commercial AFM system was utilized. An increase in root-mean-square (RMS) from 3.30 nm to 17.40 nm for the *h*-BN films with a thickness from 30 nm to 300 nm was determined. The increase in RMS presents increasing surface roughness, which introduces stronger phonon scattering, thereby reducing $\kappa_{\perp}$.

Lastly, the Zeiss Gemini 500 Scanning Electron Microscope (SEM) was utilized to capture high-resolution images of the sample surfaces, as shown in Figure 2b. As thickness increases, voids/cracks start to form and are evident in the thicker *h*-BN films, which leads to strong phonon-defect scattering, thereby reducing $\kappa_{\perp}$.

In conclusion, among two-dimensional materials (2D), hexagonal boron nitride (*h*-BN) stands out as a highly promising candidate for use in both micro and nanoscale devices, given its exceptional mechanical, electrical, and thermal properties. The PLD-grown *h*-BN at 30 nm showed a larger $\kappa_{\perp}$ value than that of the single exfoliated flake at 7 nm and 40 nm [4], and a larger value that of the sonicated-assisted exfoliated nanosheets at 20 nm [5]. These thinner samples provide the high $\kappa_{\perp}$, suitable for integrated circuits and high-power electrics, which are in need of heat dissipation while maintaining a compact and lightweight design.

References:

[1] Ferain, I., Colinge, C., and Colinge, J. Nature, 310-316 (2011).
[2] Balandin, A. IEEE Spectr 46, 34-39 (2009).
[3] Jiang, P., Qian, X., and Yang, R. RSI 88, 074901 (2017).
[4] Jaffe, G. R., et al. Condensed Matter (2021).
[5] Wang, Y., et al. Nanoscale 10, 167-173 (2017).

First Demonstration of AlBN/GaN High Electron Mobility Transistors

CNF Project Number: 2800-19
Principal Investigator(s): Huili Grace Xing, Debdeep Jena
User(s): Kazuki Nomoto

Affiliation(s): School of Electrical & Computer Engineering, Cornell University

Primary Source(s) of Research Funding: ARO

Contact: grace.xing@cornell.edu, kn383@cornell.edu

Primary CNF Tools Used: Autostep i-line Stepper (GCA AS200), Heidelberg Mask Writer DWL2000, P7 Profilometer, FilMetrics, AFM Veeco Icon, Zeiss SEM, PT770, Oxford81, Oxford PECVD, Oxford ALD, SC4500 Evaporators, AJA Sputter Deposition tools, RTA AG610, JEOL 9500

Abstract:

Epitaxial aluminum boron nitride (AlBN) is a potential barrier material for gallium nitride (GaN) high electron mobility transistors (HEMTs) due to large energy bandgap high-κ dielectric properties [1,2]. This work reports the first demonstration of AlBN/GaN HEMTs.

Summary of Research:

A 2 nm GaN passivation layer / 2 nm AlBN high-κ barrier / 600 nm GaN channel / 125 nm AlN buffer structure was grown on a 6H silicon carbide substrate using plasma-assisted molecular beam epitaxy (PA-MBE) (Figure 1(a)). Hall-effect measurements at room temperature revealed a two-dimensional gas (2DEG) sheet concentration of 9.25×10^{12} /cm^2, electron mobility of 524 cm^2/V·s, and sheet resistance of 1290 Ω/sq.

First, BCl_3 inductively coupled plasma (ICP) etching was performed for device isolation, followed by ohmic metallization. A Ta/Al/Ni/Au (20/150/50/50 nm) metal stack was deposited using an electron-beam evaporator (SC4500) and alloyed in N_2 ambient using a rapid thermal annealing system (RTA AG610). The resulting contact resistance was ~ 2 Ω·mm. A gate metal stack of Ni/Au (30/220 nm) was deposited directly on the sample surface using SC4500. Gate lengths were defined via photolithography (L_g = 1.3 μm) using an Autostep i-line stepper (GCA AS200).

Figure 1(b) shows the scanning electron microscope (SEM) image of the completed AlBN/GaN HEMT.

Figure 2 shows the 500 kHz *C-V* results of AlBN/GaN and AlN/GaN Schottky barrier diodes. The extracted dielectric constants of AlBN from on-wafer capacitance measurements at various frequencies exibit higher values than AlN.

Figure 3(a) shows the measured output characteristics of the AlBN/GaN HEMTs of 1.3 μm gate length, and 2.3 μm source-drain distance. The saturated on-current reaches 266 mA/mm, and repeatable current saturation, pinch-off, and similar performance is measured for several devices of similar size. Figure 3(b) shows the transfer characteristics of the Schottky-gated AlBN/GaN HEMTs, which exhibit an on/off ratio of > 10^3. Since this is limited by the gate leakage of the Schottky diode. Figure 3(b) also shows the threshold voltage of -0.5 V and the subthreshold slope of 150 mV/dec. Figure 3(c) shows a peak $gm_{,ext}$ of 139 mS/mm, all at room temperature. The promising first AlBN/GaN HEMT performance will be boosted by higher mobility in the future.

References:

[1] Chandrashekhar Savant, et al., 65th EMC, O10 (2023).
[2] J. Hayden, et al., Physical Review Materials, 5, 044412 (2021).

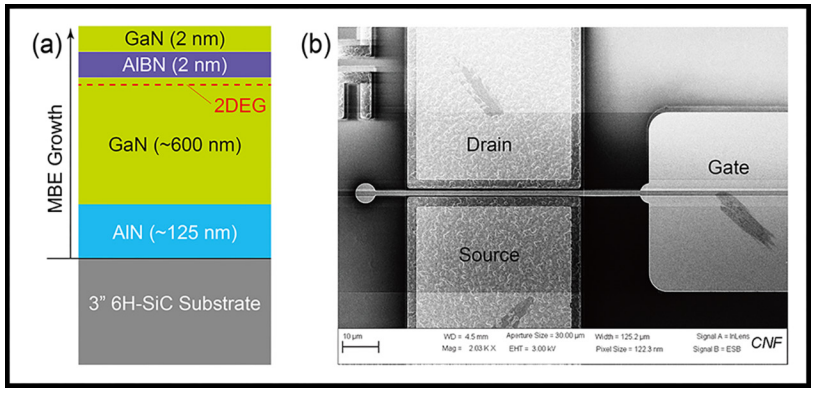

Figure 1: (a) Layer structure of the epitaxial film grown by MBE, dashed line indicating where a high-density 2D electron gas (2DEG) is present. (b) 70° angled-view SEM image of the fabricated AlBN/GaN HEMT with L_g *= 1.3 µm,* W_g *= 50 µm, and* L_{sd} *= 2.3 µm.*

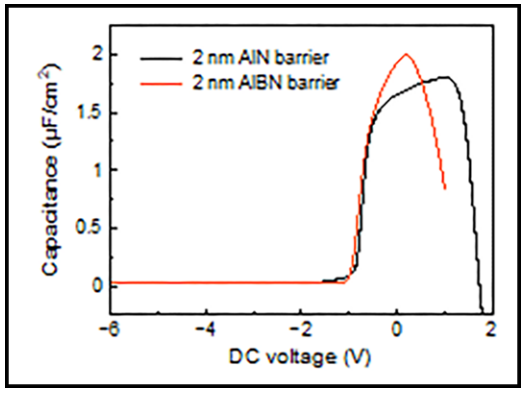

Figure 2: C-V *data at 500 kHz of AlBN and AlN showing higher dielectric constant of AlBN.*

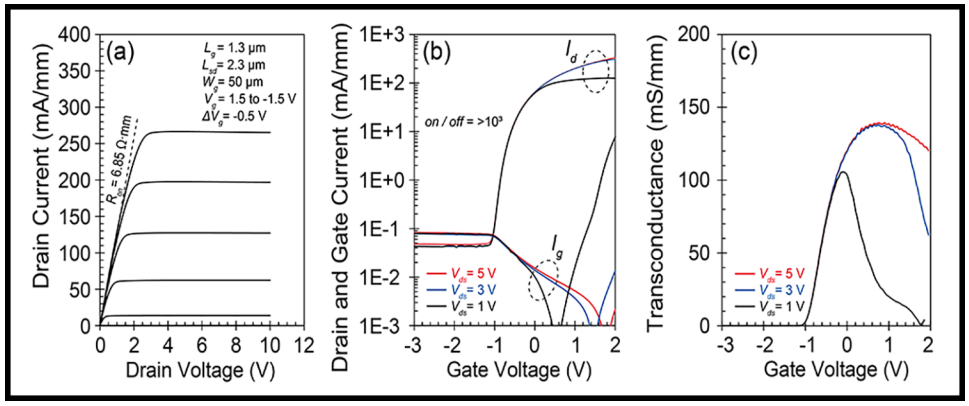

Figure 3: (a) Output I-V *curves show current saturation and an on-resistance of 6.85 Ω·mm at* V_g *= -1.5 V. (b) Log-scale transfer curves show more than three orders of* I_{on} */* I_{off} *modulation, limited by Schottky gate leakage. (c) The linear-scale transfer curve shows normally-on operation and a peak* $gm_{,ext}$ *of 139 mS/mm at* V_d *= 5 V.*

Low Contact Resistance Non-Alloyed Contacts to (010) β-Ga_2O_3 for kV Radio Frequency Applications

CNF Project Number: 2802-19
Principal Investigator(s): Huili Grace Xing[1], Debdeep Jena[1]
User(s): Kathleen Smith[2]

Affiliation(s): 1. School of Electrical and Computer Engineering,
2. Department of Applied and Engineering Physics; Cornell University

Primary Source(s) of Research Funding: Air Force Office of Scientific Research (AFOSR)

Contact: grace.xing@cornell.edu, djena@cornell.edu, kts57@cornell.edu

Primary CNF Tools Used: ABM Contact Aligner, SC4500 Odd-Hour E-Beam Evaporator, Angstrom E-Beam Evaporator, RTA-AG610a, Glen 1000 Resist Strip, SAMCO UV-1 UV/Ozone, PT770, AJA Sputter Deposition

Abstract:

We demonstrate non-alloyed Ti/Au contacts to n+ (010) β-Ga_2O_3 doped by both *in-situ* doping during metal oxide chemical vapor deposition (MOCVD) and sub-oxide molecular beam epitaxy (MBE) with dopant concentrations well above 1×10^{19} cm^{-3}. The resulting contacts have sufficiently low (much less than 1 Ω-mm) contact resistance (R_c) even without alloying of the contacts.

Summary of Research:

Gallium(III) oxide (β-Ga_2O_3) has attracted interest in recent decades as a promising material candidate for kV radio frequency (RF) applications, especially in extreme environments, due to its large bandgap and critical electric field, decent carrier mobility, and availability of native substrates via melt-growth techniques. In order to enable high speed device applications, the parasitic resistance originating from the contacts should be much less than 1 Ω-mm. However, the low electron affinity associate with the wide bandgap leads to a lack of sufficiently low work-function metals to form ohmic metal-semiconductor junctions. Instead, ohmic contacts to Ga_2O_3 rely on tunnel junctions between a metal and heavily doped semiconductor region. However, the reliable formation of such junctions is non-trivial.

Previously, alloyed Ti/Au ohmic contacts were successfully formed to unintentionally doped (UID) epitaxy on semi-insulation Fe-doped (010) ion implanted with Si to a 100 nm box concentration of 5×10^{19} cm^{-3} by electron-beam evaporation and liftoff, resulting in an R_c of 0.16 Ω-mm. However, contacts formed by an identical process to MOCVD-grown Ga_2O_3 *in-situ* doped with Si to a concentration of 1.3×10^{20} cm^{-3} displayed highly rectifying behavior prior to alloying. While the contacts appeared ohmic post-alloying, the resultant contacts were spatially non-uniform, preventing extraction of R_c. We currently ascribe the abnormal behavior of these contacts to formation of a spatially non-uniform interfacial layer on the Ga_2O_3 surface.

In this work, a 102.5 nm UID buffer layer followed by 222.5 nm of Si-doped layer was grown on semi-insulating Fe-doped (010) β-Ga_2O_3 substrate via MOCVD. Room-temperature Hall measurements with In-dot contacts showed a free carrier concentration of 5.3×10^{19} cm^{-3} and a sheet resistance (R_{sh}) of 52 Ω/□. Transfer length method (TLM) patterns were fabricated using RIE for mesa isolation followed by non-alloyed Ti/Au (50/110 nm) contacts deposited by e-beam evaporation and patterned via liftoff. The as-deposited contacts were highly rectifying and spatially non-uniform.

The existing contacts were removed and Ti/Au ohmic contacts were re-deposited to form the device structure shown in Figure 1. Specific process details are anticipated for publication in the future. The resulting contacts demonstrate highly-leaky Schottky behavior, as seen in Figure 2a. At an applied current bias of 25 mA, the TLM patterns have an R_c of 0.49 Ω-mm without alloying as seen in Figure 2b.

Following this result, a 1 μm Si-doped layer was grown on semi-insulating Fe-doped (010) β-Ga_2O_3 substrate via suboxide MBE. Room-temperature Hall measurements with In-dot contacts showed a sheet resistance (R_{sh}) of 34 Ω/□. The carrier concentration was measured by secondary ion mass spectroscopy to be 2.99×10^{19} cm^{-3}. Non-alloyed Ti/Au (10/110 nm) were deposited by e-beam evaporation and patterned to form circular TLM (CTLM) patterns using a similar process to the non-alloyed MOCVD contacts. The device structure is shown in Figure 3. The resulting contacts are again highly-leaky Schottky in character, as shown in Figure 4a. At an applied current bias of 25 mA, the CTLM patterns have an R_c of 1.0 Ω-mm as show in Figure 4b, likely due to the lower doping level which naturally results in a thicker tunneling barrier and higher metal-semiconductor contact resistance.

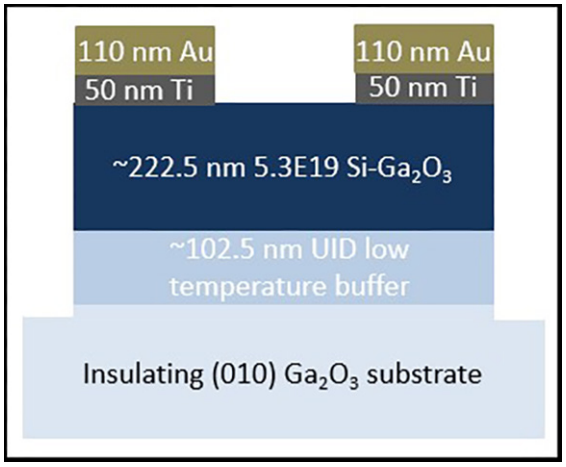

Figure 1: Device structure of the MOCVD-grown sample.

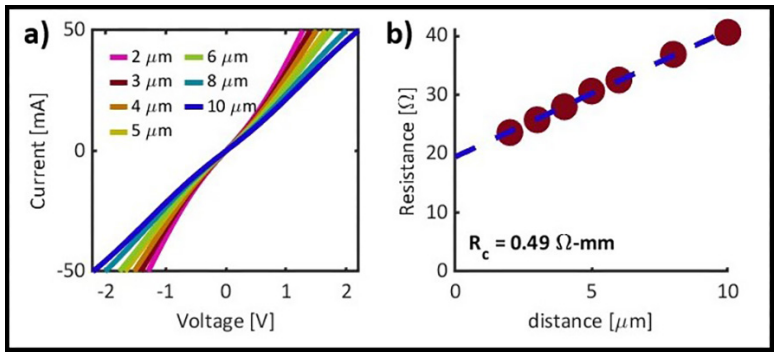

Figure 2: a) IV measurements of non-alloyed contacts display super-leaky Schottky behavior. b) TLM extraction of contact resistance at 25 mA applied current bias gives an R_c of 0.49 Ω-mm.

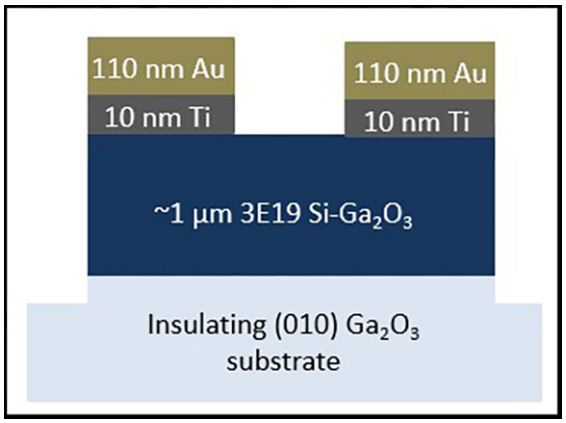

Figure 3: Device structure of the suboxide MBE-grown sample

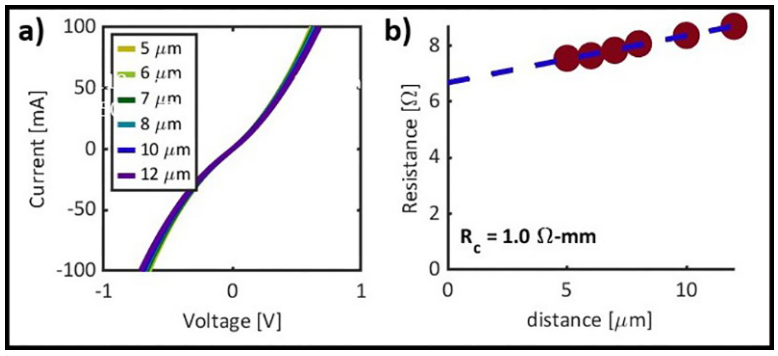

Figure 4: a) IV measurements of non-alloyed contacts display super-leaky Schottky behavior. b) TLM extraction of contact resistance at 25 mA applied current bias gives an R_c of 1.0 Ω-mm.

Conclusions and Future Steps:

In this work, we successfully demonstrate non-alloyed contacts on both MOCVD and suboxide MBE grown (010) n+ β-Ga_2O_3. Future work includes extensive characterization of the Ti/Ga_2O_3 interface to identify any interfacial layers that may have contributed to the non-uniformity observed in previous work and the initial MOCVD process. Further contact studies will extend to patterned regrowth of n+ β-Ga_2O_3 on n- doped epitaxy to investigate the resistance of the n+/n- semiconductor interface.

We acknowledge support from the AFOSR Center of Excellence Program FA9550-18-1-0529. This work was performed in part at the Cornell NanoScale Science & Technology Facility (CNF), a member of the National Nanotechnology Coordinated Infrastructure NNCI), which is supported by the National Science Foundation (Grant NNCI-2025233).

High Frequency Sensors and Actuators for Ultrasonic Imaging and Sensing

CNF Project Number: 2876-20
Principal Investigator(s): Robert Scharf, Amit Lal
User(s): Anuj Baskota, Justin Kuo, Scott Zimmerman

Affiliation(s): Geegah Inc.

Primary Source(s) of Research Funding: DARPA, ARPA-E, DOE

Contact: rms248@cornell.edu, amit@geegah.com, anuj@geegah.com, justin@geegah.com, scottez@geegah.com

Website(s): www.geegah.com

Primary CNF Tools Used: Olympus BX-51 Fluorescence Microscope, Zygo Optical Profilometer, VersaLaser Engraver, Harrick Plasma Generator

Abstract:

Geegah, Inc., specializes in developing ultrasonic imagers that are compatible with complementary metal-oxide-semiconductor (CMOS) technology and operate at gigahertz (GHz) frequencies. These imagers are designed with an array of transducers made with thin film of aluminum nitride (AlN), each measuring 50 × 50 μm. The acquisition of high-resolution images consisting of 128 × 128 pixels can be performed at a sampling rate up to 20 fps. Geegah's technology finds applications in diverse fields. It can be used in agriculture for soil imaging [1] and nematode detection [2]. It also enables the monitoring of fluid flow and mixing [3] of colorless liquids in opaque substrate microfluidic channels. Other applications currently being explored include lens imaging [4], microbes and biofilm analysis, water quality sensing, tissue imaging [5], and skin analysis. While the imaging chips are manufactured in a commercial CMOS foundry, early packaging of these systems was done in CNF. Furthermore, other packaging and analysis tasks performed in CNF include fabrication and bonding of Polydimethylsiloxane (PDMS) microfluidic channels on Geegah chips, fluorescence imaging to validate biofilm growths, and height profile analysis of thin films on imaging surface.

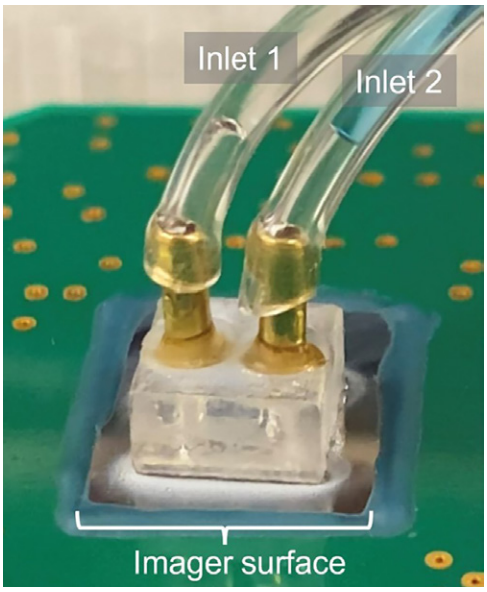

Figure 1: Ultrasonic imager with a microfluidic chip attached to the sensing surface.

Summary of Research:

Microfluidic channels on-chip enable real-time visualization of fluid flow and mixing based on the acoustic impedance differences between the liquids. This enables monitoring photo-sensitive liquids in dark, transparent fluids without the aid of color dyes, and visualization of fluids inside opaque microfluidic channels. The device that consists of a semi-transparent microfluidic channel bonded on the imager chip is shown in Figure 1. Various shapes of channels were patterned on PDMS molds using the VersaLaser Engraver and plasma bonded to the silicon surface using Harrick Plasma Generator. This device is then used to visualize mixing of two transparent liquids, alcohol and water, as shown in Figure 2. Note the benefit of acoustical approach when it comes to imaging of optically transparent liquids as the captured contrast stems from the acoustical impedance differences, not from the differences in optical properties.

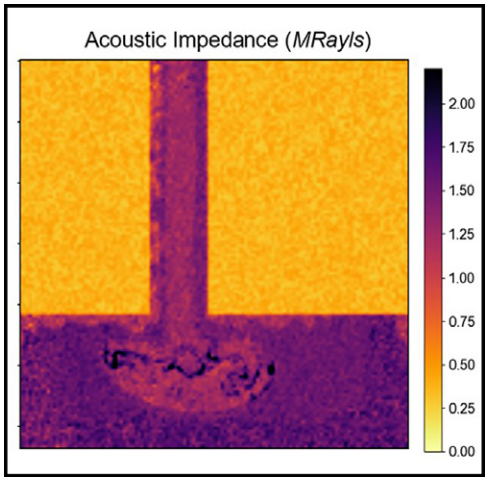

Figure 2: Acoustic impedance map showing jet of ethanol (99%) mixing with water in microfluidic channel captured at 1.853 GHz.

Conclusions and Future Steps:

Overall, various applications have been demonstrated using the GHz ultrasound imaging technology, including but not limited to microfluidics monitoring, biofilm tracking, soil sensing, and tissue imaging. The visualization of structures/layers, in addition to the measurement of acoustic impedance, enables the exploration of various biological and chemical processes using this novel chip. In the future, various patterned PDMS structures as well as other substrates will be attached and tested on the Geegah imager. Furthermore, chemical reactions forming precipitates along with exothermic and endothermic reactions will be monitored using GHz ultrasound imaging.

References:

[1] Baskota, A., Kuo, J., Ardanuç, S., and Lal, A. 2022, October. Nematode Species Differentiation Using GHz Ultrasonic Micro-Imager. In 2022 IEEE International Ultrasonics Symposium (IUS) (pp. 1-4). IEEE.

[2] Baskota, A., Kuo, J., and Lal, A., 2022, January. Gigahertz Ultrasonic Multi-Imaging of Soil Temperature, Morphology, Moisture, and Nematodes. In 2022 IEEE 35th International Conference on Micro Electro Mechanical Systems Conference (MEMS) (pp. 519-522).

[3] Baskota, A., Kuo, J., Ardanuç, S., and Lal, A. (2023, June). Visualization Of Fluid Mixing Using GHz Ultrasonic Imaging. In 2023 22nd International Conference on Solid-State Sensors, Actuators and Microsystems (Transducers).

[4] Hwang, J., Baskota, A., Davaji, B., Kuo, J., and Lal, A. (2022, October). Gigahertz Metamaterial Ultrasonic Lens Characterization Using GHz CMOS Integrated Ultrasonic Micro Imager. In 2022 IEEE International Ultrasonics Symposium (IUS) (pp. 1-4).

[5] Baskota, A., Kuo, J., Ardanuç, S., and Lal, A. (2023). Compact GHz Ultrasonic Micro-Imager for Cells and Tissues. Microscopy and Microanalysis, 29(Supplement_1), 1116-1117. https://doi.org/10.1093/micmic/ozad067.572.

Developing a Passivation-First Recessed T-Gate Procedure for AlN/GaN/AlN HEMTs

CNF Project Number: 2975-21
Principal Investigator(s): Austin Hickman
User(s): Austin Hickman, Shankar Miller-Murthy

Affiliation(s): Soctera Inc.

Primary Source(s) of Research Funding: National Science Foundation (NSF)

Contact: austin.hickman@soctera.edu, shankar.murthy@soctera.com

Primary CNF Tools Used: I-line stepper, PT770 Etcher, Oxford 81 Etcher, Odd hour E-beam evaporator, JEOL 6300 EBL, Oxford PECVD, AJA Sputter Deposition, Woolam Ellipsometer, Zeizz Ultra SEM, Leica Critical Point Dryer, Glen1000 resist stripper, P7 profilometer

Abstract:

In this work, we report functional recessed T-gate structures fabricated using a procedure compatible with the AlN/GaN/AlN structure. The devices were fabricated on an AlGaN/GaN chip using a combination of gentle fluorine-based plasma etching and a buffered oxide etch (BOE) wet process to selectively remove passivation without implanting fluorine-based trap states. The devices demonstrated on-currents over 1.15 A/mm with an on-resistance of 1.8 Ω·mm. Transfer characteristics revealed I_{on}/I_{off} ratio of 10^4 and peak transconductance of 0.3 S/mm.

Summary of Research:

Next-generation (6G) wireless communication and high-resolution radar systems target high-power operation in the terahertz regime. Gallium nitride high-electron-mobility transistors (GaN HEMTs) are well-suited for this high-power, high-frequency application. However, the conventional AlGaN/GaN heterostructure provides poor quantum confinement of the two-dimensional electron gas (2DEG), generating short channel effects at high frequencies. Additionally, its RF power performance is limited by the breakdown voltage. The AlN/GaN/AlN heterostructure offers material and device design advantages over the conventional AlGaN/GaN HEMT: the AlN buffer tightly confines the 2DEG and offers a higher thermal conductivity path than a thick GaN buffer, and the AlN barrier induces higher density 2DEGs at thinner distances (5 nm). AlN also maximizes the barrier bandgap, improving breakdown voltage.

Recently, fully realized T-gated AlN/GaN/AlN HEMTs were fabricated and characterized. The T-gates were defined via two-stage electron beam lithography using a single followed by a double-layer resist stack. The first single-layer resist was used to define the gate stem combined with a chrome mask layer to ensure vertical side-walls, which was etched out of the SiN passivation using a combination of SF_4 plasma etching and a single minute of buffered oxide etch exposure to remove the last remaining SiN and expose the AlGaN without implanting any ions. The resulting structure is shown in Figure 1. The second, double-resist electron beam lithography exposure was used to define the head area, where Ni/Au (50/200 nm) gate metal was deposited via e-beam evaporation. The resulting structure is shown in Figure 2.

The devices demonstrated on-currents over 1.15 A/mm with an on-resistance of 1.8 Ω·mm. Transfer characteristics revealed I_{on}/I_{off} ratio of 10^4 and peak transconductance of 0.3 S/mm. All DC characteristics are shown in Figures 3 and 4.

These positive results, even at this early stage of the project, illustrate the effectiveness of this technique. With some refinement, it may allow the AlN platform to enable the next generation of high-power, mm-wave communication.

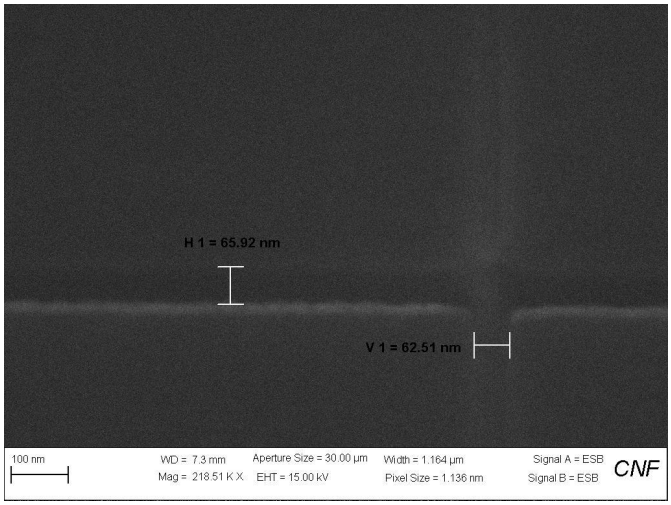

Figure 1: T-gate stem trench demonstrating a gate length of 65 nm.

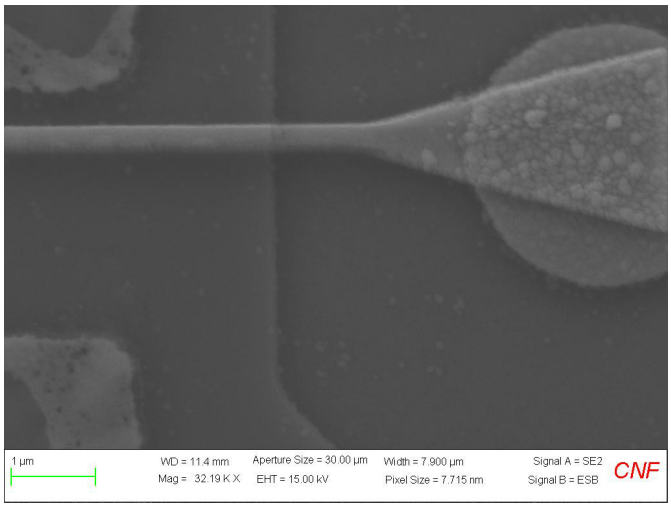

Figure 2: T-gate head with buried trench demonstrating a gate head width of ~250 nm.

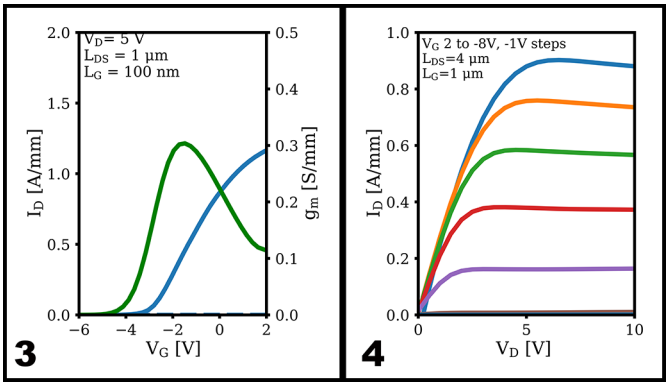

Figures 3 and 4: DC characteristics for AlGaN/GaN recessed T-Gate HEMT.

Redistribution Layers on Glass Wafers

CNF Project Number: 3018-22
Principal Investigator(s): Dr. Shelby F. Nelson, Dr. Lee Tutt
User(s): Dr. Lee Tutt

Affiliation(s): Mosaic Microsytems, LLC

Primary Source(s) of Research Funding: Commercial revenue from early prototypes

Contact: shelby.nelson@mosaicmicro.com, lee.tutt@mosaicmicro.com

Primary CNF Tools Used: Photolithography suite (both spinning and laminating photosensitive materials, and align & develop), CHA Mark50 for evaporation of metals, thermocompression bonder

Abstract:

Mosaic Microsystems is a small company with cleanroom facilities in Rochester NY, specializing in thin glass interposers for the microelectronic packaging industry. Mosaic has used CNF primarily for early exploration of interconnect metallizations. As a small company bringing up many processes simultaneously in-house, Mosaic was grateful for the already-functional facilities offered by the CNF to be able to explore tools and processes for early prototypes. For a variety of customer projects, some one-off and others early versions of processes that may become main-stream for Mosaic, the access to good equipment that is well maintained accelerated our delivery and helped build our business.

Summary of Research:

Mosaic has a proprietary process for bonding thin glass to a handle wafer, allowing the thin glass to be processed in mainstream semiconductor equipment. Mosaic used CNF to metallize and pattern such bonded glass wafers with platinum, copper, aluminum, tantalum, titanium, and gold. In some cases, Mosaic used the thermocompression bonder to create multilayer glass stacks. Even such relatively "standard" processes must be adapted for new materials, and Mosaic has been very grateful to have the Cornell NanoScale Facility relatively near-by to allow explorations when we have not yet been able to bring similar equipment up in our own cleanrooms.

Conclusions:

In the world of semiconductor packaging, small companies face a significant challenge in acquiring sufficient capital equipment to build the business at a rate that allows the business to grow. Having access to the CNF equipment and expertise has been highly valuable.

D-Band Filters and Splitters Based on SiC Substrate-Integrated Waveguides

CNF Project Number: 3078-23
Principal Investigator(s): James C.M. Hwang
User(s): Xiaopeng Wang

Affiliation(s): School of Electrical and Computer Engineering, Department of Materials Science and Engineering; Cornell University

Primary Source(s) of Research Funding:

Contact: jch263@cornell.edu, xw569@cornell.edu

Primary CNF Tools Used: ABM Contact Aligner, SÜSS MA6-MB6 Contact Aligner, AJA Sputter Deposition - 1 & 3, AJA Ion Mill, Electroplating - Au & Ni

Abstract:

The objective of this project is to demonstrate the feasibility for monolithic integration of antennas, filters, and high-electron mobility transistors (HEMTs) on SiC. To demonstrate that individual components survive the monolithic integration, the D-band filters based on SiC substrate-integrated waveguides (SIW) are designed, fabricated, and measured. The resulted D-band (110.170 GHz) SIWs exhibit a record low insertion loss of 0.22 ± 0.04 dB/mm, which is four times better than that of the GCPWs. A 3-pole filter exhibits a 1.0-dB insertion loss and a 25-dB return loss at 135 GHz, which represents the state of the art of SiC SIW filters and is order-of-magnitude better than Si on-chip filters. The compact filters are designed, fabricated, and measured but exhibit high insertion loss due to the high resistance of the through-substrate vias (TSVs). Solid TSVs can minimize the resistance of the TSVs and thus decrease the insertion loss. The new process is under development and optimization. The D-band splitters are designed and will be fabricated and measured.

Summary of Research:

SiC SIWs are attractive because high-power and high-efficiency GaN amplifiers are usually fabricated on SiC. SiC is high in dielectric constant, electrical resistivity, breakdown strength, mechanical toughness, and thermal conductivity, but low in loss tangent and thermal expansion coefficient. Previously, for proof of principle, we used the custom process at Cornell University to design and fabricate a 3-pole filter comprising three SIW resonators, which exhibited a 1-dB insertion loss and a 25-dB return loss at 135 GHz [1]. These record performances (Table I and Table II) make SIW promising for monolithic integration of high-quality SIW filters, edge-firing SIW antennas, and GaN HEMTs as shown in Figure 1.

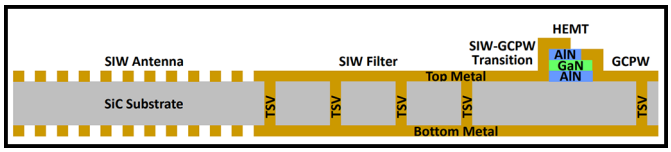

Figure 1: Schematics of an MMIC with an edge-firing SIW antenna, an SIW filter, and a GaN HEMT on the same SiC chip.

The first custom process is using Ni/Al as the top and bottom metal because of the limitation of the CNF tools. On the other hand, sidewalls of the TSVs are covered by sputtering Al. To further reduce the conductor loss, Au was used to replace the Al as the bottom metal. The Au is deposited planetary evaporation to cover the sidewalls of the TSVs. Since the depth of the TSV is 100 μm while the TSV diameter is 50 μm, the Au cannot cover the TSVs due to such high aspect ratio as depicted in Figure 2. The solid TSVs by electroplating Au could solve this issue but needs better control of the ICP-RIE etching of the SiC substrate. The etching recipe has been successfully transferred to Notre Dame.

In addition to the changes in metal, 4" SiC wafers are replacing the small chips (1 cm by 1 cm). The hard mask is critical for the ICP-RIE etching. Ni is the typical choice with the high selectivity and simple process. The SiC substrate is 100 μm in thickness which requires at least 3.3-μm thick Ni hard mask. In the first custom process, pure Ni was sputtered on small chips as the seed layer for Ni electroplating. When handling the 4" SiC wafers, the pure Ni seed layer cannot sustain such high stress strength from the 3.3-μm Ni. The combination of Ti and Ni can bear high stress strength from the thick Ni. The potential problem along with Ti is that Ti is hard to get removed thoroughly and if it's the case, the following ICP-RIE etching will fail and the whole wafer will be useless.

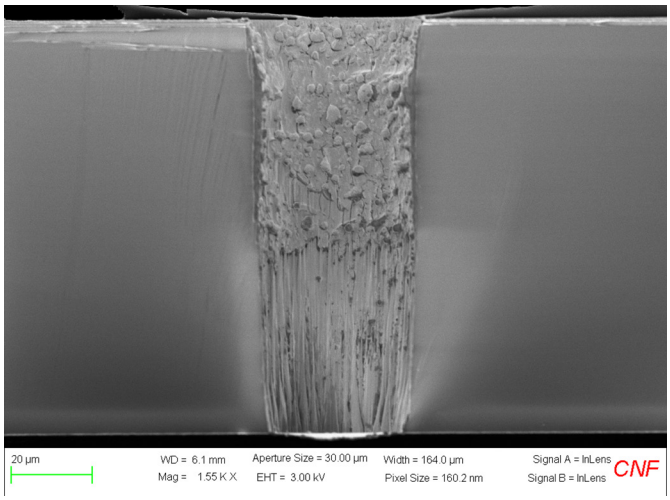

Figure 2: SEM image of the cross-section of the TSV after Au planetary evaporation.

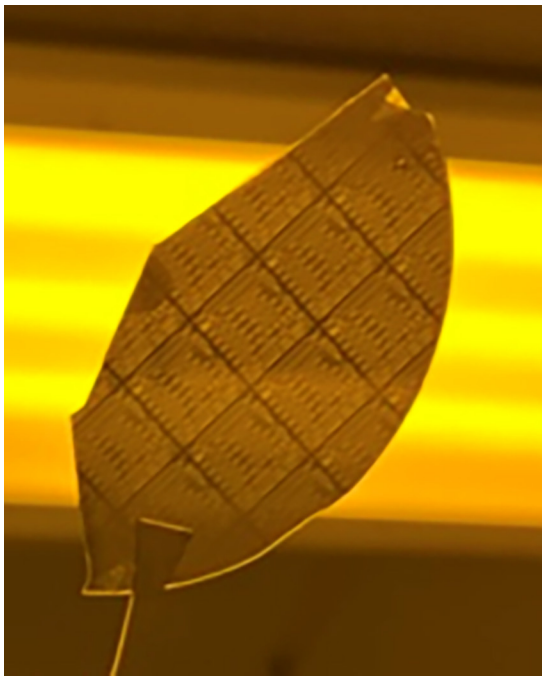

Figure 3: SiC test chip after ICP-RIE etching.

The test has been performed with the sequential processes of Ti/Ni seed layer sputtering, Ni hard mask electroplating, Ion mill, and then ICP-RIE etching. The results have proved that Ti will not affect the SiC etching as shown in Figure 3.

Conclusion and Future Steps:

The compact filters are designed, fabricated, and measured exhibiting high insertion loss due to the high resistance of TSVs. The new process on 4" SiC wafers are under development using Au for top and bottom metal layer, solid TSVs by electroplating Au. Meanwhile, the D-band splitters are designed. The new masks including filters and splitters are prepared. Each individual process has been validated except the Au electroplating on the 4" SiC wafers.

The new run of fabrication has started and will move on if the tools in CNF work well. The Au electroplating will be verified. The measurement will be performed in HFTL (Bard 315) using the 220 GHz single-sweep probe station system at Cornell University and banded probe station system in University of Notre Dame, respectively, for cross check and validation.

References:

[1] M. J. Asadi, L. Li, K. Nomoto, Y. Tang, W. Zhao, P. Fay, D. Jena, H. G. Xing, and J. C. M. Hwang, "SiC Substrate-Integrated Waveguides for High-Power Monolithic Integrated Circuits Above 110 GHz," 2021 IEEE MTT-S Int. Microw. Symp. (IMS), Atlanta, GA, USA, 2021, pp. 669-672.

Electrical Interconnects Based on Delafossite Thin Films

2023 CNF REU Intern: Paul Bloom
Intern Affiliation: Optical Engineering, University of Rochester

CNF REU Principal Investigator: Dr. Hari Nair, Materials Science and Engineering, Cornell University

CNF REU Mentor: Bilal Azhar, Chemical and Biomolecular Engineering, Cornell University

Program & Primary Source of Research Funding: 2023 Cornell NanoScale Facility Research Experiences for Undergraduates (CNF REU) Program via the National Science Foundation under Grant No. NNCI-2025233

Contact: pbloom2@u.rochester.edu, hn277@cornell.edu, ba428@cornell.edu

Website(s): https://cnf.cornell.edu/education/reu/2023

Primary CNF Tools Used: Veeco Savannah ALD, Woollam RC2 Spectroscopic Ellipsometer, Rapid Thermal Anneal - AG Associates Model 610, Everbeing SR-4 4-Point Probe Station

Abstract:

The dramatic increase in the resistivity of three-dimensional (3D) metal interconnects with decreasing dimensions presents a significant bottleneck for further downscaling of integrated circuits [1]. This rise in resistivity is due to increased interface electron scattering as the interconnect dimensions approach their electron mean free path. Metallic delafossite oxides, specifically $PtCoO_2$ and $PdCoO_2$, present an alternative solution due to their Quasi-2D nature which mitigates interface electron scattering due to a 2D Fermi surface (Figure 1). Synthesis of high quality single-crystal delafossite thin films has been previously demonstrated by molecular beam epitaxy (MBE) [2], however, the challenge remains to demonstrate similarly high quality growth with a back-end-of-the-line (BEOL) synthesis technique such as atomic layer deposition (ALD).

We want to realize high quality single-crystal ALD synthesis of $PtCoO_2$ for which we need to develop a ternary ALD process made up of the PtO and Co_xO_y binary cycles, with overlapping processing conditions. In this study, we will present on the development of the Co_xO_y binary cycles under favorable conditions for ternary $PtCoO_2$ growth. We optimized Co_xO_y growth with respect to temperature, Co-pulse length, O_3 exposure time, purging conditions, adhesion layer, and the number of cycles. We characterized the growth with ellipsometry, X-ray diffraction, and X-ray reflectivity.

Summary of Research:

To grow high-quality, single-crystal $PtCoO_2$ films, we had to determine the optimal ALD conditions for the $PtCoO_2$ process, which combined Co_xO_y and PtO binary cycles. The Co_xO_y binary cycle was calibrated at a substrate temperature suitable for deposition of PtO to support our ternary deposition process. Temperature windows with the Cobalt precursor Bis(N,N''-di-i-propylacetamidinato)cobalt(II) [$Co(iPr\text{-}MeAMD)_2$] and O_3 as a co-reactant are documented above 200°C [3] while the Pt deposition process is characterized above 175°C at the Cornell NanoScale Science and Technology Facility (CNF) using the same deposition tool where we calibrated our Co_xO_y cycle.

We found growths per cycle (GPC) of Co_xO_y films at 150 and 175°C that were greater than growth values documented in literature at higher temperatures using similar processes (Figure 2). Increased GPC was observed by splitting up long precursor pulses into shorter, successive pulse/purge sub-cycles that resulted in the same cumulative precursor exposure (Figure 3). Linear GPC at substrate temperature of 150°C growth was observed without saturating O_3 vapor pressure, which indicated ALD growth, but yielded growth rates an order of magnitude lower than with a saturated O_3 pulse (Figure 4).

Deposition of Co_xO_y was calibrated on an Al_2O_3 adhesion layer as well as native SiO_2 layer and no difference in film growth was observed. The N_2 flow rate of the chamber was determined not to affect the film growth because the ratio of precursor to carrier gas remained constant and residence time of the precursor did not increase. With an unsaturated O_3 co-reactant vapor pressure, we found Co saturation at 0.5 seconds, but with very low GPC.

$PtCoO_2$ films were grown via ALD at an increased O_3 vapor pressure, but preliminary anneals in oxygen — measured using X-ray diffraction (XRD) — did not yield crystalline $PtCoO_2$ films.

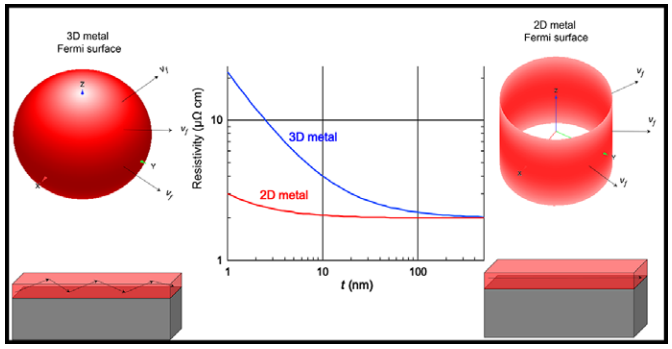

Figure 1: The quasi-2-dimensional crystal structure of the metallic delafossite oxides yield a nearly cylindrical Fermi surface with limited electron mobility out-of-plane. 3D metals (such as Cu) have a nearly spherical Fermi surface. We expect to see that the thickness of these interconnects will have a less dramatic impact on the resistivity of our quasi-2D material films.

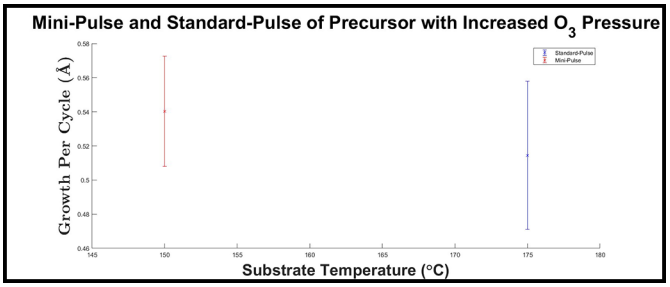

Figure 2: GPC plotted against substrate temperature at an increased O_3 pressure showing a growth rate greater than literature values documented at higher substrate temperatures.

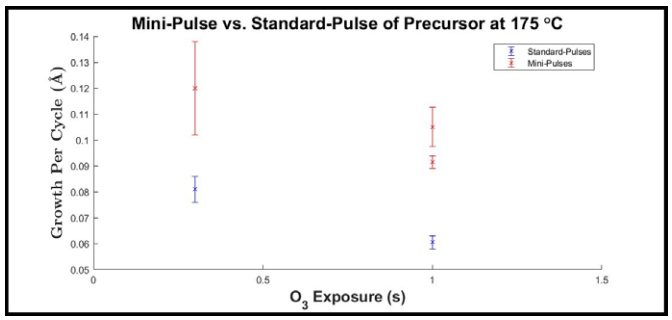

Figure 3: Increased GPC is shown using mini-precursor-pulses and multiple O_3 exposures.

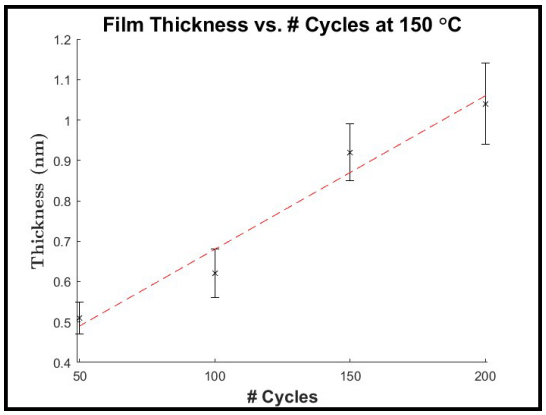

Figure 4: Average Co_xO_y film thickness vs. number of cycles at 150°C substrate temperature. Co_xO_y film thickness was measured at 65 points across a wafer using ellipsometry with a fixed refractive index. Co_xO_y thickness accounts for any adhesion layer (Al_2O_3) and native SiO_2.

Conclusions and Future Steps:

So far, we have shown Co_xO_y ALD growth at suitable temperature for ternary $PtCoO_2$ supercycle and determined that mini-precursor-pulses greatly increase GPC of binary ALD processes. We have also calibrated this cycle at 150°C, which we believe would overlap with the PtO binary cycle.

We must now calibrate the PtO binary cycle to determine the ratio between binary cycles in our supercycle that will yield optimal $PtCoO_2$ films. After we deposit amorphous $PtCoO_2$, we must anneal the films to achieve our desired crystallinity. We must calibrate the annealing conditions of these films to produce single-crystal $PtCoO_2$ films without PtO or Co_xO_y contamination. We will also measure the electrical properties of these films at varying thickness to assess the resistivity scaling curves of these materials at decreasing dimensions.

Acknowledgements:

Special thanks to the Cornell NanoScale Science & Technology Facility Research Experiences for Undergraduates (CNF REU) Program for hosting this internship and to the CNF staff for their support. Many thanks to the Nair Research Group for their mentorship. This work was funded in part by the National Science Foundation via grant no. NNCI-2025233.

References:

[1] D. Gall, J. Appl. Phys. 127, 050901 (2020).
[2] J. Sun, M.R. Barone, C.S. Chang, M.E. Holtz, H. Paik, J. Schubert, D.A. Muller, and D.G. Schlom, APL Mater. 7, 121112 (2019).
[3] Wan, Z., Zhang, T. F., Zeng, Z., Xi, B., Atomic Layer Deposition of CoxOy Films: Oxidants versus Composition. Adv. Mater. Interfaces 2022, 9, 2200097. https://doi.org/10.1002/admi.202200097.

Etching of Topological Metals for Interconnect

2023 CNF REU Intern: Astrid Dzotcha Kengne
Intern Affiliation: Electrical Engineering, Morgan State University

CNF REU Principal Investigator: Prof. Jeeyoung Judy Cha, Materials Science and Engineering, Cornell University

CNF REU Mentors: Gangtae Jin, Han Wang, Quynh P. Sam; Materials Science and Engineering, Cornell University

Program & Primary Source of Research Funding: 2023 Cornell NanoScale Science Facility Research Experiences for Undergraduates (CNF REU) Program via the National Science Foundation under Grant No. NNCI-2025233

Contact: asdzo1@morgan.edu, jc476@cornell.edu, gj98@cornell.edu, hw578@cornell.edu, qps2@cornell.edu

Website(s): https://cnf.cornell.edu/education/reu/2023

Primary CNF Tools Used: Scanning electron microscope (SEM), Nabity Nanometer Pattern Generator System, Reactive Ion Etcher PT720, Atomic Force Microscope (AFM), RC2 ellipsometer

Abstract:

On-chip interconnects are electrical wiring systems that connects transistors and other components in an integrated circuit. Copper (Cu) has been our main interconnect for over two decades. Over the years, the dimensions of Cu interconnects have decreased for better computing performance, and finally Cu has reached its limitations where under 15 nm of the interconnect width, signal delays and larger energy consumptions are significant due to the high resistivity of Cu interconnects stemming from surface and grain boundary scattering of electrons.

In contrast, topological metals, especially molybdenum phosphide (MoP), have shown promise as our next interconnect metals owing to their topological surface states that are resistant to scattering. We convert molybdenum sulfide (MoS_2) flakes to MoP by chemical vapor deposition and use electron beam and etching to create narrow nanoribbons. Four-point probe measurements show the resistivity to be 13 microohm-cm, demonstrating the viability of MoP as future interconnects.

Summary of Research:

Within the first two weeks of the program, we had several conferences, an in-person safety training course, a general online chemical safety training and lastly a cleanroom safety training while simultaneously reading relevant publications.

First, we got trained in the atomic force microscope (AFM). Then we got trained on the scanning electron microscope (SEM) with Nabity alongside. Later we were trained on how to use the RC2 ellipsometer. Then we were trained in the reactive ion etcher (RIE), specifically the PT720 Model.

And lastly, we were trained on the electron beam evaporator that uses a method of deposition to deposit various metals on wafers.

To start, our group already had silicon (Si) wafers coated with silicon dioxide (SiO_2) which only required us to clean the wafer to use. After cleaning the wafer using acetone and N-Methylpyrrolidone (NMP) for three minutes each, we exfoliated $MoSi_2$ on the SiO_2/Si wafer by pressing $MoSi_2$ crystals on the coated wafer using a double-sided tape.

We would then put our substrate under an optical microscope (OM) to see if any flake can potentially be used for the project. The flake would then be transferred to another wafer using either wet or dry transfer. This process was done by my mentors (Gangtae and Han) because it involved hydrofluoric acid (HF).

Later, using phosphine gas (Ph_3) in a tube furnace for one and a half hours, we were able to convert $MoSi_2$ to MoP. Shortly, after determining the thickness of our MoP flake under the AFM and optical microscope, we can now use a computer aided design (CAD) to cut out our desired width which was < 300 nm. Then protect our sample with 495 PMMA A4 resist by spin coating the wafer and baking it for two minutes at 2000 revolutions per minute (rpm) twice.

Then using the electron-beam and reactive ion etcher (RIE) etcher, we exposed and etched the target areas on the flake to get our desired width. We looked under both the AFM and the OM to see if both of those processes were successful. If we were successful, we then developed our samples in acetone for five to six hours to remove any residual resist. We then had to re-coat our sample with PMMA to prepare for the next e-beam exposure. This consisted of patterning 4-probe electrodes using CAD. Then go through the e-beam process to allow us to deposit

chromium (Cr) and gold (Au) using the e-beam evaporator to facilitate contact when measuring the nanowire's resistivity. If the second e-beam process was successful, we would then develop the sample with isopropyl alcohol (IPA) for about two minutes or less to see if the exposure was successful so we can do deposition then measure the resistivity of the nanowire.

Conclusions and Future Steps:

We successfully fabricated our narrow MoP nanoribbons to determine the resistivity of MoP under 20 nm. The resistivity of the etched nanoribbon was high, possibly due to damage during the fabrication process.

Potential improvements to this process include exploring other etching processes and limiting ambient exposure during the whole fabrication process. Also use X-ray diffraction (XRD) throughout the fabrication process to determine whether our sample changed states or if it remains MoP throughout the fabrication process.

Acknowledgements:

A.D.K. acknowledges the support from the National Science Foundation REU program. The project made use of the Cornell NanoScale Science and Technology Facility supported by the NSF grant no. NNCI-2025233. Characterization of the samples was carried out at Cornell Center for Materials Research. Many thanks to Judy J. Cha as the principal investigator.

References:

[1] Gall, D., Cha, J.J., Chen, Z. et al. Materials for interconnects. MRS Bulletin 46, 959-966 (202jj1). https://doi.org/10.1557/s43577-021-00192-3.

[2] Han, H. J., Kumar, S., Jin, G., Ji, X., Hart, J. L., Hynek, D. J., Sam, Q. P., Hasse, V., Felser, C., Cahill, D. G., Sundararaman, R., Cha, J. J., Topological Metal MoP Nanowire for Interconnect. Adv. Mater. 2023, 35, 2208965. https://doi.org/10.1002/adma.202208965.

[3] Wang, W., Qi, J., Zhai, L., Ma, C., Ke, C., Zhai, W., Wu, Z., Bao, K., Yao, Y., Li, S., Chen, B., Repaka, D. V. M., Zhang, X., Ye, R., Lai, Z., Luo, G., Chen, Y., He, Q., Preparation of 2D Molybdenum Phosphide via Surface-Confined Atomic Substitution. Adv. Mater. 2022, 34, 2203220. https://doi.org/10.1002/adma.202203220.

[4] Wang, W., Qi, J., Zhai, L., Ma, C., Ke, C., Zhai, W., Wu, Z., Bao, K., Yao, Y., Li, S., Chen, B., Repaka, D. V. M., Zhang, X., Ye, R., Lai, Z., Luo, G., Chen, Y., He, Q., Preparation of 2D Molybdenum Phosphide via Surface-Confined Atomic Su.

[5] Wang, J., Wu, Z., Mao, C. et al. Effect of Electrical Contact Resistance on Measurement of Thermal Conductivity and Wiedemann-Franz Law for Individual Metallic Nanowires. Sci Rep 8, 4862 (2018). https://doi.org/10.1038/s41598-018-23291-9.

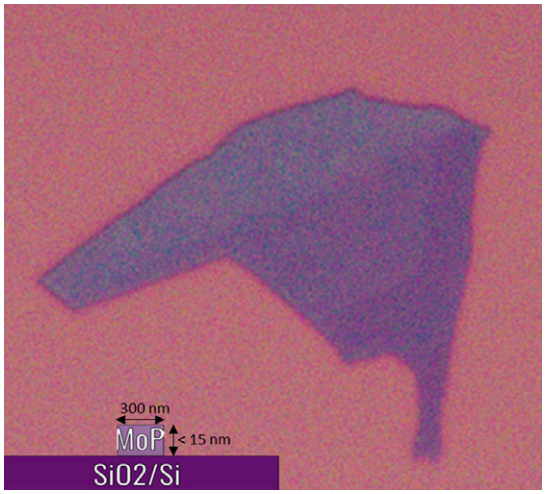

Figure 1: MoP flake.

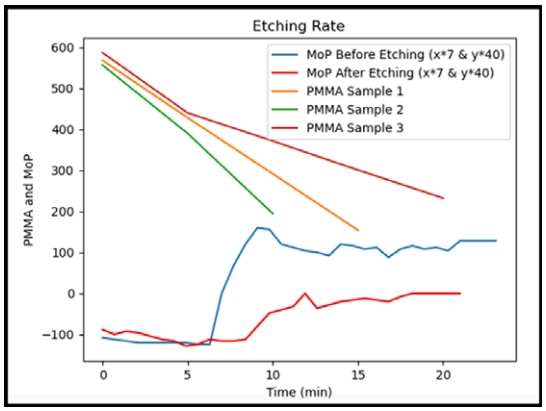

Figure 2: PMMA and MoP etching.

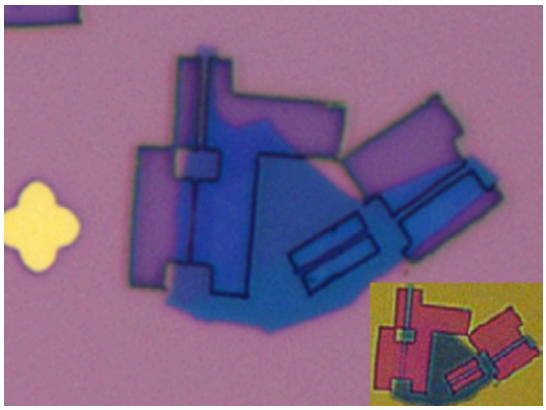

Figure 3: MoP before and after etching.

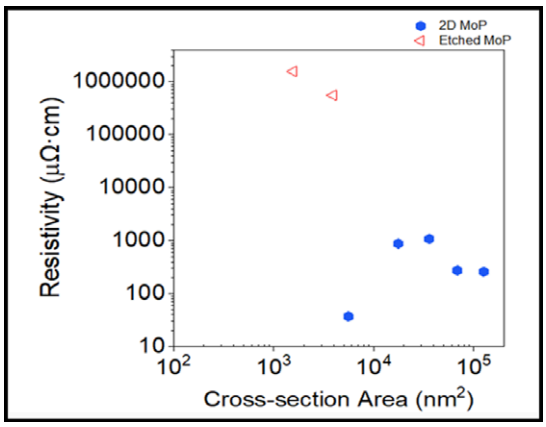

Figure 4: Resistivity measurement.

Palladium Thin Films for Hydrogen-Driven Actuation and Liquid Crystal Sensing in Microrobotics

2023 CNF REU Intern: Bryan Junsuh Kim
Intern Affiliation: Chemistry, University of California, Berkeley

CNF REU Principal Investigator: Nicholas Lawrence Abbott, Chemical & Biomolecular Engineering, Cornell
CNF REU Mentor(s): Hanyu Alice Zhang, Ayushi Tripathi; Physics, Chemical & Biomolecular Engineering, Cornell
Program & Primary Source of Research Funding: 2023 Cornell NanoScale Facility Research Experiences for Undergraduates (CNF REU) Program via the National Science Foundation under Grant No. NNCI-2025233
Contact: bryanjskim@berkeley.edu, nla34@cornell.edu, hz496@cornell.edu, at885@cornell.edu
Website(s): https://cnf.cornell.edu/education/reu/2023
Primary CNF Tools Used: AJA3 Sputtering Deposition, ABM Contact Alignment, Zeiss SEM, Bruker Energy Dispersive X-ray Spectroscopy (EDS), Oxford PECVD, Critical Point Dryer

Abstract:

Microrobots rely on actuation and sensing as two key functions to navigate their environment. Chemomechanical actuation leverages gaseous fuels such as hydrogen to drive mechanical movement, while liquid crystals can sense hydrogen by generating an optical signal. Here, we study sputter-deposited thin films of palladium for micron-scale actuation and liquid crystal responsive sensors. Through a photolithographic process, we fabricate a palladium-titanium bimorph hinge between two silicon dioxide (SiO_2) panels, one fixed while the other free to rotate, as a working microactuator device. By exposing the microhinge to gaseous hydrogen, hydrogen diffuses into the palladium bulk and induces a phase transition from a hydrogen-poor alpha (α) phase to a hydrogen-rich beta (β) phase in which the lattice parameter increases from 3.89 angstroms (Å) to 4.03 Å, bringing about a volumetric expansion that drives actuator bending. To promote faster actuation, we also introduce gold to create a palladium-gold alloy hinge, for the palladium-gold-hydride system facilitates a second-order phase transition with an alloy composition of 15-20% gold. Furthermore, our study reveals that sputter-deposited palladium induces surface anisotropy, observed via a preferential azimuthal direction of the liquid crystals when planarly aligned by hydrogen.

Summary of Research:

This research was conducted across two channels: fabricating microactuator devices and running hydrogen experiments for liquid crystal sensing.

Based on a past study in the Abbott group, the chemomechanical actuator device was composed of a platinum-titanium hinge between two SiO_2 panels: one fixed while the other free to rotate [1]. By applying gaseous hydrogen or oxygen, platinum surface stress drives reversible curvature changes for microactuation. A merit of chemomechanical actuation is the circumvention of intermediate conversion processes (unlike photovoltaic actuators that convert light to voltage, then voltage to mechanical bending).

Here, platinum was switched out for palladium. Because gaseous species only interact with the platinum surface, the bending curvature is relatively weak. On the other hand, hydrogen diffuses into the palladium bulk and facilitates a phase transition from hydrogen-poor α-phase to hydrogen-rich β-phase. An increase in unit cell lattice parameter from 3.89Å to 4.03Å results in increased bulk volume [2]. Through bulk volumetric expansion instead of surface stress, a palladium-based actuator hinge can drive stronger mechanical bending than a platinum-based actuator hinge.

Through a photolithographic process, the palladium hinge actuators were fabricated. Two square SiO_2 panels, ten microns (μm) in length, were attached to a palladium-titanium hinge with dimensions 10 μm by 5 μm in length. The hinge was made by sputtering 50 nanometers (nm) of palladium on 10 nm of titanium. Additionally, a tether was attached to the bottom SiO_2 panel for support.

After fabrication, the devices were exposed to cycles of hydrogen and air. As observed in Figure 1, the actuation was gradual over three minutes of hydrogen exposure. Furthermore, the curvature change is jolty and abrupt rather than linear and smooth.

To remediate, gold was incorporated into the palladium hinge. In the palladium-hydride system, the transition from α to β is characterized by a 1st-order phase transition. Because the two phases must nucleate separately, an energy barrier exists. In the palladium-gold-hydride system, however, a 2nd-order phase transition is facilitated, meaning that phase separation is lost and the energy barrier is minimized. This absence of phase separation can lead to smoother, faster actuation.

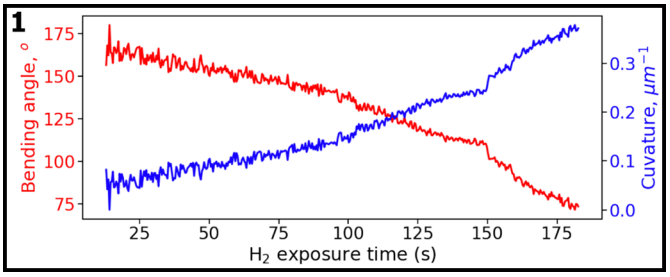

Figure 1: Hydrogen response for the Pd actuator hinge. Bending angle is defined as the angle between the two SiO_2 panels, and curvature is the change in the angle of deformation per unit length.

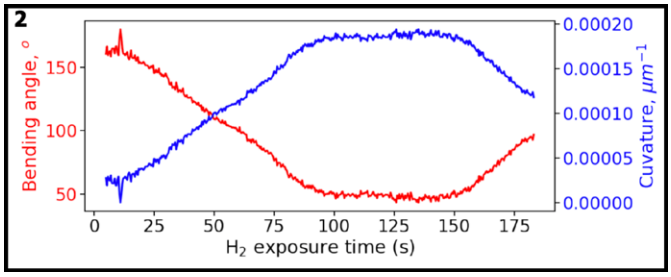

Figure 2: Hydrogen response for the palladium-gold actuator hinge.

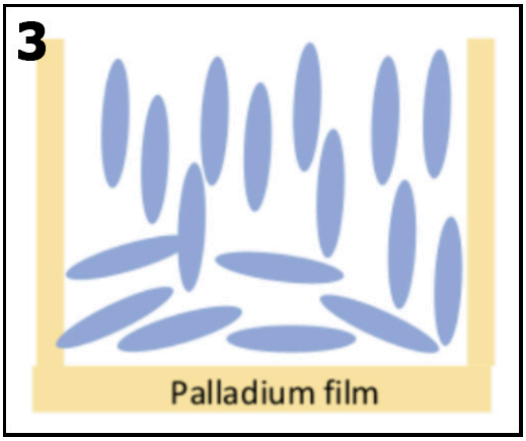

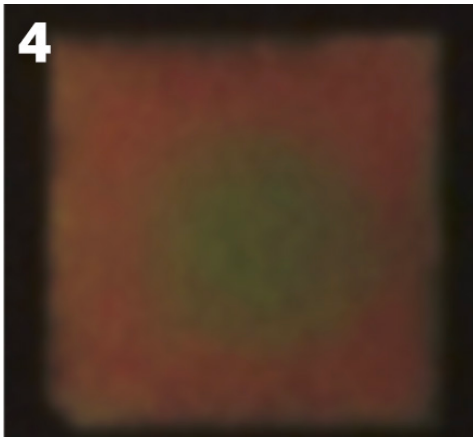

Figure 3, left: Side view of a schematic of planarly-aligned 5CB liquid crystals on the surface of sputtered palladium thin film. Figure 4, right: Top-down view of the bright optical response of 5CB liquid crystals on sputtered Pd.

From literature for the palladium-gold-hydride system, 15-20% gold concentration for a palladium-gold alloy is known to pass the critical point for phase separation [3].

The palladium-gold hinge was deposited via co-sputtering, which allowed tunable gold concentration. As shown in Figure 2, faster bending was observed over three minutes of hydrogen exposure. However, around 2.5 minutes, the hinge began to curve backwards, a behavior that remains to be investigated.

For liquid crystal sensing, 4-cyano-4'-pentylbiphenyl (5CB) liquid crystals were deposited on a sputtered palladium thin film. After two minutes of hydrogen exposure, the liquid crystals' surface alignment reoriented from homeotropic to planar as illustrated in Figure 3. The bright optical response is observed in Figure 4. Furthermore, it was discerned that the liquid crystals were uniformly aligned in a specific azimuthal direction. By rotating the sample along one of the cross-polarizer directions, the bright optical response briefly dimmed. Thus, sputtering deposition seems to induce surface anisotropy, observed by the preferential in-plane alignment of the liquid crystals.

Conclusions and Future Steps:

For the palladium-gold actuators, the hinge's behavior of curving backwards remains to be understood, necessitating fabrication of more palladium-gold actuator samples. A possible explanation is crack formation in the hinge, causing hydrogen to drive out and reverting the α-to-β volumetric expansion.

For liquid crystal sensing, the origins of the surface anisotropy induced by sputtering remain to be investigated. Sputtering instrumentation parameters, such as target-to-substrate distances and angles, could elucidate so, as well as understanding the surface grain shape, orientation, etc.

Acknowledgements:

I would like to acknowledge the National Science Foundation (NSF) grant no. NNCI-2025233, the National Nanotechnology Coordinated Infrastructure (NNCI), and the Cornell NanoScale Facility for funding and curating the Research Experiences for Undergraduates (CNF REU) opportunity. I would also like to acknowledge and thank Prof. Nicholas Abbott, Alice Zhang, Ayushi Tripathi, and Tom Pennell for their research mentorship, as well as Melanie-Claire Mallison for her guidance as REU coordinator.

References:

[1] Bao, N., et al. (2023). PNAS, 120(19).
[2] Wang, B., et al. (2021). Micromachines, 12(11).
[3] Maeland A., Flanagan, T.B. (1965). J. Phys. Chem., 1965, 69(10).

In-situ and *Ex-situ* Si Doping of β-Ga_2O_3

CNF Project Number: 150-82
Principal Investigator(s): Michael Thompson, Hari Nair
User(s): Cameron Gorsak, Katie Gann

Affiliation(s): Department of Materials Science and Engineering, Cornell University

Primary Source(s) of Research Funding: AFOSR/AFRL ACCESS Center of Excellence under Award No. FA9550-18-10529

Contact: cag284@cornell.edu, krg66@cornell.edu, mot1@cornell.edu, hn277@cornell.edu

Website(s): https://www.thompson.mse.cornell.edu/

Primary CNF Tools Used: DISCO Dicing Saw, Oxford ALD FlexAL

Abstract:

Recently, there is great interest in the material β-Ga_2O_3, which has an ultra-wide bandgap of ~ 4.8 eV. β-Ga_2O_3 is of interest for its application for radio frequency (RF), high power electronics, and solar-blind UV detectors. β-Ga_2O_3 substrates can be grown from the melt, which will make scaling-up production favorable. Additionally, the facile n-type doping of β-Ga_2O_3 is achieved due to the availability of shallow donors. In this work, we demonstrate controllable *in-situ* and *ex-situ* Si doping of β-Ga_2O_3, by MOCVD and ion-implantation respectively.

Summary of Research:

In this work, Fe doped β-Ga_2O_3 substrates were acquired from Novel Crystal Technology and then subsequently diced into a square geometry for Hall effect measurements, typically 5 × 5 or 10 × 10 mm.

In-situ Si doping was performed during the metal organic chemical vapor deposition (MOCVD) growth in an Agnitron Agilis 100 system. Figure 1 shows the controllability of *in-situ* Si doping by tuning the moles of Si per nm of β-Ga_2O_3 growth at a chamber pressure of 15 Torr. Doping is controlled over three orders of magnitude from mid × 10^{16} to low × 10^{19} cm^{-3} with competitive mobilities. Even higher *in-situ* doping up to 1 × 10^{20} cm^{-3} can be achieved by increasing the chamber pressure for 40 Torr to increase the cracking efficiency of the Si precursor, silane.

Ex-situ Si doping was performed by ion-implanted of unintentionally doped (UID) β-Ga_2O_3 grown by plasma-assisted molecular beam epitaxy (MBE). Prior to ion implantation, a 20 nm SiO_2 cap was deposited on the sample via atomic layer deposition (ALD) in order to tailor the Si implant profile. After ion implantation, the samples were annealed under a controlled ultra-high purity nitrogen ambient in order to activate the dopants. The best anneal condition was found to be 950°C for five minutes for implant concentrations between 5 × 10^{18} to 1 × 10^{20} cm^{-3}, achieving greater than 80% activation with mobilities all recovered to greater than 70 cm^2/ V • s for all conditions.

This work has laid the groundwork for current device processing by enabling high channel mobilities via *in-situ* doping and ohmic contacts via *ex-situ* ion implantation.

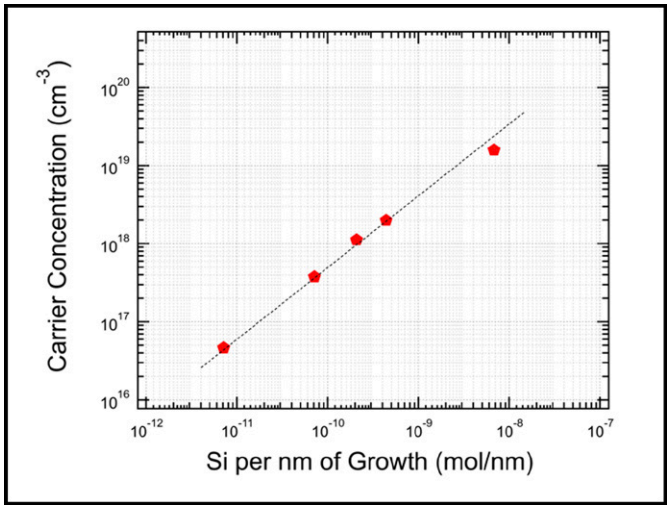

Figure 1: Demonstrated in-situ *Si doping concentration from mid × 10^{16} to low × 10^{19} cm^{-3} by controlling the molar flow of Si per nm of MOCVD* β-Ga_2O_3 *growth.*

The Effect of Nitrogen on the Stability of the β Phase in W Thin Films

CNF Project Number: 699-98
Principal Investigator(s): Shefford P. Baker
User(s): Yue Zhao, Jiayi Cao, Samantha Wang, Hannah Morgan-Smith Myers

Affiliation(s): Department of Materials Science and Engineering, Cornell University

Primary Source(s) of Research Funding: National Science Foundation DMR-1810138

Contact: shefford.baker@cornell.edu, yz2722@cornell.edu, jc2732@cornell.edu, mw842@cornell.edu, hem66@cornell.edu

Primary CNF Tools Used: AJA Sputter Deposition, FleXus Film Stress Measurement, P7 Profilometer, Dektak XT Profilometer, CDE ResMap Resistivity 4-pt Probe, Panalytical X-ray Diffractometer, Veeco Icon Atomic Force Microscope, Zeiss Supra Scanning Electron

Abstract:

The body centered cubic (BCC) phase (α-W) is the only known stable structure in tungsten. However, a metastable phase (β-W) having A15 structure can be produced using atom-by-atom deposition methods. Interest in the metastable phase recently spiked it has been shown to exhibit a giant spin Hall effect (GSHE) [1], which is expected to enable significant miniaturization in next-generation magnetoresistive random access memory (MRAM). To be useful in technology, it must be possible to reliably produce β-W and to retain it during production and use. It is known that inclusion of small amounts of nitrogen facilitates production of the β-phase [2] {Liu, 2016 #3025}. However, little is known about the stability of this metastable phase or how and why it forms. In this work we explore the effects of N on the formation and thermal stability of β-W. We deposit W films with different N contents in CNF and use x-ray diffraction to determine the fractions of α- and β-W before and after thermal cycling. Results are modeled to examine the kinetics and mechanisms of the β-α phase transformation.

Summary of Research:

Tungsten thin films were deposited onto 4" Si <100> wafers with native oxide using the AJA DC magnetron sputtering system in CNF and a 99.95% 3" W target. The Si wafers were plasma cleaned for 60 seconds before deposition. The base pressure was better than 2×10^{-8} Torr. Each film was sputtered at a power of 400 W in a working gas pressure of 3 mTorr for 1000 s. A total flow rate of 30 sccm of Ar and N was maintained with N flow rates of 0, 0.5, 1, 1.5, and 2 sccm. A temperature indicator was affixed to the back of the Si wafer to determine the maximum temperature the wafer reached during deposition. A "witness sample" of Si with a photoresist pattern was also attached to the substrate carrier. After deposition, the photoresist was lifted-off using acetone, and the thicknesses of the remaining W was measured using the Dektak® XT profilometer at CNF. The stresses in the as-deposited films were determined using the FleXus® film stress measurement instrument at CNF.

The as-deposited films were cleaved into 1 cm × 1 cm samples. Individual pieces were then heated at 10°C/min in a high vacuum furnace to temperatures of 300, 400, 500, 600 and 700°C, under a base pressure better than 10^{-7} Torr. No thermal oxidation was detected after the annealing.

The textures and phase fractions of α- and β-W were determined using x-ray diffraction on the as-deposited and the annealed samples. Symmetric 2θ scans were performed from 20° to 90° with a step size of 0.02°. Rocking curve scans using the ω geometry were obtained for all α and β peaks visible on the 2θ scans.

The deposited films had thicknesses of 190 ± 5 nm, the maximum temperature during the depositions was 66-71°C, and the stress in the as-deposited films was -2.3 to -2.1 GPa. Nitrogen concentrations in the as-deposited films were estimated from the flow rates to be 2.53, 4.95, 7.27, and 9.49 at% for films deposited in 0.5, 1.0, 1.5, and 2.0 sccm N_2, respectively.

For the as-deposited samples, all the 2θ diffraction peaks were identified as β, except for a small α(211) peak at 2θ = 73.193°. After thermal annealing, α(110) peaks emerged, indicating the initiation of the β to α transformation. With increasing annealing temperature, the intensities of the α peaks increase while those of the β peaks decrease. Eventually, all the β peaks vanished, indicating complete transformation to the α phase.

The rocking curves were analyzed to estimate the phase fractions in the samples. The phase fractions as a function of annealing temperature are shown in Figure 1. A Johnson-Mehl-Avrami-Kolmagorov type model

(similar to [3]) was developed to describe the phase transformation as a function of temperature in terms of the different activation energies involved. The results of the model are also shown in Figure 1.

Conclusions and Future Steps:

The model suggests that nitrogen stabilizes the β phase by accumulating in phase boundaries, slowing their motion. In the future, we will use CNF equipment to attempt to make N-free β-W films and to measure their properties (e.g., resistivity) as a function of N content.

References:

[1] Pai, C.F., L.Q. Liu, Y. Li, H.W. Tseng, D.C. Ralph, and R.A. Buhrman, Spin transfer torque devices utilizing the giant spin Hall effect of tungsten. Applied Physics Letters, 101(12) (2012).

[2] Liu, J. and K. Barmak, Topologically close-packed phases: Deposition and formation mechanism of metastable β-W in thin films. Acta Mater 104, 223-227 (2016).

[3] Denis, S., D. Farias, and A. Simon, Mathematical-Model Coupling Phase-Transformations and Temperature Evolutions in Steels. ISIJ International, 32(3) 316-325 (1992).

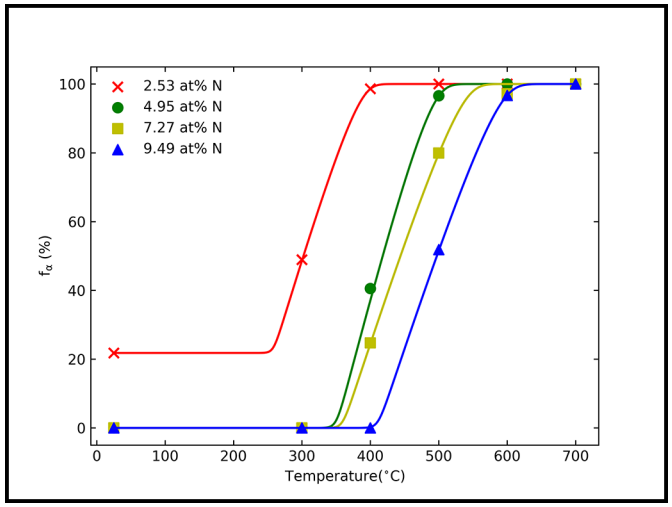

Figure 1: Volume fraction of α-W as a function of annealing temperature for films of varying N content. Points indicate experimental measurements, lines indicate results of a model.

Reactive Ion Etching (RIE) Reveals Biphasic Self-Assembled Mesostructures in Block Copolymer Thin Films

CNF Project Number: 1356-05
Principal Investigator(s): Ulrich Wiesner
User(s): Fei Yu

Affiliation(s): Department of Materials Science and Engineering, Cornell University

Primary Source(s) of Research Funding: U.S. Department of Energy (DOE), Office of Science (Basic Energy Sciences (DE-SC0010560)

Contact: ubw1@cornell.edu, fy84@cornell.edu

Website(s): http://wiesner.mse.cornell.edu/

Primary CNF Tools Used: Oxford 81 Etcher

Abstract:

The surface morphology of thin films of a triblock terpolymer was first characterized by atomic force microscopy, which shows a different mesostructure from the one suggested by small-angle X-ray scattering. Reactive ion etching by CF_4 plasma of the polymer film was carried out at CNF to bring out the substructure beneath the surface, which turned out to be biphasic. The plasma etching, combined with microcopy and scattering techniques, offers a powerful tool for a comprehensive probe of the self-assembled mesostructure inside the block copolymer thin films.

Summary of Research:

The surface morphology of block copolymer thin films can be characterized by scanning electron microscopy (SEM) or atomic force microscopy (AFM). It is challenging, however, to gain a real-space picture of the underlying structures with microscopy techniques. In our experiment, thin films of the triblock terpolymer poly(isoprene)-*block*-poly-(styrene)-*block*-poly(N,N-dimethylaminoethyl methacrylate) (PI-*b*-PS-*b*-PDMAEMA, or ISA) were prepared by spin-coating a 5.0 wt% solution in tetrahydrofuran (THF) onto a silicon wafer. After solvent vapor annealing (SVA) in THF for 19 h, Figure 1a,b shows the top surface morphology, as imaged with AFM. Films displayed periodically ordered hexagonal patterns with distinct regions attributed to each of the three blocks: PI?PS core?shell cylinders in a majority PDMAEMA matrix. Figure 2c,d depicts this structure schematically, with PI cylinder cores represented in green, PS cylinder shells in blue, and the PDMAEMA matrix in light pink.

In addition to the surface morphological characterization by AFM, grazing-incidence small-angle X-ray scattering (GISAXS) was performed to better understand the subsurface structures. The observed scattering pattern (Figure 2) was consistent with a core?shell double gyroid structure with the (211) planes parallel to the substrate and compressed 52% along [211] axis, i.e., along the film normal. The associated lattice parameters were as follows: a = 90.7 nm and $b = c$ = 121.4 nm, with angles α = 98° and $\beta = \gamma$ = 113°. According to the lattice parameters, the distance between neighboring (211) planes is 25.5 nm. Compression of the film was likely a result of rapid drying that occurred immediately upon the removal of samples from the SVA environment.

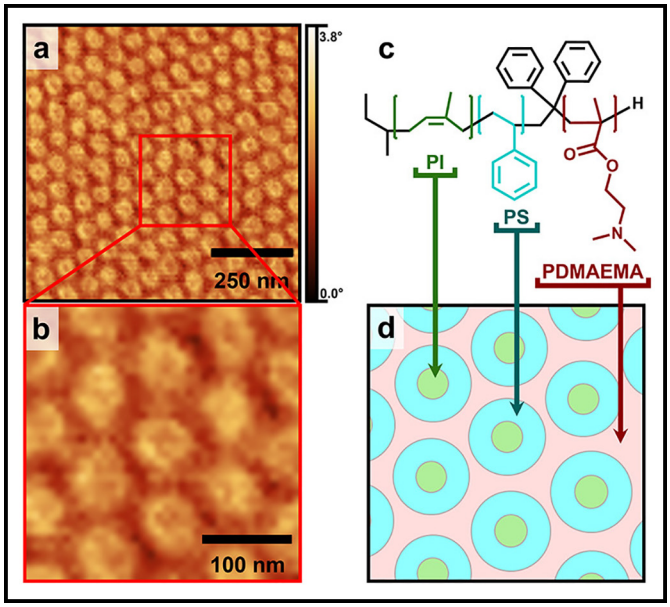

Figure 1: (a) AFM phase image of an ISA thin film. A magnified region marked with a red square in (a) is shown in (b), enabling identification of all three top surface blocks of the ISA structure depicted in (c). A schematic of the top surface morphology consistent with the AFM images is depicted in (d), showing PI cylinder cores (green), PS cylinder shells (blue), and the PDMAEMA matrix (light pink).

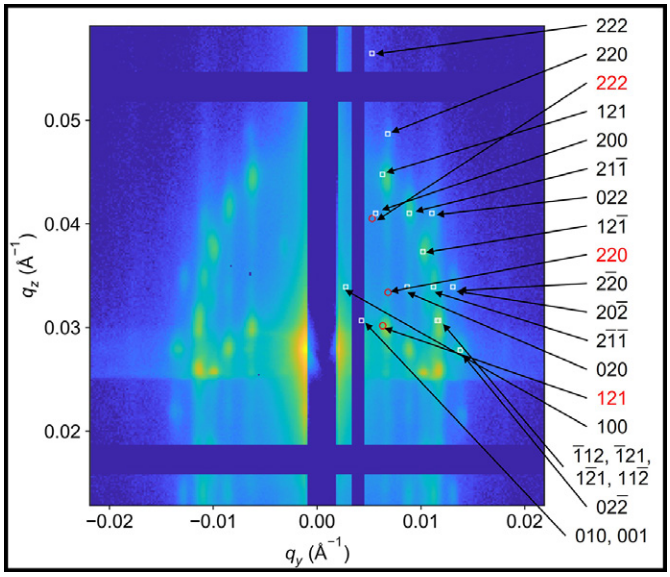

Figure 2: GISAXS patterns of an ISA thin film showing indexed peaks matching a double gyroid structure with the (211) plane parallel to the surface and compressed along the film normal. White squares and red circles correspond to expected peak positions through the reflection and transmission channels, respectively, in GISAXS.

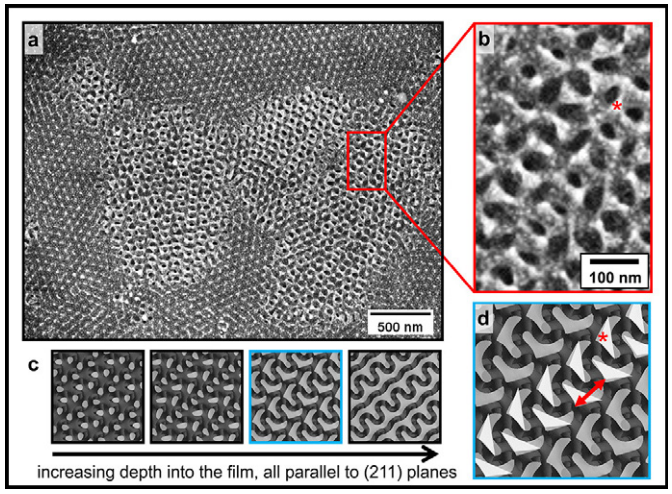

Figure 3: (a) SEM image with a selected area at higher magnification in the (b) red box of an ISA thin film surface after etching with CF_4 plasma for 7 s and (c) simulated (211) plane morphologies of the co-continuous double gyroid along the [211] axis at different depths. Comparing (d) a specific slice, outlined in blue, from the simulation stack to the area enlarged in (c) reveals clear similarities. Red asterisks in (b) and (d) indicate PI-rich locations that appear brighter in SEM due to preferential staining of the PI block with RuO_4. The red double arrow in (d) indicates the spacing between neighboring repetitive features in the (211) plane.

The GISAXS results suggest a different morphology from that revealed by AFM on the surface, but a straightforward comparison is difficult due to the scattering pattern in the reciprocal space. To reconcile these structural differences, it was of interest to investigate the change in structure when moving away from the top surface layer, i.e., deeper into the film. To visualize this transition, the thin films were etched with CF4 plasma and stained with RuO_4 for ~ 15 min to increase contrast in the subsequent SEM images. Figure 3a shows an SEM image of a film etched for 7 s. While there are still regions displaying hexagonal order, the image of the etched film now also clearly reveals areas that resemble a co-continuous structure. Regions with hexagonal lattice structure had a center-to-center cylinder distance of 71.2 ± 1.6 nm. The spacing between the neighboring repetitive features in the (211) plane (see red double arrow in Figure 3d) was 117.0 ± 4.1 nm, similar to the 112.7 nm spacing calculated from GISAXS data. Figure 3b shows an enlarged SEM image area that displays features consistent with a co-continuous structure. By comparing this pattern to simulated (211) planes of the double gyroid along the [211] axis at different depths (Figure 3c), a bent-triangular structure alternating from one side to another is clearly recognizable (see the blue box in Figure 3c). With the PI block stained more heavily as compared to PS, the corner marked with a red asterisk indicates a PI-rich location. These areas appear brighter in the SEM image from greater electron scattering and can be assigned to a similar structure in the simulation (compare Figure 3b,d). Therefore, reactive ion etching enables real-space microscopy characterization of underlying structures in self-assembled block copolymer thin films, which could differ from the surface.

References:

[1] Lee, W. Y., Chapman, D. V., Yu, F., Tait, W. R., Thedford, R. P., Freychet, G., Zhernenkov, M., Estroff, L. A., and Wiesner, U. B. (2022), Triblock Terpolymer Thin Film Nanocomposites Enabling Two-Color Optical Super-Resolution Microscopy. Macromolecules, 55(21), 9452-9464.

Low Loss Superconducting LC Resonator for Strong Coupling with Magnons

CNF Project Number: 2126-12
Principal Investigator(s): Gregory David Fuchs
User(s): Srishti Pal, Qin Xu, Varshith Kandula

Affiliation(s): Department of Applied Physics & Engineering, Department of Physics; Cornell University

Primary Source(s) of Research Funding: Department of Energy (DOE), Center for Molecular Quantum Transduction (CMQT)

Contact: gdf9@cornell.edu, sp2253@cornell.edu, qx85@cornell.edu, vk332@cornell.edu

Primary CNF Tools Used: AJA Sputter Deposition, Heidelberg Mask Writer - DWL2000, GCA 6300 DSW 5X g-line Wafer Stepper, YES Asher, AJA Ion Mill, PT770 Etcher - Left Side, P7 Profilometer, Zeiss Supra SEM, Nabity Nanometer Pattern Generator System (NPGS), JEOL 6300, Dicing Saw - DISCO, Westbond 7400A Ultrasonic Wire Bonder

Abstract:

We present a hybrid quantum system based on strong coupling between microwave photons host by micro-structured resonators and magnon modes of the molecular ferrimagnet vanadium tetracyanoethylene ($V[TCNE]_x$). Using Cornell NanoScale Facility (CNF), we develop a process to integrate the fabrication of thin-film superconducting LC resonators and the deposition of lithographically patterned $V[TCNE]_x$ films. We explore ways to enhance the quality factors of our LC resonators with the aim to elevate its performance in the strong coupling regime. We also focus on designing and fabricating new resonator structures capable of decoupled excitation and read-out of the hybrid magnonic system.

Summary of Research:

This research is focused on studying a strongly coupled hybrid photon-magnon system where the coupling strength between the two sub-systems exceeds the mean energy loss in either of them. The key figure-of-merit of this hybrid system is its cooperativity $C = 4g^2/\kappa_m\kappa_r$, where g is the coupling strength between magnons and photons, and κ_m and κ_r are the damping rates for magnons and photons, respectively. The system operates in strong-coupling regime if $C>1$.

In this work, we use lumped-element planar LC resonators fabricated on superconducting niobium thin-film offering high quality factor (Q-factor) and thus low κ_r. The basic steps for patterning our LC resonators using photolithography are shown in Figure 1(a). First, we sputter a 50 nm thick niobium film (thickness measured using P7 profilometer) on MOS cleaned sapphire substrate using AJA sputter. The superconducting transition temperature (T_c) of our niobium film comes out to be ~ 8.8K, which is high enough to offer low damping. The resonator design, patterned on a photomask using Heidelberg Mask Writer-DWL2000, is then cast onto the resist coated wafer (we spin-coat a resist bi-layer of LOR3A and S1813) using 5X g-line Stepper. The developed resist (in AZ726MIF) is descummed in the YES Asher followed by dry etching of niobium in AJA Ion Mill (and recently in PT770). Finally, we strip the resist in 1165 and dice the wafer using Dicing Saw-DISCO to separate the chips patterned on the wafer.

For the magnon sub-system, we use the low-loss organic ferrimagnet $V[TCNE]_x$ with a low Gilbert damping $\alpha \sim 10^{-4}$ offering long magnon lifetime and thus low κ_m. Using e-beam lithography in the JEOL 6300 or Nabity Nanometer Pattern Generator System (NPGS) connected to Zeiss Supra SEM, we pattern a 6 μm wide and 600 μm long bar on the 10 μm wide and 600 μm long inductor wire using the steps shown in Figure 1(b). We then ship the exposed resonator chips to our collaborators in Ohio State University for $V[TCNE]_x$ growth and liftoff.

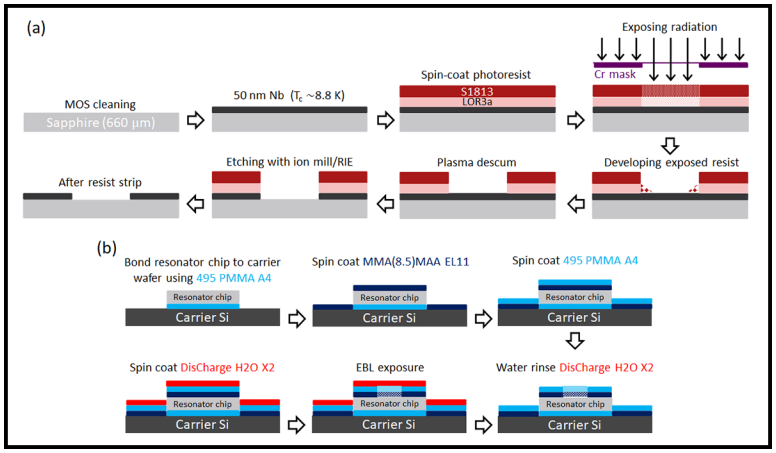

Figure 1: Process flow for (a) patterning the LC resonator using photolithography, and (b) e-beam patterning for $V[TCNE]_x$ deposition.

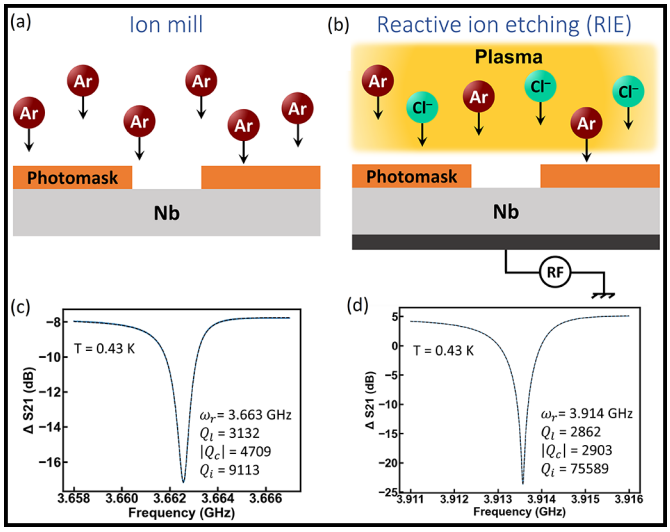

Figure 2: (a)-(b) The schematics of the ion mill and reactive ion etching processes, respectively. (c)-(d) Fitted resonator response with extracted Q-factors for the ion milled and reactive ion etched chips, respectively.

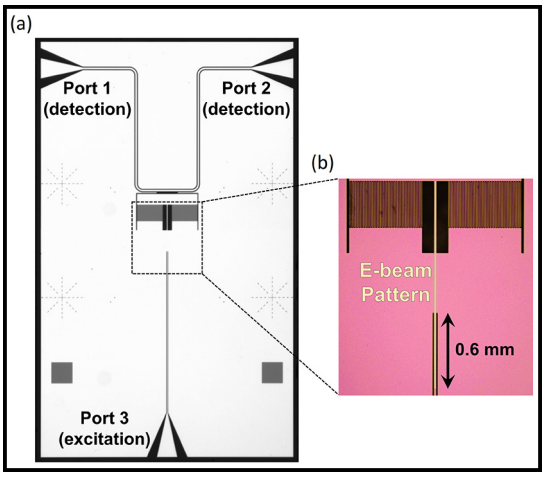

Figure 3: (a) Microscope image of the 3-port LC resonator with separated excitation and detection ports. (b) E-beam pattern with resist on (exposed and developed) for V[TCNE]$_x$ deposition.

The results on our first-generation coupled resonator-V[TCNE]$_x$ system are summarized in our recent arXiv article [1]. Our first-generation 2-port LC resonators were etched by ion milling (AJA Ion Mill) by neutral argon beam [Figure 2(a)]. The process of ion milling for our resonator design suffers from the drawbacks of — (i) slow overall etch-rate, (ii) non-uniform etch-rates at different parts of the design (especially drastically lower etch-rates for interdigitated capacitor fringes than that at other parts), (iii) substrate heating during the physical bombardment process of the high-energy Ar-beam, and (iv) possibly the etching residues of ejected niobium. These factors contributed to limit the internal Q-factor of our LC resonators to $\sim 10^3$ as shown in the transmission spectrum of Figure 2(c). The details of the fitting parameters are elucidated in reference [1]. To overcome the limitations of ion milling, we have recently adopted a chlorine-based reactive ion etching (RIE) process (PT770) shown in Figure 2(b). The key advantages of this etching method are — (i) extremely high etch-rates, (ii) uniform etching at all parts of the resonator, (iii) minimal heating of the substrate, and (iv) niobium is etched in the form of volatile niobium chlorides minimizing the contamination by residues. Upgradation to this RIE process resulted in an increase in the internal Q-factor of our LC resonators by a factor of ~ 8 [Figure 2(d)].

The performance of our old 2-port resonator design is limited due to the inseparable excitation and detection mechanism of the hybrid system. To get around this limitation, we have modified our resonator design where the V[TCNE]$_x$ bar is extended over a third port employed to excite the magnons without driving the resonator. The magnons are then expected to travel to the resonator which, in this case, can be used solely for sensing. Figure 3(a) shows our very first design for the 3-port resonators. We are currently in the process of optimizing this design with a primary goal of achieving high internal-Q, moderate co-operativity for the coupled magnon-resonator system, and a minimal crosstalk between the excitation port and the LC resonator system. The e-beam pattern for a future V[TCNE]$_x$ deposition on the 3-port resonator chip is shown in Figure 3(b).

Conclusions and Future Steps:

We have demonstrated the fabrication and integration of a low-loss hybrid photon-magnon system based on strong coupling between superconducting LC resonators and the organic ferrimagnet V[TCNE]$_x$. We have been able to enhance the intrinsic quality factor of our LC resonator by improved fabrication. We have further modified our resonator design for future experiments envisioned to disentangle the excitation and read-out mechanisms. After a successful optimization of our primordial 3-port resonator design, we plan to impose further modification to the design for developing experiments for magnon lasing and sensing magnon Bose-Einstein condensate (mBEC) states.

References:

[1] Q. Xu, H. F. H. Cheung, D. S. Cormode, T. O. Puel, H. Yusuf, M. Chilcote, M. E. Flatté, E. Johnston-Halperin, and G. D. Fuchs, "Strong photon-magnon coupling using a lithographically defined organic ferrimagnet", arXiv:2212.0442.

Ordering of Liquid Crystals on Photocatalytic Titania Surfaces

CNF Project Number: 2736-18
Principal Investigator(s): Prof. Nicholas L. Abbott
User(s): Ayushi Tripathi

Affiliation(s): Robert Frederick Smith School of Chemical and Biomolecular Engineering, Cornell University
Primary Source(s) of Research Funding: IIS-1837821, DMR-1921722
Contact: nla34@cornell.edu, at885@cornell.edu
Website(s): https://nlabbottcornell.weebly.com/
Primary CNF Tools Used: Arradiance ALD, Odd hour evaporator, Woollam RC2 Spectroscopic Ellipsometer

Abstract:

We have fabricated thin films of titania by atomic layer deposition (ALD). We used the photocatalytic activity of the films to design liquid crystalline systems that can be triggered to undergo orientational transitions upon illumination. Polarization modulation-infrared reflection-adsorption spectroscopy (PMIRRAS) was used to provide evidence that the orientational transitions arise from photocatalytic generation of a carboxylic acid-containing species in the liquid crystal. This study reports the first design of liquid crystalline systems that respond to the photocatalytic activity of metal oxide films.

Summary of Research:

We used the ALD process to fabricate titania (TiO_2) thin films using tetrakis(dimethylamino)titanium (TDMATi) and water (H_2O) as precursors and a deposition temperature of 225°C. After 60 cycles of deposition, we measured the ellipsometric thickness of the TiO_2 films to be 3.27±0.03 nm (Woollam spectroscopic ellipsometer). TiO_2 thin films were then annealed at 500°C for 15 h in air to obtain the anatase (101) phase of titania, as confirmed by X-ray diffraction analysis [1]. The films were also analyzed by X-ray photoelectron spectroscopy and the ratio of O to Ti was determined to be 2.04:1, consistent with the expected stoichiometry of titania [1].

The aim of our study was to couple photocatalytic reactions on the surface of titania with orientational transitions in liquid crystalline materials. Titania is a well-known photocatalyst with a wide band gap of 3.2 eV and is photoactive under UV illumination (<385 nm). We characterized the orientations of the nematic LC 4-cyano-4'-pentylbiphenyl (5CB) (structure shown in Figure 1(a)) on TiO_2(101) by preparing micrometer-thin films of 5CB on TiO_2(101) and characterizing their optical appearance using polarized light microscopy. We discovered that the orientations of 5CB on TiO_2(101) are dependent on ambient relative humidity (RH) levels. At low humidity (0-20% RH) or under dry conditions, 5CB exhibits a homeotropic (perpendicular) orientation on TiO_2(101) (Figure 1(b), (d)) whereas upon increasing RH, 5CB tilts away from the surface normal to ultimately assume a planar (parallel) orientation

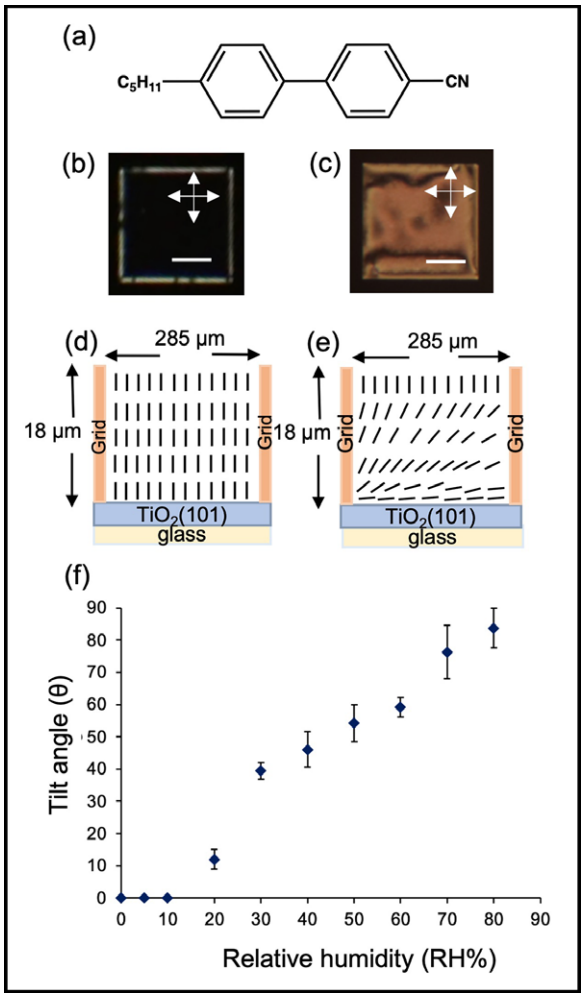

Figure 1: (a) Molecular structure of 4-cyano-4'-pentylbiphenyl (5CB). Optical micrographs (crossed polarizers) of 5CB hosted in copper grids on 3.27 ± 0.03 nm-thick films of TiO_2(101) under dry nitrogen conditions (b) and under 80% RH air (c). Schematic illustrations of director profiles of (d) homeotropic and (e) planar orientations of 5CB at TiO_2(101). (f) Plot of change in tilt angle of 5CB from surface normal on TiO_2(101) as a function of RH level. Scale bar: 100 µm.

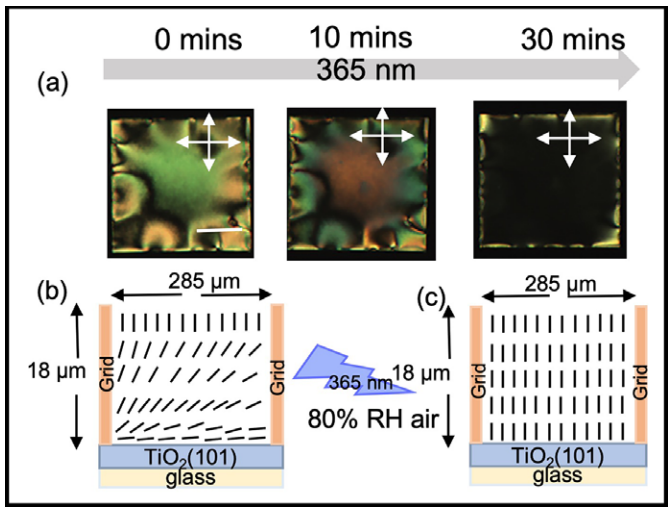

Figure 2: (a) Optical micrographs (crossed polarizers) of 5CB hosted in copper grids on 3.27 ± 0.03 nm-thick films of TiO_2(101) under 80% RH air upon illumination by a UV lamp of wavelength 365 nm and intensity 1.8 mW/cm² at time 0 mins, 10 mins, and 30 mins. Schematic illustrations of director profiles for (b) planar and (c) homeotropic orientations of 5CB on TiO_2(101).

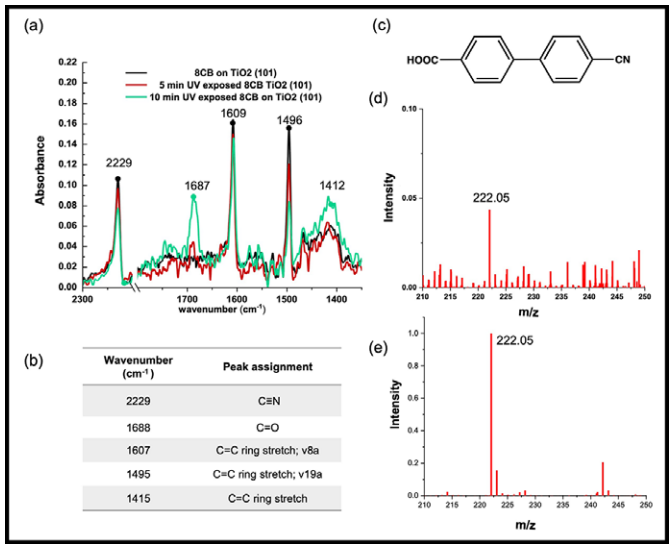

Figure 3: (a) PMIRRAS spectra of nanometer-thick layers of 8CB on TiO_2(101) (black), exposed to 365 nm UV illumination for 5 mins (red) and 10 mins (green). (b) Vibrational frequency (cm^{-1}) assignments for peaks in (a) ν represents stretching, and β represents in-plane bending. (c) Molecular structure of 4'-cyanobiphenyl-4-carboxylic acid (CBCA). Electrospray ionization-mass spectra plot of (d) 25 µM 5CB reacted under 365 nm UV illumination on TiO_2(101) (e) 5 µM CBCA in methanol collected in negative ionization mode.

at 80% RH (Figure 1(c), (e), (f)). Prior studies have reported that water can adsorb to metal oxides such as titania under ambient humidity conditions and that the surface coverage of water is dependent on the humidity level [2]. Ongoing experiments are testing the hypothesis that increasing water coverage on TiO_2(101) weakens the binding of 5CB in the perpendicular mode and triggers an orientational transition.

To study the influence of the photocatalytic activity of TiO_2(101) on the orientations of nematic 5CB, we illuminated micrometer-thick films of 5CB on TiO_2(101) at a wavelength of 365 nm under 80% RH. Upon UV illumination, the optical appearance of the nematic 5CB film changed from bright to dark, indicating an orientational transition from planar to homeotropic as shown in Figure 2(a), (b). In contrast, no change in optical appearance was observed when a micrometer-thick film of 5CB supported on a photo-inactive silica surface was illuminated with UV light. Additional support for our conclusion that the orientational transition of 5CB observed on TiO_2(101) was driven by photocatalytic activity was obtained by using PMIRRAS measurements of nanometer-thin films of 8CB (a homolog of 5CB) supported on TiO_2(101) on platinum-coated Si wafers. Platinum films were e-beam deposited on Si wafers. Upon UV illumination, we measured a new peak in the IR spectrum corresponding to a C=O group (1688 cm^{-1}), consistent with photo-oxidation of 8CB to a carbonyl-containing compound as indicated in Figure 3 (a), (b). Mass-spectrometry confirmed that photo-oxidation of 5CB on TiO_2(101) forms the acid-containing molecule 4'- cyanobiphenyl-4-carboxylic acid (CBCA) (structure shown in Figure 3(c)) as indicated in Figure 3(d), (e).

Prior studies have revealed that carboxylic acid-containing molecules bind strongly to titania in the perpendicular mode [1]. This prior result provides support for our conclusion that the photocatalytic activity of TiO_2(101) can generate a carboxylic acid-containing compound within a nematic film of 5CB and thus trigger homeotropic anchoring of the LC mixture. This result provides the first evidence that photocatalytic transformations on titania can be coupled to orientational transitions in LCs.

Current work in this project is focused on understanding how the ligand environment created by a LC can modify the catalytic activity of titania.

References:

[1] Nanqi Bao, Jake I. Gold, Jonathan K. Sheavly, James J. Schauer, Victor M. Zavala, Reid C. Van Lehn, Manos Mavrikakis, and Nicholas L. Abbott, Ordering Transitions of Liquid Crystals Triggered by Metal Oxide-catalyzed Reactions of Sulfur Oxide Species. J. Am. Chem. Soc. 2022, 144, 36, 16378-16388. https://pubs.acs.org/doi/full/10.1021/jacs.2c03424

[2] A. L. Goodman, E. T. Bernard, and V. H. Grassian, Spectroscopic Study of Nitric Acid and Water Adsorption on Oxide Particles: Enhanced Nitric Acid Uptake Kinetics in the Presence of Adsorbed Water. J. Phys. Chem. A 2001, 105, 6443-6457. https://pubs.acs.org/doi/abs/10.1021/jp003722l

Investigation of Dry Chemical Actuators using Palladium and Palladium-Gold Thin Films

CNF Project Number: 2736-18
Principal Investigator(s): Nicholas Lawrence Abbott[1]
User(s): Hanyu Alice Zhang[2]

Affiliation(s): 1. Smith School of Chemical and Biomolecular Engineering, Cornell University, Ithaca NY, USA; 2. School of Applied and Engineering Physics, Cornell University, Ithaca NY, USA

Primary Source(s) of Research Funding: Cornell Center for Materials Research with funding from the National Science Foundation Materials Research Science and Engineering Centers program (DMR-1719875)

Contact: nla34@cornell.edu, hz496@cornell.edu

Website(s): https://nlabbottcornell.weebly.com/

Primary CNF Tools Used: Heidelberg DWL2000 Mask Writer, ABM Contact Aligner, Oxford 81/82/100 Etchers, AJA Sputter Deposition Tool, Oxford PECVD, Plasma-Therm Takachi HDP-CVD, SC4500 Odd-Hour Evaporator, Plasma-Therm 770 Etcher (Left Side), OEM Endeavor Aluminum Nitride Sputtering System, Leica CPD300, DISCO Dicing Saw

Abstract:

This project is focused on the fabrication of chemical actuators from palladium or palladium-gold thin films and characterization of their actuation using hydrogen gas. Previously, we reported on the design of chemical actuators using surface reactions on platinum thin films [1]. In contrast to platinum, atomic hydrogen can diffuse into palladium and palladium-gold thin films, thus generating strains and stresses that are larger than those that can be realized using surface reactions of platinum. In this report, we describe our results with palladium actuators, as well as present some initial results with the palladium-gold bimetallic system.

Summary of Research:

We are exploring how palladium can be used in microscopic bimorph structures that function as chemically-driven hinges. The work is motivated by prior studies of the dissociation of hydrogen on the surface of palladium and diffusion of atomic hydrogen into the palladium lattice to trigger a phase transition [2].

The goal of this project is to harness the bulk absorption of atomic hydrogen into palladium and the subsequent phase transition to drive actuation on the microscale. By fabricating bilayers of palladium and titanium (equal in thickness), we have shown that it is possible to selectively strain one half of the device relative to the other half thus generating a bending of the bimorph. Preliminary results hint that the actuation dynamics are influenced by a first-order phase transition upon exposure to hydrogen gas.

In addition to palladium, we have also started fabricating actuators using a palladium-gold bimetallic system due to its ability to surpass the first order phase transition and undergo a second-order phase transition beyond a certain gold concentration in the alloy. We predict that the order of the phase transition will be reflected in the dynamics of the actuator response [3].

To accomplish this goal, we purchased palladium sputtering targets for CNF and are co-sputtering palladium and gold. Pure sputtered palladium grains were first characterized with a scanning electron microscope as seen in Figure 1, and the smallest possible grain size (obtained by sputtering at 3mTorr) was chosen to build actuators.

To fabricate these devices, a sacrificial layer of aluminum nitride is sputtered onto a fused silica wafer with the OEM Endeavor sputtering system and a layer of aluminum oxide is grown with the Oxford FlexAl on top of the aluminum nitride. Both layers are then patterned and etched in the PT770. After the aluminum nitride is etched, a layer of silicon dioxide is grown with plasma enhanced chemical vapor deposition (PECVD) or high density plasma chemical vapor deposition (HPD-CVD) techniques and patterned. Finally, the bimorph microactuator consisting of titanium and either palladium or palladium-gold is sputtered onto the chip and patterned via lift-off. After the devices are fully fabricated, the chip is soaked in MIF 726 overnight to etch away the aluminum nitride and aluminum oxide layers. It is then dried in the Leica critical point dryer. The chips are then moved to a custom-built exposure chamber for testing in different gaseous environments.

Conclusions and Future Steps:

We have fabricated hinges that show a repeatable actuation upon the application of hydrogen, as shown in Figure 2.

In addition, initial results with palladium-gold show that the alloy responds faster than the pure metal under hydrogen exposure, as shown in Figure 3.

In the future, we aim to characterize further the phase transitions that occurs when palladium is exposed to hydrogen and the influence of the phase transitions on actuation dynamics. Additionally, we will characterize a wider range of compositions of palladium-gold to develop an understanding of how changes in the order of the phase transitions impacts actuator performance.

References:

[1] Nanqi Bao, et al. Gas-phase microactuation using kinetically controlled surface states of ultra-thin catalytic sheets. PNAS, 120(19), 2023.

[2] Noah J. J. Johnson, et al. Facets and vertices regulate hydrogen uptake and release in palladium nanocrystals. Nature materials, 18(5), 2019.

[3] A. Maeland, and T.B Flanagan. X-ray and thermodynamic studies of the absorption of hydrogen by gold-palladium alloys. The Journal of Physical Chemistry, 69(10), 1965.

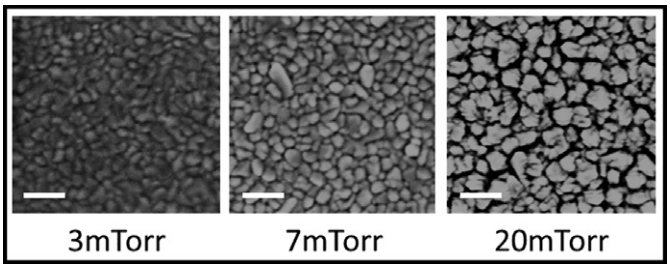

Figure 1: SEM images of grain structures of palladium films sputtered at 3, 7, and 20 mTorr. Scale bars are 100 nm.

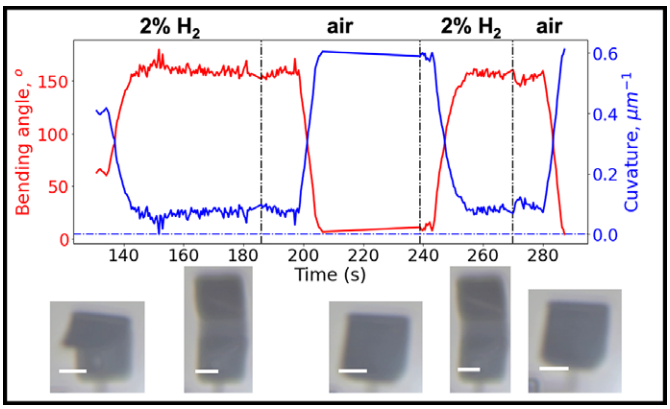

Figure 2: Single palladium hinge (bimorph) responding to hydrogen and air. Scale bars are 5 μm.

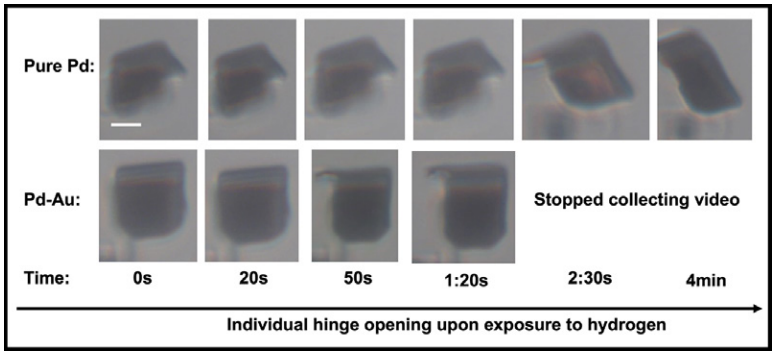

Figure 3: Comparison of responses of actuators fabricated from palladium versus a 24% palladium-gold alloy. Scale bar is 5 μm.

Auto-Fluorescent Polymer Brushes for Glucose Detection

CNF Project Number: 2751-18
Principal Investigator(s): Christopher Kemper Ober
User(s): Gozde Aktas Eken

Affiliation(s): Department of Material Science and Engineering, Cornell University
Primary Source(s) of Research Funding: National Science Foundation
Contact: cko3@cornell.edu, ga352@cornell.edu
Website(s): https://ober.mse.cornell.edu/
Primary CNF Tools Used: E-beam Resist Spinners, JEOL 9500, Oxford 81, Zeiss Ultra SEM, Optical Microscope

Abstract:

Polymer brushes possess considerable potential for designing smart surfaces suited for a diverse range of applications, such as controlled cell adhesion, self-cleaning surfaces, and smart actuators. Introduction of luminescent properties to polymer brushes has facilitated novel characterization techniques and opened up new applications in sensing and optoelectronics. In this study, we introduce a fluorescent glucose sensing platform that utilizes auto-fluorescent copolymer brushes functionalized with phenylboronic acid (PBA). These brushes exhibit conformational changes upon binding with glucose, leading to alteration in aggregation-induced emission (AIE). An integrated process involving electron-beam lithography, surface-initiated polymerization, and post-polymerization modification was employed to create nanopatterned polymer brushes.

Summary of Research:

Smart polymeric materials that exhibit prompt feedback when exposed to external stimuli hold great potential, particularly in biomedical field. These materials find applications in drug delivery, sensing, and diagnostics [1]. Consequently, the development of smart (bio) interfaces capable of sensing and responding to changes in the local environment presents intriguing possibilities for surface-based sensing concepts [2]. Polymer brushes are highly suitable for designing adaptive and responsive interfaces due to their diverse range of functional and structural options. Notably, these thin polymeric coatings offer rapid response times while minimally affecting the physical properties of the underlying cores or substrates [3]. By integrating these systems with sensing and reporting entities, such as colorimetric or luminescent components, efficient transduction mechanisms can be achieved [4].

Previously, we demonstrated that polymer brushes built from AIE polymers can generate optical signals from pH-induced conformational changes without conventional fluorophores [5]. In this work, we extend the application of AIE polymers to design glucose responsive surfaces by combining auto-fluorescent poly(styrene-*alt*-maleic anhydride) (pSMA) copolymer brushes with boronic acid receptors. This work builds on the nanopatterning process reported earlier [6]. Preparation of boronic acid containing pSMA brushes was achieved via an integrated fabrication process of area-selective deposition of initiator, surface-initiated polymerization, and post-polymerization modification (PPM). Polymer brushes were grown from both patterned and non-patterned substrates.

E-Beam Resist Mask Preparation. E-beam resist was patterned via JEOL 9500, which was later used as the mask for the vapor deposition of silane coupling agent. Prior to the deposition, the substrate was descummed via the Oxford 81 etcher to remove residual debris in the unmasked area.

Initiator Immobilization. The vapor deposition of the silane coupling agent was carried out in a closed chamber at 1 torr and 70°C for 18 hours. The substrate was cleaned with organic solvents to remove the resist mask and then transferred into a sealed flask with a solution of azo-initiator. The immersion time was 24 hours.

Brush Synthesis and Modification. Polymer brushes were synthesized via surface-initiated radical polymerization in acetonitrile at 85°C, using equimolar amounts of styrene and maleic anhydride. PPM with 3-aminophenylboronic acid with was conducted at room temperature and the degree of functionalization was adjusted through the reaction time.

Characterization and Results:

The patterned e-beam resist was characterized using Zeiss Ultra scanning electron microscopy. Patterned

brushes, thickness and morphology of non-patterned samples were analyzed by atomic force microscopy (AFM) after each step using the Asylum Research Cypher ES (Figure 1). The fluorescence characteristics and the response of the brushes to changes in pH and glucose levels were monitored using two-photon confocal microscopy (Zeiss LSM i880) (Figure 2). Fluorescence images were scanned in λ mode from 413 to 693 nm (λex = 800 nm) and the corresponding emission spectra were generated through 64 spectral sections. Figure 3 illustrates the changes in emission intensity observed when brushes were subjected to the buffer solutions with varying glucose concentrations. An increase in glucose concentration led to a substantial change in fluorescence intensity, wherein the increase in brush height from 136 to 460 nm corresponded to 83% decrease in fluorescence intensity. The steep decline in fluorescence intensity is attributed to the hydration and highly extended conformation of the polymer chains. In this state, the intra- and interchain interactions are constrained, limiting cluster formation, and subsequently affecting the fluorescence properties.

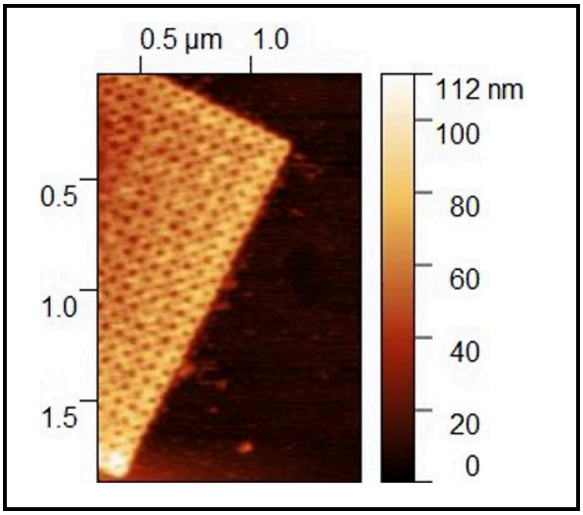

Figure 1: AFM height image of patterned pSMA brushes.

Conclusions and Future Steps:

Glucose responsive luminescent surfaces were prepared through an integrated process involving electron-beam lithography, surface-initiated polymerization, and post-polymerization modification. Utilizing auto-fluorescent polymer brushes, we have successfully demonstrated their ability to translate conformational transitions, triggered by binding events, into fluorescent readouts. Our primary objective is to optimize both sensitivity and pH parameters, thereby obtaining polymer brushes capable of operating within the physiologically relevant range.

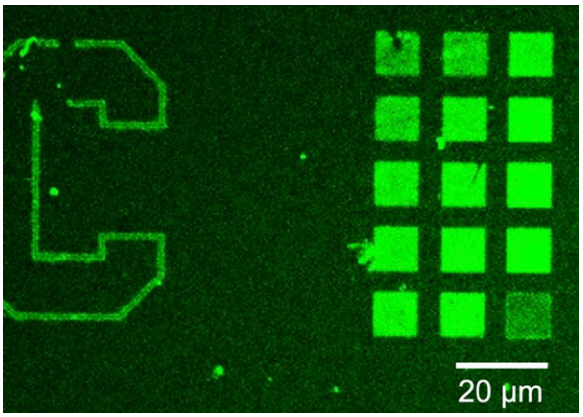

Figure 2: Confocal laser scanning microscopy images of the patterned brushes in collapsed state (pH 3).

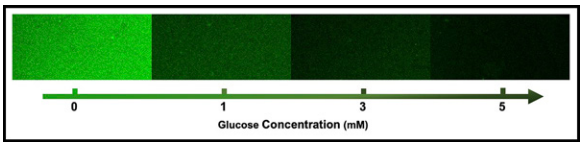

Figure 3: Confocal laser scanning microscopy images of brushes captured in solutions with varying glucose concentrations (pH 9).

References:

[1] Wei, M.; Gao, Y.; Li, X.; Serpe, M. J., Stimuli-responsive polymers and their applications. Polym Chem-Uk 2017, 8 (1), 127-143.

[2] Chen, W.-L.; Cordero, R.; Tran, H.; Ober, C. K., 50th Anniversary Perspective: Polymer Brushes: Novel Surfaces for Future Materials. Macromolecules 2017, 50 (11), 4089-4113.

[3] Li, D.; Xu, L.; Wang, J.; Gautrot, J. E., Responsive Polymer Brush Design and Emerging Applications for Nanotheranostics. Advanced Healthcare Materials 2021, 10 (5), 2000953.

[4] Poisson, J.; Hudson, Z. M., Luminescent Surface-Tethered Polymer Brush Materials. Chemistry - A European Journal 2022, 28 (32), e202200552.

[5] Aktas Eken, G.; Huang, Y.; Guo, Y.; Ober, C., Visualization of the pH Response through Autofluorescent Poly(styrene-alt-N-maleimide) Polyelectrolyte Brushes. ACS Applied Polymer Materials 2023, 5 (2), 1613-1623.

[6] Huang, Y.; Tran, H.; Ober, C. K., High-Resolution Nanopatterning of Free-Standing, Self-Supported Helical Polypeptide Rod Brushes via Electron Beam Lithography. ACS Macro Letters 2021, 10 (6), 755-759.

Fluorination Effect on Anti-Penetration Performance of Polystyrene-*Block*-Poly(vinylmethylsiloxane)

CNF Project Number: 2751-18
Principal Investigator(s): Christopher Kemper Ober
User(s): Zhenglin Zhang

Affiliation(s): Department of Material Science and Engineering, Cornell University
Primary Source(s) of Research Funding: Defense Threat Reduction Agency
Contact: cko3@cornell.edu, zz288@cornell.edu
Website(s): https://ober.mse.cornell.edu/
Primary CNF Tools Used: YES LP-III vacuum oven, Photolithography Spinners, DISCO Dicing Saw, Jelight 144AX UVO-Cleaner, Veeco Icon AFM, Woollam RC 2 Ellipsometer

Abstract:

A series of fluorinated polystyrene-*block*-poly(vinylmethylsiloxane) (PS-*b*-PVMS) polymers were synthesized by anionic polymerizations and thiol-ene reactions. The synthesized fluorinated PS-*b*-PVMS polymers were further characterized by nuclear magnetic resonance (NMR), differential scanning calorimetry (DSC), and small-angle X-ray scattering (SAXS). The introduction of fluorine can enhance intra and intermolecular interactions, which limit the flexibility of polymer chains and improve polymers' anti-penetration performance.

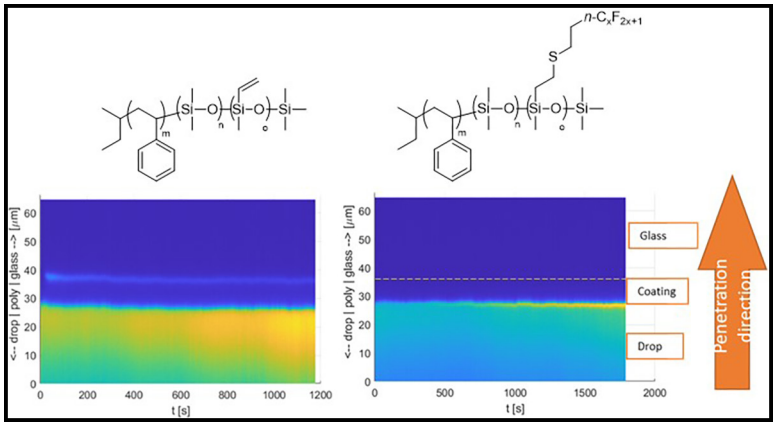

*Figure 1: Anti-penetration performance of nonfluorinated PS-*b*-PVMS (left) and fluorinated PS- PS-*b*-PVMS (right).*

Summary of Research:

Polydimethylsiloxane (PDMS) based surface coating materials are widely explored in antifouling and fouling release materials for marine vessels, as PDMS has low surface energy and elastic modulus, and is chemically stable and eco-friendly. Current research is highly focused on modifying PDMS with different functional groups to tune surface hydrophobicity, hydrophilicity, and amphiphilicity to adjust polymers' antifouling and fouling release performance on the surface [1].

Although fouler or contamination on the surface can be cleaned by water jet, the contamination just under the surface would be a problem that may damage the exposed surface performance and durability, as PDMS is a flexible backbone with nano-sized intermolecular spaces (free volume) and molecular level penetration into PDMS films can occur [2]. The introduction of fluorine is supposed to increase inter/intramolecular interactions [3], and is able to limit polymers' flexibility and movability of the free volume, which should restrict penetration theoretically.

In this research, a series of fluorinated alkyl chains with different lengths are attached to PVMS by thiol-ene click reaction to explore the fluorination effect on the penetration of PDMS.

NMR spectra show that the chemical shifts of fluorine shift to upfield and the chemical shifts of silicon shift to downfield after the fluorinated alkyl chains were grafted to PS-*b*-PVMS backbone, which indicates interactions between fluorine atoms and silicon atoms, as electron acceptors and donors, respectively. DSC results show that the glass transition temperature (T_g) for the PVMS block increases with the length of the fluorinated alkyl chain. SAXS results show that more ordered patterns of hexagonal columns can be observed after the fluorination. Fluorinated PS-*b*-PVMS polymers were dissolved, and spin-coated on glass slides, which were cleaned, and processed by YES LP-III vacuum oven. The test of contact angles of the films shows that fluorination increased the contract angle (water) from 92° of the nonfluorinated precursor to 111°. Penetration

tests on films of fluorinated PS-*b*-PVMS were recorded by a laser confocal microscope with aqueous solutions of Rhodamine B as a dye, which showed that fluorination can effectively improve the anti-penetration performance of PS-*b*-PVMS (see Figure 1).

Conclusions:

Our current results support that the introduction of fluorine in PS-*b*-PDMS enhances intra/intermolecular interactions, which can restrict the movements of free volumes in PVMS and improve its anti-penetration performance.

References:

[1] Leonardi, A. K.; Ober, C. K. Annu. Rev. Chem. Biomol. Eng. 2019, 10, 241.264.
[2] Saito, M.; Nishimura, T.; Sakiyama, K.; Inagaki, S. AIP Adv. 2012, 2, 042118.
[3] Kim, S.; Saxena, A.; Kwak, G.; Fujiki, M.; Kawakami, Y. Chem. Commun. 2004, 538.539.

Design, Synthesis, and Multiscale Structural Investigation of Polymer-Grafted Nanoparticles (PGNs) for Application in Pyrolysis and Self-Assembly Processes

CNF Project Number: 2955-21
Principal Investigator(s): Christopher Kemper Ober
User(s): Chenyun Yuan

Affiliation(s): Department of Materials Science and Engineering, Cornell University
Primary Source(s) of Research Funding: Air Force Office of Scientific Research (AFOSR)
Contact: cko3@cornell.edu, cy479@cornell.edu
Primary CNF Tools Used: Malvern Nano ZS Zetasizer, Dicing Saw, Zeiss Ultra SEM

Abstract:

The research team has made extensive strides in the study of polymer-grafted nanoparticles (PGNs) over the past year, utilizing the top-tier resources and support from the Cornell NanoScale Facility (CNF) as well as other facilities on campus. Two critical aspects of PGNs — self-assembly and pyrolysis to make polymer-derived ceramics (PDCs) — were investigated, providing key insights into how grafting density influences self-assembly and how varying pyrolysis conditions can tailor PGN-derived inorganic nanostructured materials. Our findings have the potential to transform various applications, including optical devices, magnetic devices, catalysis, energy storage, and the broader field of materials science.

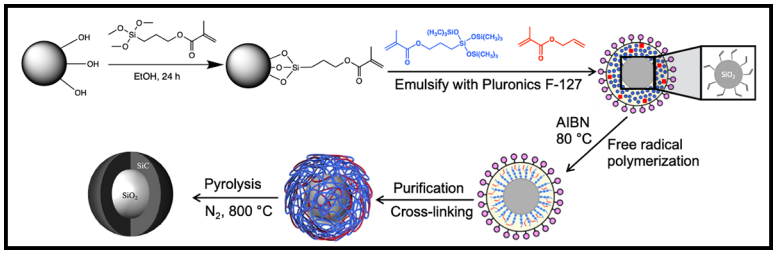

Figure 1: "Grafting-through" approach in mini-emulsion to covalently attach preceramic polymer chains to the silica surface, crosslinking of the preceramic polymer brushes via the allyl groups, and pyrolyze the PGNs to get SiO_2-SiC core-shell nanoparticles.

Summary of Research:

Synthesis, Functionalization and Self-Assembly of Polymer-Grafted Nanoparticles (PGNs). Our research began with the robust synthesis of PGNs with varied grafting densities [1]. A modified initiator, APTES-BIBB, was employed to functionalize silica nanoparticles (Ludox TM-40), which were then grafted with different polymers containing either hydrogen bonding donors or acceptors to create the PGNs. This process was optimized through iterative testing to yield PGNs with a range of grafting densities, thus enabling us to explore their impacts on self-assembly.

Utilizing transmission electron microscopy (TEM) and scanning transmission electron microscopy (STEM), we analyzed the PGNs' self-assembly behaviors. Our research established a direct link between the grafting density and self-assembly behavior of PGNs. This has opened a gateway to the predictable design of PGNs, enabling a more refined approach to their utilization in fields such as nanoparticle-based optical devices.

Pyrolysis of PGNs. In our other piece of work, we delved into the pyrolysis of preceramic polymer-grafted nanoparticles and its implications (Figure 1). Our objective was to understand how synthesis and pyrolysis conditions, impact the resultant structure, morphology, and composition of the preceramic PGN-derived nanostructured materials. CNF's state-of-the-art facilities enabled in-depth analysis and characterization of the outcomes.

Our findings, derived from thermogravimetric analysis, Fourier-transform infrared spectroscopy, scanning electron microscope (SEM) and high-resolution TEM, indicated that PGNs' pyrolysis led to the creation of SiO_2-SiC core-shell nanomaterials.

Future Plans:

Our groundbreaking progress over the past year paves the way for ambitious future research. We are particularly interested in investigating the influence of polymer chemistry on both the self-assembly behavior and pyrolysis outcomes of PGNs.

CNF's state-of-the-art facilities will enable us to take a deep dive into the structures derived from PGNs assembly and pyrolysis. Additionally, we're planning to focus our efforts on uncovering new applications of PGNs in areas such as optical and magnetic devices, as well as polymer-derived ceramic nanostructures.

References:

[1] Yuan, C., Käfer, F., and Ober, C. K. (2021). Polymer-Grafted Nanoparticles (PGNs) with Adjustable Graft-Density and Interparticle Hydrogen Bonding Interaction. Macromolecular Rapid Communications, 43(12), 2100629. https://doi.org/10.1002/marc.202100629

Imaging the TaS_2 Charge Density Wave Transition in Real-Space with Electron Microscopy

CNF Project Number: 2967-21
Principal Investigator(s): Jeeyoung Judy Cha
User(s): James L. Hart, Saif Siddique

Affiliation(s): Department of Materials Science and Engineering, Cornell University

Primary Source(s) of Research Funding: Gordon and Betty Moore Foundation, EPiQS Synthesis Investigator Award

Contact: jc476@cornell.edu, jlh478@cornell.edu, ms2895@cornell.edu

Website(s): cha.mse.cornell.edu

Primary CNF Tools Used: CHA evaporator, Zeiss Supra scanning electron microscope, Nabity system for Supra

Abstract:

We studied the charge density wave (CDW) and insulator-to-metal transition in the two-dimensional (2D) material tantalum(IV) sulfide (TaS_2). We highlight two key findings: first, basal dislocations strongly influence the transition, acting as both nucleation and pinning sites, and second, the bias-induced CDW switching is driven by Joule heating. Both findings are relevant to the design of next-generation electronics based on TaS_2.

Summary of Research:

Tantalum(IV) sulfide (TaS_2) is a prototypical 2D quantum material that hosts several CDW phases. At low temperature, the TaS_2 ground state is the commensurate (C) CDW phase, which is insulating [1]. Above 200 K, TaS_2 transitions to the nearly commensurate (NC) CDW phase, which is defined by a network of phase slips in the CDW order parameter, i.e. discommensurations [1]. The NC phase is metallic. Hence, the C to NC phase transition is accompanied by a large change in electrical resistance, and is promising for device applications. Moreover, the transition can be triggered with an applied electric field, with potential application for 2-terminal devices [2]. However, implementing nanoscale TaS_2 devices requires a detailed understanding of how the CDW phase transition occurs on nanoscale dimensions, which is currently lacking. Direct real-space imaging of the CDW transition is needed.

We developed a four-dimensional scanning transmission electron microscopy (4D-STEM) approach which allows the visualization of the CDW transition. In 4D-STEM, an electron beam is focused to a nanoscale probe, rastered across the sample surface, and a full diffraction pattern is captured at each spatial coordinate [3]. Our method provides significant advantages over prior attempts to image the CDW transition [4,5].

Figure 1 shows the resistance versus temperature for a TaS_2 device measured within the electron microscope. A clear insulator-to-metal transition is observed around ~ 200 K. For each of the datapoints in Figure 1, a full 4D-STEM dataset was collected and used to map out the CDW phase; select temperature scans are shown in Figure 2. For the C to NC CDW transition, the appropriate order parameter is the coherent domain size DNC. At 120 K in the insulating phase, the measured domain size DNC is > 100 nm, which is consistent with the C CDW phase. At 250 K, in the metallic phase, the DNC is < 10 nm, consistent with the NC CDW phase. Interestingly, at the insulator-to-metal transition (195 K), we find that the DNC map displays sharp lines and domains. Hence, the CDW transition is highly inhomogeneous.

To understand the nature of the sharp lines seen in the CDW map, we performed additional electron microscopy experiments. We find that all of the lines seen in the CDW map correspond to basal dislocations, i.e. both the burgers vector and the line vector lie in the ab-plane. A plan-view STEM image of one such dislocation is shown in Figure 3. We find that dislocations both nucleate and pin the CDW transition in TaS_2, thus, device engineering efforts should consider the role of dislocations.

Next, we investigate electric field-induced switching of TaS_2. Nearly a decade ago, several research groups showed that starting in the insulating C phase, application of a strong electric field can trigger a rapid transition to a metallic phase. The switching is fast, reversible, and energy-efficient, making this switching process appealing for 2-terminal devices [2]. However, the actual switching mechanism is still under debate.

To resolve this question, we operate a 2-terminal device within the electron microscope. In doing so, we can image the CDW during device operation, offering unprecedented insight to the switching process. Here, we

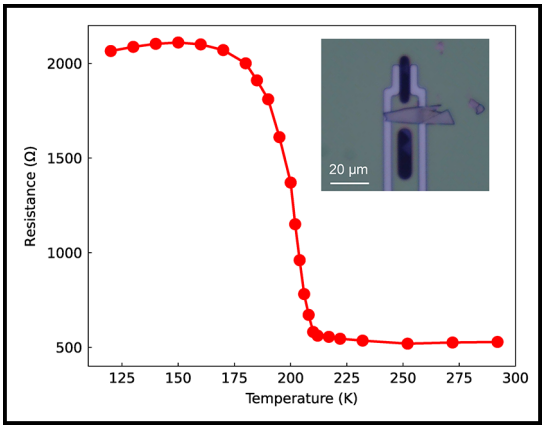

Figure 1: In situ *STEM resistance versus temperature for a TaS_2 device upon heating. Inset shows optical image of device.*

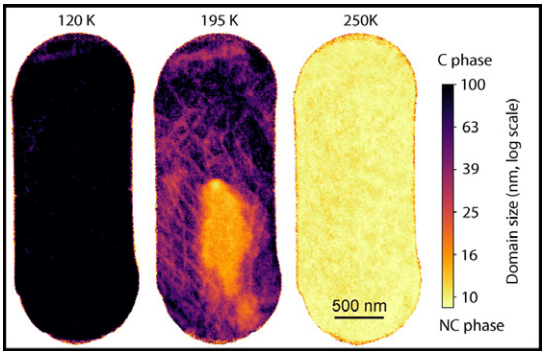

Figure 2: Select 4D-STEM maps of the CDW order parameter, captured simultaneous with the resistance data in Figure 1.

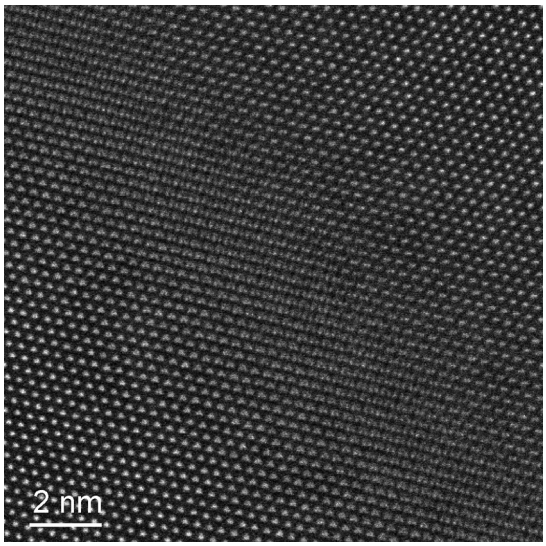

Figure 3: Atomic-resolution STEM image of a basal dislocation, imaged in the ab-plane. The dislocation line runs from the top-left to the bottom-right of the image.

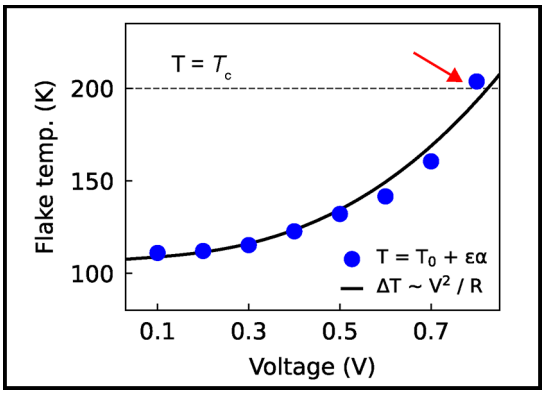

Figure 4: The measured flake temperature versus applied voltage. Resistive switching occurs when the temperature surpasses the CDW transition temperature T_c (red arrow).

highlight one key finding from these experiments, which proves that switching is driven by Joule heating. First, we apply a DC voltage to our flake, while simultaneously measuring the flake resistance and collecting diffraction data. From the diffraction data, we extract the flake strain, and using the thermal coefficient of expansion, we can then determine the flake temperature. Figure 4 shows the measured flake temperature as a function of applied voltage. For voltages from 0.1 to 0.7 V, the flake is highly resistive (> 2 kΩ). Then, at 0.8 V, the resistance drops to 400 Ω. At the resistive transition, we see that the flake temperature surpasses 200 K, which is the thermal transition point for the TaS_2 C to NC phase transition. Hence, our data shows that at the critical voltage which causes resistive switching, the Joule heating is sufficient to raise the flake temperature above the CDW transition temperature.

Conclusions:

We used in operando 4D-STEM to study the CDW behavior of the 2D quantum material TaS_2. We showed that dislocations both nucleate and pin the CDW transition, and that the bias-induced transition is driven by Joule heating. These findings are important for the optimization of next-generation TaS_2 devices.

References:

[1] Ishiguro, T., and Sato, H. Phys. Rev. B 44, 2046-2060 (1991).
[2] Vaskivskyi, I., et al. Nat. Commun. 7, 11442 (2016).
[3] Ophus, C. Microsc. Microanal. 25, 563-582 (2019).
[4] Frenzel, A. J., et al. Phys. Rev. B 97, 035111 (2018).
[5] Walker, S. M. et al. Nano Lett. 22, 1929-1936 (2022).

Photolithographic Patterning of Alignment Fiducials for X-Ray Nano-Diffraction

CNF Project Number: 2989-21
Principal Investigator(s): Andrej Singer
User(s): Aileen Luo, Saptarshi Das

Affiliation(s): Materials Science and Engineering, Cornell University

Primary Source(s) of Research Funding: National Science Foundation, Department of Energy

Contact: asinger@cornell.edu, al2493@cornell.edu, sd724@cornell.edu
Website(s): https://singer.mse.cornell.edu/

Primary CNF Tools Used: Heidelberg Mask Writer - DWL2000, Hamatech Mask Chrome Etch, ABM Contact Aligner

Abstract:

Alkaline fuel cells and electrolyzer cells are promising alternative forms of energy conversion and storage devices due to their potential for eliminating the need for precious-metal catalysts. Epitaxially grown transition metal oxide thin films have demonstrated promising activity for the oxygen reduction reaction [1], the rate-limiting step for catalysis in alkaline fuel cells. To better understand localized structural and electronic changes in the catalyst under operating conditions, we aim to study them using x-ray nano-diffraction and x-ray absorption near-edge structure at the hard x-ray nanoprobe beamline at the National Synchrotron Light Source II.

Summary of Research:

Focusing of x-rays to a 25 nm spot on a sample requires alignment fiducial markers with sharp edges of less than half a micron in width. Using the computer-aided design software L-Edit and the Heidelberg Mask Writer - DWL2000, we designed and wrote a 5-inch photomask with multiple configurations of the pattern shown in Figure 1. Using S1800 series positive tone photoresist and the ABM Contact Aligner, we transferred the pattern onto samples of sizes 5 mm × 5 mm and 10 mm × 10 mm. DC magnetron sputtering (Cornell Center for Materials Research) was used to deposit 10 nm of titanium and 50 nm of copper metal onto the samples. Sonication in acetone was used to lift off the excess metal and complete the process.

Conclusions and Future Steps:

The fabrication of alignment features was completed successfully and tested at the hard x-ray nanoprobe beamline. For future measurements, we will design and make proof-of-concept devices at the Cornell NanoScale Facility (CNF) for a three-electrode electrochemical cell compatible with the limitations of the beamline. Prior work that used CNF tools was published and presented as detailed below.

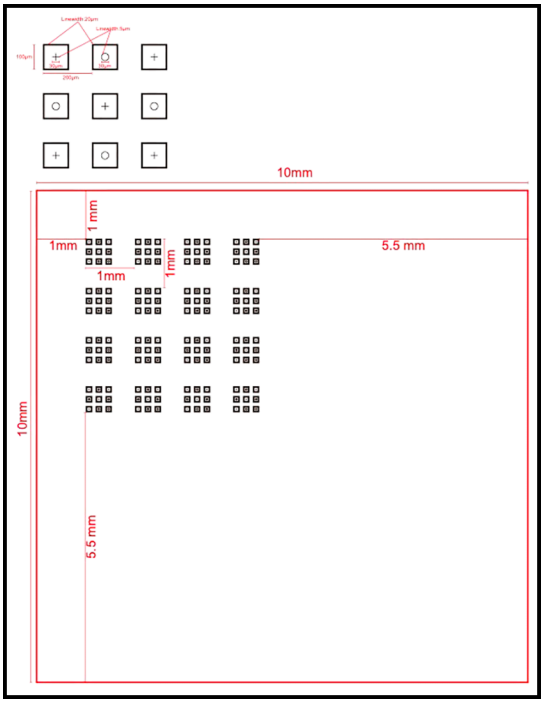

Figure 1: Schematic credit to Dr. Ludi Miao. Arrays of circles and crosses contained in larger squares.

Publication:
https://doi.org/10.1063/5.0125268

Conference presentation, 2022 Materials Research Society (MRS) Fall Meeting: Title: "X-ray Nano-Imaging of Defects in Thin-Film Catalysts via Cluster Analysis."

References:

[1] Y. Yang, et al. J. Am. Chem. Soc. 2019, 141, 1463-1466.

Quasi-2D Materials for Ultra-Low Resistance Electrical Interconnects

CNF Project Number: 3007-22
Principal Investigator(s): Hair P. Nair
User(s): Bilal Azhar, Cameron Gorsak

Affiliation(s): Department of Materials Science and Engineering, Cornell University

Primary Source(s) of Research Funding: Semiconductor Research Corporation (SRC)

Contact: hn277@cornell.edu, ba428@cornell.edu, cag284@cornell.edu

Primary CNF Tools Used: General Materials Anneal Furnace, Veeco Savannah ALD, Woollam RC2 Spectroscopic Ellipsometer, AFM -Veeco Icon

Abstract:

The dramatic increase in the resistivity of interconnect lines with decreasing dimensions presents a significant bottleneck for further downscaling of integrated circuits [1]. This is because current interconnects use 3-dimensional metals that experience increased interface electron scattering as the interconnect dimensions approach their electron mean free path. A possible solution is to use metals with much lower electron mean free paths such as: W, Mo, and Ru. Metallic delafossite oxides are an alternative solution because of their inherent advantages over traditional metals such as: ultra-low room temperature resistivity, potential mitigation of interface/surface scattering due to their 2D Fermi surface, potentially decreased likelihood of electromigration, and potentially better compatibility with low-κ oxide dielectrics. Metallic delafossite can prove to be a disruptive new material for ultra-scaled electrical interconnects.

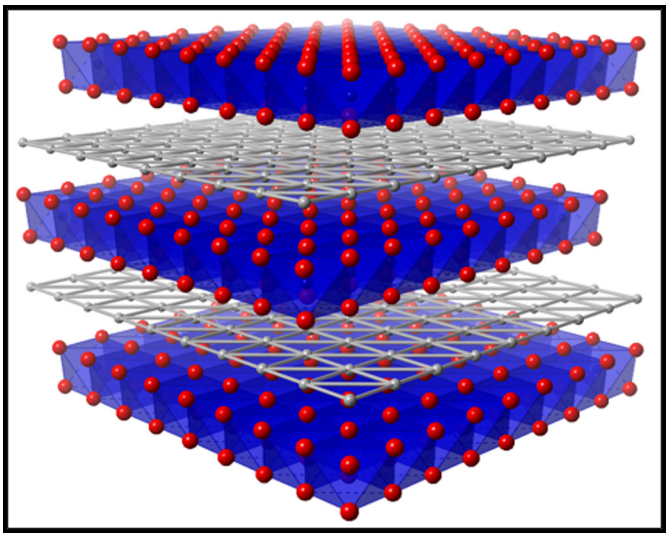

Figure 1: Crystal structure of delafossite PtCoO2 illustrating the sheets of Pt responsible for the anisotropic conductivity.

Introduction:

Delafossites are layered oxides with the formula ABO_2 where A is a metal cation that forms 2D sheets separated by the BO_2 transition-metal oxide octahedra, Figure 1. In this study we focus on metallic delafossites $PtCoO_2$ and $PdCoO_2$ because of their ultra-low room temperature resistivity of 2.1 $\mu\Omega$.cm and 2.6 $\mu\Omega$.cm, respectively, which is comparable to the current semiconductor industry standard interconnect metal, Cu, Figure 2 [2]. The metallic delafossite structure has an anisotropic nature with resistivity along the c-axis a factor of 1000 higher than resistivity within the Pt/Pd sheet. Due to the layered crystal structure, the Fermi surface of the metallic delafossites is cylindrical as for a 2D metal. This quasi-2D crystal structure can potentially mitigate interface and surface scattering since the electron Fermi velocity does not have components perpendicular to the Pd/Pt sheets. This can potentially overcome the resistivity penalty encountered by conventional 3D metals in ultrathin films (< 20 nm). Additionally, the unique Fermi surface topology allows for an electron-phonon coupling constant that is a factor of 3 lower than copper [3].

Our focus has been to demonstrate metallic delafossites as a disruptive new material for ultra-scaled electrical interconnects, for which we have two goals. The first goal is to realize their unique electrical properties and the second goal is to demonstrate the growth of highly quality delafossite thin films via atomic layer deposition (ALD) a back-end-of-the-line (BEOL) compatible synthesis technique.

Summary of Research:

To realize the unique electrical properties of delafossite thin films we have been investigating the structural and electrical properties of $PdCoO_2$ thin films grown via molecular beam epitaxy (MBE). MBE has been shown to achieve highly crystalline films which is critical for electrical property characterization due to the structure-property relation [4,5]. We used high-resolution X-Ray diffraction (HRXRD) to confirm that the films are phase-pure. We measured the resistivity of the films using a van der Pauw geometry and modelled the resistivity scaling with film thickness using Fuchs-Sondheimer (FS) and Mayadas-Shatzkes (MS) model. The upshot being that a 50 nm thick $PdCoO_2$ film has a resistivity of 5 $\mu\Omega$.cm. It should be noted that while our XRD phi scans did reveal in-plane twinning our resistivity fitting did not find twin boundaries to be a significant contributor to resistivity.

We have also combined thermodynamic modelling with *ex-situ* annealing to characterize the amorphous to crystalline transition in molecular beam epitaxy (MBE) grown $PdCoO_2$ thin films. This characterization was very insightful in finding the relevant temperature range and secondar phases. This characterization allows us to transition from MBE to BEOL-compatible ALD which typically deposits amorphous films. This complements our ALD growth $PtCoO_2$ thin films for which we are currently calibrating the Co_xO_y and PtO binary cycles to later combine into the $PtCoO_2$ supercycle.

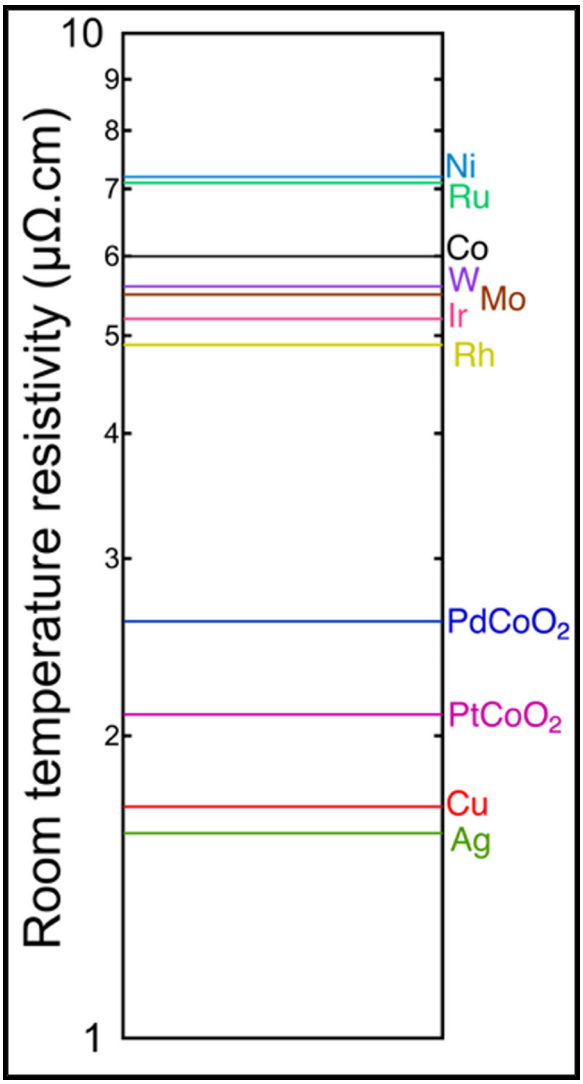

Figure 2: Comparison of room temperature resistivity of $PdCoO_2$ and $PtCoO_2$ to conventional interconnect metals.

Conclusions and Future Steps:

We have two main future goals: (1) The first goal is to characterize electrical properties in decreasing dimensions, similar to interconnect dimensions, for which we are planning to fabricate nanowires of MBE-grown $PdCoO_2$ thin films, via photolithography and e-beam lithography, and (2) the second goal is to demonstrate the growth of highly crystalline $PtCoO_2$ films via ALD and post-deposition annealing.

References:

[1] D. Gall, J. Appl. Phys. 127, 050901 (2020).

[2] V. Sunko, P.H. McGuinness, C.S. Chang, E. Zhakina, S. Khim, C.E. Dreyer, M. Konczykowski, M. König, D.A. Muller, and A.P. Mackenzie, Phys. Rev. X 10, 021018 (2020).

[3] C.W. Hicks, A.S. Gibbs, A.P. Mackenzie, H. Takatsu, Y. Maeno, and E.A. Yelland, Phys. Rev. Lett. 109, 116401 (2012).

[4] J. Sun, M.R. Barone, C.S. Chang, M.E. Holtz, H. Paik, J. Schubert, D.A. Muller, and D.G. Schlom, APL Mater. 7, 121112 (2019).

[5] Q. Song, J. Sun, C.T. Parzyck, L. Miao, Q. Xu, F.V.E. Hensling, M.R. Barone, C. Hu, J. Kim, B.D. Faeth, H. Paik, P.D.C. King, K.M. Shen, and D.G. Schlom, APL Mater. 10, 091113 (2022).

Lithography for Topological Nanowires

CNF Project Number: 3032-22
Principal Investigator(s): Jeeyoung Judy Cha
User(s): Yeryun Cheon, Khoan Duong, Han Wang, Mehrdad Kiani, Quynh Sam, Gangtae Jin

Affiliation(s): Department of Materials Science and Engineering, Cornell University

Primary Source(s) of Research Funding: The Gordon and Betty Moore Foundation's EPiQS Initiative, Grant GBMF9062; Semiconductor Research Corporations (SRC) JUMP 2.0 SUPREME; The National Science Foundation, Division of Materials Research #2240956

Contact: jc476@cornell.edu, yc2458@cornell.edu, nd399@cornell.edu, hw578@cornell.edu, mtk73@cornell.edu, qps2@cornell.edu, gj98@cornell.edu

Website(s): cha.mse.cornell.edu

Primary CNF Tools Used: Nabity System for Supra SEM, Zeiss Ultra SEM, SC4500 Odd-Hour Evaporator

Abstract:

Topological materials in nanowire forms can transform future computing technologies by enabling fault-tolerant quantum computing using topological superconductor nanowires or energy-efficient interconnects using topological semimetal nanowires. The major challenge remains synthesis of these materials in nanowires. We employ the recently developed thermomechanical nanomolding [1] to fabricate nanowires of topological materials. In this project, we fabricate nanodevices using the molded nanowires to measure their transport properties.

Summary of Research:

We have successfully molded various topological semimetals [2] and layered materials into nanowires using thermomechanical nanomolding. We have further extended the nanomolding method to two-dimensions (2D) and demonstrated wafer-scale fabrication of 2D nanostructures [3]. We are fabricated nanodevices on these molded nanostructures to test if some of the topological semimetals may be promising interconnect materials that can replace the state-of-the-art copper interconnects and to measure topological protected surfaces states in transport in these molded nanowires.

Conclusions and Future Steps:

Thermomechanical nanomolding is a promising synthesis technique that can rapidly and with scale fabricate nanowires of topological materials. We have produced several classes of topological materials into nanowires using this method. Future steps include fabrication of nanodevices using standard e-beam lithography on these molded nanowires to measure their transport properties.

References:

[1] M. T. Kiani, J. J. Cha, Nanomolding of topological nanowires, APL Mater. 10, 080904 (2022).

[2] M. T. Kiani, Q. P. Sam, G. Jin, B. Pamuk, H. J. Han, J. L. Hart, J. R. Stauff, J. J. Cha, Nanomolding of metastable Mo_4P_3, Matter doi:10.1016/j.matt.2023.03.023 (2023).

[3] M. T. Kiani, Q. P. Sam, Y. S. Jung, H. J. Han, J. J. Cha, Wafer-scale fabrication of 2D nanostructures via thermomechanical nanomolding, arXiv: 2306.10167 (2023).

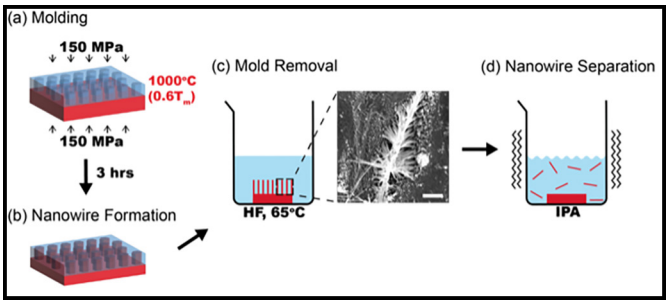

Figure 1: Schematic of thermomechanical molding. (a) Bulk feedstock of topological material (red) is pressed onto the nanostructured mold, in this case anodized aluminum oxide (blue). (b) After molding, nanowires form. (c) The molded nanowires are extracted from the mold by etching the mold. (d) the molded nanowires are separated from the bulk feedstock by sonication.

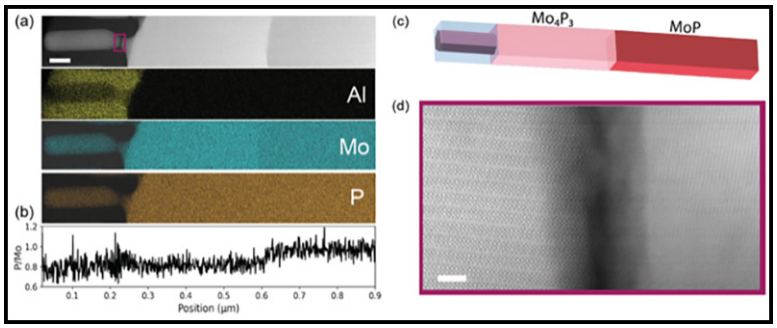

Figure 2: Thermomechanically molded Mo_4P_3 nanowires. (a) Cross-section scanning transmission electron microscopy (STEM) and chemical mapping images of the Mo_4P_3 nanowire molded into the aluminum oxide mold, with the bulk feedstock also intact. (b) The P/Mo composition changes at the mold entrance as phosphorus vapor leaves the apparatus during molding. (c) Schematic of the molding process for Mo_4P_3 nanowire. (d) Atomic-resolution high-angle annular dark field STEM image of the molded nanowire.

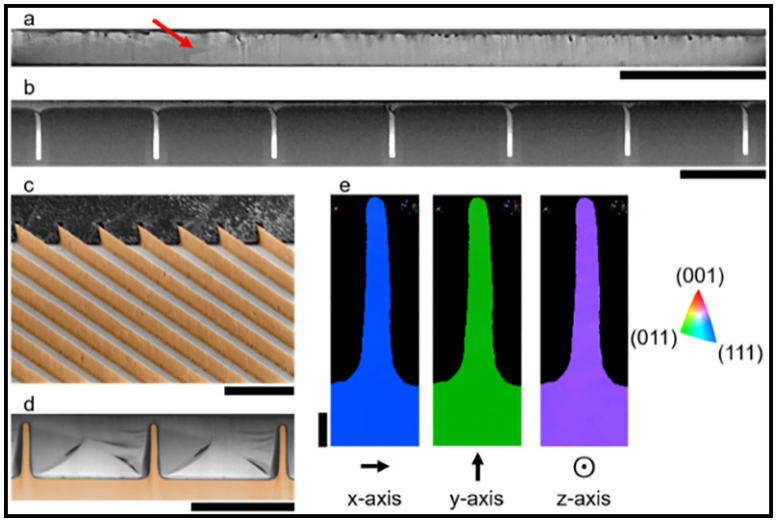

Figure 3: Nanomolded 2D Cu-filled trenches and free-standing 2D Cu fins. (a, b) Scanning electron microscopy (SEM) images of the Cu-filled trenches at the wafer scale, using Si mold. (c, d) Free-standing 2D Cu fins, after etching away the Si mold. (e) Single-crystalline Cu-filled trench at the nanoscale.

Lithography for 2D Materials

CNF Project Number: 3035-22
Principal Investigator(s): Jeeyoung Judy Cha
User(s): Shiyu Xu, Natalie Williams

Affiliation(s): Department of Materials Science and Engineering, Cornell University

Primary Source(s) of Research Funding: The National Science Foundation, CBET-CAREER #2240944

Contact: jc476@cornell.edu, sx269@cornell.edu, nlw49@cornell.edu
Website(s): cha.mse.cornell.edu

Primary CNF Tools Used: Heidelberg Mask Writer - DWL2000, SC4500 Odd-Hour & Even-Hour Evaporator

Abstract:

Intercalation is a reversible insertion of ions, atoms, and molecules into empty spaces in crystalline materials (Figure 1). For layered materials, intercalation can tune the materials properties greatly and even induce new phases. We electrochemically intercalate lithium ions into layered transition metal dichalcogenides and rare-earth tri-tellurides to induce new phases, change materials properties, and study nanoscale effects on the thermodynamics of lithium (Li) intercalation. For this, we fabricate electrochemical cells on individual nanodevices using exfoliated flakes, which allows us to measure the changes in the structure and electrical properties of the host material as we controllably intercalate lithium.

Summary of Research:

We discovered that semimetallic molybdenum ditelluride ($MoTe_2$) becomes semiconducting when enough lithium gets intercalated. The intercalation-induced semiconducting phase takes on a new crystal structure not found in existing polymorphs of $MoTe_2$, observed by Raman spectroscopy (Figure 2). We constructed electrochemical cells that are compatible with *in situ*, single-crystal X-ray diffraction experiments so that we can identify the new crystal structure. X-ray data were successfully obtained, and we are currently analyzing them. Further, we observed that the intercalation-induced phase change in these layered materials can be affected greatly by the interactions with the substrate; this is clearly observed by the intercalation-induced phase change getting delayed for thinner samples, where the substrate effects will be more enhanced. Finally, we observed that lithium intercalation into lanthanum tritelluride ($LaTe_3$) modifies the uni-directional charge density wave (CDW) that is present in $LaTe_3$. From Raman spectroscopy, it appears that uni-directional CDW gets suppressed with increasing concentrations of lithium intercalation into $LaTe_3$.

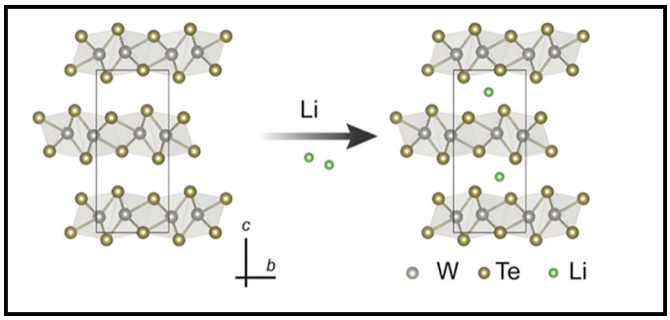

Figure 1: Schematic of lithium intercalation into tungsten ditelluride (WTe_2).

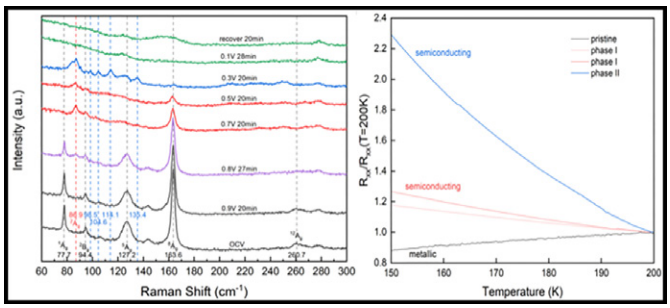

Figure 2: (Left) New structure is observed by intercalating lithium into molybdenum ditelluride ($MoTe_2$), which we denoted as Phase I and Phase II. (Right) These new phases are semiconducting, as confirmed by increasing resistance with decreasing temperature, in contrast to the initial metallic $MoTe_2$.

Conclusions and Future Steps:

Three manuscripts are in preparation to report our findings regarding lithium intercalation into layered materials: (1) new semiconducting phase in $MoTe_2$ by lithium intercalation, (2) thickness effects in intercalation-induced phase transition in WTe_2, and (3) changes in CDW in $LaTe_3$ by lithium intercalation. We will continue investigate the origin for the apparent suppression of the CDW phase in $LaTe_3$ with lithium intercalation. We will extend the study by including other rare-earth tritellurides that also have CDW phases. Transport measurements will also be carried out as a function of lithium intercalation, *in situ*.

Measuring the Mechanical and Electrical Properties of Ionically Conductive Polymers

CNF Project Number: 3058-23
Principal Investigator(s): Meredith Silberstein
User(s): Max Tepermeister, Ellen van Wijngaarden

Affiliation(s): Sibley School of Mechanical and Aerospace Engineering, Cornell University
Primary Source(s) of Research Funding: DARPA
Contact: meredith.silberstein@cornell.edu, mt845@cornell.edu
Website(s): silbersteinlab.com
Primary CNF Tools Used: DISCO Dicing Saw, Harrick Plasma Generator, Malvern Nano ZS Zetasizer

Abstract:

The mechanical and electrical properties of polymers enable their use in biosensors, biohybrid robotics and energy conversion devices. This research focused on how the mechanical and electrical properties of ionically conductive properties can be tuned for different applications. We used photolithography to fabricate an electrode setup to characterize a range of ionic polymers, revealing unexpected trends including increase in conductivity with ion size. Recent work has focused on the properties of biopolymers, specifically extracellular polymeric substances from bacteria including *Sphingomonas* and *Pseudomonas Aeruginosa*. Preliminary results demonstrate our ability to tune properties based on the blend of polymers present.

Summary of Research:

The primary goal of this research project is to characterize mechanical and electrical properties of ionically conductive polymers. This includes describing synthetic soft materials that use ionic transport as well as characterizing soft biopolymers with potential applications in ionic circuits. Traditional materials for circuit design are metal and semiconductor substrates; hard materials that are typically incompatible with biosystems. Biosystems utilize circuits to achieve environmental responses as seen in neurons and membrane ion channels. These systems have been previously studied from a biomechanical perspective, however, few reduced order circuit models have been developed. Research into soft ionic conducting materials has focused primarily on maximizing conductivity for use in electrochemical conversion and storage device membranes, with limited progress in the development of experimental wetware.

As part of this broader effort, we have experimentally characterized the ionic conductivity of a wide range of polymers. Impedance spectroscopy experiments were conducted on a Gamry 3000AE in the Silberstein lab. CNF tools were used to fabricate a gold-on-glass electrode using S1800 series photoresist patterned onto fused quartz wafers as shown in Figure 1. Electron-beam thermal evaporation was used to deposit a titanium adhesion layer followed by a gold layer. The water-jet liftoff machine was used to remove any excess gold before photopatterning spacers on the periphery of the electrodes. The SU-8 spacer can be seen in Figure 1 as the small lighter rectangles in a square around the central gold square. Impedance spectroscopy measurements were performed by adding the sample between the electrodes to create a parallel plate capacity. An oscillating electric field at various frequencies was applied to determine the electrical response of the test material. The system was used to test metal ligand coordinated polymers, polyionic hydrogels, and ionomers swollen with ionic liquids. Figure 3 depicts the ionic conductivity of a broad range of materials that have been characterized using this device.

Results showed that the ionic conductivity of ligand functionalized polydimethylsiloxane (PDMS) with metal salts incorporated was far greater than the conductivity of unfunctionalized PDMS. Additionally, the conductivity of metallo-PDMS depended on both the type of anion and cation within the salt and the salt concentration. Notably, the larger anions led to higher conductivity values despite having a lower diffusivity due to their size. This trend resulted from the larger anions dissolving into the polymer and dissociating better than smaller anions. Further details can be found in the recently published manuscript [1].

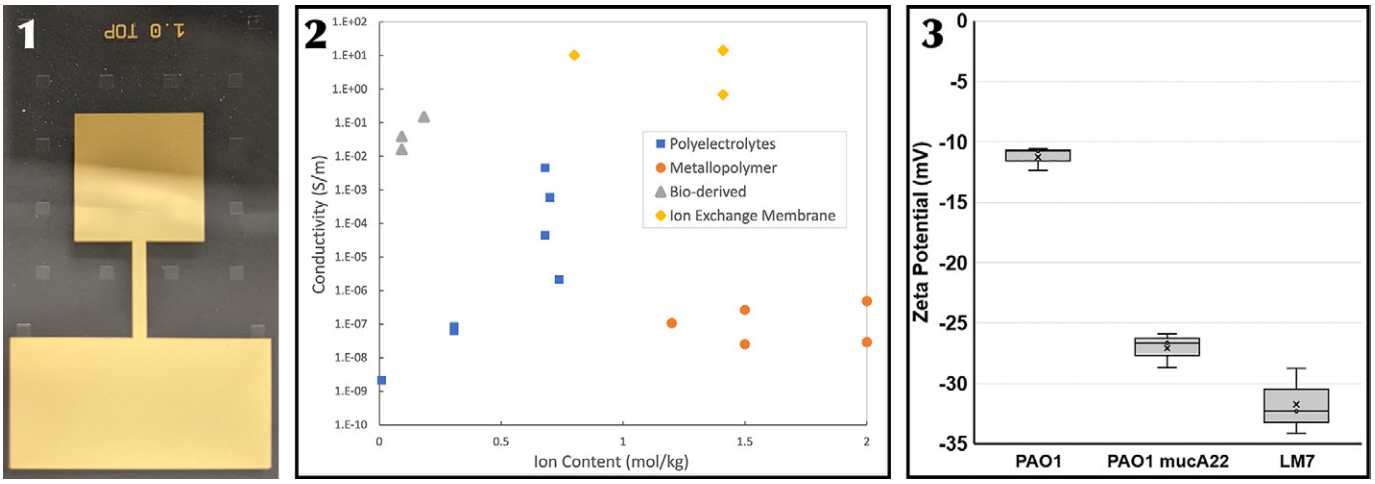

Figure 1, left: Experimental setup showing one electrode out of four on a wafer. Figure 2, middle: Conductivity vs ion content for four material classes. Figure 3, right: Zeta Potential results comparing ionic polymers from wild type Pseudomonas Aeruginosa, (PAO1), an alginate overexpression strain (PAO1 mucA22), and Sphingomonas LM7.

Initial tests completed for the characterization of biofilms have focused on a recently isolated strain of *Sphingomonas* bacteria, *LM7*. *Sphingomonas* bacteria are known for the production of high molecular weight polymers, primarily made of polysaccharides, that are widely used in applications in oil and gas as well as food processing. The work aimed to identify the initial properties for comparison to materials from other species, such as *Pseudomonas Aeruginosa*, and various material characterization methods were used to establish the properties of the *Sphingomonas* biofilms. The malvern nano-s zetasizer was used to measure molecular weight, size and zeta potential, as shown in Figure 3, to compare the biofilm from *Sphingomonas LM7* to strains of *P. Aeruginosa* and biopolymers from literature, such as gellan gum. Biofilms were grown over a period of four days before cultures were centrifuged to remove cells and the polysaccharide was removed from the supernatant using cold ethanol precipitation. Enzymes and phenol extraction were used to break down and remove DNA, RNA and proteins. The final material was dialyzed, lyophilized and then rehydrated as per zetasizer specifications for the desired measurements.

The zeta potential results from *Sphingomonas LM7* were compared to material from the well-known biofilm producer *P. Aeruginosa* wild type (PAO1) and PAO1mucA22, a strain of *P. Aeruginosa* modified to overexpress alginate, a negatively charged polymer. The zeta potential values indicate a negative charge for the *LM7* polymer similar to the PAO1mucA22 strain and significantly lower than the wild type biofilm. The value for *LM7* is similar to the values for zeta potential reported in literature for a similar biopolymer, gellan gum from another *Sphingomonas* strain [2]. Next steps will include additional materials characterization tests to better understand the ionic and mechanical properties of these biopolymers and testing a wider variety of biopolymer blends.

Conclusions and Future Steps:

The tools and technical expertise provided at the CNF was essential to the rapid design and fabrication of the experimental setup for material characterization providing novel insight into the behavior of ionic polymers. In the coming months, we will investigate device/junction through the design of additional microscale devices. We will also expand on our preliminary material tests of extracellular polymeric substances to include material from bacteria genetically modified to produce specific polymer blends.

References:

[1] Xinyue Zhang, Jinyue Dai, Max Tepermeister, Yue Deng, Jingjie Yeo, and Meredith N. Silberstein. Macromolecules 2023 56 (8), 3119-3131 DOI: 10.1021/acs.macromol.2c02519.

[2] Duarte LGR, Alencar WMP, Iacuzio R, Silva NCC, Picone CSF. Synthesis, characterization and application of antibacterial lactoferrin nanoparticles. Curr Res Food Sci. 2022 Mar 26;5:642-652. doi: 10.1016/j.crfs.2022.03.009. PMID: 35373146; PMCID: PMC8971344.

Magnetic-Field Driven By-Stable Switching of Magnetic Cantilevers/ Beams via Microscale Magnetic Controls

CNF Project Number: 2866-20
Principal Investigator(s): Amal El-Ghazaly
User(s): Ludovico Cestarollo, Karthik Srinivasan, Zexi Liang, Melody Xuan Lim

Affiliation(s): Electrical and Computer Engineering, Materials Science and Engineering; Cornell University

Primary Source(s) of Research Funding: National Science Foundation

Contact: ase63@cornell.edu, lc942@cornell.edu, ks934@cornell.edu, zl467@cornell.edu, mxl3@cornell.edu
Website(s): https://vesl.ece.cornell.edu

Primary CNF Tools Used: Heidelberg Mask Writer - DWL2000, SÜSS MicroTec Gamma Cluster Tool, ASML PAS 5500/300C DUV Wafer Stepper, Oxford 81 Etcher, Xactix XeF_2 Isotropic Silicon etch system, C&D SmartProP9000, DISCO Dicing Saw, Zeiss Ultra SEM, AFM - Veeco Icon, P7 Profilometer

Abstract:

The primary objective of this research is to establish large-deformation tactile displays using magnetic elastomer actuators. Magnetic actuators require reproducible, small-scale approaches for controlling the magnetic field gradient and direction used to drive the actuation. Over the past year our research group has been investigating the design and fabrication of micro-magnetic controls capable of generating localized magnetic fields and gradients necessary to actuate deformations in these magnetic elastomers. We have fabricated and optimized control micromagnets with different magnetic states and properties. The efforts have then been focused on experimentally demonstrating the ability of these control magnets to cause actuation via a system composed of a magnetic cantilever/beam.

Summary of Research:

One of the favored modes of actuation in large-scale mechanical systems (motors, relays, etc.) is magnetic because of its ability to generate large forces from relatively compact form-factors. However, the scaling down of magnetic actuation controls has posed numerous challenges. In the case of magnetic materials used for control, thin-film processing and smaller dimensions cause reduced flux density and demagnetization of the films. In the case of electromagnetic coils, the smaller size increases resistance and leads to unreasonably high-power consumption and heating. On the other hand, if successfully scaled down and integrated with Oersted-field or spintronic switching, magnetic actuation can potentially offer a low-power and compact solution to micro-actuators, including MEMS relays, microfluidic pumps, and novel haptic interfaces with the desired micrometer-scale resolution of magnetic fields and gradients [1-4].

This research project focuses on enabling the development of high-resolution, programmable haptic interfaces by developing a system of control magnets able to control the deflection of microscale beams/cantilevers.

A system of control magnets is designed to generate the local magnetic fields that would cause actuation. Two control magnets are engineered to have magnetizations preferentially pointing along two orthogonal axes, leading to the coupling of the magnetic flux densities between them and the generation of a field (and gradient) localized with micrometer resolution. These two control magnets are referred to as PMA (perpendicular magnetic anisotropy) and IMA (in-plane magnetic anisotropy) magnets. To investigate the ability of this system of magnets to generate useful forces for haptic applications, the team has designed a system composed of the two controls and an ALD (atomic layer deposition) beam/cantilever, which is made magnetic by embedding very thin soft magnets on its surface. The proposed design allows localization of a strong magnetic flux density and its gradient to a confined region of space between the two control magnets, enabling the magnetic actuation of the beam/cantilever with micro-scale resolution (Figure 1).

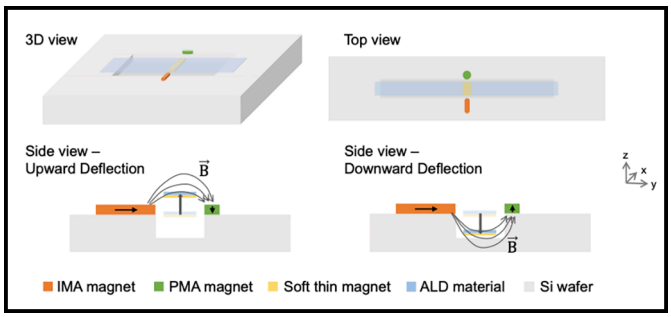

Figure 1: Magnetic actuation of a magnetic ALD beam via system of control PMA/IMA magnets.

Simulations have been designed and run to show that at these small microscales the generated magnetic flux density gradients between the two magnets are on the order of 10^4 T/m at vertical distances of hundreds of nanometers above (below) the magnets. These field gradients would act of the beam/cantilever by deflecting it to where the magnetic field is the strongest. This is at roughly 100 nm above the control magnets in the case of the PMA magnet being downward magnetized, and 100 nm below the magnets when the PMA magnet is upward magnetized.

The magnetic pull force exerted on the cantilever/beam, expressed as $F_z = m_x B_{xz} + m_y B_{yz}$ (where m=magnetic moment, and B=magnetic flux density), is computed. Simulations show that the B_{xz} component of the field gradient (rate of change of B_x as a function of z) is order of magnitudes larger than B_{yz}. This indicates that the soft thin magnets on the cantilever/beam should be designed with an elongated shape in the x-direction to promote magnetic anisotropy along this axis and maximize the magnetic force F_z. Furthermore, this magnetic force is shown to be greater than the mechanical force from the beam/cantilever, proving that the control magnets exert a magnetic field and gradient that are sufficient to mechanically deflect the beam/cantilever (Figure 2).

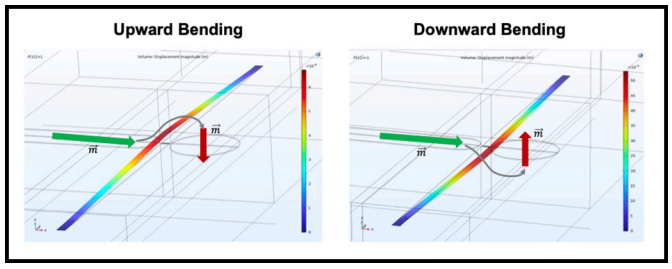

Figure 2: Magneto-mechanical simulation showing bipolar switching of a magnetic ALD beam via system of control PMA/IMA magnets.

The team is currently working on fabricating the system presented above. Deposition and patterning steps have been optimized to obtain the designed structures.

Conclusions and Future Steps:

This research shows that IMA and PMA magnets can be engineered and combined to generate magnetic flux density coupling useful for high-resolution magnetic actuation. Localization of a magnetic field (and a gradient) is achieved in a very narrow region of space with micrometer resolution. This system of magnets is integrated into a device with a narrow cantilever/beam, which is made responsive to applied magnetic fields by adding small magnets to it. In conclusion, this work will enable the realization of high-resolution, micrometer-scale magnetic actuators for haptics and numerous other mechanical applications.

References:

[1] L. Cestarollo, S. Smolenski, and A. El-Ghazaly, "Nanoparticle-based magnetorheological elastomers with enhanced mechanical deflection for haptic displays," ACS Applied Materials & Interfaces, vol. 14, no. 16, pp. 19002-19011, 2022.

[2] S. Marchi, et al., "Highly magneto-responsive elastomeric films created by a two-step fabrication process", ACS Applied Materials & Interfaces, vol. 7, no. 34, pp. 19112.19118, 2015.

[3] K. J. Dorsey, et al., "Atomic layer deposition for membranes, metamate-rials, and mechanisms," Advanced Materials, vol. 31, no. 29, 1901944, 2019.

[4] J. Streque, et al., "New magnetic microactuator design based on PDMS elastomer and MEMS technologies for tactile display," IEEE Trans. Hap-tics, vol. 3, no. 2, pp. 88-97, 2010.

Fabrication of Micro Scale Triboelectric Microphone

CNF Project Number: 2929-21
Principal Investigator(s): Shahrzad Towfighian
User(s): Mohammad Alzgool

Affiliation(s): Mechanical Engineering, Binghamton University

Primary Source(s) of Research Funding: National Science Foundation Grant #1919608

Contact: stowfigh@binghamton.edu, malzgoo1@binghamton.edu, mmalzgool14@gmail.com

Primary CNF Tools Used: YES Asher, Unaxis PT770, OEM AlN sputtering, AJA sputter deposition, Heidelberg DWL-2000 Mask writer, Oxford PECVD, Oxford 81 etcher, PT770 etcher, DISCO dicing saw, SÜSS MA6-BA6 contact aligner, YES polyimide curing oven, PRIMAXX vapor etcher

Abstract:

We were previously able to fabricate the smallest triboelectric generator and we used it for switching a MEMS parallel-plate switch and as an accelerometer. The generator was utilized as a vibration sensor by connecting it to a MEMS-switch, this switch operates once the frequency or acceleration of vibration surpasses a threshold, the operating modes are called frequency sensitive mode and acceleration sensitive mode. Nowadays, we are trying to fabricate a microphone that operates by using the mechanical structure and the triboelectric property of polyimide and aluminum with a back-etched wafer with aluminum nitride-aluminum layer as our diaphragm. The back-plate consists of polyimide and aluminum. The polyimide is thick and is a substitute for the amorphous silicon that we used in previous design as a proof mass. The motivation of this project comes from the promising results acquired from the MEMS triboelectric accelerometer which gave high signal-to-noise ration and the high and linear response of the output voltage.

Research Summary:

There are many advantages of triboelectric generators over piezoelectric generators such as lower cost, high flexibility, and superior electrical output. The operation of triboelectric generators depends on contact of a metal and a dielectric material with different affinity to electrons, the contact will result in charged conductive plates and separation with high impedance in between the plates will result in high voltage.

The triboelectric generator fabricated in this project was connected to a MEMS switch with a summer electronic circuit to apply DC voltage to the system (Figure 1). The triboelectric generator in this work is responsible for the AC voltage supply which is generated as a response to outside vibration excitation. When the vibration exceeds certain amplitude or frequency the switch closes as a result of the dynamic behavior of the MEMS switch which is characterized in previous works.

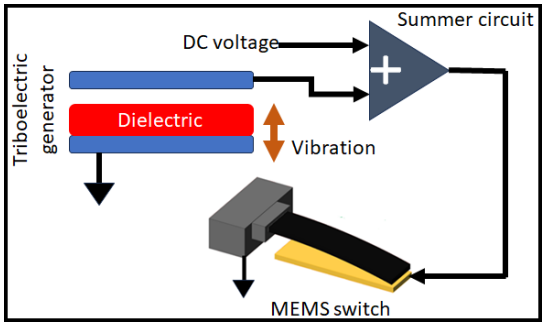

Figure 1: Experimental setup schematic.

Fabrication:

The fabrication process for triboelectric generator starts with aluminum nitride insulation, aluminum is sputtered and patterned for bottom electrode, polyimide spin-coating, curing, and patterning is carried out. This will result in the bottom layer of the generator. Then, the gap is created by silicon oxide layer which is patterned to create top layer anchors. And top layer is created by sputtering aluminum and depositing amorphous silicon for proof-mass.

Nowadays, we are trying to change the fabrication process so that polyimide layer is part of the top electrode and to have a hole under the bottom electrode to create a microphone. A triboelectric microphone as we envision will have a back-etched silicon wafer as sound inlet, a membrane of aluminum nitride which vibrates with input, a small gap between the membrane and the back-plate, and a back-plate of polyimide-aluminum pair. The design of membrane and the back-plate is carried out with frequency mismatching in mind to guarantee contact between them as sound is received.

The fabrication process starts with 500 nm deposition of aluminum nitride followed by 100 nm sputtering of titanium nitride-aluminum to create the diaphragm. Both layers are patterned using ICP-RIE PT770 etcher. Then, 1.0 μm sacrificial layer for the gap is deposited using PECVD and etched using oxford 81 RIE. Then, the inlets are made by back-etching the wafer which is done by depositing 100 nm aluminum nitride which is patterned with back-side-alignment. The aluminum nitride is used as a hard-mask for back etching which is done using Unaxis PT770 for > 1000 loops. For the top layer, we start with spin-coating and curing of polyimide (HDmicron PI 2574). Then, aluminum is sputtered on top and patterned with PT770. Patterned aluminum can be used as a hard mask for polyimide patterning which is done by RIE machine oxford 81 with CF_4-O_2 recipe. Finally, the wafer is diced and wire-bonded for testing.

Results:

The pull-in for the beam used in this work happens at 2.1 V statically. Dynamically, the generator provides AC voltage up to 0.6 V peak to peak. In frequency sensitive mode of operation, the pull-in happens at different frequencies depending on the applied DC voltage, at 1.6 V it happens at 10.6 kHz, and at 1.7 V it happens at 8.9 kHz as shown in Figures 2 and 3.

For amplitude sensitive mode, the acceleration was raised gradually in 10 seconds period while measuring the response of the beam, it was noticed that there is an amplitude of oscillation that provides AC voltage that is enough to close the switch. This experiment is shown in Figure 4.

Conclusions and Future Steps:

The triboelectric generator previously fabricated was useful for vibration measurements, it can operate a switch in different modes by using the dynamic of the switch and the generator. The output of the generator increases with the excitation amplitude and, thus, can drive the switch to close in amplitude sensitive mode once a threshold is past. And because the switch has natural frequency that changes with DC voltage, the frequency of the vibration that causes the switch to close can be tuned.

Currently, we are working on fabricating a triboelectric microphone by adding a back-etch to the fabrication process and swapping the position of the polyimide from bottom to top so that it will act as a dielectric and a proof-mass layer.

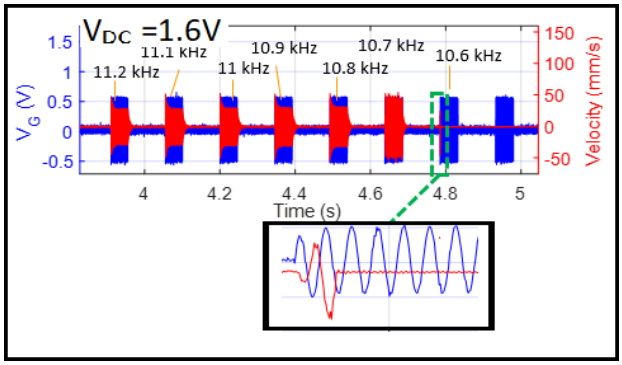

Figure 2: Frequency sensitive vibration sensor at V_{DC} = 1.6 V.

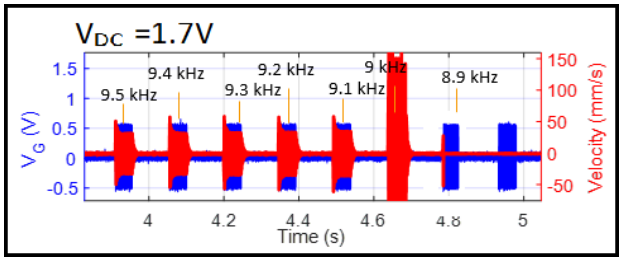

Figure 3: Frequency sensitive vibration sensor at V_{DC} = 1.7 V.

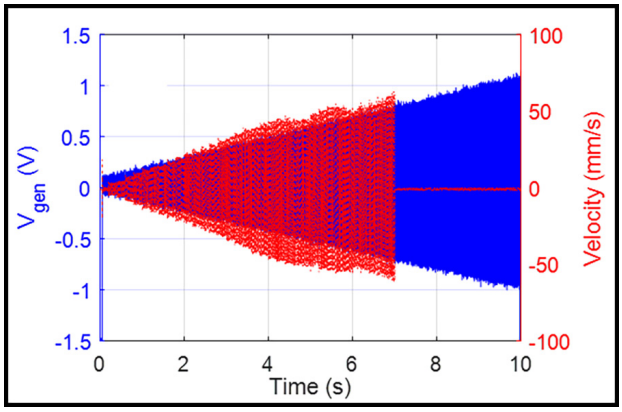

Figure 4: Acceleration sensitive vibration sensor.

References:

[1] Alzgool, M., Tian, Y., Davaji, B., and Towfighian, S. (2023). Self-powered triboelectric MEMS accelerometer. Nano Energy, 109, 108282.

[2] Mousavi, M., Alzgool, M., Davaji, B., and Towfighian, S. (2023). Event-driven MEMS vibration sensor: Integration of triboelectric nanogenerator and low-frequency switch. Mechanical Systems and Signal Processing, 187, 109921.

Programmable Microscopic Magnetic Self-Assembly

CNF Project Number: 2964-21
Principal Investigator(s): Itai Cohen, Paul L. McEuen
User(s): Zexi Liang, Melody Xuan Lim, Conrad Smart

Affiliation(s): Kavli Institute at Cornell for Nanoscale Science, School of Applied and Engineering Physics, Laboratory of Atomic and Solid-State Physics, Department of Physics; Cornell University

Primary Source(s) of Research Funding: National Science Foundation, Alfred P. Sloan Foundation

Contact: itai.cohen@cornell.edu, plm23@cornell.edu, zl467@cornell.edu, mxl3@cornell.edu, cs2239@cornell.edu

Primary CNF Tools Used: Oxford 81/82 etcher, YES EcoClean Asher, ASML DUV stepper, Gamma Automatic Coat-Develop Tool, JEOL 6300 EBL, SC 4500 odd-hour evaporator, AJA Sputter Deposition, Heidelberg DWL2000, PT770 etcher (left side), Unaxis 770 Deep Silicon Etcher, Plasma-Therm Takachi HDP-CVD, Oxford PECVD, Oxford ALD, Zeiss SEM, Veeco AFM

Abstract:

We develop an experimental platform for programmable microscopic magnetic self-assembly. We manufacture these microparticles at the wafer-scale, and have precisely designed shapes, magnetic moments, and magnetic interactions. Once released, we drive particles to explore their configuration space by a rotating magnetic field, generating chaotic flows that mix particles and drive assembly at the air-water interface. As a first example, we control self-limiting assembly by designing the shape and net magnetic moment of clusters at various stages in the assembly process. In particular, we show that spontaneous decoupling of the final product from the reaction forms a powerful principle for self-limiting assembly.

Summary of Research:

Recent progress has been made towards the self-assembly of structures that terminate at a finite size, rather than growing indefinitely. Such structures require a mechanism to detect when a cluster of a specific size is formed, and to prevent larger clusters from growing. Current strategies for such a self-sensing mechanism include geometric self-closing [1], geometric frustration [2], and strain accumulation [3].

Here, we demonstrate a new mechanism for non-equilibrium self-limiting assembly, which relies on programmable magnetic interactions between constituent particles. Our strategy makes use of the fact that the net moment of a magnetically assembled cluster is the vector sum of the constituent moments. We design a cluster which, when assembled, has no net magnetic moment and thus spontaneously decouples from external magnetic driving. This spontaneous decoupling ensures that once a cluster is fully formed, it achieves stability and ceases to interact with the external driving field.

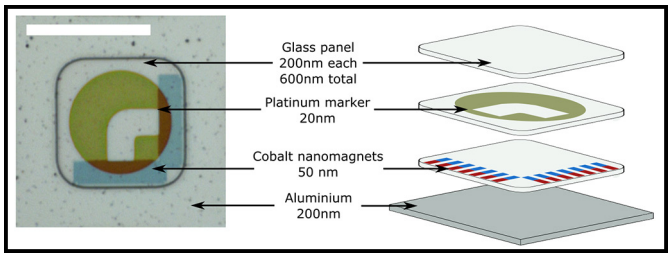

Figure 1: Schematic and optical microscope image of magnetic device layer structure.

Consequently, this halts the cluster's growth at a specific size, while other magnetically driven particles remain actively engaged in mixing and assembly.

Our devices are completely fabricated at CNF (see Figure 1 for device schematic). On top of a aluminum/aluminum oxide sacrificial layer, we pattern single-domain cobalt nanomagnets using electron-beam lithography [4] and metallize by liftoff. These nanomagnets are then embedded in silicon oxide thin films, whose shape and size are precisely patterned by a deep-ultraviolet (DUV) stepper. The combination of photolithography and electro-beam lithography allow us to pattern magnetic devices where the strength and shape of the magnetic interaction, placement of magnets, and contact interactions from the silicon oxide panel can all be harnessed to design a landscape for magnetic self-assembly.

We release these panels and observe their dynamics in the lab under an optical microscope. In order to do so, we deep reactive ion etch through the back of the silicon wafer, leaving only the sacrificial layers and magnetic devices. The magnetic devices are coated with a hydrophobic polymer layer, such that when TMAH solution is added to etch the sacrificial layer, the magnetic devices are released to float on the liquid-air interface.

Surface tension (combined with the hydrophobic particle surface) confines the particles to a single layer, allowing us to record and observe their interactions.

The very low friction environment of the liquid-air interface enables us to visualize the effect of small magnetic forces, as well as to introduce out-of-equilibrium driving. In this case, we use rotating magnetic fields to generate particle rotation. As the particles align to follow the applied magnetic torque, the fluid around them is forced to rotate with each particle. When particles are sufficiently close, these rotating hydrodynamic flows become collectively chaotic, acting to effectively mix particles and "thermalize" the system.

The exact parameters of the magnetic driving control the final distribution of assembly products (see Figure 2 for assembly design, and Figure 3 for distribution of final product as a function of magnetic driving). For example, if particles are consistently driven at a high amplitude (40 Oe) magnetic field, particles remain separated and do not assemble, since the magnetic torque dominates over local interactions that drive assembly. Driving particles at a small amplitude (10 Oe) magnetic field results in disordered aggregation: all products of the assembly are formed in equal proportion, since the magnetic driving is insufficient to thoroughly mix the particles. However, driving magnetic assembly at an intermediate magnetic field (20-30 Oe) produces the maximum conversion into the final assembly product. At this magnetic field condition, particles are able to overcome the applied torque and assemble into higher order products, while also being mixed sufficiently to explore their local environment.

We can further enhance the fraction of successfully assembled final product by dynamically changing the magnetic field driving conditions. This strategy makes use of the fact that the final assembled product spontaneously decouples from the external field, so that raising the magnetic driving to a high amplitude will break incomplete or undesired structures, but not the final product. As a result, cyclically lowering and raising the magnetic field will gradually enhance the number of particles that successfully assemble into the final product (see Figure 4).

This work demonstrates a general design principle for out-of-equilibrium self-limiting assembly by spontaneous decoupling. Future work will leverage these ideas to generate complex structures, particularly those that harness energy from external magnetic fields to perform useful work. Combining these principles with programmable magnetic bindings [4-6] will provide a powerful platform for complex, functional magnetic microstructures.

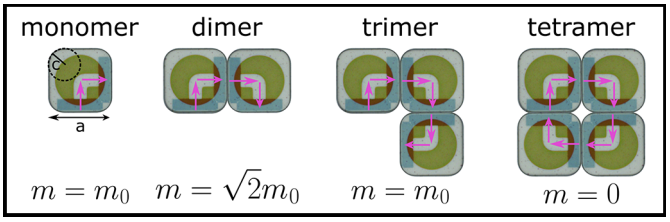

Figure 2: Schematic of assembly products from four identical magnetic devices, with magnetic moments indicated as arrows.

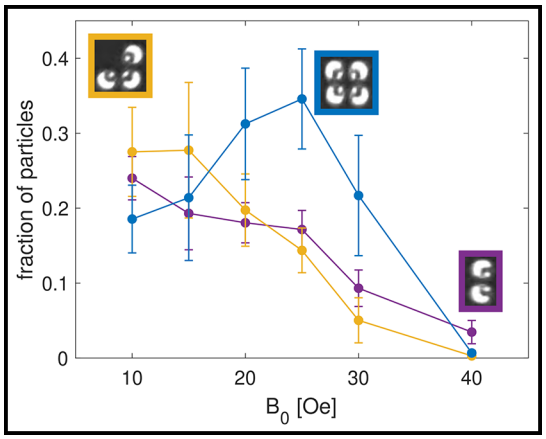

Figure 3: Plot of the distribution of assembly products (dimer, trimer, and tetramer) as a function of the amplitude of magnetic driving. The total yield (including monomer) sums to 1.

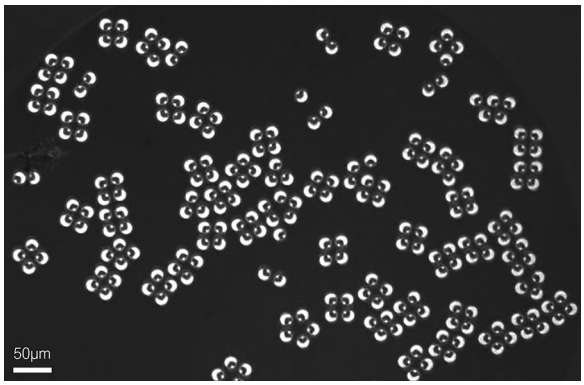

Figure 4: Optical microscope image of the product of several cycles of magnetic cyclic driving, where almost all panels have assembled into tetramers.

References:

[1] Hayakawa, Daichi, et al. Proceedings of the National Academy of Sciences 119.43 (2022): e2207902119.

[2] Long, Cheng, and Jonathan V. Selinger. Soft Matter 19.3 (2023): 519-529.

[3] Berengut, Jonathan F., et al. ACS nano 14.12 (2020): 17428-17441.

[4] Cui, J., Huang, TY., Luo, Z. et al. Nature 575, 164-168 (2019).

[5] Du, Chrisy Xiyu, et al. Soft Matter 18.34 (2022): 6404-6410.

[6] Niu, Ran, et al. Proceedings of the National Academy of Sciences 116.49 (2019): 24402-24407.

Periodically Poled Lithium Niobate for Visible Light Generation

CNF Project Number: 1997-11
Principal Investigator(s): Qiang Lin[1,2]
User(s): Jeremy Staffa[1]

Affiliation(s): 1. Institute of Optics, University of Rochester, Rochester NY;
2. Department of Electrical and Computer Engineering, University of Rochester, Rochester NY

Primary Source(s) of Research Funding: Defense Advanced Research Projects Agency (DARPA) LUMOS program under Agreement No. HR001-20-2-0044, the Defense Threat Reduction Agency-Joint Science and Technology Office for Chemical and Biological Defense (grant No. HDTRA11810047), and the National Science Foundation (NSF) (ECCS-1810169, ECCS-1842691, and OMA-2138174)

Contact: qiang.lin@rochester.edu, jstaffa@ur.rochester.edu

Website(s): https://arxiv.org/abs/2207.03071

Primary CNF Tools Used: JEOL 9500, AJA ion mill, CVC SC4500 odd-hour evaporator, Veeco Icon Atomic Force Microscope, DISCO Dicing Saw

Abstract:

We report efficient quasi phase matched second harmonic generation of 532 nm green light in periodically poled nanophotonic waveguides on the Lithium-Niobate on Insulator (LNOI) platform.

Summary of Research:

Visible light generation on an integrated photonic platform is of great interest for applications ranging across quantum optics, atomic physics, sensing, biophotonics, and AR/VR, to name a few. The (LNOI) platform boasts a broad transparency window, with low loss into the visible band [1], and exceptional quadratic optical nonlinearity for efficient conversion of long wavelength pump light into the visible spectrum [2,3]. Here we demonstrate efficient chip-scale generation of green light by second harmonic generation of a NIR source.

Quasi phase matched second harmonic generation of a 1064 nm pump source is realized by periodically poling the LN waveguide to bridge the phase mismatch between the 1064 nm and 532 nm optical modes. The fundamental TE_{00} modes are utilized for their near-unity nonlinear mode overlap and alignment with the largest quadratic nonlinear tensor element (d_{33} = 25pm/V) of LN. A relatively short poling period $\Lambda = \lambda_{SH}/\Delta n_{eff}$ of ~ 2.2 μm is necessary for quasi phase matching due to the difference in effective refractive indices Δn_{eff} of the TE_{00} modes. Poling with close to 50% duty cycle ensures optimal efficiency of the devices.

The PPLN waveguide devices are fabricated on MgO doped x-cut thin film lithium-niobate-on-insulator (LNOI), with 400 nm LN sitting upon a 2 μm silica layer. ZEP-520A resist is used for a first e-beam lithography step (JEOL 9500), followed by 300 nm Ar-ion milling (AJA Ion Mill) to create the alignment marks. A second e-beam writing step is performed on PMMA resist, and 300 nm poling electrodes are created using a gold evaporation and lift-off process (CVC SC4500 odd-hour evaporator). High voltage pulses realize the periodically inverted domains in the unprocessed LN thin film [4] and are verified by Piezo Response Force Microscopy (Veeco Icon AFM) (Figure 1b). The electrodes are removed in an acid clean step, and a third e-beam lithography step with ZEP-520A, followed again by Ar-ion milling, is used to define the waveguides along the periodically poled domains.

The 1064 nm light is amplified by a ytterbium-doped fiber amplifier and coupled to the waveguide facet by a 780HP lensed fiber. The residual pump light and generated visible light is collected from the output facet by a 780HP lensed fiber as well. A narrow $sinc^2$-like phase matching spectrum is observed (Figure 1d), indicating good uniformity of the periodically poled domains along the waveguide length. An absolute on-chip conversion efficiency in excess of 12% is measured with 16 mW of pump power, generating slightly more than 2 mW of green light on chip (Figure 1e). The sublinear efficiency trend agrees well with pump-depletion theory of colinear SHG, verifying strong pump conversion efficiency of the nonlinear waveguides.

References:

[1] Boris Desiatov, et al. "Ultra-low-loss integrated visible photonics using thin-film lithium niobate," Optica 6, 380-384 (2019).
[2] Cheng Wang, et al. "Ultrahigh-efficiency wavelength conversion in nanophotonic periodically poled lithium niobate waveguides," Optica 5, 1438-1441 (2018).
[3] Taewon Park, et al. "High-efficiency second harmonic generation of blue light on thin-film lithium niobate," Opt. Lett. 47, 2706-2709 (2022).
[4] Jonathan Tyler Nagy, et al. "Submicrometer periodic poling of lithium niobate thin films with bipolar preconditioning pulses," Opt. Mater. Express 10, 1911-1920 (2020).

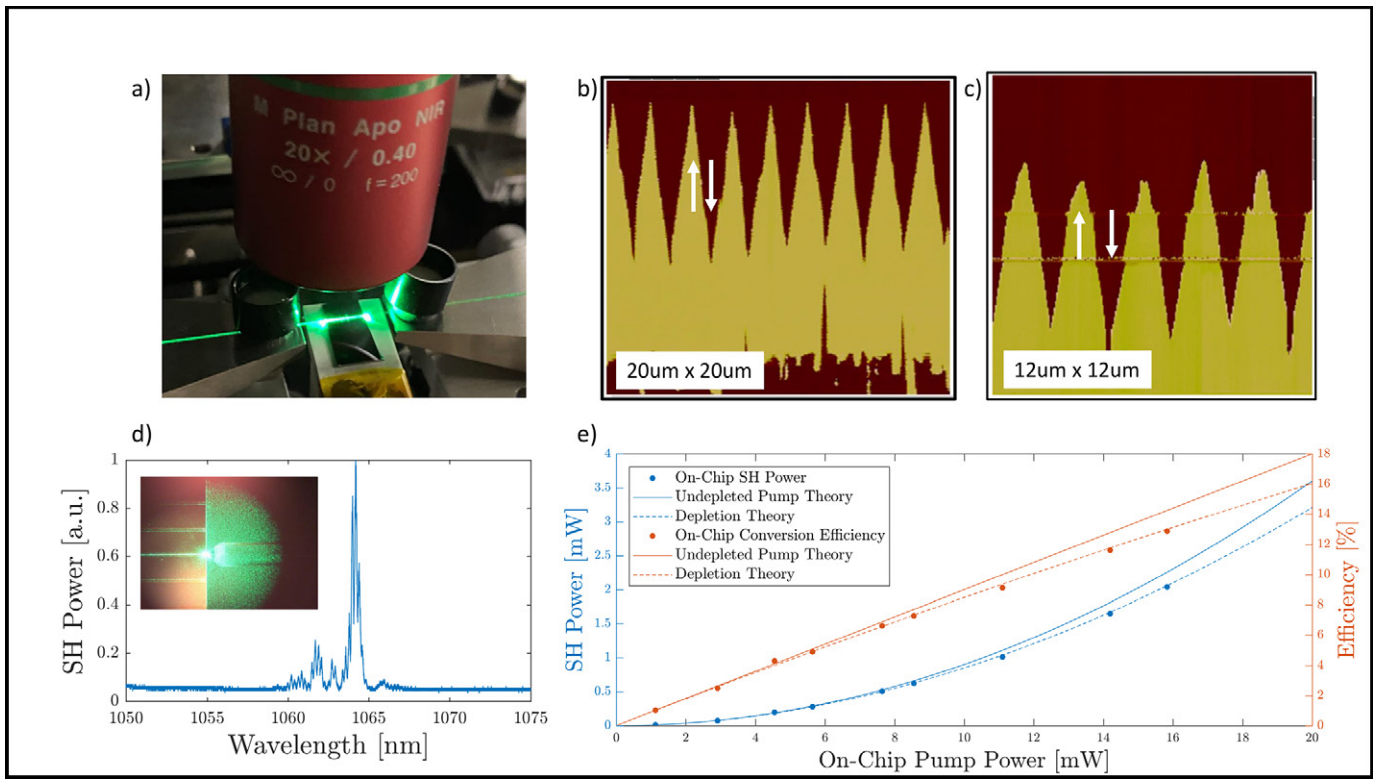

Figure 1: (a) Image of efficient green light generation on the PPLN chip. Piezo Response Force Microscopy of the periodically inverted domains before (b) and after (c) waveguide fabrication. (d) Measured phase matching spectrum of the device, centered around 1064 nm. (e) On-chip conversion efficiency and generated visible light power from the quasi phase matched SHG process.

Full-Spectrum Visible Electro-Optic Modulator

CNF Project Number: 1997-11
Principal Investigator(s): Qiang Lin
User(s): Shixin Xue, Jingwei Ling, Jeremy Staffa, Qili Hu, Zhengdong Gao

Affiliation(s): Department of Electrical and Computer Engineering, University of Rochester; Institute of Optics, University of Rochester

Primary Source(s) of Research Funding: Meta Platform Technologies LLC; Defense Advanced Research Projects Agency (LUMOS, HR001-20-2-0044)

Contact: qiang.lin@rochester.edu, sxue4@ur.rochester.edu, jling8@ur.rochester.edu, jstaffa@u.rochester.edu, qhu17@ur.rochester.edu, zgao14@ur.rochester.edu

Primary CNF Tools Used: JEOL JBX9500FS Electron-Beam Lithography System, Odd Hour Evaporator, AJA Ion Mill, Zeiss Ultra SEM

Abstract:

We report an on-chip high-speed visible-band electro-optic modulator that can operate over the full visible spectrum of 400-700 nm, with a record low $V\pi{\cdot}L$ of 0.48, 0.25, and 0.17V·cm at red, green, and blue wavelengths of 630, 520, and 450 nm, respectively, and an operation bandwidth of > 20 GHz.

Summary of Research:

The visible spectral region underpins many important applications including sensing, optical clocks, 3D displays, and augmented/virtual reality (AR/VR). All of these applications rely crucially on precise control and efficient modulation of visible light. Recently, there has been significant interest in transferring these applications onto chip-scale platforms [1,2] that would offer great advantages in size, power, functionality, and design flexibility. However, development of chip-scale electro-optic modulators (EOMs) in the visible band remains fairly limited [3-5]. Here, we demonstrate an on-chip lithium niobate (LN) EOM that can operate over the full spectrum covering the entire visible band from 400 to 700 nm. We show that the visible-band EOM exhibits record high modulation efficiency with $V\pi{\cdot}L$ as low as 0.48, 0.25, and 0.17V·cm at wavelengths of 630, 520, and 450 nm, respectively, which are the smallest ever reported for LN traveling-wave EOMs developed to date.

Figure 1(a) shows a fabricated EOM that consists of a pair of 3 dB multimode interference (MMI) couplers, an 8-mm-long phase modulation section operating in the push-pull fashion, and a spatial-mode filter section placed in the front.

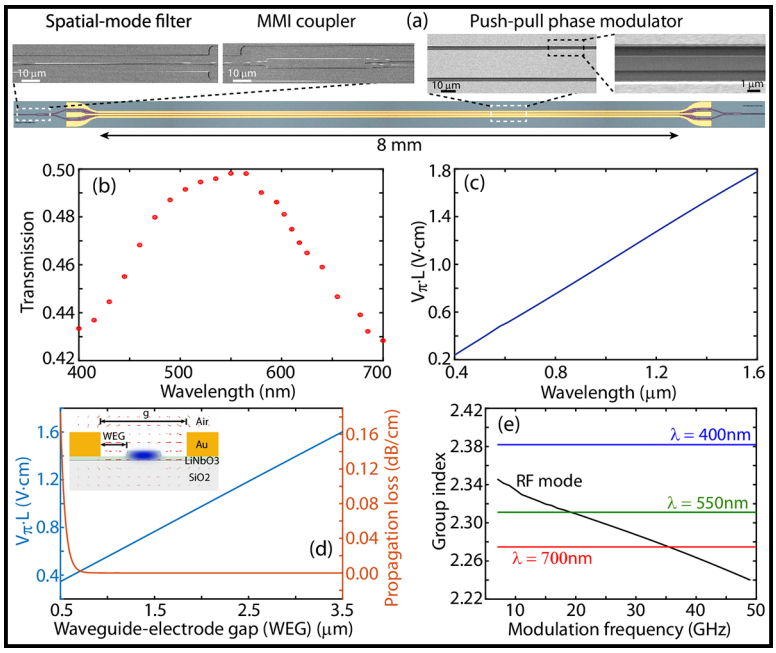

The devices are made on a 300-nm-thick x-cut LN-on-insulator wafer, partially etched down by 180 nm. The modulator waveguide has a width of 1 μm and a waveguide-electrode gap (WEG) of 0.8 μm, with an electrode spacing of 2.6 μm in order to enhance modulation efficiency. The electrodes contact directly with the LN layer to improve the optical-microwave mode overlap. For the EOM to operate over the full visible spectrum, the MMI coupler is designed to be broadband with a transmission of 43.3%, 49.8%, and 42.8% at wavelengths of 400, 550, and 700 nm, respectively [Figure 1(b)]. The SMF is a tapered waveguide to cut off higher-order guided modes to ensure single-mode operation of the EOM.

Figures 2(a)-2(c) show the modulation performance of the EOM. The device exhibits a $V\pi$ of 0.60 V, 0.31 V, and 0.21 V, respectively, at the red, green, and blue wavelengths of 630, 520, and 450 nm, which corresponds to a $V\pi{\cdot}L$ of 0.48, 0.25, and 0.17V·cm. The extinction ratio (ER) is measured to be 16 dB at 630 nm [Figure 2(a)]. The ER decreases to 7 dB and 12 dB at 520 and 450 nm [Figures 2(b) and 2(c)], respectively, which is dominantly due to the green and blue FP lasers (Thorlabs, LP-520 and LP-450) with a poor polarization ER of ~ 10 dB that interferes with the ER characterization. The recorded WEG dependence of $V\pi{\cdot}L$ [Figure 2(d)] shows a slightly better performance than the theoretical expectation, which is likely due to a smaller fabricated WEG than the designed WEG. Figure 2(e) shows that the EOM exhibits a 3 dB bandwidth of 16 GHz (blue curve). This value is simply limited by the frequency response of the optical detector (Newport, 1544-B) [Fig. 2(e), red curve]. By factoring out the detector response, the EOM itself exhibits a 3 dB bandwidth > 20 GHz [Fig. 2(e), green curve]. The insertion loss of the EOM is measured to be 6.8 dB at 630 nm, which is primarily attributed to the fabrication imperfections of the SMF and the MMI couplers.

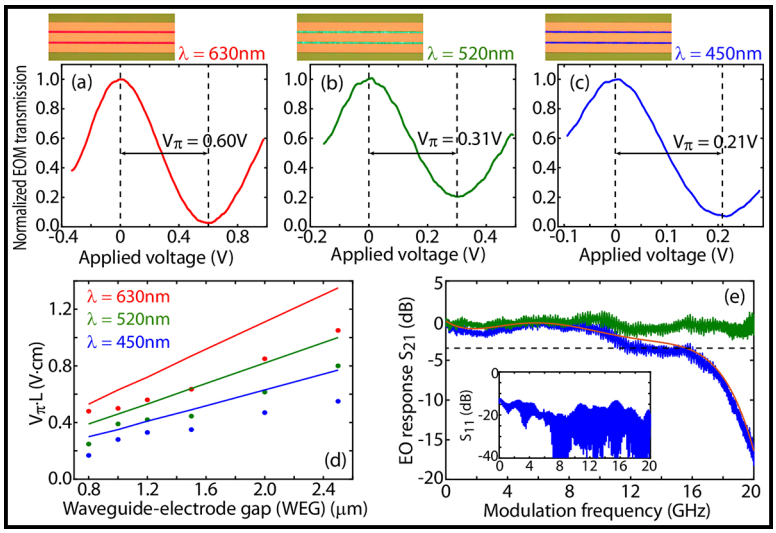

The demonstrated full-spectrum EOM with record performance achieves a key step toward energy-efficient and high-speed visible photonics, opening up a great avenue toward chip-scale miniaturization and integration of versatile functionalities in sensing, atomic clocks, AR/VR, etc., on the promising thin-film LN platform.

References:

[1] T. J. Morin, L. Chang, W. Jin, C. Li, J. Guo, H. Park, M. A. Tran, T. Komljenovic, and J. E. Bowers, Optica 8, 755 (2021).

[2] M. Dong, G. Clark, A. J. Leenheer, M. Zimmermann, D. Dominguez, A. J. Menssen, D. Heim, G., Gilbert, D. Englund, and M. Eichenfield, Nat. Photonics 16, 59 (2022).

[3] B. Desiatov, A. Shams-Ansari, M. Zhang, C. Wang, and M. Lon.ar, Optica 6, 380 (2019).

[4] O. T. Celik, C. J. Sarabalis, F. M. Mayor, H. S. Stokowski, J. F. Herrmann, T. P. McKenna, N. R. Lee, W. Jiang, K. K. Multani, and A. H. Safavi-Naeini, Opt. Express 30, 23177 (2022).

[5] C. Li, B. Chen, Z. Ruan, H. Wu, Y. Zhou, J. Liu, P. Chen, K. Chen, C. Guo, and L. Liu, Opt. Express 30, 36394 (2022).

Monolithic Ultrabroadband Multispectral Color Filter Array

CNF Project Number: 2524-17
Principal Investigator(s): Jaime Cardenas
User(s): Jiewei Xiang

Affiliation(s): The Institute of Optics, University of Rochester

Primary Source(s) of Research Funding:

Contact: jaime.cardenas@rochester.edu, jxiang6@ur.rochester.edu

Website(s): https://www.hajim.rochester.edu/optics/cardenas/

Primary CNF Tools Used: ASML stepper, Oxford 100 ICP-RIE, YES EcoClean Asher, Oxford PECVD, JEOL 9500, Heidelberg Mask Writer-DWL2000, ABM Contact Aligner, Oxford Cobra ICP Etcher, Woollan RC2 Spectroscopic Ellipsometer, Logitech Orbis CMP, AJA Sputter System

Abstract:

We use a modified Fabry-Perot structure with selectively suppression and subwavelength structures in cavity to realize MSFAs that can cover the range from 450 - 910 nm.

Summary of Research:

Multispectral imaging (MSI) has found applications in various fields such as metrology, medical spectrum diagnoses, and industrial processes, offering scenes with multiple narrowband spectral channels. Conventional multispectral systems typically rely on dispersive elements like diffraction gratings or prisms, which limit further miniaturization and integration [1]. To overcome this limitation, snapshot multispectral imaging systems based on multispectral filter arrays (MSFAs) have been developed [2]. These systems enable the capture of a parallel array of images with different spectral channels in a single shot, eliminating the need for spatial or spectral scanning and allowing for highly compact and integrated designs. However, the design and fabrication of a monolithic broadband MSFA with narrow bandwidth and high color purity present significant challenges.

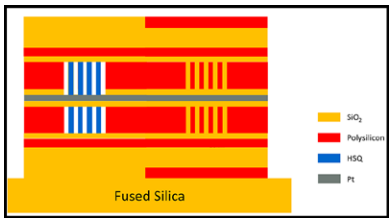

Figure 1: Schematic of the stack structure of the color filters.

People have demonstrated integratable color filter arrays (CFAs) using various approaches such as plasmonic resonance [3], Mie resonance [4], and guided mode resonance [5]. Among these, CFAs based on Fabry-Perot (FP) resonators offer advantages such as polarization insensitivity, angle insensitivity, high transmission, and narrow full-width at half-maximum (FWHM), which are desirable for multispectral filter arrays (MSFAs). However, traditional thin film color filter arrays based on FP cavities often require multiple filter stacks, leading to fabrication challenges and limited spectral range [6]. Increasing the number of detection channels also necessitates additional lithography and etching steps, further complicating the fabrication process. To address these challenges, subwavelength grating structures have been introduced to modify the optical length of the cavity without altering the physical thickness. Nevertheless, in FP resonators, multiple resonances can impact color purity and the free spectral range (FSR). Furthermore, the spectral tuning range is restricted by the nanofabrication process, as the fill ratio of the subwavelength grating cannot be excessively high.

We present a CMOS compatible multispectral FP color filter arrays which have a large spectral range (450nm-910nm) with narrow FWHM (<40nm) based on selective suppression and a subwavelength grating (Figure 1). We demonstrate the broadband MSFAs based on modified FP structure with second order resonance which can cover the wavelength range from 630 nm to 960 nm [7]. One of the limitations of extending the color filters to shorter wavelength is the effective index range that can be obtained with polysilicon and silicon dioxide subwavelength structures. To extend the working wavelength range to cover visible spectra, we enlarge the effective index range by introducing air in the cavity. To cap air in the cavity, we need the air gaps in the cavity have a relatively small feature size and high aspect ratio such that we can cap as much as air in the cavity rather than fill it out with top deposition. To circumvent the high aspect ratio etch step, we directly use 11% HSQ as the cavity layer and expose the HSQ layer with hexagonal subwavelength grating or mesh structures. After development, we can have around 50 nm width and 170 nm depth air gaps without the need of high aspect ratio etching. We cap the air with top deposition based

on the filling capability of deposition recipe. To enhance the transmission, we use one 35 nm layer as the reflection mirror. We combine the HSQ and air cavity design with the polysilicon and silicon dioxide cavity design such that we can cover the range from visible to NIR.

The main fabrication steps for our design are shown in Figure 2. We use polysilicon as the high index material in the DBRs. Polysilicon is deposited by plasma-enhanced chemical vapor deposition (PECVD) and anneal it at 700°C for two hours to make it crystalize. We use JEOL 9500 and negative resist hydrogen silsesquioxane (HSQ) to pattern the cavity and use inductively coupled plasma reactive ion etching with HBr to transfer the pattern from HSQ to polysilicon. We fill the gap by TEOS (Tetraethyl orthosilicate) SiO_2. After finishing the fabrication of long polysilicon and silicon dioxide cavity, we etched away the silicon dioxide for the area with HSQ and air cavity. The 11% HSQ is spun at 2000 rpm to have around 210 nm thickness. After exposure and development, we use PECVD to deposit silicon dioxide to cap the air gaps and use chemical mechanical polishing (CMP) to planarize the surface. We anneal our sample to make HSQ turn into silicon dioxide material. After testing, there is about 20% thickness decrease after annealing. However, there is no obvious lateral dimension change or structure deformation (Figure 3). Through the similar processes we can fabricate the top part of our design.

We present a broadband multispectral color filter arrays covering from 450 nm to 910 nm with transmissions over 40% and FWHM less than 40 nm (Figure 4). The simulation is based on Rigorous coupled-wave analysis (RCWA). To overcome the effective index range limitations, we lower the cavity effective index by mixing air with silicon dioxide. To alleviate the fabrication challenges, we use the e-beam resist HSQ as the cavity layer which is close to silicon dioxide after annealing. We show that the patterned HSQ will not have obvious deformation after annealing at 700°C which make it a good alternative for silicon dioxide when pattern relatively small features.

Conclusion and Future Steps:

We present a MSFAs design that can cover the wavelength range from 450 nm to 910 nm aligned with the detection range of most silicon CMOS imaging sensors. We demonstrate the potential of using HSQ directly as a part of nanostructure which can have relatively small feature size after development and have similar optical property as silicon dioxide after anneal. With the HSQ and air cavity, the effective index range is extended which enables monolithic MSFAs to cover a wavelength range from visible to NIR.

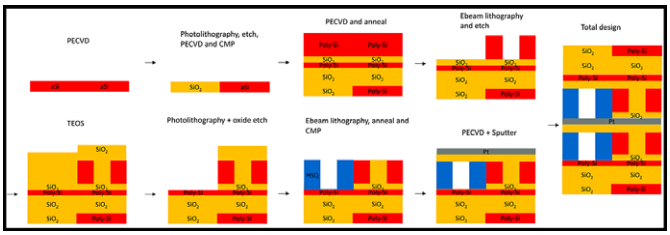

Figure 2: The main fabrication steps.

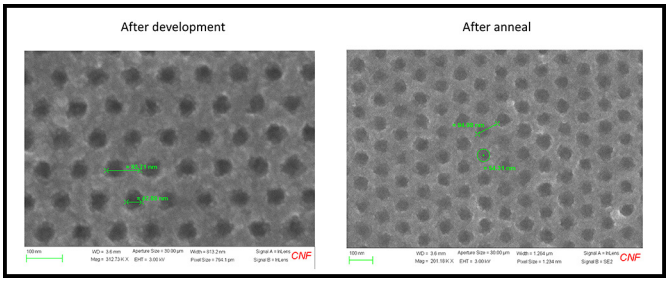

Figure 3: SEM images of patterned HSQ layers after development and anneal.

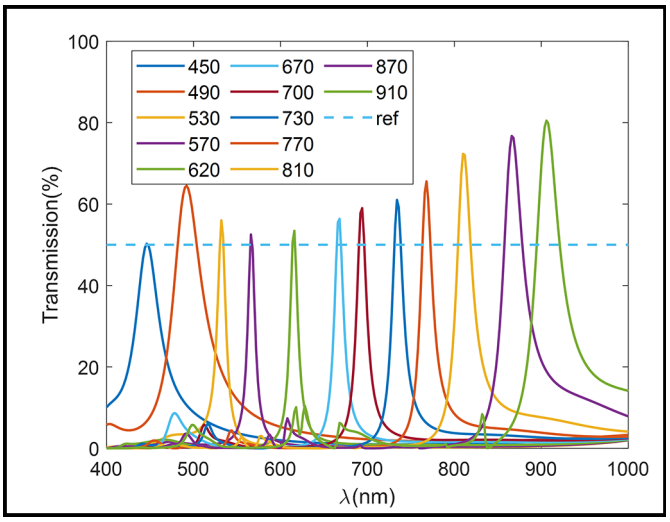

Figure 4: The relative transmission of different color filters based on simulation.

References:

[1] Lapray, P.-J., et al. Multispectral Filter Arrays: Recent Advances and Practical Implementation. Sensors 14, 21626-21659 (2014).

[2] McClung, A., et al. Snapshot spectral imaging with parallel metasystems. Sci. Adv. 6, eabc7646 (2020).

[3] Xu, T., et al. Plasmonic nanoresonators for high-resolution colour filtering and spectral imaging. Nat. Commun. 1, 59 (2010).

[4] Dong, Z., et al. Printing Beyond sRGB Color Gamut by Mimicking Silicon Nanostructures in Free-Space. Nano Lett. 17, 7620-28 (2017).

[5] Ferraro, A., et al. Guided-mode resonant narrowband terahertz filtering by periodic metallic stripe and patch arrays on cyclo-olefin substrates. Sci Rep 8, 17272 (2018).

[6] Park, C., Shrestha, V., Lee, S., and Choi, D., Trans-Reflective Color Filters Based on a Phase Compensated Etalon Enabling Adjustable Color Saturation. Scientific Reports 6, 25496 (2016).

[7] Xiang, J., Song, M., Zhang, Y., Kruschwitz, J., and Cardenas, J. Broadband tunable, narrow linewidth multispectral color filter. in Frontiers in Optics + Laser Science 2022 (FIO, LS) (2022).

High-Quality-Factor SiN Ring Resonator of 12 GHz Repetition Rate

CNF Project Number: 2524-17
Principal Investigator(s): Jaime Cardenas
User(s): Yi Zhang

Affiliation(s): The Institute of Optics, University of Rochester

Primary Source(s) of Research Funding: National Science Foundation

Contact: jaime.cardenas@rochester.edu, yzh239@ur.rochester.edu
Website(s): https://cardenaslabphotonics.com/

Primary CNF Tools Used: JEOL 9500, ASML PAS 5500/300C DUV Stepper, Oxford PECVD, PT Takachi HDP-CVD, LPCVD Furnace, Oxford 100 ICP Dielectric Etcher, Unaxis 770 Deep Silicon Etcher, PT Deep Silicon Etcher, YES EcoClean Asher, Xactix Xenon Difluoride Etcher

Abstract:

We demonstrate a high-quality-factor silicon nitride ring resonator of 12 GHz repetition rate. Special fabrication techniques are applied to acquire an intrinsic quality factor of 10 million as well as anomalous dispersion (for fundamental modes) in the resonator.

Summary of Research:

Silicon nitride (Si_3N_4) [1] is a high-performance material platform for chip-scale photonic devices. Benefiting from its ultra-low loss and good CMOS-compatibility, Si_3N_4 is a preferable choice for making waveguides, resonators, and other passive components for photonic integrated circuits (PICs). In addition, Si_3N_4 supports not only applications in the optical communications band but also in the visible [2] and the mid-infrared band, such as (bio)medical and (bio)chemical sensing, due to its broad transparency window (400-6700 nm [3]).

Ring resonator is one of the fundamental components in integrated photonics. It can work for versatile purposes, including laser cavity, modulator, filter, etc. In this work, we design and fabricate a Si_3N_4 ring resonator with anomalous dispersion (for fundamental modes) for generating dissipative Kerr solitons (DSK) [4]. The resonator has a cross-section of 1.6 μm × 0.76 μm. Such a structure supports a very confined fundamental transverse electric (TE0) mode (inset in Figure 1) and, therefore, leads to an anomalous dispersion [5].

We design the cavity length of the resonator to be 11.6 mm and have a repetition rate (the inverse of its round-trip time) of 12.3 GHz according to $T_R = L/c_0 n_g$ where T_R is the round-trip time, L is the cavity length, c_0 is the light speed in vacuum, and n_g is the group index of the guide mode (2.11 for TE_0 mode in our case). This repetition rate allows the incorporation of the generated solitons with radio frequency (RF) applications. Figure 1 shows a fabricated device.

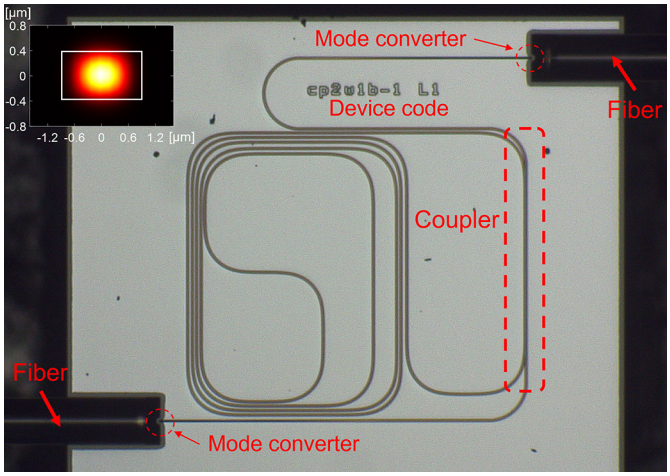

Figure 1: Camera picture of a fabricated device. Inset: TE_0 mode of the device.

We use adiabatic turnings in our spiral-like ring resonator to minimize the bending loss. The radius of curvature of the waveguide smoothly changes from 3 mm to 0.1 mm through a tanh function [6] instead of a conventional abrupt turning of fixed radius. We use SiO_2 mode converters [7] and tapered Si_3N_4 waveguides (Figure 2(c)) to optimize the power coupling efficiency from the fiber to the device.

The fabrication steps are shown in Figure 2(a-b). We deposit 0.76 μm stoichiometric Si_3N_4 using low pressure vapor chemical deposition (LPCVD) over 4 μm of thermally-grown silicon oxide (SiO_2) on silicon wafer. We rotate the wafer by 45° after every 300 nm deposition to alleviate the total strain accumulated in the film and prevent it from cracking [8]. We pattern the device using 100 kV electron-beam lithography. The pattern is exposed twice with half of the required dose each time ('double pass') for better lithography accuracy and better sidewall roughness. We etch the structure

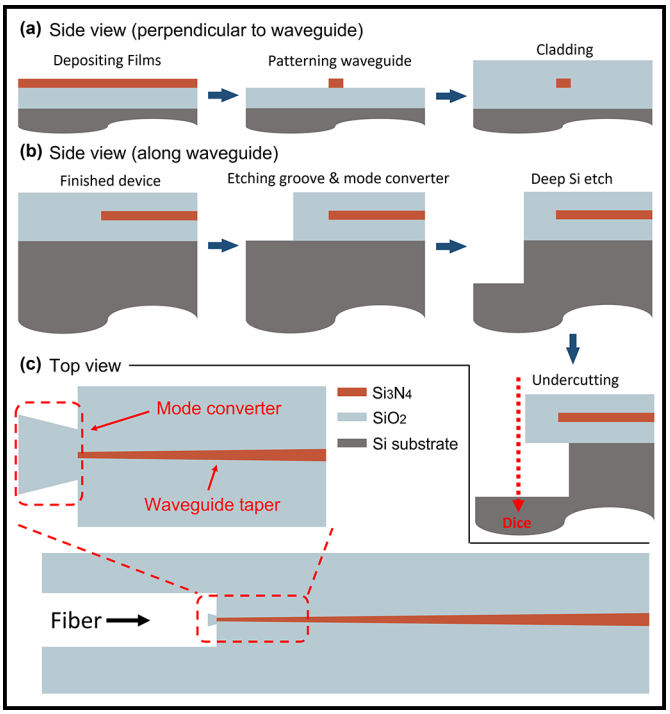

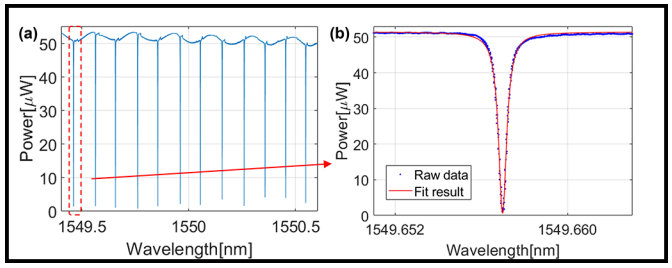

Figure 2, left: (a-b) Fabrication procedures of the device. (c) A zoom-in view of the waveguide taper and the mode converter.

Figure 3, above: (a) Measured typical transmission spectrum of the device. (b) Typical fitting result of a resonance.

with inductively coupled plasma reactive-ion etching (ICP-RIE). The etched structures are then clad with 4 μm SiO_2 through plasma-enhanced chemical vapor deposition (PECVD). Afterward, we pattern the mode converters and the grooves, which are used to ensure stable fiber-to-chip power coupling, with deep ultraviolet (DUV) lithography. The SiO_2 outside the chip boundary is etched using ICP-RIE. We continue to etch down the exposed Si substrate by approximately 100 μm using a Bosch process so that fibers can be pushed all the way to the mode converter (vertically aligned) after dicing without being blocked by the substrate. We anneal the device at 1200°C to improve the material quality and mitigate the material loss. Finally, we use the isotropic XeF_2 etch to remove the Si beneath the mode converter and make it suspended after dicing the wafer into chips.

We then measure the transmission spectrum (Figure 3(a)) of the fabricated device and characterize its performance. Figure 3(a) shows a typical spectrum. We numerically fit (Figure 3(b)) the resonances in the spectrum using a Lorentzian equation [9]

$$T = T_0 \frac{(a-t)^2 + \frac{4at\pi^2}{FSR^2}(\lambda-\lambda_0)^2}{(1-at)^2 + \frac{4at\pi^2}{FSR^2}(\lambda-\lambda_0)^2}$$

where T stands for power transmission, T_0 is a constant, t is the field transmission of the coupler, a is the round-trip field transmission of the ring, FSR is the free spectral range, λ is the testing laser wavelength, and λ_0 is the central wavelength of the resonance. The round-trip is approximately 1% across the 1480-1640 nm bandwidth, which corresponds to a propagation loss of 0.04 dB/cm and an intrinsic quality factor of 10 million in our 11.6 mm ring.

We further extract the group index and the group velocity dispersion of the device (TE_0) to be 2.11 (corresponding to 12.3 GHz repetition rate) and -1.84 × 10^5 fs^2/m, respectively.

Conclusions and Future Steps:

In conclusion, we demonstrate a silicon nitride ring resonator with anomalous dispersion, 12.3 GHz repetition rate, and 10 million intrinsic quality factor. This work will help to enable RF-frequency applications directly based on high-performance Si_3N_4 ring resonators.

References:

[1] Blumenthal, Daniel J., et al. "Silicon nitride in silicon photonics." Proceedings of the IEEE 106.12 (2018): 2209-2231.

[2] Porcel, Marco AG, et al. "Silicon nitride photonic integration for visible light applications." Optics & Laser Technology 112 (2019): 299-306.

[3] Soref, Richard. "Mid-infrared photonics in silicon and germanium." Nature photonics 4.8 (2010): 495-497.

[4] Kippenberg, Tobias J., et al. "Dissipative Kerr solitons in optical microresonators." Science 361.6402 (2018): eaan8083.

[5] Foster, Mark A., et al. "Broad-band optical parametric gain on a silicon photonic chip." Nature 441.7096 (2006): 960-963.

[6] Ji, Xingchen, et al. "Exploiting ultralow loss multimode waveguides for broadband frequency combs." Laser & Photonics Reviews 15.1 (2021): 2000353.

[7] Nauriyal, Juniyali, et al. "Fiber-to-chip fusion splicing for low-loss photonic packaging." Optica 6.5 (2019): 549-552.

[8] El Dirani, Houssein, et al. "Crack-free silicon-nitride-on-insulator nonlinear circuits for continuum generation in the C-band." 2018 IEEE Photonics Conference (IPC). IEEE, 2018.

[9] Cardenas, Jaime, et al. "High Q sic microresonators." Optics express 21.14 (2013): 16882-16887.

Ultrathin Infrared Photonic Devices Based on Semiconductor-Metasurfaces

CNF Project Number: 2979-21
Principal Investigator(s): Gennady Shvets
User(s): Melissa Bosch

Affiliation(s): School of Applied and Engineering Physics, Department of Physics; Cornell University
Primary Source(s) of Research Funding: Office of Naval Research (ONR), National Science Foundation (NSF)
Contact: gs656@cornell.edu, mb2583@cornell.edu
Website(s): http://shvets.aep.cornell.edu
Primary CNF Tools Used: JEOL 9500, Zeiss Ultra SEM, Oxford 100 Etcher, Oxford PECVD, Woollam RC2 Ellipsometer

Abstract:

Metasurfaces, composed of planar arrays of sub-wavelength-scale optical antennae, provide tailored resonant modulations to electromagnetic fields. We fabricate semiconductor-based metasurfaces fit for a range of photonic applications in the near-and mid-infrared. For instance, we apply an amorphous silicon (aSi) metasurface to demonstrate an ultrathin wide-aperture multicolor lens. In another application, we exploit tailored field enhancements of silicon-on-sapphire (SOI)-metasurfaces to facilitate deeply-subwavelength femtosecond (fs) laser machining.

Multicolor aSi-Metalens:

Modern imaging systems rely on compact, wide-aperture, and aberration-free lenses. Although submicron-thick optical metasurfaces have achieved high-performance focusing [1], they exhibit high chromatic aberrations, making them unsuitable multicolor imaging applications. Various approaches to achromatic metalensing have been developed [2], but they are typically limited by computational complexity or low numerical aperture (NA). Our project considers a new type of high-NA multi-color metalens, engineered to reuse identical discrete phase requirements in every consecutive 2π phase increment (Fresnel zone) of its phase profile, thereby significantly simplifying its design. To test this concept, we fabricated a spherical metalens with a diameter of 1 mm. Figure 1(a) shows a representative scanning electron microscope of the building blocks of the metalens, which are 600-nm-thick rectangular aSi bricks arranged periodically on a silica substrate. These structures support Mie-type optical resonance modes that can be customized by altering the resonator's geometrical parameters. The metalens comprises only fifteen distinct resonator geometries that are optimized to provide a wavelength- and radially-dependent phase profile resulting in the multicolor focusing of two near-infrared wavelengths. Metalens fabrication consisted of six total steps: plasma-enhanced chemical vapor deposition (Oxford PECVD) of aSi onto fused silica substrate; HSQ-6% spincoat, baking, and electron beam lithography (EBL) exposure at 6mC/cm^2 (JEOL9500FS); development in TMAH/NaCl (0.25/0.7N) salty solution; and pattern transfer to the aSi layer through an inductively coupled HBr plasma reactive ion etch (Oxford Cobra). The resulting samples were characterized using a scanning electron microscope (Zeiss Ultra). Our simulations predict diffraction-limited and chromatic-aberration-free focusing of the two operation wavelengths at a focal distance of z = 5 mm. The experimental characterization of our first-generation device shows a primary focal spot at the predicted z-position (5mm) for both wavelengths of light (as shown in Figure 1b). However, there are a few unintended spurious maxima appearing at different z-positions. The production of improved devices is underway.

Subwavelength fs-Laser Nanomachining using SOI-Metasurfaces:

In a second application, we employ tailored electromagnetic field distributions of resonant semiconductor microstructures to enhance the spatial resolution and control of laser-nanostructuring. While laser-machining approaches are typically restricted by the diffraction limit to yield a smallest resolvable dimension equal to half the laser wavelength [3], our project considers deeply-subwavelength-scale ($\sim\lambda/50$) modifications to Si-based microresonators illuminated

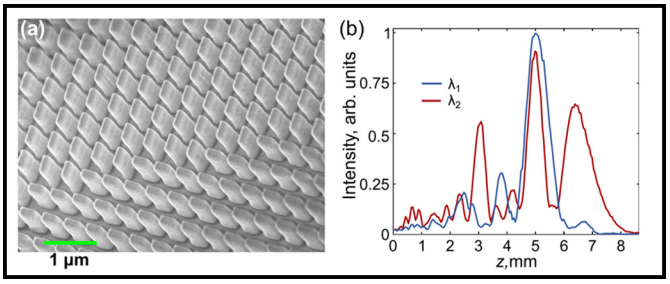

Figure 1: (a) A zoomed-in scanning electron microscopy (SEM) image of rectangular aSi pillars on a silica substrate, comprising the aSi metalens. (b) Experimental on-axis intensity of light transmitted through a first-generation multicolor aSi-metalens. The lens focuses wavelengths of λ_1 = 980 nm (blue line) and λ_2 = 735 nm (red line) into a primary intensity maximum at z = 5 mm.

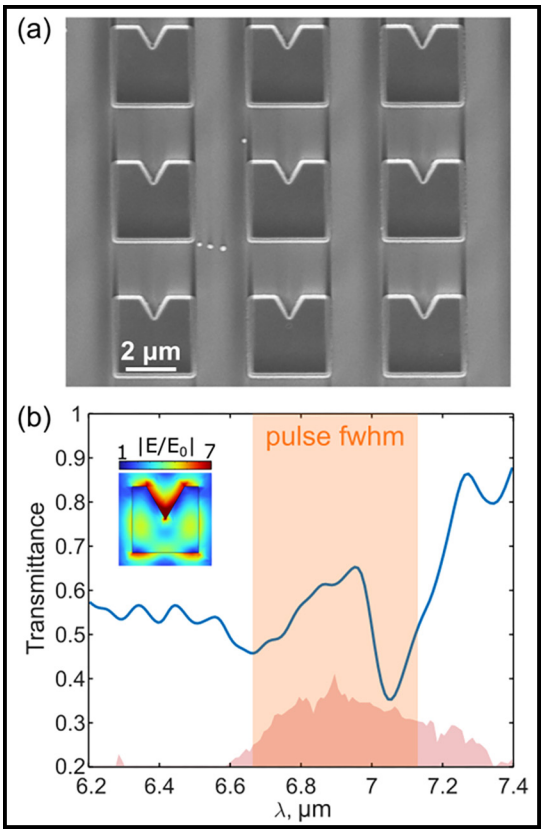

Figure 2: (a) SEM image of a SOI-metasurface designed to enhance the field intensity at the apex of its triangular notch. (b) Representative experimental transmission spectra of the metasurface. Inset: simulated electric field profile of the resonator.

by fs laser pulses. We accomplish this result by designing SOI metasurfaces that resonate near the laser wavelength and exhibit highly-nonlinear photoinduced free carrier production. Illuminating the Si-resonators with few-pulse trains below the single-pulse damage threshold facilitates localized phase explosions and gradual volumetric material ablation in the region of peak field intensity. For device fabrication, we start with the RIE etching of a commercial SOI wafer to the desired thickness, followed by a standard PMMA spin-coat, baking, EBL exposure at 900 μC/cm^2 (JEOL 9500FS), development in MIBK:IPA 1:3 for 90s, e-beam evaporation of 30 nm chromium (Cr) or 80 nm alumina hard mask (CVC SC4500), liftoff in room-temperature sonicated acetone for 30 min, RIE etching to substrate; and removal of Cr or alumina mask by wet etchant. Figure 2 presents an SEM image of the fabricated metasurface prior to laser irradiation alongside its experimental transmission spectra. Figure 3 shows examples of nanotrench formation under various conditions of laser pulse intensity and number.

References:

[1] Pan, Meiyan, et al. Light: Science & Apps 11.1 (2022): 195.
[2] Wang, Shuming, et al. Nature Nanotech 13.3 (2018): 227-232.
[3] Perry, M. D. et al., Journal of Applied Physics 85, 6803 (1999).

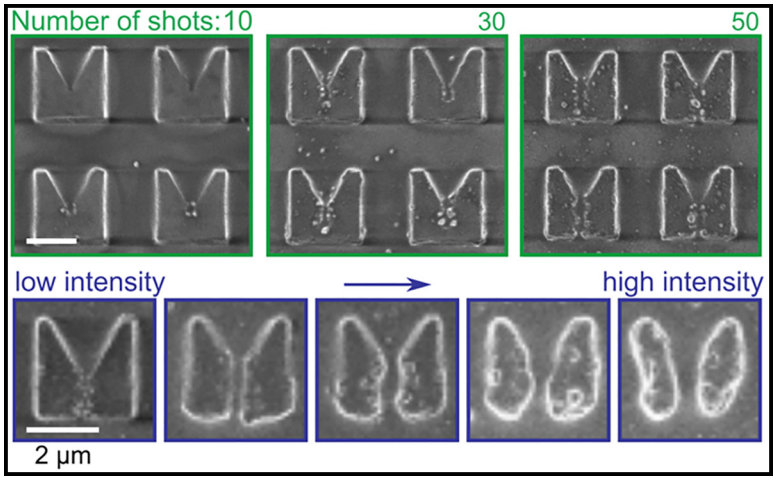

Figure 3: Trench formation in SOI-resonator arrays illuminated with variable (a) shot-numbers and (b) intensities of 7 µm-wavelength incident laser pulses, increasing from left to right.

HfO_2-Based Platform for High Index Contrast Visible and UV Integrated Photonics

CNF Project Number: 2985-21
Principal Investigator(s): Karan Kartik Mehta[2]
User(s): Oscar Jaramillo[1,2], Joshua Tensuan[2]

Affiliation(s): 1. School of Applied and Engineering Physics,
2. School of Electrical and Computer Engineering; Cornell University

Primary Source(s) of Research Funding: Cornell University

Contact: karanmehta@cornell.edu, oj43@cornell.edu

Primary CNF Tools Used: Metricon, Zeiss Ultra SEM, JEOL 9500, PT770 Etcher, WoollamRC2 Spectroscopic Ellipsometer, AFM, Furnace, Oxford PECVD, Oxford FlexAL

Abstract:

We study HfO_2/Al_2O_3 composites for high-index visible/ultraviolet photonics, exhibiting single-mode waveguides losses of 1.9 ± 1 dB/cm for λ = 405 nm.

Summary of Research:

Integration of photonic devices in the visible and UV is necessary for several applications such as spectroscopy and control of ion systems on chip [1-3]. However, photonic devices operating in the visible and UV have lagged behind those operating in the near infrared devices since common materials used in photonic devices absorb at short wavelengths, and scattering losses increase as wavelengths decrease.

Alumina (Al_2O_3) is a CMOS compatible material that can be deposited in amorphous form, and has been used to demonstrate single-mode (SM) propagation as low as 3 dB/cm at 371 nm [4]; however, its relatively low index (n~1.7) is a limitation. High refractive index is desirable in many settings since it allows, for example, strong optical confinement, compact device footprints, high efficiency grating devices (grating strengths scale approximately as $\sim (n_{core}^2 - n_{cladding}^2)^2$), and efficient acousto-optic interaction (scaling as n^6). HfO_2 is promising material — a wide band-gap (5.65 eV) [5] with a high refractive index (n~2.1), can be deposited amorphously, and is CMOS compatible. However, its propensity to crystallize results in significant optical loss, and its use in photonics has been limited to settings where the optical interaction length is on the order of 100s of nm [6,7]. Incorporation of moderate proportions of Al_2O_3 dramatically reduces losses in films; this is attributed to inhibited crystallization of HfO_2 [8]. Here, we demonstrate methods to lithographically pattern nanophotonic structures composed of alternating layers of Al_2O_3 and HfO_2, deposited via atomic layer deposition (ALD), and present preliminary SM propagation losses in patterned waveguides formed from the composite.

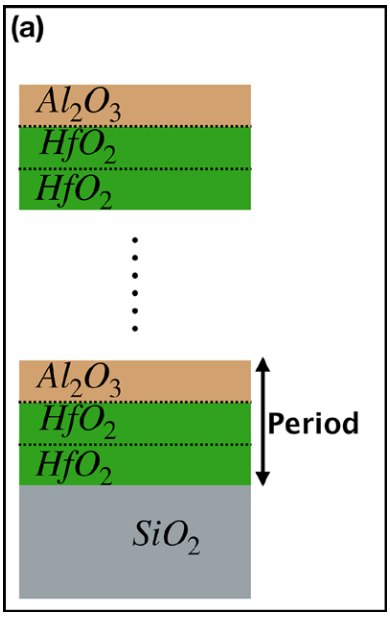

Figure 1: Single layers of HfO_2 and Al_2O_3 are deposited on top of SiO_2 in an inter-layered periodic way. A DC = 0.33 is shown here with P=3 layers.

Our approach to mitigating loss from crystallization relies on depositing alternating HfO_2 and Al_2O_3 layers at different duty cycles (DC) and periods (P) in a plasma enhanced ALD (PEALD) process. Figure 1 shows the structure of the composite films; P represents the total number of layers per period, with DC the fraction of atomic layers per period that are Al_2O_2. Previous work [8], showed that as the DC changes from 0 (HfO_2 only) to 1 (Al_2O_3 only), the refractive index decreases as if the index of the composite was the weighted average of n(Al_2O_3) and n(HfO_2) according to fractional composition. Measurements of slab mode propagation loss at λ = 406 nm by the prism coupling method showed that losses can be 4.2 dB/cm for a period of three layers and a DC ~ 0.3. In contrast, losses in pure HfO_2 at this wavelength were well above 30 dB/cm. The observed decrease in loss is accompanied by a reduction in index to n = 1.95, though still preserving most of HfO_2's advantage over Al_2O_3.

Work to pattern the composite material into photonic devices was conducted at the Cornell NanoScale Facility (CNF). Devices were fabricated on a silicon wafer with

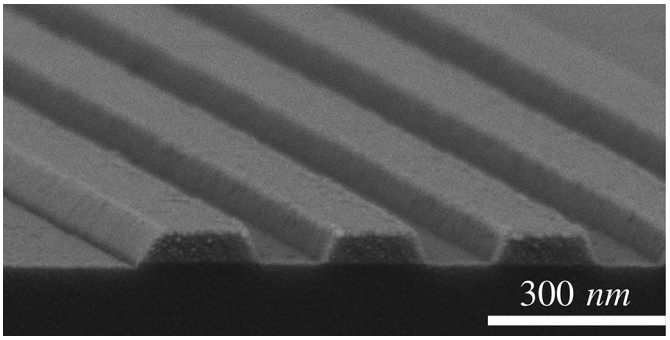

Figure 2: SEM image of ridges etched into the composite films as test structures.

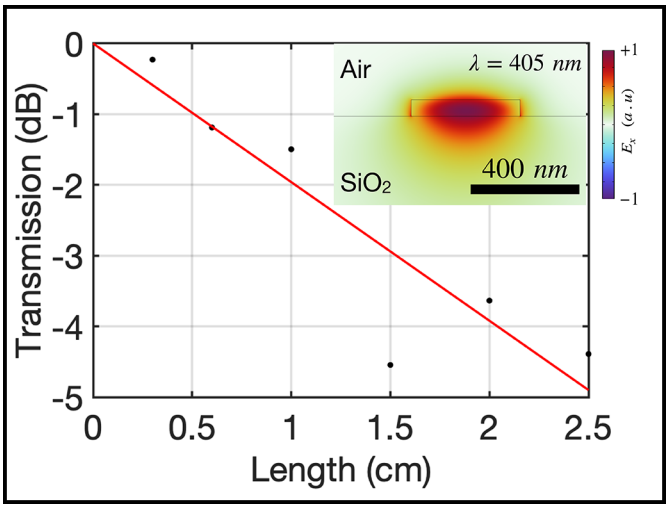

Figure 3: Measured fiber-fiber transmission at λ = 405 nm as a function of propagation length for a 200 by 60 nm waveguide. Points represent measured values, the slope of the fit indicates propagation losses of 1 dB/cm. Inset: Mode profile of measured transmission.

3 mm of thermally grown wet silicon oxide (SiO_2) provided by Rogue Valley Microdevices. Composite films of HfO_2 and Al_2O_3 at DC = 0.33 and P = 3 layers deposited at CNF exhibited material losses of 8 dB/cm at λ = 405 nm (<2 dB/cm at λ = 730 nm) after initial deposition and 2.8 dB/cm at λ = 405 nm (< 1 dB/cm at λ = 730 nm) after a one hour anneal at 800°C.

Test structures to measure propagation losses in SM rectangular waveguides were designed, including fiber surface grating couplers for characterization at λ = 730 nm and at λ = 405 nm. The pattern was defined with electron-beam lithography (JEOL9500) using ZEP520-A resist, and then transferred to the composite material with an inductively coupled plasma (ICP) etching process utilizing a BCl_3/Ar chemistry.

Figure 2 shows an SEM image of the resulting profile for straight waveguide strips in the composite after etching. Preliminary measurements on the resulting structures show losses of 1.9 ± 1 dB/cm for λ = 405 nm in a nominally 400 × 60 nm waveguide with top air cladding (Figure 3). Accounting for a confinement factor of ~33%, we find that propagation losses arising from surface roughness in a patterned waveguide contribute about half of the total propagation losses. SiO_2 cladding is expected to further reduce losses from surface roughness scattering, pushing waveguide transmission to be predominantly limited by the material.

Conclusions and Future Steps:

This work shows that HfO_2 /Al_2O_3 composite layers can be patterned into low-loss and high index integrated photonic structures, enabling high index contrast devices in the visible and UV. Improvement on sidewall roughness and etch profile is in progress, and future work will assess the ultimate material loss limit in this platform. This work may lead to significantly more efficient grating devices, compact footprints, and microresonant structures, among others, for photonics at blue/UV wavelengths as compared to platforms in pure Al_2O_3. High index, deposited waveguide core materials are also likely to be enabling in active electro- and acousto-optic device configurations.

References:

[1] Daniel J. Blumenthal. Photonic integration for UV to IR applications. APL Photonics 5, 020903, 2020.

[2] Galan Moody, et al. Roadmap on integrated quantum photonics. J. Phys. Photonics 4 012501. 2022.

[3] Mehta, K., Bruzewicz, C., McConnell, R., et al. Integrated optical addressing of an ion qubit. Nature Nanotech 11, 1066-1070, 2016.

[4] Gavin N. West, William Loh, Dave Kharas, Cheryl Sorace-Agaskar, Karan K. Mehta, Jeremy Sage, John Chiaverini,and Rajeev J. Ram. Low-loss integrated photonics for the blue and ultraviolet regime. APL Photonics 4, 026101, 2019.

[5] L. Kang, B. H. Lee,W.-J. Qi, Y. Jeon, R. Nieh, S. Gopalan, K. Onishi, and J. C. Lee. Electrical characteristics of highly reliable ultrathin hafnium oxide gate dielectric. IEEE Electron Device Letters, vol. 21, no. 4, pp. 181-183, 2000.

[6] P. Torchio, A. Gatto, M. Alvisi, G. Albrand, N. Kaiser, and C. Amra. High-reflectivity HfO_2/SiO_2 ultraviolet mirrors. Applied Optics, vol. 41, no. 16, pp. 3256-3261, 2002.

[7] Zhang, C., Divitt, S., Fan, Q. et al. Low-loss metasurface optics down to the deep ultraviolet region. Light Sci Appl 9, 55, 2020.

[8] Leonardo Massai. High Polarization Purity and Short-wavelength Optics for Trapped-ion Quantum Systems. Master's thesis, ETH, 2021.

Metamaterial Spectrometer: A Low SWaP, Robust, High Performance Hyperspectral Sensor for Land and Atmospheric Remote Sensing

CNF Project Number: 3003-22
Principal Investigator & User: Lori Lepak

Affiliation(s): Phoebus Optoelectronics LLC
Primary Source(s) of Research Funding: National Aeronautics and Space Administration (NASA)
Contact: llepak@phoebusopto.com
Website(s): www.phoebusopto.com
Primary CNF Tools Used: ASML DUV stepper, Oxford ALD / PECVD / 81 etcher, Logitech CMP, Supra SEM

Abstract:

Since 2003, Phoebus Optoelectronics has enabled custom R&D solutions in the fields of Plasmonics, Metamaterials, Antennas, and Sensors. We work closely with our customers throughout device development, from simulation and design, to prototype realization, testing, and small volume manufacturing. Our R&D portfolio spans the spectral ranges of visible light, infrared, THz, and microwave radiation, for applications in high resolution imaging systems, wavelength and polarization filtering, tunable optical components, beam forming and steering, solar cells, renewable energy devices, and chemical and biological toxin sensors. We routinely partner with large, industry-leading businesses to develop products in all of these areas, jointly performing advanced testing and working together to scale up to medium- and large-volume manufacturing. Our agile team makes extensive use of the resources at the CNF for our nano/micro fabrication and testing, to provide cost efficiency and rapid turnaround.

In the present report, we discuss the ongoing development of a metamaterial-based hyperspectral imaging filter.

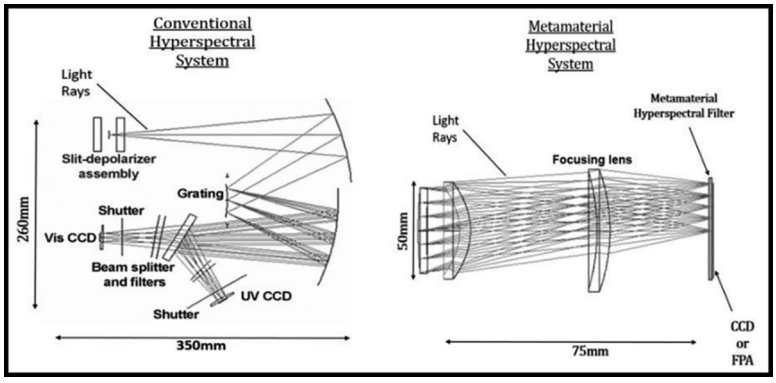

Figure 1: Phoebus's Metamaterial Spectrometer (MS) technology (right) eliminates much of the size and weight of conventional hyperspectral spectrometer technologies (left). Note the significant difference in scale of the two images.

Summary of Research:

Phoebus uses the resources of the CNF to fabricate plasmonic chips patterned with a metamaterial surface to enable Extraordinary Optical Transmission (EOT), a phenomenon unique to metastructures in which light is transmitted through apertures much smaller than the incident wavelength, at anomalously large intensities relative to the predictions of conventional aperture theory. EOT was first observed by T.W. Ebbesen in 1998 [1]. Since its founding in 2003, Phoebus has successfully harnessed EOT by incorporating metasurfaces into devices used to perform light filtering [2-3], photon sorting [4-5], polarimetric detection [6], high speed optical detection [7], and SPR plasmonic sensor chips [8].

In our current project, we are developing a hyperspectral imaging system, shown schematically in Figure 1. Our technology (Figure 1b) uses a metasurface to precisely target very narrow spectral bands of interest, enabling a significant reduction in the size and number of optical components relative to current state-of-the-art imaging systems (Figure 1a), which in turn will enable the integration of our high-performance sensor onto weight-sensitive platforms (ie. satellites) far more readily than existing systems. Our initial goal is to detect and image trace gases in the Earth's atmosphere in the midwave infrared (MWIR), defined as 3-5 μm wavelength, while minimizing dependence on the Angle of Incidence (AoI) of light upon the sensor, up to an angle of 12° off-normal.

Using the ASML DUV stepper, entire wafers can rapidly be lithographically patterned with highly uniform, large-area arrays of metastructures, as shown in Figure 2. In general, the optimal feature size and period of these metastructures depends primarily upon the desired

wavelength of operation and the refractive indices of the constituent materials. In the MWIR, typical feature sizes are on the order of ~ 1 μm. Equally critical for minimizing optical losses in photonics applications, the relatively narrow spaces between features can be etched to form high-aspect-ratio structures with nearly vertical sidewalls, as shown in Figure 3.

Conclusions and Future Steps:

With strong, ongoing support from the National Aeronautics and Space Administration (NASA), we have successfully tested our second generation MWIR devices. As shown in Figure 4, they demonstrated the desired AoI insensitivity up to 12°. As we finish optimizing a few key process improvements in our third generation devices, we are beginning to develop a fourth generation design, in which we will fully optimize and pixelate our MWIR device. In addition, we are adapting our metasurface technology to other spectral ranges, from the visible to the microwave, by substituting appropriate materials, and scaling feature sizes as appropriate to the imaging wavelength. The extensive resources of the CNF are enabling us to rapidly develop our Metamaterial Spectrometer technology for a broad range of imaging and sensing applications.

References:

[1] Ebbesen, T.W., et al., "Extraordinary optical transmission through sub-wavelength hole arrays." Nature, (1998). 391(6668): p. 667-669.

[2] Crouse, D. "Numerical modeling and electromagnetic resonant modes in complex grating structures and optoelectronic device applications." Electron Devices, IEEE Transactions on 52.11 (2005): 2365-2373.

[3] Crouse, D., and Keshavareddy, P. "Polarization independent enhanced optical transmission in one-dimensional gratings and device applications." Optics Express 15.4 (2007): 1415-1427.

[4] Lansey, E., Crouse, D., et al. "Light localization, photon sorting, and enhanced absorption in subwavelength cavity arrays." Optics Express 20.22 (2012): 24226-24236.

[5] Jung, Y.U; Bendoym, I.; Golovin, A.B.; and Crouse, D.T. "Dual-band photon sorting plasmonic MIM metamaterial sensor." Proc. SPIE 9070, Infrared Technology and Applications XL, 90702X (June 24, 2014); doi:10.1117/12.2050620.

[6] Crouse, D., and Keshavareddy, P. "A method for designing electromagnetic resonance enhanced silicon-on-insulator metal-semiconductor-metal photodetectors." Journal of Optics A: Pure and Applied Optics 8.2 (2006): 175.

[7] Mandel, I.; Gollub, J.; Bendoym, I; Crouse, D. Theory and Design of A Novel Integrated Polarimetric Sensor Utilizing a Light Sorting Metamaterial Grating. Sensors Journal, IEEE, (2012): Vol. PP, 99

[8] Lepak, L., et al. "Handheld chem/biosensor using extreme conformational changes in designed binding proteins to enhance surface plasmon resonance (SPR)" Proc. SPIE 9862, Advanced Environmental, Chemical, and Biological Sensing Technologies XIII, 9862-7 (April 17, 2016); doi:10.1117/12.2222305.

[9] Bendoym, I., Lepak, L., Leitch, J., Applegate, J., Crouse, D. "Low SWaP-C hyperspectral metamaterial spectrometer (MMS) for narrow-band, wide angle-of-incidence MWIR atmospheric sensing," Proc. SPIE 12091, Image Sensing Technologies: Materials, Devices, Systems, and Applications IX, 120910J (30 May 2022); https://doi.org/10.1117/12.2632794

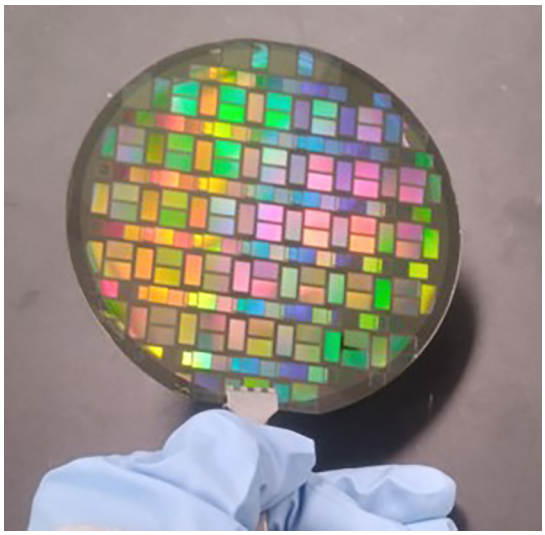

Figure 2: Wafer lithographically patterned with optical metastructures, using the ASML DUV stepper.

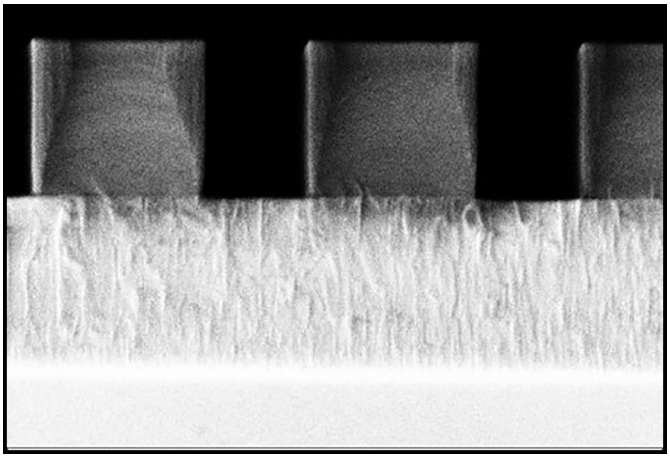

Figure 3: SEM image (cross section) of etched pillars with near-vertical sidewalls. Imaged at ~90kX in the Supra SEM, the grain structure of the etch stop layer is clearly visible.

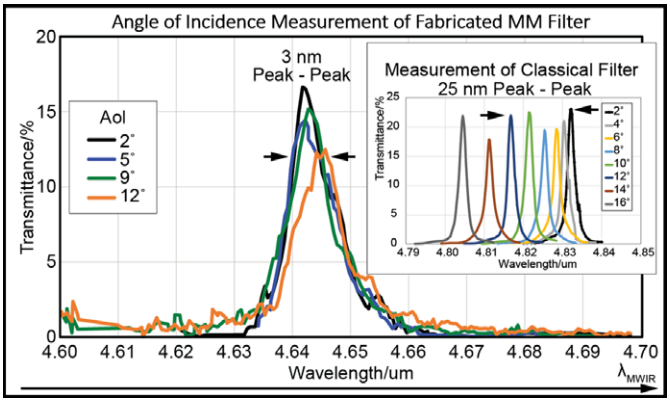

Figure 4: Measured optical performance of fabricated metamaterial filter showing the angle of incidence independence up to a cone of 12° (f/2.4). (Inset) Same measurement performed on a classical Fabry-Pérot filter. Reproduced from reference 9.

Distributed Bragg Reflectors Fabricated by Plasma-Enhanced Chemical Vapor Deposition

CNF Project Number: 3077-23
Principal Investigator(s): A. Nickolas Vamivakas[1], Todd D. Krauss[1,2]
User(s): Robert Collison[1]

Affiliation(s): 1. The Institute of Optics, University of Rochester, Rochester, NY, United States; 2. Department of Chemistry, University of Rochester, Rochester, NY, United States

Primary Source(s) of Research Funding: National Science Foundation, Centers for Chemical Innovation, Award Number CCI-2124398: Quantum Electrodynamics for Selective Transformations (CCI QuEST)

Contact: nick.vamivakas@rochester.edu, todd.krauss@rochester.edu, rcolliso@ur.rochester.edu

Website(s): https://www.rochester.edu/quest/

Primary CNF Tools Used: Oxford PECVD, PT Takachi HDP-CVD, Woollam Ellipsometer, FilMetrics F40-UV, SC-4500

Abstract:

Distributed Bragg Reflectors (DBRs) are mirrors composed of alternating layers of two different transparent materials with different refractive indices (n). When two parallel DBRs are separated by a transparent spacer layer, a Fabry-Pérot microcavity is formed. In such a cavity, the Q-factor of the cavity's resonant mode increases with the reflectivity of the DBRs. Thus, in order to create microcavities with high Q-factors, we tested several designs and compared the reflectance spectra of the resulting DBRs to determine which design produces the highest reflectance at the desired wavelengths.

Summary of Research:

Unlike metal mirrors that reflect light across a broad range of wavelengths, the high-reflectance of a DBR is limited to range of wavelengths known as a stopband. These are the wavelengths of light that are strongly reflected (e. g. reflectance R ≥ 0.99) by a DBR due to the constructive interference of the light scattered from the interfaces between the high- and low-index materials [1]. To make a DBR that reflects strongly at a certain wavelength, λ_{center}, at normal incidence, the layers are fabricated with thickness $d = \lambda_{center}/4n$ (Figure 1). With a sufficient number of layers (roughly 15 or more), a DBR thus fabricated will exhibit high reflectance at normal incidence over a range of wavelengths around λ_{center}. For example, a 31-layer DBR made with λ_{center} = 500 nm reflects light strongly (with R ≥ 0.95) from about 450 to 550 nm. Outside of this stopband region, the reflectance of the DBR is low and varies sinusoidally with wavelength, as shown in Figure 2(a).

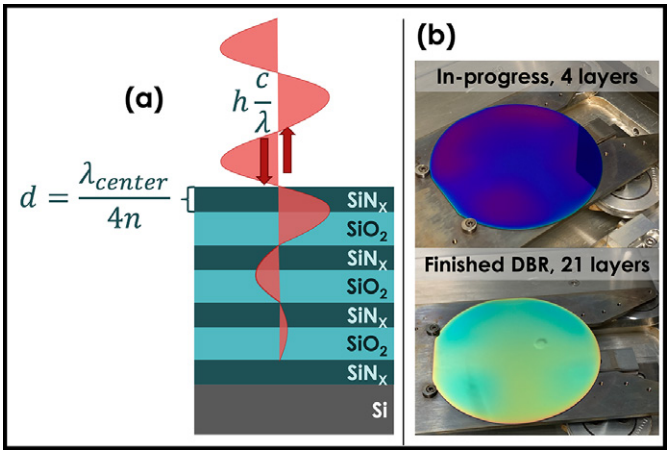

Figure 1: (a) DBR reflection at normal incidence. The impinging light wave is reflected due to the constructive interference of the individual reflections from each SiN_x/SiO_2 interface. (b) The reflection spectrum and color of the SiN_x/SiO_2 film stack on an Si wafer changes radically as layers are added during the deposition of a 21-layer DBR on Si with λ_{center} = 580 nm.

We tested several DBR designs and compared the resulting spectra. DBRs made of alternating layers of silicon nitride (SiN_x) and silicon oxide (SiO_2) were deposited using the Oxford plasma-enhanced chemical vapor deposition (PECVD) instrument. These DBRs were deposited onto 4-inch wafers of SiO_2, Si, or Si that had been coated with 200 nm of Ag in the SC4500 electron-beam evaporator.

We compared of Si- to Ag-backed DBRs (Figure 2) to determine if Ag-backed DBRs would exhibit greater reflectivity than the Si-backed DBRs, as was reported in the literature for 20-layer DBRs [2]. However, we found that, for 31-layer DBRs, the Ag-backed DBRs were not significantly more reflective than the Si-backed DBRs (Figure 2(a)). The simulated reflection spectra calculated using the transfer matrix method (TMM) likewise indicates that the Ag-backed DBR is not expected to reflect more strongly than the Si-backed DBRs for 31-layer DBRs (Figure 2(b)).

In other words, since the reflectivity of a 31-layer DBR is essentially "saturated" within the stopband region due to the constructive interference of the reflections from

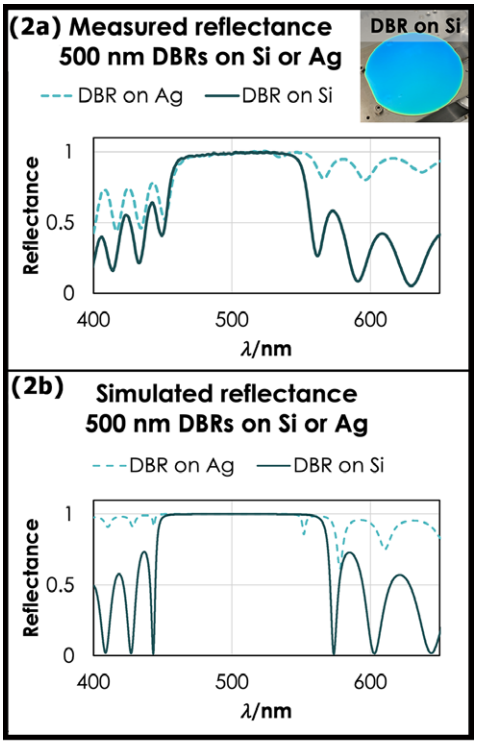

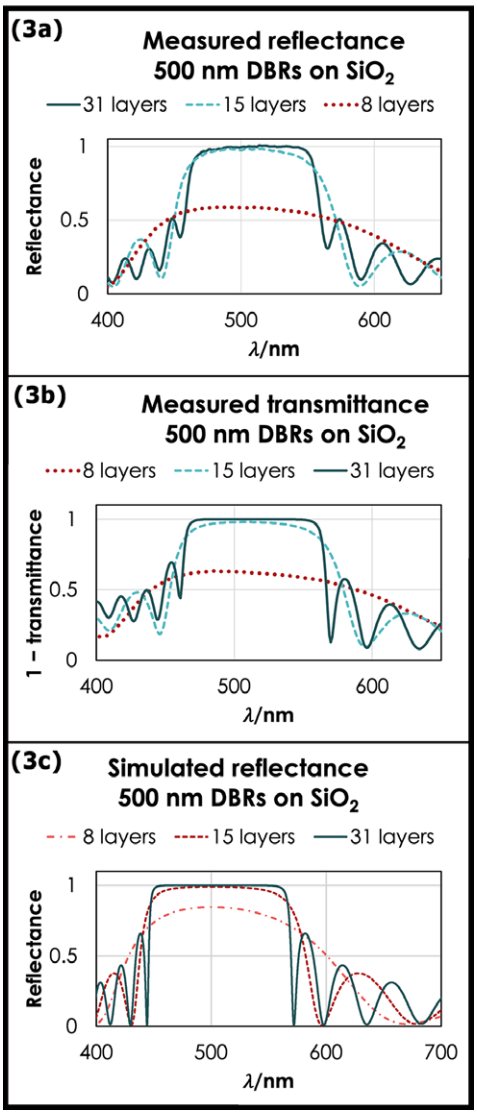

each SiO_2/SiN_x interface, no significant increase in the reflection from the underlying Ag film could be observed. Additionally, the simulated spectrum shows a distinct dip in the reflectance in the DBR stopband for the Ag-backed DBRs due absorption of light into the Tamm plasmon mode [3]. This dip is also present in the experimental reflection spectrum of the Ag-backed DBR, but the absorption peak is much less distinct in the measured spectrum than in the simulated data. This might also be due to the "saturation" of the DBR reflectance for these materials at 31 layers, such most of the impinging light in the stopband region does not reach the Ag film underneath the DBR.

We also compared the spectra of DBRs having various numbers of SiN_x and SiO_2 layers deposited on SiO_2 wafers (Figure 3). Since these samples were deposited on transparent substrates, both their reflection and their transmission spectra were measured and compared (Figure 3). The spectra show that 8 layers is too few to make a highly reflective ($R > 0.95$) DBR; that 15 layers makes a DBR with low, but non-zero, transmittance in the stopband region; and that, for 31 layers, the transmittance in the stopband region is at or below the background noise level of the spectrometer (Woollam RC2 Ellipsometer, operated in the transmission configuration). Note that these conclusions are essentially qualitative. To precisely quantify the DBRs' transmittance in the stopband region would require measurement of the reflected and transmitted light using lasers or supercontinuum white light sources.

Acknowledgements:

We thank the NSF for supporting this work as part of The Center for Quantum Electrodynamics for Selective Transformations (CCI-2124398). We would also like to thank the CNF staff, especially Jeremy Clark for his assistance with the Oxford PECVD, Alan Bleier for his assistance with the Woollam RC2 Ellipsometer, and Aaron Windsor for assistance on the electron-beam evaporator. Finally, we thank Mitesh Amin at The University of Rochester for authoring the MATLAB script used to simulate the DBR reflection spectra.

References:

[1] Maxwell Rules - Distributed Bragg Reflectors. http://maxwellrules.com/meep/distributed_bragg_reflector.html (accessed 2022-10-03).

[2] McGhee, K. E., et al. Polariton Condensation in an Organic Microcavity Utilising a Hybrid Metal-DBR Mirror. Sci. Rep. 2021, 11 (1), 20879. https://doi.org/10.1038/s41598-021-00203-y.

[3] Li, L.; Hao, H. Evolution of High-Order Tamm Plasmon Modes with a Metal-PhC Cavity. Sci. Rep. 2022, 12 (1), 14921. https://doi.org/10.1038/s41598-022-19435-7.

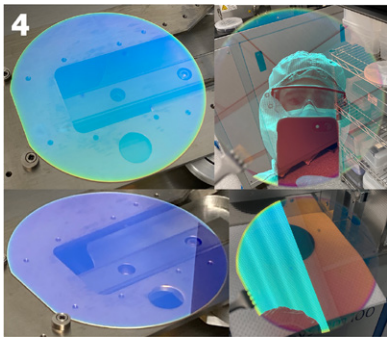

Figure 2, top left: *λ_{center} = 500 nm DBRs on Si or Ag. (a) DBR reflection spectra measured on the Filmetrics F40-UV. Inset: a photo of the 500 nm DBR on Si. (b) Simulated DBR reflection spectra calculated by TMM.* **Figure 3, bottom left:** *(a) Reflection and (b) transmission spectra of 500 nm DBRs with various layer numbers on SiO_2 wafers, measured using the Filmetrics F40-UV and Woollam RC2 Ellipsometer, respectively. (c) Simulated DBR reflection spectra calculated by TMM.* **Figure 4, above:** *31-layer 500 nm DBR on SiO_2. The transparent substrate allows the DBR's opalescence to be observed, as shown by the photos on the right, in which reflected light is cyan and transmitted light is orange or rose-colored.*

Exchange Bias between van der Waals Materials: Tilted Magnetic States and Field-Free Spin-Orbit-Torque Switching

CNF Project Number: 598-96
Principal Investigator: Daniel C. Ralph
User(s): Thow Min Jerald Cham

Affiliation(s): Laboratory of Atomic and Solid State Physics, Cornell University

Primary Source(s) of Research Funding: National Science Foundation/Division of Materials Research, Air Force Office of Scientific Research, Agency for Science Technology and Research (Singapore)

Contact: dcr14@cornell.edu, tc676@cornell.edu

Primary CNF Tools Used: Supra SEM, Nabity Nanometer Pattern Generator, AJA Sputter Deposition, Odd hour evaporator, Angstrom evaporator

Abstract:

Magnetic van der Waals heterostructures provide a unique platform to study magnetism and spintronics device concepts in the two-dimensional limit. Here, we report studies of exchange bias from the van der Waals antiferromagnet CrSBr acting on the van der Waals ferromagnet Fe_3GeTe_2 (FGT). The orientation of the exchange bias is along the in-plane easy axis of CrSBr, perpendicular to the out-of-plane anisotropy of the FGT, inducing a strongly tilted magnetic configuration in the FGT. Furthermore, the in-plane exchange bias provides sufficient symmetry breaking to allow deterministic spin-orbit torque switching of the FGT in CrSBr/FGT/Pt samples at zero applied magnetic field [1].

Summary of Research:

We study the interaction between ferromagnetic Fe_3GeTe_2 (FGT) [2] with perpendicular magnetic anisotropy (PMA) and antiferromagnetic CrSBr [3] with in-plane easy-axis anisotropy, and find that the interaction induces an in-plane exchange bias on the FGT. Since the exchange bias is an interface interaction and the anisotropy in FGT arises from a bulk mechanism, we conclude that the tilting is non-uniform through the thickness of FGT (illustrated schematically in Figure 1a).

We have also investigated whether the exchange interaction from the CrSBr can provide a sufficient symmetry-breaking field to allow for deterministic SOT switching in CrSBr/FGT/Pt heterostructures. In general, to achieve deterministic switching of a magnetic layer with PMA using SOT from a high-symmetry material like Pt requires an external symmetry-breaking field. We perform pulsed-current measurements with different fixed Bext, and after each pulse we measure the Hall voltage near zero current.

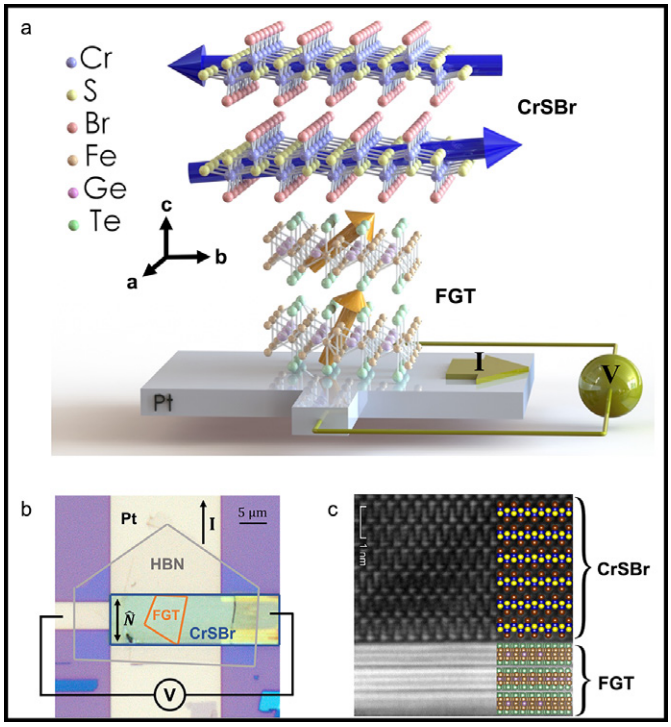

Figure 1: Device schematic and crystal structure (a) Schematic of a CrSBr/FGT het.erostructure dry transferred onto a Pt channel for spin-orbit torque pulse current switching measurements. (b) Top-view optical image of the CrSBr(30 nm)/FGT(9 nm)/Pt (10 nm) device with the b crystal axis of the CrSBr layer oriented parallel to the current (so that N^ ∥ I). (c) High angle annular dark field (HAADF) STEM cross-sectional image of the vdW interface of a different CrSBr/FGT heterostructure.

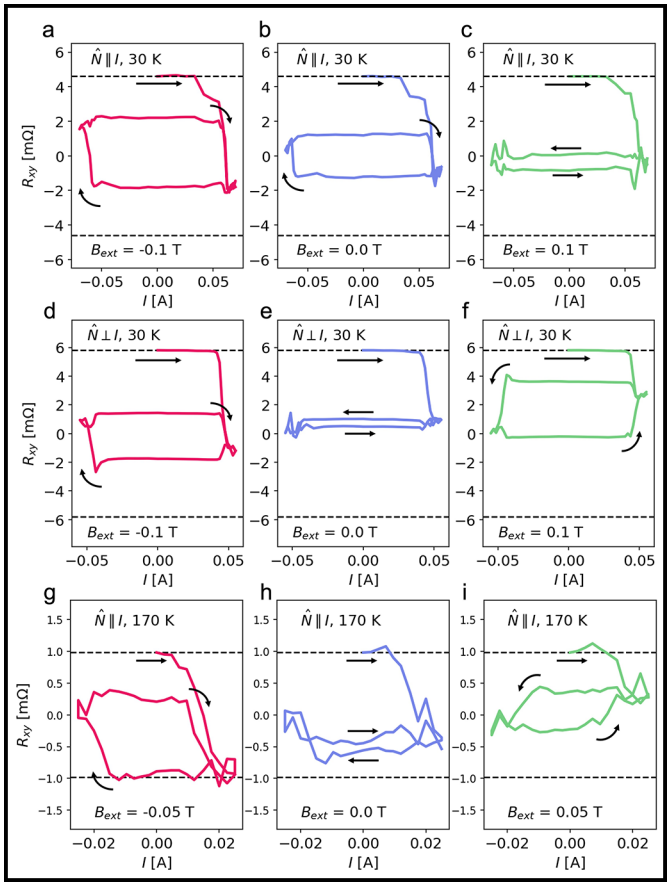

Figure 2: Pulsed-current-switching hysteresis loops of CrSBr/FGT/Pt samples. (a-c) Pulsed-current-switching hysteresis loops at 30 K for the sample with N^ ∥ I. The uniaxial exchange bias field enables deterministic spin-orbit-torque switching within the FGT layer at 0 T (panel (b)). (c) With a positive field of 0.1 T, the magnetization reversal hysteresis is quenched. (d-f) Pulsed-current switching hysteresis loops at 30 K for the sample with N^ ⊥ I. (g-i) Pulsed-current-switching hysteresis loops at 170 K, for the device with N^ ∥ I.

Figures 2a-c show the resulting switching loops for the device with $N^ \parallel I$ at 30 K. We observe deterministic switching (Figure 2b) for B_{ext} = 0 T, with the same switching chirality as when B_{ext} = -0.1 T (Figure 2a). When B_{ext} = 0.1 T, we see a quenching of the hysteresis (Figure 2c). In comparison, in the device for which $N^ \perp I$, there is negligible hysteresis at 0 T (Figure 2e) and the chirality of the magnetization reversal is opposite for ± 0.1 T (Figure 2d,f). When the temperature is raised above T_N to 170 K in the device with $N^ \parallel I$, we see no switching at 0 T (Figure 2h) and opposite switching chiralities at ± 0.05 T (Figure 2g,i). These findings indicate that a net exchange bias is induced parallel to the Néel vector of CrSBr when the temperature is lowered below *T*N.

Conclusion and Future Steps:

In conclusion, we report measurements of an in-plane exchange bias from CrSBr acting perpendicular to the out-of-plane anisotropy of FGT, in a direction parallel to the in-plane anisotropy axis of CrSBr. This exchange field results in a strongly-tilted magnetic configuration within the FGT, and can serve as an in-plane symmetry-breaking field that enables field-free deterministic switching driven by SOT in CrSBr/FGT/Pt devices. Although the CrSBr in our samples is likely in a multidomain state, we can make a rough estimate of the exchange bias strength from the external magnetic field required to cancel the exchange field and eliminate the deterministic switching. We estimate values as large as 0.15 T at low temperature, decreasing gradually with increasing temperature up to the T_N of CrSBr. A CrSBr thickness greater than ≈ 10 nm is required to provide exchange bias for switching at 30 K. This work opens possibilities for exploiting unique characteristics of vdW magnets and heterostructures to enable new functionality in spintronics.

References:

[1] Thow Min Jerald Cham, Reiley J Dorrian, Xiyue S Zhang, Avalon H Dismukes, Daniel G Chica, Andrew F May, Xavier Roy, David A Muller, Daniel C Ralph, and Yun.qiu Kelly Luo. Exchange bias between van der waals materials: tilted magnetic states and field-free spin-orbit-torque switching. arXiv preprint arXiv:2306.02129, 2023.

[2] Cheng Tan, Jinhwan Lee, Soon-Gil Jung, Tuson Park, Sultan Albarakati, James Partridge, Matthew R Field, Dougal G McCulloch, Lan Wang, and Changgu Lee. Hard magnetic properties in nanoflake van der waals fe3gete2. Nat. Commun., 9(1):1554, 2018.

[3] Evan J. Telford, Avalon H. Dismukes, Kihong Lee, Minghao Cheng, Andrew Wieteska, Amymarie K. Bartholomew, Yu-Sheng Chen, Xiaodong Xu, Abhay N. Pasupathy, Xiaoyang Zhu, Cory R. Dean, and Xavier Roy. Layered antiferromagnetism induces large negative magnetoresistance in the van der waals semiconductor CrSBr. Ad.vanced Materials, 32(37):2003240, 2020.

Physics of nm-Scale Superconductors and Magnets

CNF Project Number: 598-96
Principal Investigator(s): Daniel C. Ralph
User(s): Xiaoxi Huang

Affiliation(s): Department of Physics, Cornell University

Primary Source(s) of Research Funding: Semiconductor Research Corporation-
Superior Energy-efficient Materials and Devices

Contact: dcr14@cornell.edu, xh384@cornell.edu

Primary CNF Tools Used: Heidelberg Mask Writer - DWL66FS, JEOL 6300, AJA Sputter Deposition

Abstract:

We have been actively using the Heidelberg Mask Writer - DWL66FS to make spin torque ferromagnetic resonance and second harmonic Hall devices for spin-orbit torque generation study. JEOL 6300 electron beam writer has been employed to make non-local devices for spin transport study.

Summary of Research:

In the past year, one of our research focuses is to study unconventional spin-orbit torque generation in exotic material systems, consisting of a spin-orbit coupled material and a ferromagnet. The ferromagnet serves as a sensitive spin detector, whose magnetization state is subject to the perturbation induced by spin current generated in the spin-orbit coupled material. Two different techniques were employed to study spin-orbit torque generation in these systems. Since the device dimension is in the order of microns (Figure 1a, b), a photolithography recipe is developed to fabricate those devices. To begin with, spin torque ferromagnetic resonance is the mostly commonly used technique to measure spin orbit torque generation. The device made with the Heidelberg Mask Writer - DWL66FS at Cornell NanoScale Facility is shown in Figure 1a. The device consists of a T shaped bar made of the target material systems and a symmetric Ground-Signal-Ground contact that produces no net Oersted field when the applied high frequency current travels through. Moreover, second harmonic Hall measurement is another technique that Ralph group has pioneered to measure spin-orbit torque generation. The second harmonic Hall measurements are performed on Hall devices (Figure 1b), with external magnetic field rotated in the device plane. To make the Hall devices, Hall bars with three Hall crosses are first exposed with DWL 66fs. Then an ion mill step is followed to remove the material that is not protected by the photoresist. Finally, a second step exposure is performed to align contacts to the Hall crosses. Contacts made of Pt are deposited in the AJA sputter system for both spin torque ferromagnetic resonance and second harmonic Hall devices.

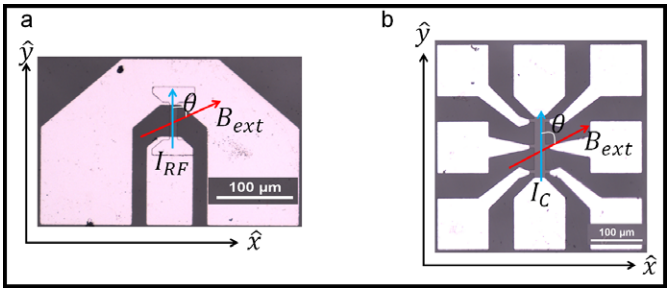

Figure 1: Devices for spin orbit torque generation study. a) Spin torque ferromagnetic resonance devices made with the Heidelberg Mask Writer - DWL66FS. b) Hall devices made with the DWL66FS. Mark alignments were used for the second step exposure.

The other project we have been actively working on at the Cornell NanoScale Facility is the non-local spin transport in magnetic materials. Magnetic materials such as ferrimagnets [1,2] and antiferromagnets [3,4] have been shown to have the capability of carrying spin information over long distance. To study spin transport in magnetic insulators, non-local devices shown in Figure 2 [5] consisting of an injection channel and a detection channel that are separated by various distances are made with electron beam lithography. To achieve sub-micron down to 200 nm of distances between the two channels, electron beam lithography tool JEOL 6300 is used to expose features as small as 200 nm.

Conclusions and Future Steps:

We have successfully measured spin-orbit torque generation in spin-orbit coupled materials and spin transport in magnetic insulator in the devices fabricated at the Cornell NanoScale Facility. Our future steps include: 1. Study spin-orbit torque generation in the same material with various orientations. 2. Study the distance dependence of spin transport in the magnetic insulators.

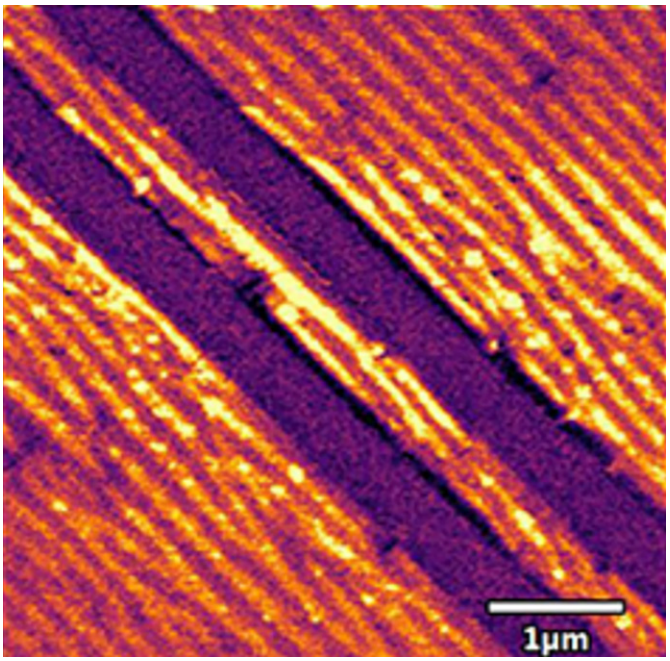

Figure 2: Non-local devices for long distance spin transport study. The channel width and spacing between two channels are 500 nm.

References:

[1] L. J. Cornelissen, J. Liu, R. A. Duine, J. Ben Youssef, and B. J. van Wees. "Long-distance transport of magnon spin information in a magnetic insulator at room temperature". Nat. Phys. 11, 1022(2015).

[2] X.-Y. Wei, O. Alves Santos, C. H. Sumba Lusero, G. E. W. Bauer, J. Ben Youssef, and B. J. van Wees. "Giant magnon spin conductivity in ultrathin yittrium iron garnet films". Nat. Mater. 21, 1352(2022).

[3] R. Lebrun, A. Ross, S. A. Bender, A. Qaiumzadeh, L. Baldrati, J. Cramer, A. Brataas, R. A. Duine, and M. Klaui. "Tunable long-distance spin transport in a crystalline antiferromagnetic iron oxide". Nature 561, 222(2018).

[4] Jiahao Han, Pengxiang Zhang, Zhen Bi, Yabin Fan, Taqiyyah S. Safi, Junxiang Xiang, Joseph Finley, Liang Fu, Ran Cheng, and Luqiao Liu. "Birefringence-like spin transport via linearly polarized antiferromagnetic magnons". Nat. Nanotechnol. 15, 563(2020).

[5] Xiaoxi Huang et al. "Manipulating chiral-spin transport with ferroelectric polarization". https://arxiv.org/abs/2306.02185.

Thermally-Generated Spin Current in the Topological Insulator Bi_2Se_3

CNF Project Number: 598-96
Principal Investigator(s): Daniel C. Ralph
User(s): Rakshit Jain

Affiliation(s): Physics Department, Cornell University
Primary Source(s) of Research Funding: Department of Energy, National Science Foundation
Contact: dcr14@cornell.edu, rj372@cornell.edu
Primary CNF Tools Used: AJA sputter deposition, 5X g-line stepper

Abstract:

We present measurements of thermally-generated transverse spin currents in the topological insulator Bi2Se3, thereby completing measurements of interconversions among the full triad of thermal gradients, charge currents, and spin currents. We accomplish this by comparing the spin Nernst magneto-thermopower to the spin Hall magnetosistance for bilayers of Bi_2Se_3/CoFeB. We find that Bi_2Se_3 does generate substantial thermally-driven spin currents. A lower bound for the ratio of spin current density to thermal gradient is shown in Equation (A) at right, and a lower bound for the magnitude of the spin Nernst ratio is -0.61 ± 0.11. The spin Nernst ratio for Bi_2Se_3 is the largest among all materials measured to date, 2-3 times larger compared to previous measurements for the heavy metals Pt and W.

$$\frac{J_s}{\nabla_x T} = (4.9 \pm 0.9) \times 10^6 \left(\frac{\hbar}{2e}\right) \frac{Am^{-2}}{K\mu m^{-1}} \quad \textbf{(A)}$$

$$J_s = \frac{\hbar}{2e}\frac{\theta_{SH}}{\rho_{SS}}E. \quad \textbf{(1)}$$

$$\Delta R(\hat{m}) = (1 - m_y^2)\Delta R_{SMR} = \Delta R_{SMR} cos^2\theta \quad \textbf{(2)}$$

$$J_s = -\frac{\hbar}{2e}\frac{\theta_{SN}}{\rho_{SS}}S_{SS}\nabla_x T. \quad \textbf{(3)}$$

$$\Delta V_{th}^x = -l\nabla_x T(1 - m_y^2)S_{SNT} = -l\nabla_x T S_{SNT} cos^2\theta \quad \textbf{(4)}$$

Equations (A) through (4).

Summary of Research:

By taking advantage of the electron's spin as well as its charge, the field of spin caloritronics has provided new strategies for energy harvesting from thermal gradients, for thermal management within electronics, and for magnetic manipulation [1]. However, the field has been limited by low efficiencies for interconversion between thermal gradients and spin currents within the materials studied to date. Here, we provide measurements of the efficiency of transduction from a thermal gradient to spin current density in a topological insulator. Topological insulators have already been demonstrated to provide very high efficiencies for interconversion between the other two legs of the triad of thermal gradients, charge currents, and spin currents. Topological insulators have achieved record efficiencies for transduction between charge current density and spin current density that are of interest for applications in spin-orbit-torque manipulation of magnetic devices [2], and also highly-efficient transduction of thermal gradients to electric field with potential for thermoelectric applications [3]. We find that the topological insulator Bi_2Se_3 also enables highly-efficient transduction of thermal gradients to spin currents, with by far the largest spin Nernst ratio among materials measured to date.

We measure thermally-generated spin currents using the same physics by which electrically-generated spin currents give rise to the spin Hall magnetoresistance (SMR) effect [4]. In the electrically-generated case, an electric field E applied in the plane of a spin-source/ferromagnet bilayer gives rise to a vertically-flowing spin current density J_s via the spin Hall effect, with an efficiency characterized by the spin Hall ratio, θ_{SH} Equation (1) above, where $\hbar$ is the reduced Planck constant, e is the magnitude of the electron charge, and ϱ_{SS} is the electrical resistivity of the spin-source material. The degree of reflection of this spin current at the magnetic interface depends on the orientation of the magnetization $m\hat{}$ in the magnetic layer. The reflected spin current produces a voltage signal by the inverse spin Hall effect, causing the resistance of the bilayer to depend on the magnetization angle (4), which can be further simplified in geometry studied in this work (Figure 1 (A)), Equation (2).

Here m_y is the component of the magnetization unit vector that is in-plane and perpendicular to the electric field. Similarly, the thermally-generated spin current and voltages takes the form in Equations (3) and (4) where θ_{SN} is the spin Nernst ratio, S_{SS} is the Seebeck coefficeint

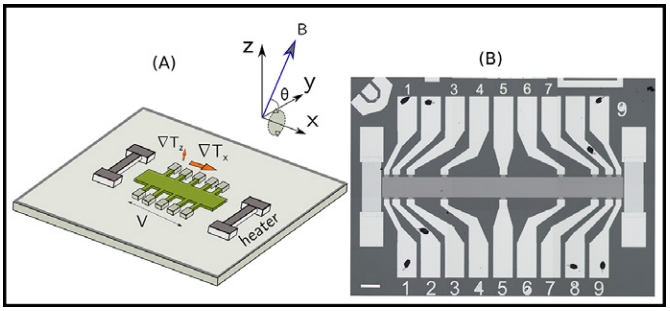

Figure 1: (A) Sample geometry for the spin Nernst magneto-thermopower experiments. (B) Microscope image of the device used for measuring spin Nernst magneto-thermopower. Scale bar is equivalent to 200 μm.

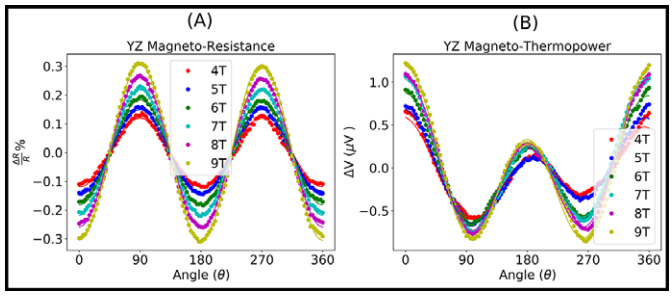

Figure 2: (A) Magnetoresistance percentage ratio $(\frac{\nabla R}{R} \times 100)$ as a function of the magnetic field angle and R magnitude for bilayers of Bi_2Se_3 (8 nm)/CoFeB (5 nm) at room temperature, for magnetic field rotated in the YZ plane. The four-point device resistance R = 2.137 kOhms. (B) YZ magneto-thermopower voltage as a function of the magnetic field angle and magnitude for the same sample. The heater power used for these sweeps was fixed at 442 mW (equivalent to a temperature drop of 6.8 K along the l = 1.8 mm length of the device).

of the spin source, S_{SNT} is the coefficient of the spin Nernst magneto-thermopower, which represents voltage arising from thermally generated spin currents, $\nabla_x T$ is the in-plane thermal gradient and l is the length of the device.

The results are plotted in Figure 2 for both electrically and thermally generated voltages. After accounting for field dependent magneto-resistance and magneto-thermopower arising from the Bi_2Se_3 (5) layer, we report, $100 \times \Delta R_{SMR}/R = 0.126 \pm 0.008$ where R is the resistance of the device and $S_{SNT} = 90 \pm 10\ nV/\kappa$. Using these values, we can estimate the ratio $\theta_{SN}/\theta_{SH} = -0.83 \pm 0.15$ and θ_{SN} is approximately -0.61 ± 0.11.

These numbers can be used to estimate the net thermally generated spin currents as $J_s / \nabla_x T$ is $(4.9 \pm 0.9) \times 10^6$ $(\hbar/2e)$A m^{-2} / κ μm^{-1}.

Conclusions:

In summary, by comparing measurements of the spin Nernst magneto-thermopower in Bi_2Se_3/CoFeB bilayers to the spin Hall magnetoresistance, we find a lower bound for the magnitude of the spin Nernst ratio for Bi_2Se_3 of -0.61 ± 0.11, roughly three times greater than that of previously measured values for Pt and 2-3 times greater than that of W. Moreover, the net spin current generated per unit thermal gradient $J_s/\Delta T_x$ is higher in Bi_2Se_3 than for W and of a similar magnitude as Pt despite the higher resistivity of Bi_2Se_3.

References:

[1] Bauer, G. E., Saitoh, E., and Van Wees, B. J. Spin caloritronics. Nature Materials 11, 391-399 (2012).

[2] Mellnik, A., et al. Spin-transfer torque generated by a topological insulator. Nature 511, 449-451 (2014).

[3] Hor, Y., et al. p-type Bi_2Se_3 for topological insulator and low-temperature thermoelectric applications. Physical Review B 79, 195208 (2009).

[4] Nakayama, H., et al. Spin Hall magnetoresistance induced by a nonequilibrium proximity effect. Physical Review Letters 110, 206601 (2013).

[5] Jain, R., et al. Thermally-generated spin current in the topological insulator Bi_2Se_3. arXiv preprint arXiv:2210.05636 (2022).

Fabricating Micron-Sized Skyrmion-Spintronic Devices

CNF Project Number: 598-96
Principal Investigator(s): Daniel C. Ralph
User(s): Maciej Olszewski

Affiliation(s): Laboratory of Atomic and Solid State Physics (LASSP), Cornell University

Primary Source(s) of Research Funding: Defense Advanced Research Projects Agency (DARPA), National Science Foundation (NSF)

Contact: dcr14@cornell.edu, mwo34@cornell.edu

Website(s): https://ralphgroup.lassp.cornell.edu/

Primary CNF Tools Used: GCA 6300 DSW 5X g-line Wafer Stepper, GCA AutoStep 200 DSW i-line Wafer Stepper, Heidelberg Mask Writer - DWL2000, AJA Ion Mill, AJA Sputter Deposition, YES Asher, DISCO Dicing Saw

Abstract:

Magnetic skyrmions are a candidate for next-generation spintronic devices. Their topological nature makes them robust, allowing for a non-volatile, high-speed, and low-power-consumption method of storing and processing information. In addition, recent advances in skyrmionics have demonstrated both electrical and thermal techniques for controlling skyrmion densities in thin films. Here, we present initial measurements of magnetic resonance in ferromagnetic multilayers with interfacial Dzyaloshinskii-Moriya interaction. We have performed room temperature experiments utilizing both conventional field-driven ferromagnetic resonance and spin-torque ferromagnetic resonance. We find a difference in the resonance readout between the phases with and without skyrmions but are yet to find direct evidence for resonance readout of skyrmions themselves. Our work is further supported by Lorentz transmission electron microscopy with spatial resolution on the order of a few nanometers, where we directly observe skyrmions in our thin films.

Summary of Research:

Conventional spin-torque ferromagnetic resonance (ST-FMR) devices consist of two layers, one heavy metal (HM) spin Hall layer and one ferromagnet (FM) with in-plane anisotropy [1]. As current passes through the HM layer a spin current is generated in the direction perpendicular to the current direction. The generated spin current then proceeds into the FM layer and exerts a torque on the magnetization. If alternating current is passed, the spin current generated will also be alternating, and under certain conditions the spin torque can cause the FM to resonate. The resonance of the magnet can be captured with the changes in the magnetoresistance of the device. Further, the resonances can be fitted to extract various parameters, such as the strength of the torques, magnetic damping, and effective magnetization.

Skyrmions, topologically protected spin textures, present a novel and robust system for resonance-based spintronic devices. They can be found in a variety of systems, including thin ferromagnetic films with the presence of the Dzyaloshinskii-Moriya interaction and broken inversion symmetry [2]. Due to their topological nature, skyrmions are stable under small perturbations from defects and other external fluctuations, making them a great candidate for various memory-based applications. Further, it has been demonstrated that skyrmions can be observed via the topological Hall effect and their density can be controlled with current pulses [3].

The main goal of our work is to incorporate thin films which host skyrmions into ST-FMR devices to directly measure skyrmion resonances and control their density to increase or decrease the resonance readout. We grow our skyrmion multilayers, consisting of platinum, cobalt, and ruthenium on a sapphire substrate, using our own AJA magnetron sputtering tool. After depositing the films, we perform one round of photolithography on either the g-line or i-line stepper to outline the shape of the devices and use the AJA ion mill to mill our film to the proper device size. Next, we do either one or two rounds of photolithography for writing the contacts for the devices. Finally, we use the AJA sputter to deposit titanium and platinum to make proper electrical connection to the devices. This process usually yields very consistent results with device fabrication, and we can fabricate

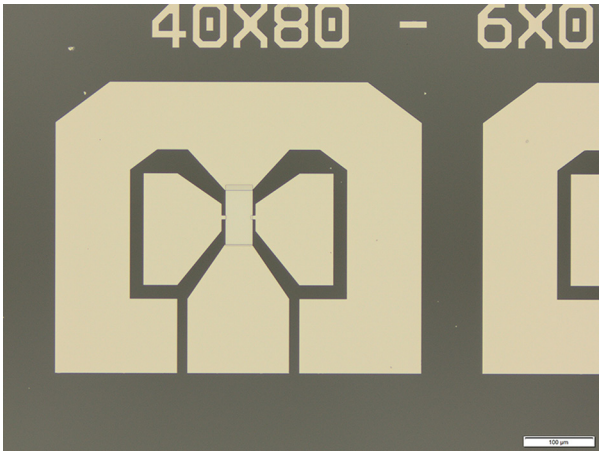

Figure 1: An image of fabricated thin film devices with contacts on a sapphire substrate.

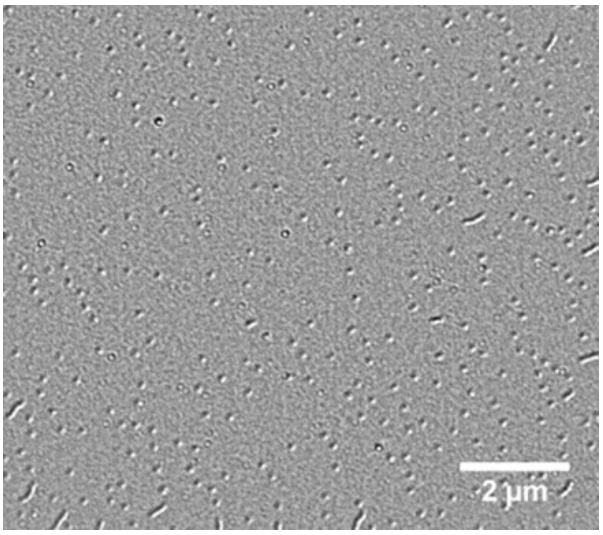

Figure 2: A Lorentz transmission electron microscopy scan of out thin film showing the density and size of the skyrmions.

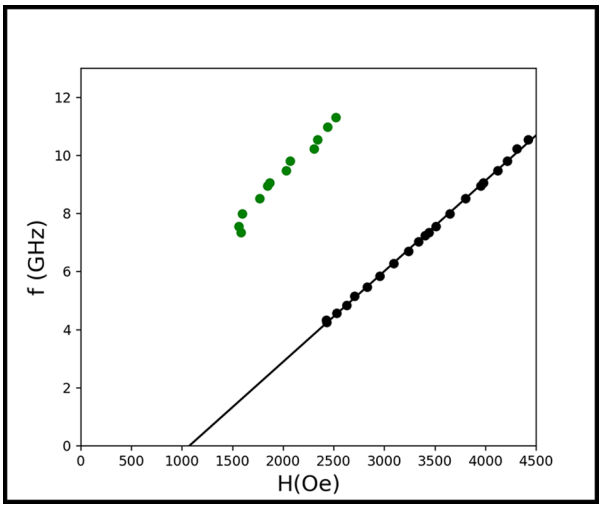

Figure 3: Positions of the magnetic resonances of the skyrmion film as a function of frequency and magnetic field.

around 100 devices of different shapes and sizes during this procedure, an example of which is shown in Figure 1.

We can directly observe if skyrmions are present in our samples by conducting Lorentz transmission electron microscopy (L-TEM) and looking at the changes in the reflections of the transmitted electrons, as shown in Figure 2. After, ensuring that we have skyrmions present, we conduct standard ST-FMR measurements as a function of the frequency of the current applied and the strength of the external magnetic field. In Figure 3, we show the positions of the resonance peaks as a function of frequency and magnetic field. Unfortunately, our preliminary work does not show any resonances in the regions where skyrmions are present, based on the L-TEM scans. We are continuing our efforts to find skyrmion resonance by considering other device geometries and slight changes to the thin films.

References:

[1] Karimeddiny, et al., Phys. Rev. Applied 14, 024024 (2020).
[2] Fert, et al., Nature Review Materials, 2, 17031 (2017).
[3] Park, et al., Journal of Applied Physics 128, 23 (2020).

Surface Acoustic Waves in Magnetic Materials

CNF Project Number: 598-96
Principal Investigator(s): Daniel C. Ralph
User(s): Yongjian Tang

Affiliation(s): Physics, Cornell University
Primary Source(s) of Research Funding: DE-SC0017671 Department of Energy
Contact: dcr14@cornell.edu, yt498@cornell.edu
Website(s): https://ralphgroup.lassp.cornell.edu
Primary CNF Tools Used: JEOL 6300, SC4500 evaporator, Zeiss Supra SEM, AJA sputter, 5X stepper

Abstract:

We have developed both photolithography and e-beam lithography recipes for interdigital transducers (IDTs) based on multiferroic $BiFeO_3$ (BFO) thin films. Using ultra-high-frequency lock-in (UHFLI) measurements, we successfully demonstrated the generation of surface acoustic waves (SAWs) in BFO epitaxial films. Pulse echo measurements and vector network analyzer are deployed to further characterize the properties of the SAWs.

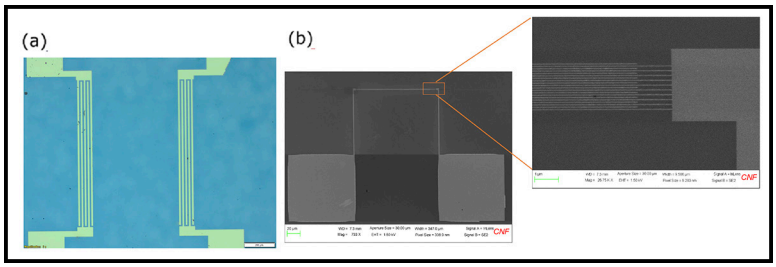

Figure 1: (a) Optical image of IDTs patterned by photolithography and (b) SEM image of IDTs patterned by e-beam lithography.

Summary of Research:

SAWs have been extensively used in electronic components which include delay lines, filters, transformers, etc., devices that are based on transduction from electric energy to mechanical energy in piezoelectric materials. Because SAWs can be easily generated and launched into elastic materials, they become a powerful tool for fundamental research in condensed matter physics, widely used to characterize, manipulate, and detect electrical and magnetic properties. For instance, mismatch of sound velocities in SAW substrate and fluidic medium is exploited to drive fluid actions such as pumping, mixing and jetting. Intrinsic parameters of a material can be obtained by measuring the speed and attenuation of SAWs. The combination of SAWs with magnetism gives rise to novel phenomena such as acoustically driven spin pumping, SAW-induced ferromagnetic resonance, magnetic domain motion as well as nonreciprocal SAW propagation, via magnon-phonon coupling. Dynamic strain field induced by SAWs allows manipulation of photoluminescence in low-dimensional materials.

BFO is a room temperature multiferroic where ferroelectricity, antiferromagnetism, and a weak spin-canted magnetization coexist. It would be interesting to investigate the coupling between these order parameters. Since all ferroelectric materials are intrinsically piezoelectric, SAWs are also expected to be generated in BFO. Via piezoelectric effect, an IDT converts electrical energy into mechanical energy that propagates at the surface in the form of surface acoustic waves. In this project, we aim to fabricate input and output IDTs to verify the generation of SAWs in BFO-based devices, which would open new possibilities to control, manipulate and detect the change in these order parameters.

The fabrication was done on a 100 nm thick BFO sample. 15 pairs of IDTs are patterned in a 10 mm by 10 mm square using 5X stepper. An IDT consists of two interlocking comb-shaped arrays of metal electrodes. The geometry of these electrodes determines the wavelength of the SAW. For the IDT shown in Figure 1(a), it has five fingers that span a distance range of 101.25 μm, which means the width of each finger is 11.25 μm, and the wavelength is four times that, 45 μm. As shown in Figure 1(b), we have also developed method for patterning IDTs using e-beam lithography. These IDTs can have extremely small wavelength (down to 20 nm) and hence gigahertzworking frequency range.

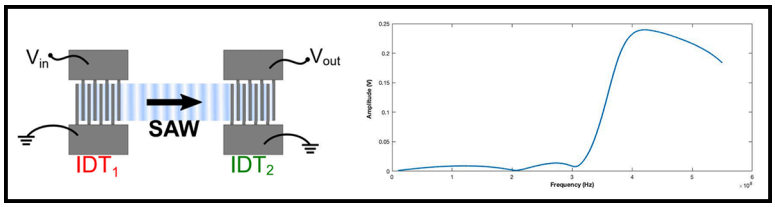

Figure 2: UHFLI measurement.

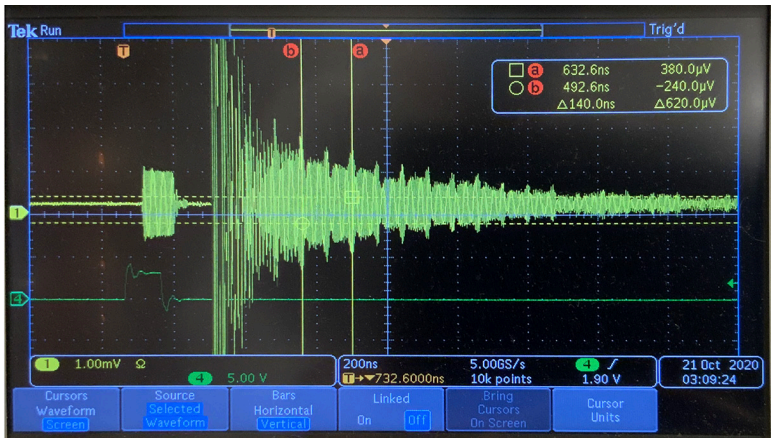

Figure 3: Pulse echo measurement.

UHFLI measurement was performed on the photolithographically defined IDTs (Figure 2). The amplitude of the voltage at output IDT is measured at different frequency with a fixed input voltage of 1 V. We observe a sharp increase of amplitude after 300 MHz and amplitude peaks at around 410 MHz. This indicates that in this range of frequency, SAWs are generated with highest efficiency. More SAWs are generated at these frequencies, and they propagate to the output IDT and are converted back into electric signal.

We also performed a pulse echo measurement on the same sample. For this measurement, we excited SAW at 410 MHz to generate as many SAWs as possible. The SAWs are bouncing back and forth between the IDTs and thus we observed echoes with an oscilloscope. Considering that the transmission at the IDTs, the echo signal will decay eventually. Ideally, we would like to see separated packs of signal with decreasing amplitude, but our echoes are overlapping making them hard to be distinguished. This can be solved by increasing the spatial separation between IDTs and shorted the pulse width. Still, we observe evenly spaced spiles, which also indicate the generation of SAWs. From the spacing between the echoes, we can calculate quantities such as SAW velocity, attenuation, etc.

Nanofabricated Superconducting Devices for Vortex Dynamics and Qubits

CNF Project Number: 1314-05
Principal Investigator(s): Britton L.T. Plourde
User(s): Brad Cole, Kenneth Dodge, Clayton Larson, Eric Yelton

Affiliation(s): Department of Physics, Syracuse University
Primary Source(s) of Research Funding: Army Research Office
Contact: bplourde@syr.edu, bgcole@syr.edu, krdodgej@syr.edu, cllarson@syr.edu, epyelton@syr.edu
Primary CNF Tools Used: ASML Photostepper, JEOL 6300, Plasma-Therm 770

Abstract:

We fabricate superconducting microwave devices for studying the dynamics of vortices at low temperatures and for forming novel qubits. Vortices are quantized bundles of magnetic flux that thread many different superconductors over a particular range of applied magnetic field. By using disordered superconducting thin films to form high kinetic inductance wires combined with novel arrays of Josephson junctions, we are able to build structures that can lead to qubits that are topologically protected against decoherence. With charge-sensitive superconducting qubits, we are able to probe sources of correlated errors in quantum processors.

Summary of Research:

Superconducting microwave circuits play an important role in quantum information processing. Circuits composed of Josephson junctions and capacitors with superconducting electrodes can serve as qubits, the fundamental element of a quantum computing architecture. Various loss mechanisms limit the ultimate performance of these devices, including trapped magnetic flux vortices. Vortices can be trapped in the superconducting electrodes when background magnetic fields are present and contribute dissipation when driven with microwave currents [1]. Thus, techniques for controlling the trapping of vortices are critical to the development of large-scale quantum information processors with superconducting circuits.

By arranging nanoscale Al-AlOx-Al Josephson tunnel junctions in novel arrays, it is possible to implement new qubit designs that are protected against decoherence [2-4]. We are also able to use such Al-AlOx-Al tunnel junctions in superconducting qubits to probe poisoning effects from nonequilibrium quasiparticles, which are a source of correlated errors in quantum processors. We can mitigate this quasiparticle poisoning through the use of electroplated Cu metallic reservoirs for downconversion of high energy phonons [5].

We fabricate our microwave resonators from various superconducting films, including aluminum and niobium, deposited onto silicon wafers in vacuum systems at Syracuse University. We define the patterns on the ASML stepper and transfer them into the films with a combination of reactive ion etching and liftoff processing. For defining Josephson junctions, we use the JEOL 6300 along with a dedicated deposition system at Syracuse University. We measure these circuits at temperatures of 100 mK and below in our lab at Syracuse University.

References:

[1] Song, C., Heitmann, T.W., DeFeo, M.P., Yu, K., McDermott, R., Neeley, M., Martinis, John M., Plourde, B.L.T.; "Microwave response of vortices in superconducting thin films of Re and Al"; Physical Review B 79, 174512 (2009).

[2] Doucot, B., Ioffe, L.; "Physical implementation of protected qubits"; Reports on Progress in Physics75, 072001 (2012).

[3] Liu, Y., Dodge, K., Cole, B., Shearrow, A., Brann, E., Snyder, M., Klots, A., Ioffe, L., McDermott, R., Plourde, B.; "Quantum stabilizers implemented with superconducting hardware"; Bull. Am. Phys. Soc. 2023, https://meetings.aps.org/Meeting/MAR23/Session/M75.3

[4] Dodge, K., Liu, Y., Klots, A., Cole, B., Shearrow, A., Senatore, M., Zhu, S., Ioffe, L., McDermott, R., Plourde, B.; "Hardware implementation of quantum stabilizers in superconducting circuits"; arXiv:2303.00625.

[5] Iaia, V., Ku, J., Ballard, A., Larson, C.P., Yelton, E., Liu, C.H., Patel, S., McDermott, R., Plourde, B.L.T.; "Phonon downconversion to suppress correlated errors in superconducting qubits"; NatureCommunications 13, 6425 (2022).

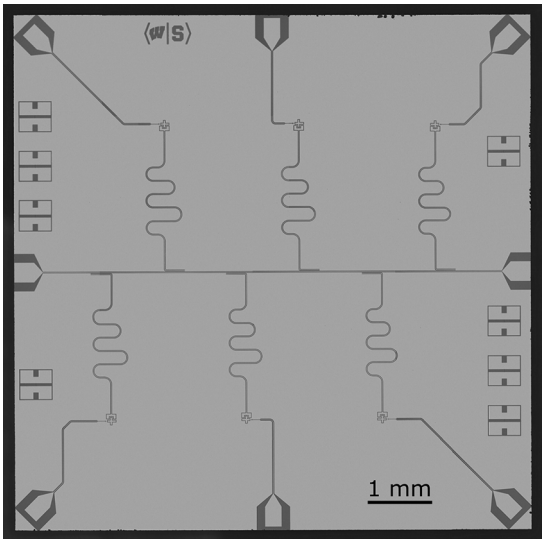

Figure 1: Optical micrograph of multi-qubit chip with Nb base layer and Al-AlOx-Al tunnel junctions for probing phonon-mediated correlated errors.

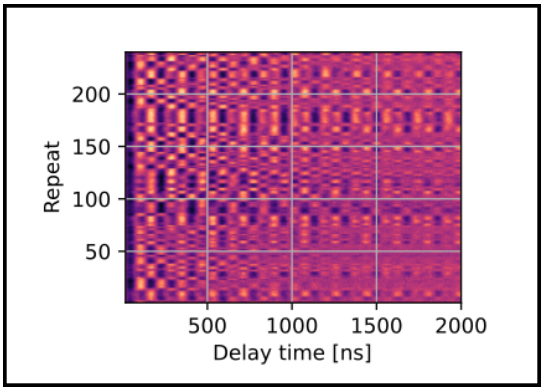

Figure 2: Repeated measurements of Ramsey fringe oscillations for charge-sensitive superconducting qubit subject to random offset charge jumps due to high energy particle impacts on device.

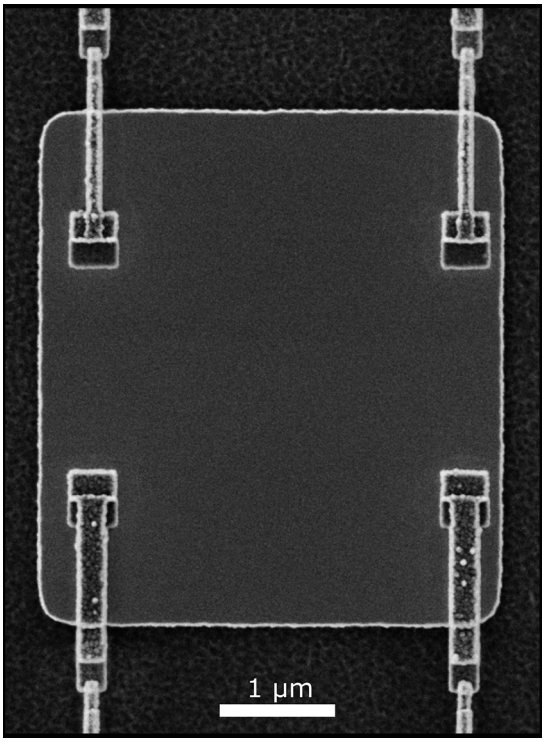

Figure 3: SEM image of central superconducting Nb island connected to four Al-AlOx-Al tunnel junctions for topologically protected superconducting circuit.

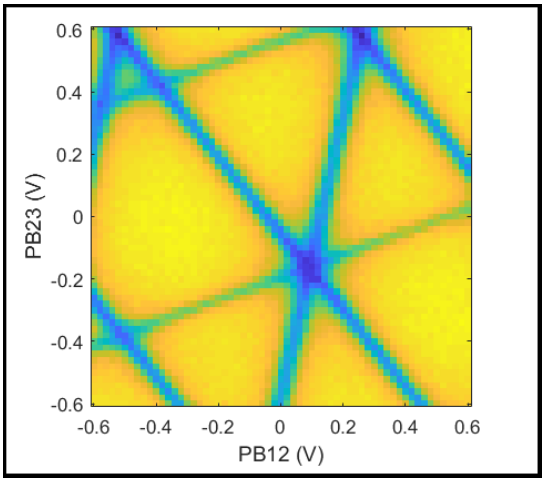

Figure 4: Measurement of microwave readout cavity modulation with magnetic flux using on-chip control lines coupled to topologically protected superconducting circuit.

Fabrication of Nanoscale Josephson Junctions for Quantum Coherent Superconducting Circuits

CNF Project Number: 1735-08
Principal Investigator(s): Britton L.T. Plourde
User(s): Brad Cole, Tianna McBroom, JT Paustian

Affiliation(s): Department of Physics, Syracuse University
Primary Source(s) of Research Funding: Air Force Research Lab, Air Force Office of Scientific Research
Contact: bplourde@syr.edu, bgcole@syr.edu, tamcbroo@syr.edu, jtpausti@syr.edu
Primary CNF Tools Used: ASML Photostepper, JEOL 6300, Plasma-Therm 770

Abstract:

We fabricate nanoscale superconductor tunnel junctions and other structures for experiments involving quantum coherent circuits. Such circuits have shown great promise in recent years for explorations of quantum mechanics at the scale of circuits on a chip and for forming qubits, the foundational elements of a quantum computer. The quantum state of these superconducting qubits can be manipulated with microwave radiation at low temperatures. We are currently developing superconducting metamaterial structures with novel microwave mode spectra for coupling to superconducting qubits.

Summary of Research:

The unique properties of nanoscale Josephson junctions enable a wide range of novel superconducting circuits for investigations in many diverse areas. In recent years, circuits composed of such junctions have emerged as promising candidates for the element of a quantum computer, due to the low intrinsic dissipation from the superconducting electrodes and the possibility of scaling to many such qubits on a chip [1]. The quantum coherent properties of the circuits are measured at temperatures below 50 mK with manipulation of the qubit state through microwave excitation.

We are developing multimode microwave resonators using combinations of superconducting lumped-circuit elements to engineer metamaterial transmission lines, including metamaterial ring resonator devices. These structures exhibit novel mode structures characteristic of left-handed materials [2]. We are fabricating such metamaterial transmission lines from Al and Nb films on Si and characterizing these at low temperatures [2]. We are working on experiments to couple these left-handed lines and ring resonators to superconducting qubits for experiments involving the exchange of microwave photons [2-4].

We pattern these circuits at the CNF with nanoscale structures defined with electron-beam lithography on the JEOL 6300 integrated with photolithographically defined large-scale features. The junctions are fabricated using the standard double-angle shadow evaporation technique, in which a resist bilayer of copolymer and PMMA is used to produce a narrow PMMA airbridge suspended above the substrate. Evaporation of aluminum from two different angles with an oxidation step in between forms a small Al-AlOx-Al tunnel junction from the deposition shadow of the airbridge. We have developed a process for defining these junctions with electron-beam lithography and we perform the aluminum evaporations in a dedicated chamber at Syracuse. We pattern large-scale features using the ASML stepper, with electron-beam evaporation of Al and sputter-deposition of Nb. Measurements of these circuits are performed in cryogenic systems at Syracuse University, including dilution refrigerators for achieving temperatures below 30 mK.

References:

[1] Clarke, J. and Wilhelm, F.K.; "Superconducting quantum bits"; Nature, 453, 1031 (2008).
[2] Wang, H., Zhuravel, A., Indrajeet, S., Taketani, B., Hutchings, M., Hao, Y., Rouxinol, F., Wilhelm,F., LaHaye, M.D., Ustinov, A., Plourde, B.; "Mode Structure in Superconducting Metamaterial Transmission Line Resonators"; Physical Review Applied 11, 054062 (2019).
[3] Indrajeet, S., Wang, H., Hutchings, M.D., Taketani, B.G., Wilhelm, F.K., LaHaye, M.D., Plourde, B.L.T.; "Coupling a Superconducting Qubit to a Left-Handed Metamaterial Resonator"; Physical Review Applied 14, 064033 (2020).
[4] McBroom, T.A., Schlabes, A., Xu, X., Ku, J., Cole, B.G., Ansari, M., Plourde, B.; "Multimode entangling interactions between transmons coupled through a metamaterial ring-resonator: experiment"; Bull. Am. Phys. Soc. 2023, https://meetings.aps.org/Meeting/MAR23/Session/A73.7.

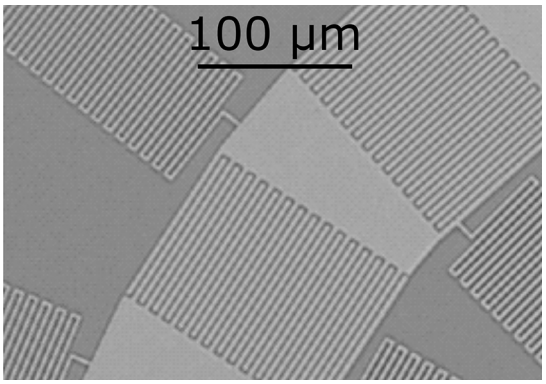

Figure 1: Optical micrograph of unit cell of left-handed metamaterial ring resonator fabricated from Nb on Si with interdigitated capacitor and meander-line inductors.

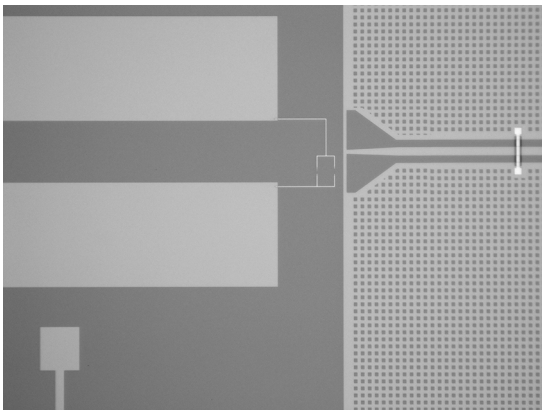

Figure 2: Zoomed-in optical micrograph of transmon qubit with Al-AlOx-Al junctions and Nb capacitor pads coupled to metamaterial ring resonator with on-chip Nb flux-bias line.

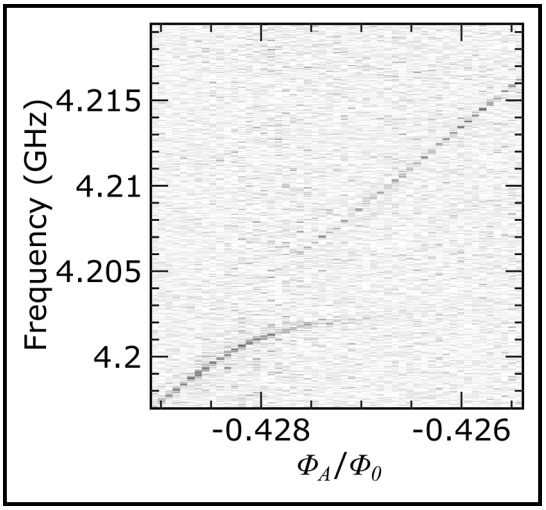

Figure 3: Measurement of qubit spectroscopy on metamaterial ring resonator with two qubits while tuning magnetic flux bias of one qubit. Splitting feature corresponds to exchange coupling between qubits when bare frequency of qubit being tuned approaches resonance with second qubit.

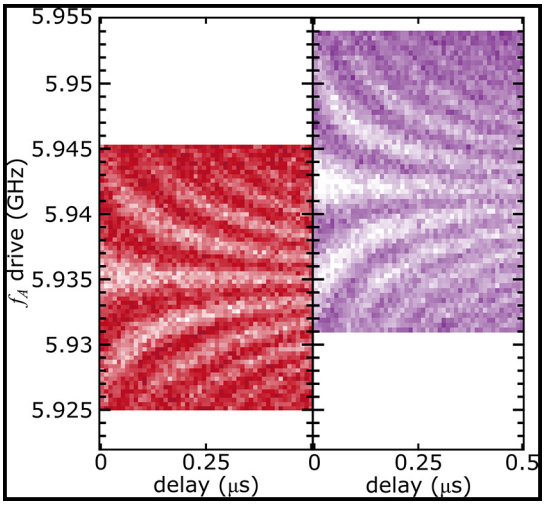

Figure 4: Measurement of Ramsey fringe oscillations on one qubit coupled to metamaterial ring resonator with and without an X pulse on second qubit.

Interfacial Optical Sensing of Ferroelectricity in Freestanding Perovskite Oxide by Using Monolayer Transition Metal Dichalcogenides

CNF Project Number: 2126-12
Principal Investigator(s): Gregory David Fuchs
User(s): Jaehong Choi

Affiliation(s): Applied and Engineering Physics, Cornell University

Primary Source(s) of Research Funding: Multidisciplinary University Research Initiatives (MURI) program

Contact: gdf9@cornell.edu, jc3452@cornell.edu

Primary CNF Tools Used: SC4500 Odd-Hour Evaporator, YES Asher, Anatech Resist Strip, GCA 6300 DSW 5X g-line Wafer Stepper, Heidelberg Mask Writer - DWL2000, Dicing Saw - DISCO, Wire Bonder

Abstract:

Two-dimensional (2D) transition metal dichalcogenides (TMDs) can be easily integrated with other functional materials such as ferroelectric materials due to their lack of dangling bonds. Also, owing to their atomic thickness, electronic and photoluminescence (PL) properties of 2D TMDs can be modulated by external perturbations, which opens new avenues for quantum sensing and optoelectronic devices. In this work, monolayer WSe_2 is integrated with a freestanding perovskite oxide $BaTiO_3$ (BTO) membrane. We observe that the relative density of charge carriers in WSe_2 changes as the polarization switches, and this gives rise to the PL intensity modulation. The relative emission intensity of neutral excitons (X^0) and trions (X^T) shows gate dependent hysteresis, which confirms that WSe_2 senses and optically reads out the ferroelectricity in BTO.

Summary of Research:

Perovskite oxides BTO have strong spontaneous polarization and moderate coercive field [1], but their epitaxial mother substrates often limit the range of device structures. Recent studies showed that perovskite oxides can be released from the substrate by using a sacrificial oxide layer [2-7], which allows integration with Si-based substrates. In our work, BTO is epitaxially grown on a $Sr_3Al_2O_6$ sacrificial layer and released in water. Isolated BTO is transferred onto a SiO_2/Si substrate (BTO growth and transfer done by Kevin Crust from the Hwang group at Stanford).

After this transfer, small BTO membranes with suitable size for device fabrication are picked up by using a polymer stamping method. Then, this freestanding BTO membrane is interfaced with WSe_2 to form a field effect device. In this device, the polarization in BTO can be switched *in-situ* by applying a gate voltage, and the polarization-induced PL modulation in monolayer WSe_2 is studied.

To study the ferroelectricity induced optical properties change in monolayer WSe_2, two voltage application modes are used: DC mode and pulse mode. In the DC mode, a continuous DC voltage is applied, and in the pulse mode, a DC mode voltage is applied for five seconds and then removed before taking spectra. In the DC mode, a negative voltage is applied to switch the polarization to an out-of-plane direction. When the polarization in BTO is in an out-of-plane direction, holes are induced in BTO near WSe_2/BTO.

In response to this polarization induced charges, the electron population increases in WSe_2, which facilitates X^0 formation in p-type WSe_2. As in Figure 1, X^0 emission intensity is enhanced when -6V was applied. When a positive voltage is applied, the polarization in BTO is flipped to an opposite direction, and electrons in BTO are accumulated near WSe_2/BTO. This results in hole accumulation in WSe_2 and leads to positively charged trion (X^+) emission intensity enhancement (Figure 1). When the voltage sweep direction is reversed, the PL modulation shows different behavior as in Figure 2. This asymmetry is the manifestation of the ferroelectricity of BTO. To further corroborate this, X^0 and X^+ emission peaks were resolved by using the Gaussian fitting method and their relative emission intensity (X^0/X^+) is plotted as a function of the gate voltage (Figure 3). X^0/X^+ shows a hysteresis loop, which confirms that the PL modulation in WSe_2 is induced by the polarization switching in BTO.

In the pulse mode, the hysteresis direction is changed (Figure 4). This is possibly due to the polarization decay after the voltage removal. Further study is needed to understand the mechanism of this hysteresis direction reversal in the pulse mode.

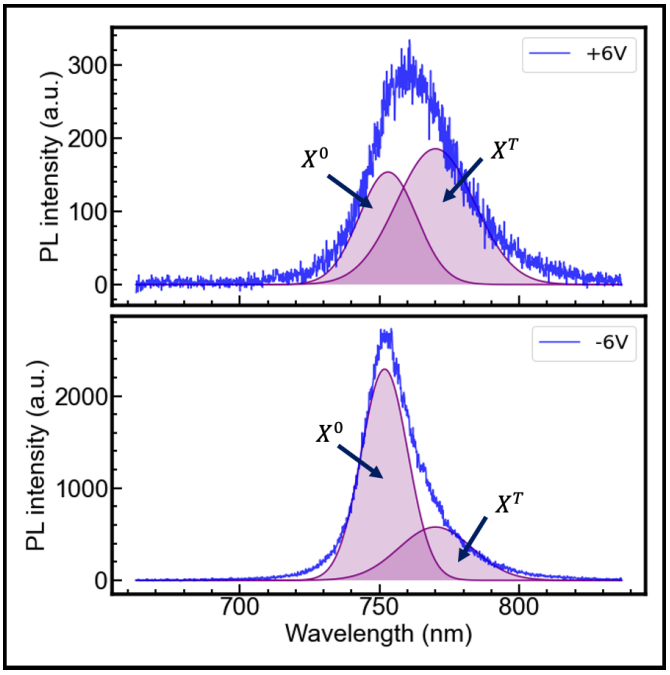

Figure 1: PL spectra at different gate voltage. X^0 and X^T emission is resolved by using the Gaussian fitting method. Spectrum at +6V (top) and spectrum at -6V (bottom).

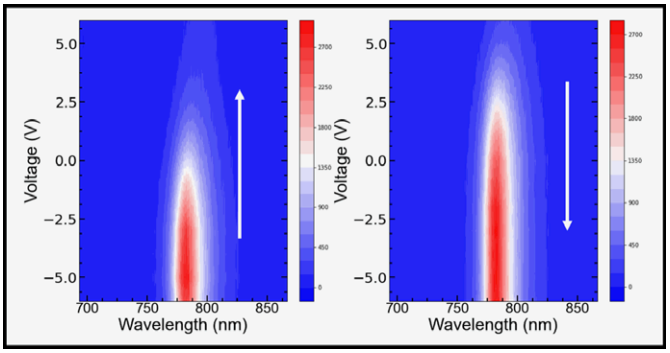

Figure 2: PL intensity modulation as a function of a gate voltage. PL intensity modulation shows different behavior when the voltage sweep direction is reversed.

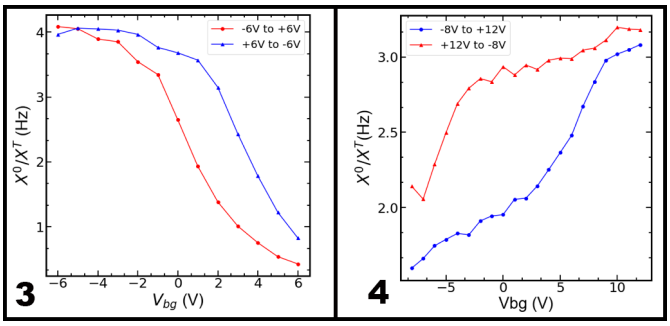

Figure 3, left: Relative ratio of X^0 and X^T emission (X^0/X^T) is plotted as a function of the DC gate voltage.

Figure 4, right: Relative ratio of X^0 and X^T emission (X^0/X^T) is plotted as a function of the pulsed gate voltage.

Conclusions and Future Steps:

In this work, we fabricate a freestanding BTO and monolayer WSe_2 based field effect device. The relative emission intensity of X^0 and X^T changes with the gate voltage and shows the hysteresis loop, which confirms that WSe_2 senses and optically reads out the polarization switching in BTO. As a next step, we will study the thickness dependent ferroelectricity in BTO by interfacing WSe_2 with BTO of various thickness. Also, BTO is known to have various phases at different temperatures [8]. We will explore the phase transitions in BTO by varying the temperature and study the optical and electronic property change in WSe_2 in response to the phase transition of BTO.

References:

[1] W. Gao,. et al. JOM 6 (2020).
[2] Lu, D., et al. Nature Mater 15, 1255-1260 (2016).
[3] Ji, D., et al. Nature 570, 87-90 (2019).
[4] Eom, K., et al. Science Advances 7 (2021).
[5] Bakaul, S., et al. Adv. Mater. 32, 1907036 (2020).
[6] Salles P., et al. Adv. Mater. Interfaces, 8, 2001643 (2021).
[7] Bakaul S. AIP Advances 11, 115310 (2021).
[8] Shu, Y.C., et al, Philos. Mag.B 81, 2021-2054 (2001).

Mechanically Driven Electron Spins with a Diamond Thin-Film Bulk Acoustic Resonator

CNF Project Number: 2126-12
Principal Investigator(s): Gregory David Fuchs[1]
User(s): Johnathan Kuan[2], Anthony D'Addario[2]
Collaborator(s): Sunil Bhave[3], Ozan Erturk[3]

Affiliation(s): 1. Department of Applied and Engineering Physics, Cornell University; 2. Department of Physics, Cornell University; 3. Department of Electrical and Computer Engineering, Purdue University

Primary Source(s) of Research Funding: Defense Advanced Research Projects Agency- DARPA DRINQS program (Cooperative Agreement #D18AC00024), Q-NEXT (U.S. Department of Energy, Office of Science, National Quantum Information Science Research Centers)

Contact: gdf9@cornell.edu, jk2788@cornell.edu, ajd344@cornell.edu

Website(s): https://fuchs.research.engineering.cornell.edu/

Primary CNF Tools Used: OEM Endeavor M1, Westbond 7400A Ultrasonic Wire Bonder

Abstract:

Lattice strain is an effective method of coherently manipulating electron spins in solid state defect centers such as the diamond nitrogen-vacancy center. To improve the achievable strain and power efficiency of bulk acoustic resonators for quantum control, we develop and characterize a released diamond thin-film bulk acoustic resonator. We demonstrate coherent driving of a double quantum transition of the NV electron spin through acoustically driven Rabi oscillations, achieving a Rabi frequency of 6 MHz. We also study the performance of the device over various powers and find that driving larger than 25 dBm deteriorates the performance of the FBAR.

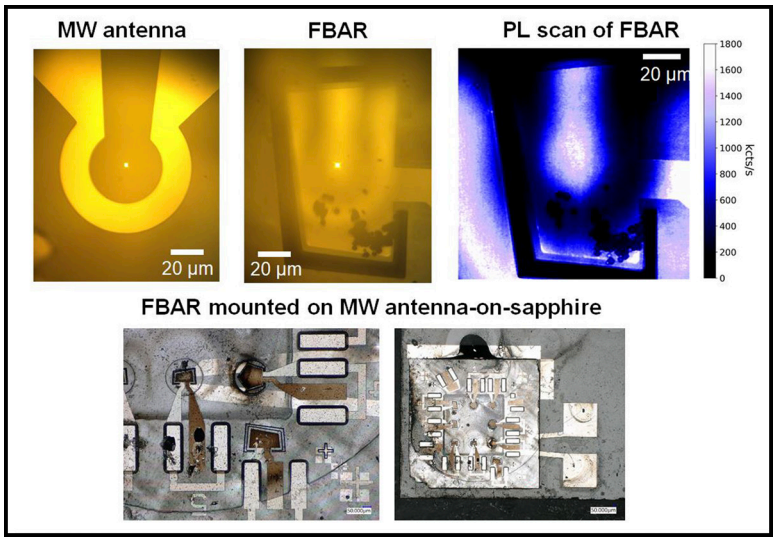

Figure 1: Microscope images of the MW antenna and FBAR device structure during our measurements, as well as a photoluminescence image of an AlN FBAR on diamond. The other two images are pictures taken of the FBAR device and antenna chip aligned on top of each other.

Summary of Research:

The diamond nitrogen-vacancy (NV) center is a solid-state defect consisting of a substitutional nitrogen adjacent to a lattice vacancy. The NV center electron spin interacts with many external fields (magnetic, electric, etc.), making it an excellent platform for quantum control and sensing. Acoustic control of the NV center with strain has been achieved with High Overtone Bulk Acoustic Resonators (HBARs) fabricated on diamond. The lattice strain provided by these devices have been used in experiments demonstrating coherent control and continuous dynamical decoupling for protecting electron spin coherence. In addition, strong driving on the electron spin can be used to protect the spin coherence of the native nitrogen spin of the NV center.

Strong driving of the electron spin can temporally average away the hyperfine interaction between the electron and nitrogen spin, effectively decoupling them. This opens avenues for using the nitrogen spin as a sensor, leveraging its long spin coherence time, while using the electron spin for optical initialization and readout.

To achieve strong driving of the electron spin with lattice strain, we fabricated a new generation of thin-film bulk acoustic resonators (FBAR) on single crystal diamond (Figure 1). The FBAR resonators consist of a 1.5 μm AlN transducer, with a bottom electrode and a top Pt electrode. The transducer deposited onto of a 10 μm thin optical grade diamond, which is created through reactive ion etching. The AlN film is sputtered using the OEM

Endeavor M1 tool at CNF. After fabricating the AlN transducer, we release the FBAR from the surrounding diamond via a backside etch. An antenna for magnetic control of the NV centers is fabricated on a separate sapphire chip that is bonded to the diamond before testing.

We perform measurements of this FBAR with an electromechanical mode at 1.9237 GHz. An external magnetic field is applied to tune the electron double quantum transition (ms = -1 to ms = +1) to be resonant with the mode. We coherently drive Rabi oscillations of to measure the strain generated by our device (Figure 2). As we increase the drive power, the oscillation frequency increases linearly. This continues up to a certain point, after which, the electromechanical response of the device is permanently degraded. The exact physical mechanism that is causing the degradation in performance is unclear, but we suspect that thermal heating due to the high power applied to the device plays a strong role, damaging the piezoelectric film and/or the Pt electrodes.

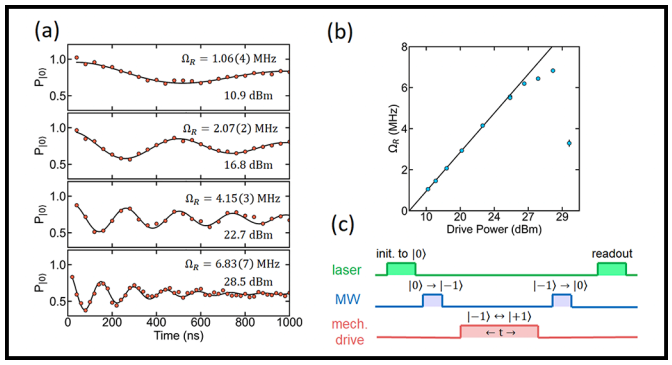

Figure 2: (a) Mechanical Rabi measurements as a function of applied power to the FBAR device. As we increase the power, the Rabi frequency increases. (b) Summary of all the mechanical rabi frequencies as a function of applied power. There is a linear relationship, until the electromechanical response of the device permanently changed with too much applied power. (c) Pulse sequence of the mechanical Rabi sequence used.

Conclusions and Future Steps:

We have developed a process for fabricating released AlN FBAR devices on diamond for NV sensing protocols. The next step is to investigate the cause of the degradation of the device performance at high powers. In addition, we hope to improve the process of depositing AlN on diamond, to mitigate losses introduced during sputtering and to consistently get high quality films.

Room Temperature Optically Detected Magnetic Resonance of Single Spins in GaN

CNF Project Number: 2126-12
Principal Investigator(s): Gregory David Fuchs[1], Farhan Rana[2]
User(s): Jialun Luo[3], Yifei Geng[2]

Affiliation(s): 1. School of Applied and Engineering Physics,
2. Department of Electrical and Computer Engineering; 3. Department of Physics; Cornell University

Primary Source(s) of Research Funding: Cornell Center for Materials Research (CCMR),
an NSF Materials Research Science and Engineering Center (DMR-1719875);
The NSF TAQS program (ECCS-1839196); Cornell Engineering Sprout program

Contact: gdf9@cornell.edu farhan.rana@cornell.edu, jl3562@cornell.edu yg474@cornell.edu

Website(s): http://fuchs.research.engineering.cornell.edu

Primary CNF Tools Used: AJA sputtering system, GCA 5x stepper

Abstract:

Optically detected magnetic resonance (ODMR) is an efficient mechanism to readout the spin of solid-state color centers based on spin-dependent relaxation between the optically excited states to the ground states. The detection of high contrast room temperature ODMR becomes the hallmark for a color center to become useful quantum sensors. Our work discovers such optically addressable spins in single defects hosted GaN. We measure two distinct ODMR responses from the defects with contrast as large as 30%, marking the existence of least two defect species in GaN. Our results lay the foundation for a promising quantum sensing platform and provide additional insights into the nature of GaN defects.

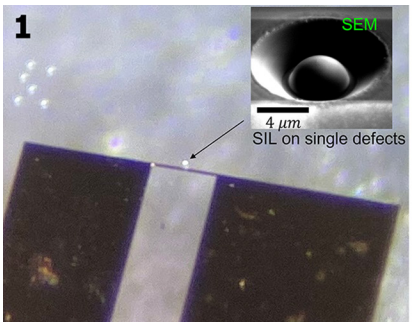

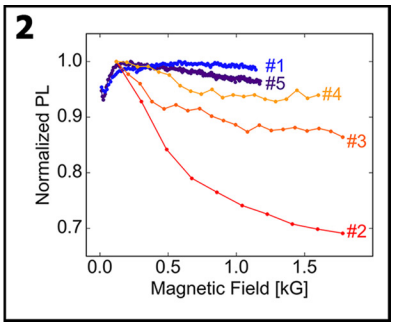

Figure 1, left: Microwave antennae under optical microscope. Inset: SEM of a solid-immersion lens. Figure 2, right: The magnetic field dependent PL of five defects.

Summary of Research:

Background. Room temperature ODMR has been detected in many solid-state color centers such as nitrogen-vacancy (NV) centers in diamond [1], silicon vacancy centers [2] and divacancy centers [3] in SiC, and recently in boron vacancy center ensembles [4,5] and unidentified single defects [6] in hexagonal boron nitride (hBN).

As the third-generation semiconductor, GaN is a mature platform with well-developed electronics applications owing to its wide direct bandgap and high breakdown field [7]. Recently, it has also been found to host bright single photon emitters with spectrally narrow photoluminescence (PL) in the visible spectrum [8,9]. These excellent optical properties, combined with the engineerability of GaN make these single-photon emitting defects attractive for on-chip photonics and relevant quantum technologies. However, the atomic structure of these defects has not yet been identified. We report [10] the discovery of high-contrast optically detected spin resonance, which is both interesting for identifying the defect structure, and for a potential application in quantum magnetometry.

Methods. We use a homebuilt laser scanning confocal microscope to measure the photoluminescence. To enhance the PL collection from the sample, we carve out a hemispherical solid-immersion-lens on top of the defect of interest with focused ion beam milling as seen in Figure 1a. We then use GCA 5x stepper to define the microwave antennae pattern and use the AJA sputter system to deposit a stack of Cr(10nm)/Cu(1um) to make the antennae shown in Figure 1b, which creates microwave that excites the spin resonances.

Results. Figure 2 shows the magnetic field dependent PL (magneto-PL) responses of 5 individual single defects, where the magnetic field is roughly aligned to the GaN crystal c-axis. Defects #1 and #5 show low PL at low magnetic field and saturate at high PL at high field. In

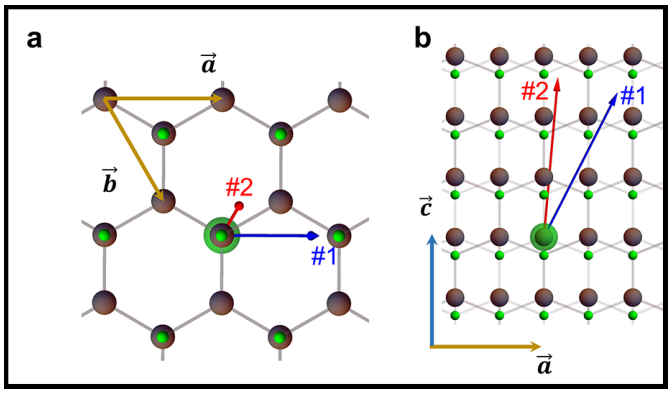

Figure 3: Spin quantization axes of defects #1 and #2 in a GaN lattice.

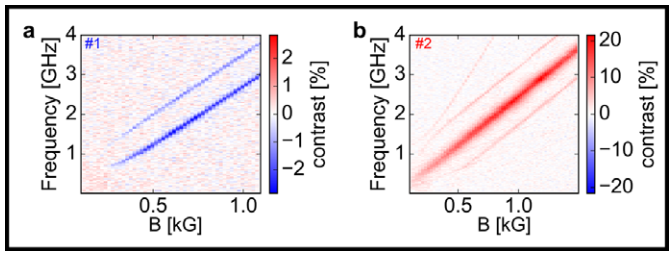

Figure 4: The ODMR spectra as a function of magnetic field of representative defects: defect #1 for group-I and defect #2 for group-II.

contrast, defects #2-#4 show monotonically decreasing PL as the magnetic field increases. The magneto-PL gives the first evidence of two distinct defect species with $S \geq 1$ spin.

The spin quantization axis is an important parameter for studying and revealing the nature of a new defect in solids. We examine the minimum Hamiltonian of a spin with $S \geq 1$ interacting with magnetic field $\vec{B}$ given by

$$H = DS_z^2 + E\left(S_x^2 - S_y^2\right) + g\mu_B \vec{S} \cdot \vec{B},$$

where S is the electronic spin operator, g the electronic g-factor, μ_B the Bohr magneton, D and E together the zero-field interaction parameters. An angle between the magnetic field $\vec{B}$ and the spin quantization axis introduces off-diagonal matrix elements between the spin eigenstates, mixing them and reducing the ODMR contrast. Thus, we find the spin quantization axes by measuring the angle resolved ODMR and finding the optimal angles that produce the largest contrast.

Figure 3 shows the spin quantization axes for defects #1 and #2, both of which lie in the a-plane but do not connect an atom with its n-th nearest neighbor for small n.

We can now further probe the spin Hamiltonian by measuring the magnetic field dependent ODMR, where the field is aligned with the spin axes. Figure 4 shows ODMR spectra of defects #1 and #2 as a function of magnetic field.

Defect #1 exhibits two negative contrast spin resonances that disperse with a gyromagnetic ratio of $\gamma_e = 2.8$ MHz/G, which confirms electron spins. The signal vanishes at low magnetic field because the spin sublevels become degenerate and mix with each other. The data can be fit by $D \approx E \approx 400$ MHz for a spin-1 Hamiltonian.

Defect #2 shows a total of four positive contrast resonances, where three of them disperse with γ_e and one with $2\gamma_e$. Worth noted is that the maximum contrast of the spin resonance of defect #2 is as large as 30%. The number resonances require a minimum model of spin-3/2 system. However, the minimum Hamiltonian can only account correctly for the three resonances that disperse with γ_e when $D \approx 370$ MHz and $E = 0$, pointing to additional terms required in the Hamiltonian.

The ODMR signatures corroborate that there are at least two different species of optically addressable single spin defects in GaN.

Acknowledgements:

We thank Len van Deurzen, Debdeep Jena, and Huili Grace Xing for useful discussions and for supplying the GaN substrates. We thank Brendan McCullian, Nikhil Mathur, Anthony D'Addario, and Johnathon Kuan for very helpful discussions on physics and microwave experiments.

References:

[1] Doherty, M. W., et al. Physics Reports 528, 1-45 (2013).
[2] Widmann, M., et al. Nature Mater 14, 164-168 (2015).
[3] Koehl, W. F., Buckley, B. B., Heremans, F. J., Calusine, G., and Awschalom, D. D. Nature 479, 84-87 (2011).
[4] Gottscholl, A., et al. Nat. Mater. 19, 540-545 (2020).
[5] Gao, X., et al. Nano Lett. 21, 7708-7714 (2021).
[6] Chejanovsky, N., et al. Nat. Mater. 20, 1079-1084 (2021).
[7] Milligan, J. W., et al. 2007 IEEE Radar Conf. 960-964 (2007).
[8] Geng, Y., et al. Sci Rep 13, 8678 (2023).
[9] Geng, Y., Jena, D., Fuchs, G. D., Zipfel, W. R., and Rana, F. Preprint at arXiv:2306.17339 (2023).
[10] Luo, J., Geng, Y., Rana, F., and Fuchs, G. D. Preprint at arxiv:2306.12337 (2023).

Coherent Acoustic Orbital Control of Diamond NV Center Excited States

CNF Project Number: 2126-12
Principal Investigator(s): Gregory David Fuchs
User(s): Brendan Andrew McCullian

Affiliation(s): School of Applied and Engineering Physics, Cornell University

Primary Source(s) of Research Funding: DARPA Driven and Nonequilibrium Quantum Systems (DRINQS) Program, Department of Energy Office of Basic Energy Sciences, Office of Naval Research

Contact: gdf9@cornell.edu, bam327@cornell.edu

Primary CNF Tools Used: GCA 6300 DSW 5X g-line Wafer Stepper, Heidelberg Mask Writer - DWL2000, AJA Sputter Deposition, Westbond 7400A Ultrasonic Wire Bonder

Abstract:

The spectrally narrow, spin-dependent optical transitions of nitrogen-vacancy (NV center) defects in diamond have been shown to be a promising platform for quantum networking. The entanglement generation rates of such networks suffer from spectral diffusion that originates from electric field fluctuations in the diamond, which couple to the excited state orbital doublet and alter the optical frequencies. With the motivation of better understanding how orbital decoherence can be overcome, we investigate quantum control of the excited state orbitals using gigahertz frequency strain. We show that coherent, multi-phonon orbital Rabi oscillations can be acoustically driven on nanosecond timescales. Additionally, we investigate orbital Rabi splitting in spectroscopy, finding good agreement between the measured orbital Rabi rate found by the two detection methods.

Summary of Research:

Diamond NV centers are a promising platform for quantum networking applications owing to their spectrally narrow, spin-preserving optical transitions at cryogenic temperatures [1]. Spectral diffusion of the optical transition frequencies decreases the entanglement generation rate [2,3]. Spectral diffusion originates from fluctuations of the local electric field environment of the defects and the coupling of these electric field fluctuations to the excited state orbital doublet which alters the optical transition frequencies and diminishes coherence [4].

Our recently published work studying the correlations between spectral diffusion and other physical parameters of the NV center found correlation with static strain [5]. Related to this, we have previously studied the coupling of GHz frequency acoustic waves to the excited state orbitals [6]. These results indicate that for some NV centers the optical transitions may be stabilized by coherently driving the excited state orbital transition using acoustic waves. With this idea in mind, we set out to demonstrate coherent acoustic orbital control in the time domain.

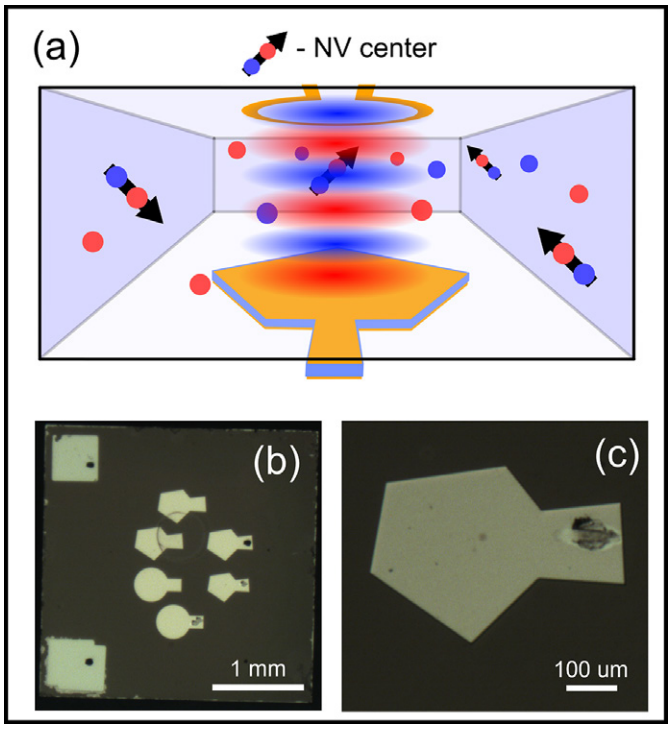

Figure 1: (a) Schematic of HBAR-on-diamond device for acoustic orbital control. HBAR transducer (orange pentagon) on diamond surface launches GHz frequency strain waves (red and blue ovals) into diamond bulk where the dynamic strain interacts with bulk NV centers. (b,c) Optical micrograph of finished HBAR-on-diamond device showing several finished HBARs on the diamond chip.

Our sample (Figure 1) is a type IIa diamond with individually addressable single NV centers formed via electron irradiation and subsequent annealing. On one diamond surface we fabricated a high-overtone bulk acoustic-wave resonator (HBAR) capable of launching GHz-frequency strain waves into the diamond bulk.

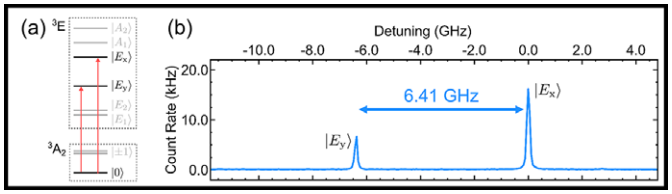

Figure 2: (a) Spin-preserving optical transitions of the spin-0 subspace (red arrows) of the NV center. (b) Laser-frequency swept PLE spectroscopy of a single NV center showing 6.41 GHz orbital splitting.

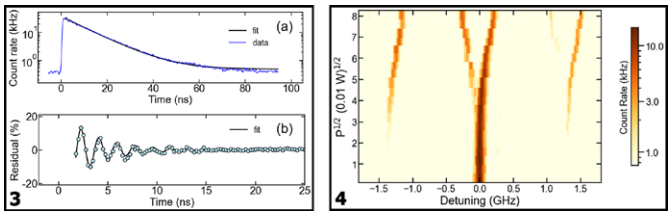

Figure 3, left: (a) Time-resolved histogram of photons emitted from our defect with respect to 1 ns resonant laser pulses (blue curve) while the HBAR is mechanically driven at 1.29 GHz. Exponential fit (black curve) used to remove exponential decay and extract residual oscillation. (b) Residual oscillation showing ns-scale precession of the orbital states in the strain field. Black fit is to a decaying sinusoid. Figure 4, right: (a) Frequency-swept PLE near the Ex transition versus acoustic drive power showing orbital splitting with increasing acoustic drive power.

The HBAR is formed by sandwiching a piezoelectric layer in between metal electrodes. The bottom electrode layer ([Ti (15 nm)/Pt (90 nm)] was deposited using the AJA Sputter Deposition system. A 1.2 μm thick layer of piezoelectric zinc oxide was then sputtered using equipment the Cornell Center for Materials Research. Finally, the top metal electrodes ([Ti (15 nm)/Pt (180 nm)] were fabricated by using the Heidelberg Mask Writer - DWL2000 to make the mask, the GCA 6300 DSW 5X g-line Stepper to write the pattern, and the AJA Sputter Deposition system to deposit the metals. After lift-off the device was wire bonded to our cryostat microwave feed lines using the Westbond 7400A Ultrasonic Wire Bonder.

We characterize the static strain splitting of a single bulk NV center in the diamond by performing photoluminescence excitation (PLE) spectroscopy [7]. We tune a red laser (~637.2 nm) across the resonant optical transitions of the NV center while counting photons emitted into the phonon sideband. The spin-preserving optical transitions are from orbital singlet, spin triplet ground states to orbital doublet, spin triplet excited states [4]. All measurements are carried out in a helium flow cryostat at 7 K. We focus solely on the spin-0 subspace. PLE spectroscopy of our defect reveals a 6.41 GHz splitting between the spin-0 orbital excited states which results from static strain in the diamond (Figure 2).

We perform time-domain resonant orbital driving experiments by tuning a red laser (~637.2 nm) onto resonance with an optical transition between the spin-0 ground state and one of the spin-0 orbital transitions (Figure 3). While continuously driving our acoustic resonator at 1.29 GHz (such that we excite orbital transitions via a 5-phonon drive) we provide 1 ns resonant laser pulses and record the arrival time of emitted photons relative to the excitation laser pulses. We observe an expected exponential decay of photoluminescence resulting from spontaneous emission as the defect leaves the excited state, and a residual photoluminescence oscillation which results from coherent orbital oscillations driven by the HBAR.

We confirm that these time domain oscillations are the result of the acoustic driving by performing PLE spectroscopy in the presence of acoustic drive (Figure 4). We observe a splitting of the PLE spectrum as the acoustic driving amplitude increases which results from coherent orbital driving. The splitting of the PLE spectrum from acoustic drive matches well with the frequency of the time-domain orbital oscillations, confirming that they originate from the same physics.

Conclusions and Future Steps:

Our results indicate that the excited state orbital doublet of NV centers can be coherently driven via acoustic drive. We confirm that our observed oscillations in the time domain match with the splitting observed in resonant optical spectroscopy under acoustic drive. Coherent orbital control will enable future studies of orbital and optical coherence of NV centers [8] under acoustic drive, where we can quantify the orbital and optical coherences and investigate orbital dynamic decoupling.

Our manuscript on time-domain coherent acoustic orbital control is currently under preparation.

References:

[1] L. Childress, et al., Phys. Rev. A 72, 052330 (2005).
[2] K. M. C. Fu, et al., Phys. Rev. Lett. 103, 256404 (2009).
[3] S. L. N. Hermans, et al., Nature 605, 663 (2022).
[4] J. R. Maze, et al., New J. Phys. 13, 025025 (2011).
[5] B. A. McCullian, et al., Phys. Rev. Appl. 18, 064011 (2022).
[6] H. Y. Chen, et al., Phys. Rev. Lett. 120, 167401 (2018).
[7] K. W. Lee, et al., Phys. Rev. Appl. 6, 034005 (2011).
[8] L. C. Bassett, et al., Science 345, 6202 (2014).

Nanostructure Integrated Silicon Vacancy in 4H-Silicon Carbide

CNF Project Number: 2126-12
Principal Investigator(s): Gregory David Fuchs
User(s): Jae-Pil So

Affiliation(s): Applied and Engineering Physics, Cornell University

Primary Source(s) of Research Funding: National Science Foundation, OMA.2137828

Contact: gdf9@cornell.edu, js3338@cornell.edu

Primary CNF Tools Used: Oxford COBRA, Oxford 81 Etcher, 5X g-line stepper, Dicing saw - DISCO, SC4500 Odd hour Evaporator, AJA Sputter, Zeiss Supra SEM, Zeiss Ultra SEM, Nabity

Abstract:

Silicon vacancy (V_{si}) centers in 4H-silicon carbide (4H-SiC) has emerged as a candidate for quantum networking applications owing to its outstanding physical properties including a long spin coherence time, a high Debye-Waller factor, and its status in a mature semiconductor with established fabrication recipes. However, the out-of-plane orientation of optical dipole of VSi introduces a challenge for optically exciting it with a free-space laser, and coupling it external optical structures. Here we demonstrate fabrication of SiC nanowires using metal-assisted chemical etching (MACE) that can be cleaved mechanically and transferred on the other substrates. Also, we demonstrate combining V_{si} with a plasmonic cavity that enhances the emission rate.

Summary of Research:

Optically accessible spin states in solids are a promising basis for establishing a quantum networking platform. 4H-SiC offers a unique opportunity for on-chip quantum photonics, as it hosts a variety of optically accessible defects [1,2]. V_{si} in 4H-SiC has shown excellent optical coherence at cryogenic temperatures with millisecond spin-coherence time, and coherent coupling to nuclear spins [3-5]. However, the out-of-plane orientation of its optical dipole prevents it from being excited by a free-space pump laser that produces only in-plane electric field oscillation. Here, we demonstrate the fabrication of SiC nanowires using a top-down method, allowing nanowires that can be cleaved mechanically and transferred on the other substrates [6]. This approach enables the excitation of the optical dipole, which is now elongated along the in-plane direction. Also, we demonstrate combining V_{si} with a plasmonic silver nanopan cavity which has both transverse electric (TE) and magnetic (TM) modes [7].

To demonstrate SiC nanowires with embedded V_{si}, we use a metal-assisted chemical etching (MACE) technique (Figure 1a) [6]. First, a monolayer polystyrene bead array is dispersed on entire SiC chip using DI-water batch

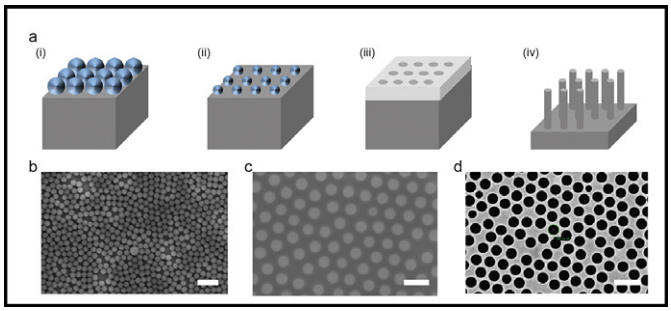

Figure 1: (a) Schematic of the fabrication procedures to create SiC nanowire. (b,c) SEM images of the polystyrene beads array on SiC substrate (b) before and (c) after reducing the diameter via RIE. Scale bar, 3 mm and 500 nm, respectively. (d) SEM image of the Pt mesh. Scale bar, 500 nm.

(Figure 1b). Next, the diameter of the beads are reduced to 260 nm to free up space between the beads via reactive ion etching (RIE) as shown in Figure 1c. Then we obtain Pt mesh via typical metal deposition method using e-beam evaporation (Figure 2d). The hole diameter of the Pt mesh determines the diameter of the SiC nanowire to be fabricated. Lastly, the SiC substrate with the PT mesh is immersed in etching solutions of $HF:H_2O_2:H_2O$ (volume ratio = 5:1:6) at room temperature while Pt mesh act as an etching catalyst. The etching front of the SiC substrate moves downward vertically, which results in the formation of vertical SiC nanowire arrays.

After being cleaved and transferred onto the Si/SiO_2 substrate, we perform optical measurements of the single nanowires using confocal laser microscope setup with continuous-wave 785 nm laser and two scanning mirrors at 10 K. The light emission from the nanowire is collected by objective lens and sent to avalanche photodiodes or monochromator/charge-coupled device via optical fibers. Figure 2a shows the measured photoluminescence (PL) intensity map of the SiC nanowire at 10 K. Bright emission spots are observed at the end of the nanowire probably due to scattered emission at the end facet of it. Additionally, the PL spectrum measured at the brightest spot exhibit three emission peaks at 859.1 nm, 861.6 nm,

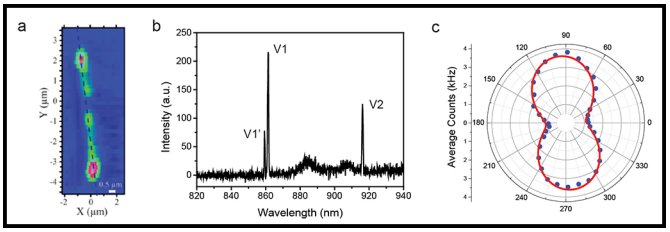

Figure 2: (a) Measured PL intensity map for the SiC nanowire on the Si/SiO_2 substrate. The pump power was 105 mW. Scale bar, 500 nm. (b) PL spectrum measured at the brightest spot in (a). (c) Polar plot of the emission as a function of the polarization angle. The line indicates the fitted curve.

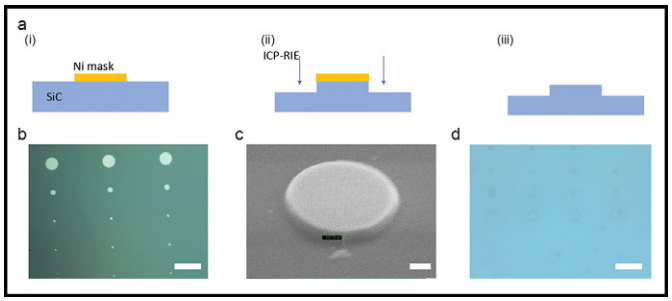

Figure 3: (a) Schematic of the fabrication procedures for SiC-Ag nanopan structure. (b) Optical microscope image of Ni masks on SiC substrate. Scale bar, 20 mm. (c) SEM image of the SiC disk prior to silver encapsulation. Scale bar, 500 nm. (d) Optical microscope image of the SiC-Ag nanopan structure from the back side of the wafer. Scale bar, 20 mm.

and 914.1 nm, which corresponds to the V1', V1, and V2 emission, respectively. This means that elongation of optical dipole along the in-plane direction enables observation of all emission lines under free-space laser pumping. To verify the optical dipole orientation of the emission, we performed emission polarization measurements. Figure 2c shows the emission polarization data obtained from the same spot used in Figure 2b and the corresponding fitting curve obtained using a cos2(q) fitting function. The emission polarization visibility is calculated to be 76% elongated along axial direction of the nanowire as expected.

Next, to demonstrate a plasmonic cavity coupled V_{si} in 4H-SiC, we employ silver nanopan resonator encapsulating the SiC microdisk structure. Figure 3a shows the fabrication procedure. First, a circular shape Ni mask with a thickness of 100 nm is deposited on 4H-SiC wafer which contains V_{si} using e-beam lithography and metal evaporation technique (Figure 3b). Next, inductively coupled plasma-reactive ion etching (ICP-RIE) is performed to etch the SiC layer (Figure 3c), and subsequently the Ni mask is removed using a Ni etchant (Figure 3d). After removing the Ni mask, 400.nm-thick silver layer is coated on the whole surface of the SiC disk substrate using an e-beam evaporator.

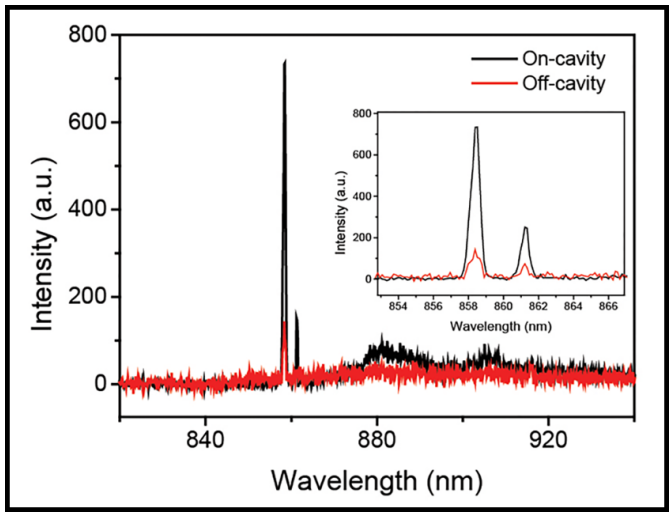

Figure 4: PL spectra measured at the nanopan (black) and the flat substrate (red). Inset shows the close-up of the emission peaks.

To access initially the characteristics of the nanopan combined V_{si}, we optically pump the nanopan region using a 785 nm continuous-wave laser and compare the emission spectrum to that from the flat surface at 10 K. We observe a 4-fold enhancement of V1' emission and 5-folds enhancement of V1 emission at the same time (Figure 4). The V1' emission is polarized along in-plane direction is predicted to couple to the TE whispery gallery mode (WGM), whereas V1 emission is probably coupled to the TM WGM.

Conclusions and Future Steps:

In this work, we demonstrate the integration of V_{si} in 4H-SiC with two types of nanostructures that enable us to excite the V1 emission via free-space laser pumping. In the future, we plan to perform the time-resolved PL measurements to extract the Purcell factor of this cavity-coupled emitter system. Also, it might be possible to apply microwave excitation to the emitter to mix the ground spin states, which will enable us to observe photoluminescence excitation (PLE) under resonant excitation.

References:

[1] Lukin, D., et al., Nat. Photonics 14, 330-334 (2020).
[2] Crook, A., et al., Nano Lett. 20, 3427-3434 (2020).
[3] Nagy, R., et al., Nat. Commun. 10, 1954 (2019).
[4] Widmann, M., et al., Nat. Mater. 14, 164-168 (2015).
[5] Babin, C., et al., Nat. Mater. 21, 67-73 (2022).
[6] Kim, J., et al., Nat. Nanotechnol. 12, 963-968 (2017).
[7] Kwon, S., et al., Nano Lett. 10, 3679-3683 (2010).

Exciton Density Waves in Coulomb-Coupled Dual Moiré Lattices

CNF Project Number: 2633-18
Principal Investigator(s): Jie Shan, Kin Fai Mak
User(s): Yihang Zeng, Zhengchao Xia

Affiliation(s): Laboratory of Atomic and Solid State Physics, Applied and Engineering Physics; Cornell University

Primary Source(s) of Research Funding: NSF, DOE, ONR

Contact: jie.shan@cornell.edu, kinfai.mak@cornell.edu, yz425@cornell.edu, zx287@cornell.edu

Primary CNF Tools Used: Autostep i-line Stepper, Hamatech Wafer Processor Develop, Heidelberg Mask Writer - DWL2000, Photolithography Spinners, SC4500 Odd/Even-Hour Evaporator, Dicing Saw - DISCO, Zeiss Supra SEM, Nabity Nanometer Pattern Generator System (NPGS)

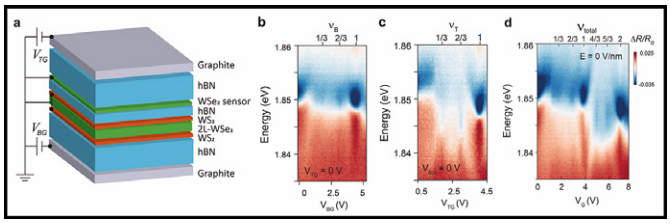

Figure 1: a, Schematic of a dual-gated device. b-d, Reflectance contrast spectrum of the sensor 2s exciton as a function of gate voltage and filling factor. In b, c one of the lattices is empty and in d two lattices are equally populated.

Abstract:

Strongly correlated bosons in a lattice are a platform to realize rich bosonic states of matter and quantum phase transitions, but in a solid-state system they are challenging to realize [1]. Here we trap interlayer excitons (bosons composed of bound electron-hole pairs) in a lattice provided by an angle-aligned WS_2/bilayer WSe_2/WS_2 heterostructure. We observe correlated insulating states when the combined electron filling factor of the two lattices equals to 1/3, 2/3, 4/3, and 5/3. These new states can be interpreted as exciton density waves in a Bose-Fermi mixture. Our results demonstrate that Coulomb-coupled moiré lattices are fertile ground for correlated many-boson phenomena.

Summary of Research:

Two-dimensional moiré materials have emerged as a highly tunable platform for the study of strongly correlated phases of matter. However, compared to fermionic systems, strongly correlated bosonic systems are much less explored. Here, we demonstrate the realization of a Coulomb-coupled dual-moiré lattice where electrons in one lattice bind with holes in the other forming bosonic particles (excitons). In such a system, we achieve independent control of the electron and exciton densities. When the combined electron filling factor of the two lattices is tuned to 1/3, 2/3, 4/3, and 5/3, we observe a new exciton density wave phase where an exciton fluid breaks the translational symmetry.

Figure 1a illustrates a dual-gated device of an angle-aligned monolayer WS_2/bilayer WSe_2/monolayer WS_2 structure. The WSe_2 bilayer provides nearly identical triangular moiré lattices of period $a_M \approx 8$ nm at the top and bottom WS_2/WSe_2 interfaces [2] and also acts as a tunnel barrier. For the relevant density range, the electrostatically doped electrons are in the WS_2 layers. The two graphite gates independently control the combined filling factor ν (doping density per moiré lattice) and the out-of-plane electric field E in two moiré lattices. The latter tunes the distribution of electrons between the two lattices. To probe the insulating states in the coupled moiré lattices, we employ an optical sensing technique [3] by placing a WSe_2 monolayer above the top WS_2 layer. Figure 1b-d show the reflectance contrast (RC) spectrum of the sensor 2s exciton as a function of gate voltage (lower axis) and total filling factor (upper axis). An insulating state in the sample is identified when the 2s exciton resonance exhibits a blueshift and an enhanced spectral weight 11. When the electrons are in one of the lattices solely (Figure 1b, c), insulating states are observed at $\nu = 1/3, 2/3, 1, 2$. When the electrons are introduced equally in two lattices by setting $E \approx 0$ V/nm (Figure 1d), we observe additional insulating states at $\nu = 4/3, 5/3$.

We use the amplitude of the sensor 2s exciton RC, R_{2s}, to identify insulating states. The largest R_{2s} is observed in Figure 2a when both lattices have integer fillings (ν_t and ν_b denoting the filling factor of the top and bottom lattices, respectively). We also observe extended regions with enhanced R_{2s} when the top lattice is insulating, and the bottom generally charge-compressible. They correspond to the red regions in Figure 2c. Similarly, one can find the blue regions in the electrostatic phase diagram in Figure 2c when the bottom lattice is insulating, and the top is generally charge-compressible. The result is fully consistent with an independent measurement based on the moiré excitons in WS_2 (Figure 2b).

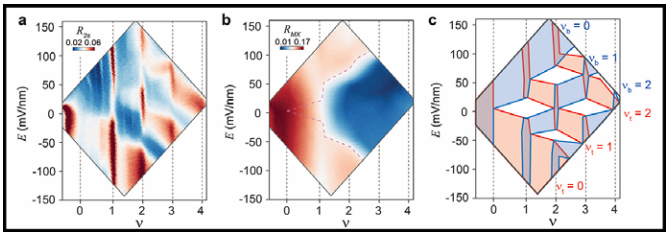

Figure 2: a,b, Reflectance contrast amplitude of the sensor 2s exciton R_{2s} (a) and WS_2 moiré exciton R_{MX} (b) as a function of total filling factor and electric field. c, Electrostatic phase diagram includes regions of gapped top lattice (red-shaded) and bottom lattice (blue-shaded).

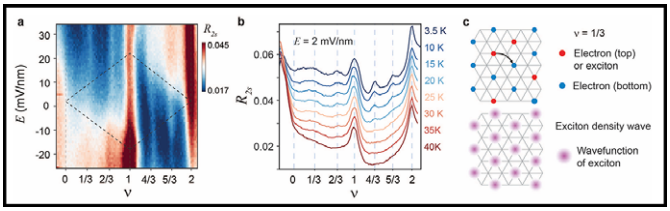

Figure 3: a, R_{2s} as a function of total filling factor and electric field. b, Horizontal linecut of a near zero field at representative temperatures. c, Schematic representation of the inter-layer Wigner crystal at v=1/3.

Upon a closer examination, we identify incompressible states from the enhanced R_{2s} at $\nu = 1/3, 2/3, 1, 4/3, 5/3$ for a wide range of electric field (Figure 3a). As temperature increases, the incompressible states at the fractional fillings disappear around 30-35 K (Figure 3b). The nature of these insulating states inside the dashed box is completely different from outside the box. We focus on the exotic fractional fillings. They are generalized Wigner crystals when electrons reside in a single lattice (outside the box). Inside the box, electrons are continuously transferred from the generalized Wigner crystal to the empty lattice as a function of electric field but remain bound to the empty sites in the original lattice by the inter-lattice long-range Coulomb repulsion. They form an "inter-layer" Wigner crystal to minimize the total intra- and inter-lattice Coulomb repulsions and can also be viewed as excitonic insulators [4]. The interlayer excitons hop along the channels defined by the Wigner crystal (Figure 3c), therefore dubbed exciton density wave (EDW). In the weak-disorder limit, EDWs are expected to possess finite superfluid densities in the ground state and are supersolids, as predicted by theoretical studies on atomic Bose-Fermi mixtures. This is an interesting direction for future studies.

References:

[1] Ma, L., Nguyen, P.X., Wang, Z., Zeng, Y., Watanabe, K., Taniguchi, T., MacDonald, A.H., Mak, K.F., and Shan, J. Strongly correlated excitonic insulator in atomic double layers. Nature 598, 585-589 (2021).

[2] Tang, Y., Li, L., Li, T., Xu, Y., Liu, S., Barmak, K., Watanabe, K., Taniguchi, T., MacDonald, A.H., and Shan, J. Simulation of Hubbard model physics in WSe_2/WS_2 moiré superlattices. Nature 579, 353-358 (2020).

[3] Xu, Y., Liu, S., Rhodes, D.A., Watanabe, K., Taniguchi, T., Hone, J., Elser, V., Mak, K.F., and Shan, J. Correlated insulating states at fractional fillings of moiré superlattices. Nature 587, 214-218 (2020).

[4] Gu, J., Ma, L., Liu, S., Watanabe, K., Taniguchi, T., Hone, J.C., Shan, J., and Mak, K.F. Dipolar excitonic insulator in a moiré lattice. Nature Physics (2021).

Gate-Tunable Heavy Fermions in a Moiré Kondo Lattice

CNF Project Number: 2633-18
Principal Investigator(s): Jie Shan, Kin Fai Mak
User(s): Wenjin Zhao, Bowen Shen, Zhongdong Han, Kaifei Kang

Affiliation(s): Kavli Institute at Cornell for Nanoscale Science, Laboratory of Atomic and Solid State Physics, School of Applied and Engineering Physics; Cornell University

Primary Source(s) of Research Funding: DOE, NSF, AFOSR

Contact: jie.shan@cornell.edu, kinfai.mak@cornell.edu, wz435@cornell.edu, bs792@cornell.edu, zh352@cornell.edu, kk726@cornell.edu

Primary CNF Tools Used: Zeiss Supra SEM, Nabity Nanometer Pattern Generator System (NPGS), SC4500 Odd/Even-Hour Evaporator, Autostep i-line Stepper, Hamatech Wafer Processor Develop, Heidelberg Mask Writer - DWL2000, Photolithography Spinners, Dicing Saw - DISCO

Abstract:

The Kondo lattice—a matrix of local magnetic moments coupled through spin-exchange interactions to itinerant conduction electrons—is a prototype of strongly correlated quantum matter [1,2]. We realize a synthetic Kondo lattice in AB-stacked $MoTe_2/WSe_2$ moiré bilayers, in which the $MoTe_2$ layer is tuned to a Mott insulating state, supporting a triangular lattice of local moments, and the WSe_2 layer is doped with itinerant conduction carriers. We observe heavy fermions with a large Fermi surface below the Kondo temperature. We also observe the destruction of the heavy fermions with an abrupt decrease in the Fermi surface size and quasi-particle mass under an external magnetic field. We further demonstrate widely and continuously gate-tunable Kondo temperatures through the itinerant carrier density or the Kondo coupling.

Summary of Research:

Common approaches to realizing strong electronic correlations rely on intermetallic compounds that involve heavy elements like lanthanides [1,2]. The use of naturally occurring elements limits the found material's tuneability. Further, these materials typically have a very complex electronic structure, which makes them hard to describe and predict by theory. We demonstrate a model Kondo system created by stacking a pair of monolayer semiconductors to study quantum phenomena ranging from heavy fermions to exotic quantum phase transitions. We use $MoTe_2/WSe_2$ moiré bilayers, in which the $MoTe_2$ layer is tuned to a Mott insulating state, supporting a triangular moiré lattice of local moments, and the WSe_2 layer is doped with itinerant conduction carriers [3,4]. We observe heavy fermions with a large Fermi surface below the Kondo temperature T^* and that the heavy fermions be destructed by an external magnetic field. The Kondo temperature can be tuned widely and continuously via an applied electric voltage. The study opens the possibility of *in situ* access to the phase diagram of the Kondo lattice with exotic quantum criticalities in a single device based on semiconductor moiré materials [5].

Figure 1 shows the schematic and optical image of a device. We fabricated dual-gated $MoTe_2/WSe_2$ devices using a layer-by-layer dry-transfer technique. We deposited 5-nm Pt contacts on hBN by standard electron-beam lithography and evaporation, followed by another step of electron-beam lithography and metallization to form a bilayer of 5-nm Ti and 40-nm Au to connect the thin Pt contacts on hBN to pre-patterned electrodes.

Figure 2 shows the temperature dependence of the resistance R_{xx} when the device is tuned to a Kondo lattice phase. There is a characteristic temperature T^*, below which resistance drops significantly, and T^* increases with the hole density in the WSe2 layer (ν_W). The inset shows the T^2-dependence of R_{xx} at low temperatures, which is a characteristic of a Landau Fermi liquid. We fit the dependence using $R_{xx} = R_0 + AT^2$, where R_0 is the residual resistance, and $A^{1/2}$ is linearly proportional to the quasiparticle mass. The value is more than an order of magnitude larger than in the region without the formation of the Kondo lattice in the same device. The large enhancement points to the emergence of heavy fermions.

Figure 3 shows the magnetic-field dependence of the Hall density, $\nu^* = B/(eR_{xy}n_M)$ for $\nu_W = 0.35$. We obtain $\nu^* \approx -\nu_W$ for $\nu_{Mo} = 2$, where the Kondo lattice is not formed. For $\nu_{Mo} = 1$, below critical magnetic field (B_c) we obtain $\nu^* \approx 1-\nu_W$. It indicates a hole Fermi surface with density of $1 + \nu_W$.

This result shows that the local moments in the $MoTe_2$ layer are hybridized with the conduction holes in the WSe_2 layer to form a large hole Fermi surface. The observed large Fermi surface, in combination with the

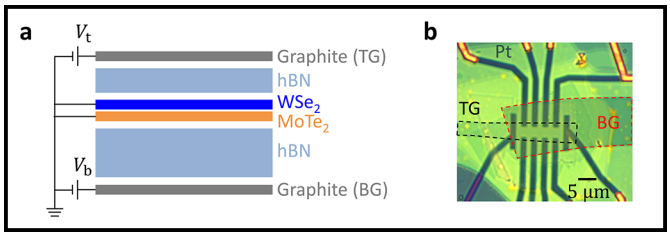

Figure 1: a, Device schematics. b, Optical microscope image of a dual-gated device. The scale bar is 5 μm.

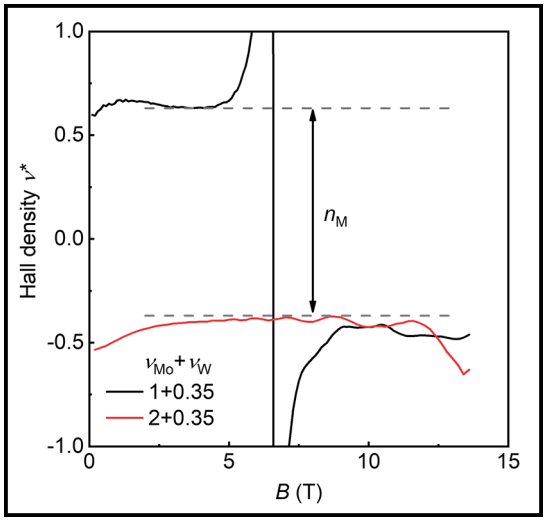

Figure 3: The corresponding magnetic-field dependence of the Hall density ν^* for $\nu = 1 + 0.35$ and $\nu = 2 + 0.35$. A density jump equaling the moiré density n_M occurs around 6 T.

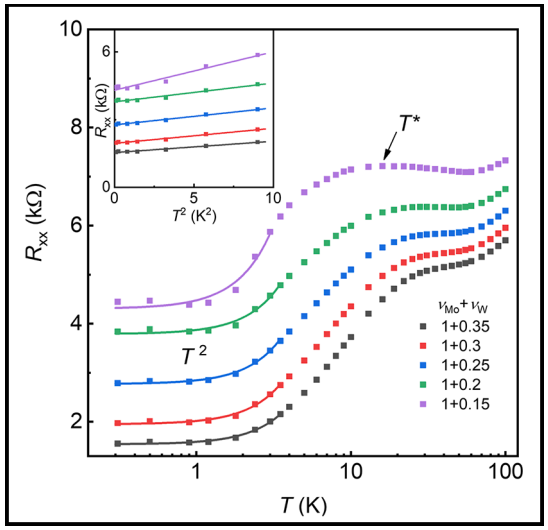

Figure 2: Temperature dependent longitudinal resistance R_{xx} at varying doping densities for $\nu = 1+ \nu_W$. The solid lines are the best fits to the quadratic temperature dependence at low temperatures. The arrows mark the Kondo temperature T^*. The insets show the scaling of R_{xx} with T^2.

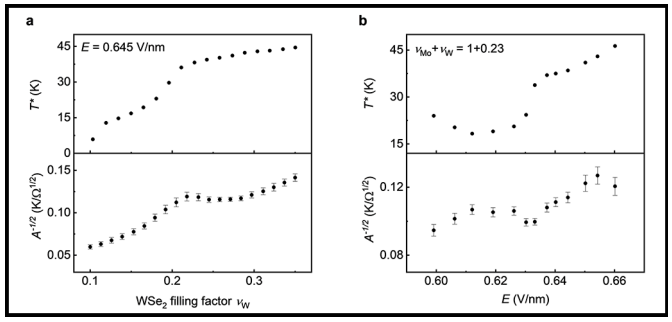

Figure 4: a, Extracted doping dependence of T^* (top) and $A^{-1/2}$ (bottom) at a fixed electric field (E=0.645 V/nm) for $\nu = 1 + \nu_W$. The two quantities show similar dependences. b, Extracted electric-field dependence of T^* (top) and $A^{-1/2}$ (bottom) at a fixed filling factor (ν=1+0.23).

quasiparticle mass enhancement, supports the realization of the Kondo lattice. The Hall measurement also shows that the large Fermi surface with hole density $1 + \nu_W$ is reduced to a small Fermi surface with hole density ν_W when a magnetic field above B_c is applied.

Figure 4 shows the tunability of the Kondo temperature T^* and the parameter $A^{-1/2}$. We show one cut along $E = 0.645$ V/nm (Figure 4a) and another cut along $\nu_W = 0.23$ (Figure 4b). The Kondo temperature (top panels) can be widely tuned by both doping and electric field. And $A^{-1/2}$ (lower panels), the inverse of the mass enhancement, largely follows T^* as expected. Increasing the doping density is expected to strengthen the Kondo effect since there are more conduction holes to screen the local moments; this is consistent with the observed dependence of T^* on ν_W.

Conclusion and Future Steps:

We have realized a Kondo lattice in AB-stacked $MoTe_2$/WSe_2 moiré bilayers. It opens exciting opportunities to study the gate-controlled Kondo destruction transition by extending the Kondo temperature further down to zero, for instance, by reducing the doping density in higher-quality devices or the interaction effect in small-twist-angle bilayers.

References:

[1] Kirchner, S., et al. Colloquium: Heavy-electron quantum criticality and single-particle spectroscopy. Rev. Mod. Phys. 92, 011002 (2020).

[2] Stewart, G. R. Heavy-fermion systems. Rev. Mod. Phys. 56, 755-787 (1984).

[3] Kumar, A., et al. Gate-tunable heavy fermion quantum criticality in a moiré Kondo lattice. Phys. Rev. B 106, L041116 (2022).

[4] Guerci, D., et al. Chiral Kondo lattice in doped $MoTe_2$/WSe_2 bilayers. Sci. Adv. 9. eade7701 (2023).

[5] Mak, K. F., and Shan, J. Semiconductor moiré materials. Nat. Nanotechnol. 17, 686-695 (2022).

Thin-Film Deposition for Surface Characterization Studies for Superconducting Radio Frequency Cavity Application

CNF Project Number: 2779-19
Principal Investigator(s): Matthias Liepe
User(s): Nathan Sitaraman, Sadie Seddon-Stettler

Affiliation(s): Cornell Laboratory for Accelerator-based Sciences and Education, Cornell University

Primary Source(s) of Research Funding: National Science Foundation under Award PHY-1549132, the Center for Bright Beams

Contact: mul2@cornell.edu, nss87@cornell.edu, sgs238@cornell.edu

Website(s): https://physics.cornell.edu/matthias-liepe

Primary CNF Tools Used: CVC SC4500 Combination Thermal/E-gun Evaporation System (Odd-Hour), AJA Sputter Deposition 1 & 2

Abstract:

Superconducting radio-frequency (SRF) cavities are a key component of particle accelerators (with applications ranging from fundamental physics research to synchrotron X-ray sources, to e-beam microscopy and lithography) and are also being developed for applications in dark matter detection and quantum computing. We are developing next-generation surface treatments to enhance the performance of niobium superconducting surfaces. By using facilities at the CNF, we investigate the effect of metallic doping on the niobium surface. We highlight our recent success in altering the niobium native oxide by zirconium doping and by gold doping.

Summary of Research:

We used CNF's AJA sputter deposition tools to deposit zirconium on niobium sample coupons. Prior to deposition, coupons received a standard pre-preparation consisting of a 60-micron electropolish, a 5-hour 800°C vacuum bake, and a 2-micron electropolish. The sputter deposition tool first removed the niobium native oxide by argon plasma sputtering, and then deposited approximately 2, 3.75, 7.5, and 10 nm of zirconium on four different samples. The deposition rate was based on the rate for similar metals and has not yet been directly calibrated. The samples then received another 800°C vacuum bake in order to fully dissolve any remaining niobium oxide and establish a uniform interface between the niobium metal and the protective zirconium oxide layer.

For increasing zirconium deposition thickness in the range of 0-3.75 nm, we find that the oxide rapidly becomes more zirconium-rich; in particular, by 3.75 nm thickness, there is no detectable niobium component in the primary oxide. Additionally, the combined intensity of the niobium and zirconium suboxide peaks decreases slightly relative to the intensity of the niobium metal peak, suggesting that the suboxide layer in the 2 nm and 3.75 nm samples is very thin. For increasing zirconium deposition thickness in the range 3.75-10 nm, however, both the primary ZrO_2 oxide and the suboxide become thicker.

We also used CNF's CVC SC4500 evaporation deposition system to deposit thin (1-2nm) layers of gold on niobium samples (prepared according to the standard pre-preparation in the earlier paragraph). This work recreated work done by a previous user from the group, Zeming Sun [1]. This work removed the oxide chemically with dilute hydrofluoric acid rather than argon plasma sputtering (as was used for zirconium deposition). We found substantial oxide still present, indicating opportunities for improvement of the process. However, we found some modification of the oxide, indicating that gold layers are promising towards oxide passivation.

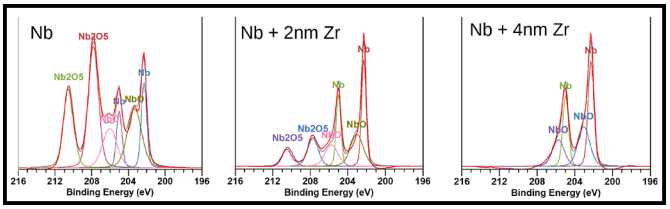

Figure 1: Peak fitting of niobium XPS data. The overallniobium oxide intensity decreases monotonically with increasing zirconium deposition thickness, and the pentoxide intensity in particular becomes undetectable by 3.75 nm zirconium deposition thickness. XPS sample analysis was performed at CCMR.

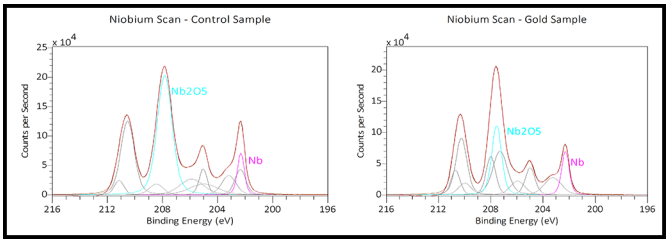

Figure 2: Preliminary peak fitting of niobium-gold XPS data. Control sample is bare niobium that has been exposed to atmosphere, gold sample has 1 nm of gold deposited on niobium. The oxide is still present, but has changed structure slightly. XPS sample analysis was performed at CCMR.

Conclusions and Future Steps:

We have demonstrated a method to eliminate the niobium pentoxide from a niobium superconducting surface. We expect that this method may be applicable to niobium superconducting devices and niobium-zirconium alloy surfaces, as well as possibly other niobium-based superconducting surfaces which typically form a niobium-rich oxide. We plan to investigate the effect of replacing niobium pentoxide with zirconium dioxide on SRF performance. We will also attempt to apply this method to the Nb_3Sn surface, and we will investigate other passive oxide layers such as hafnium, aluminum, and silicon oxide for SRF applications. We have also completed preliminary studies with thin-film depositions of gold, and will continue to investigate deposition methods to optimize the procedure for oxide passivation.

References:

[1] T. Oseroff, Z. Sun, and M. Liepe, "Measurements of the amplitude-dependent microwave surface resistance of a proximity-coupled Au/Nb bilayer," arXiv, 2023. doi:10.48550/arXiv.2305.12035.

Lithography for *in situ* Cryogenic Scanning Transmission Electron Microscopy

CNF Project Number: 2967-21
Principal Investigator(s): Jeeyoung Judy Cha
User(s): James L. Hart, Saif Siddique

Affiliation(s): Department of Materials Science and Engineering, Cornell University

Primary Source(s) of Research Funding: The Gordon and Betty Moore Foundation's EPiQS Initiative, Grant GBMF9062

Contact: jc476@cornell.edu, jlh487@cornell.edu, ms2895@cornell.edu

Website(s): cha.mse.cornell.edu

Primary CNF Tool Used: Nabity System for Supra SEM, PDMS Casting Station - Rm 224

Abstract:

Charge density waves (CDWs) of two-dimensional (2D) layered materials such as tantalum disulfide (TaS_2) and rare-earth tri-tellurides (RTe_3; R = rare-earth) can be used to make energy-efficient memory devices. To realize potential device applications, the CDW phase transitions of these materials should be studied at the nanoscale in the length scales of devices, and the changing transport properties must be correlated with the CDW phase transitions. In this project, we fabricate nanodevices of TaS_2 and RTe_3 on transmission electron microscopy (TEM) *in situ* chips such that we can operate the device inside a TEM, directly visualize the CDW phase transitions, and measure the transport properties during the CDW phase transition as a function of temperature between 100 K and 300 K.

Summary of Research:

We have successfully induced the CDW phase transitions of TaS_2 nanodevices during *in situ* cryo STEM experiments by both cooling down to 100 K (Figure 1) and by electric field. We have directly visualized the nucleation and growth of the nearly commensurate (NC) CDW out of the commensurate (C) CDW in TaS_2 nanodevices (Figure 2) and established that the nucleation of the NC-CDW state is defect-mediated (Figure 3). We have also proved that the electric-field induced phase transition from the C-CDW phase to the NC-CDW phase in TaS_2 is via Joule-heating, rather than strictly field-induced. We have also observed surprising CDW behaviors in exfoliated RTe_3 flakes due to stacking disorders present in these nanoscale samples.

Conclusions and Future Steps:

Our experiments constitute the first demonstrations of real-space direct imaging of electronic phase transitions in layered materials and the important role layer stacking disorders play on these electronic phase transitions. Three manuscripts are in preparation for submission this summer, which summarize our findings: (1) Defect-mediated CDW phase transition in TaS_2, (2) Field-induced CDW phase transition in TaS_2 is via Joule heating, and (3) Suppression of CDW phases in exfoliated RTe_3 flakes.

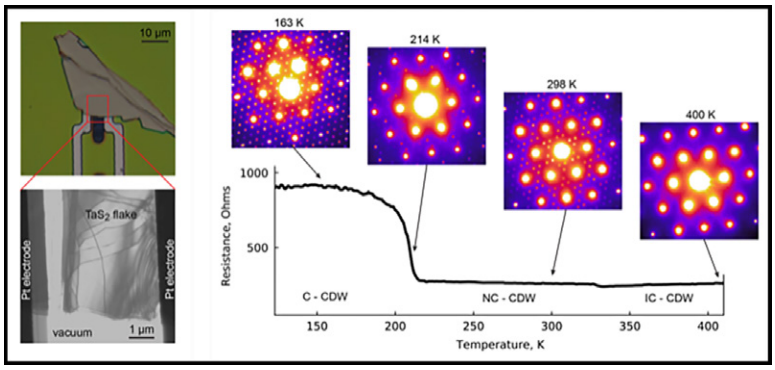

Figure 1: (Top, left) Optical micrograph of TaS_2 flake nanodevice with two electrodes. (Bottom, left) TEM image of the same TaS_2 flake, with stacking disorders shown as dark lines. (right) in situ *resistance measurement as well as* in situ *4D STEM acquisition of the TaS_2 nanodevice as a function of temperature down to 110 K. The C-CDW and NC-CDW phases can be distinguished by the superlattice patterns in the electron diffraction.*

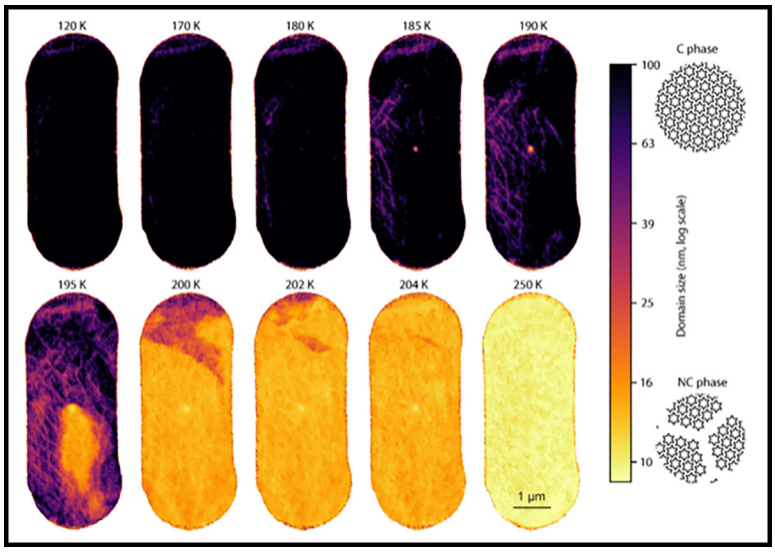

Figure 2: Nucleation and growth of the NC-CDW phase out of the C-CDW phase in the TaS_2 device as the temperature increases from 120 K to 250 K.

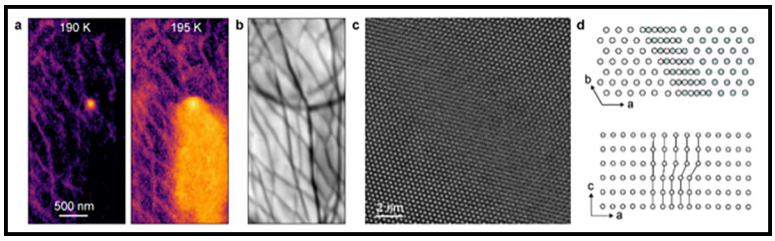

Figure 3: The nucleation of the NC-CDW phase (a) coincides with the location where the layer disorder defects (dark lines) merge (b). These dark lines were imaged in atomic resolution (c) to reveal the layer stacking disorder (d).

Novel Superconducting Microwave Devices from 2D Materials

CNF Project Number: 2998-22
Principal Investigator(s): Valla Fatemi
User(s): Luojia Zhang

Affiliation(s): Applied and Engineering Physics, Cornell University

Primary Source(s) of Research Funding: N.A (startup)

Contact: vf82@cornell.edu, lz282@cornell.edu

Primary CNF Tools Used: DWL66, DWL2000, PT770, ABM contact aligner, PT770, Nabity Nano Pattern Generating System, DISCO Dicing Saw, JEOL 6300, AJA Sputterer

Abstract:

We have made some decent progress in our nano-device fabrication within CNF this year. Our research has been focusing on measuring electronic transport properties of 2D materials Josephson junction, as well as high-Q microwave devices for qubit control / readout.

Summary of Research:

The first project was observing Josephson effect in junction made from hBN-graphene-hBN heterostructure. Although several groups have reported large Josephson supercurrent in such devices before, our device was the first successful graphene JJ fabricated completely within Cornell University. The accomplishment is from the success in the following fabrication process:

1. EBL: we performed electron-beam lithography to write the planar junction with 800 nm width and 5 μm length using the Nabity Nano Pattern Generating System (Figure 1. (a)).

2. Etching: we performed reactive ion etching using Oxford 81 to etch through the 2D materials stack and expose the graphene on the edge to form a one-dimensional contact with deposited metal (Figure 1. (b)).

3. Deposition: we have developed a good sputtering recipe for superconducting niobium which yielded 8.5K critical temperature (Figure 1. (c)).

We measured the device in a dilution refrigerator, and found a gate tunable Josephson supercurrent with maximum as large as 1.5 microamperes (Figure 1. (d)). The success of this device paved the way for the development of future more novel mesoscopic 2D materials devices.

Recently, we have fabricated a new batch of Josephson junction at CNF with bilayer graphene and WSe_2 to study the effect of spin-orbit coupling in the superconducting proximity effect.

The microwave devices we fabricated are the 2D transmission line resonators. We deposited a layer of 70 nm niobium using our sputtering recipe, then we performed photolithography on it with DWL66. We found that DWL66 is particularly useful for checking designs before finalizing them on a photomask, and handling features that are too large to be written by EBL. We first performed etching using AJA ion mill. Details of the small structures of the device are shown in Figure 2. (a) and (b). The device quality factor was measured to be around 50000. The resonance phase and magnitude of the resonator are shown in Figure 2. (d). In the second batch, we performed etching using PT770 reactive ion etcher. The quality factor was improved by a factor of 6 (more data are still being collected on these newer devices).

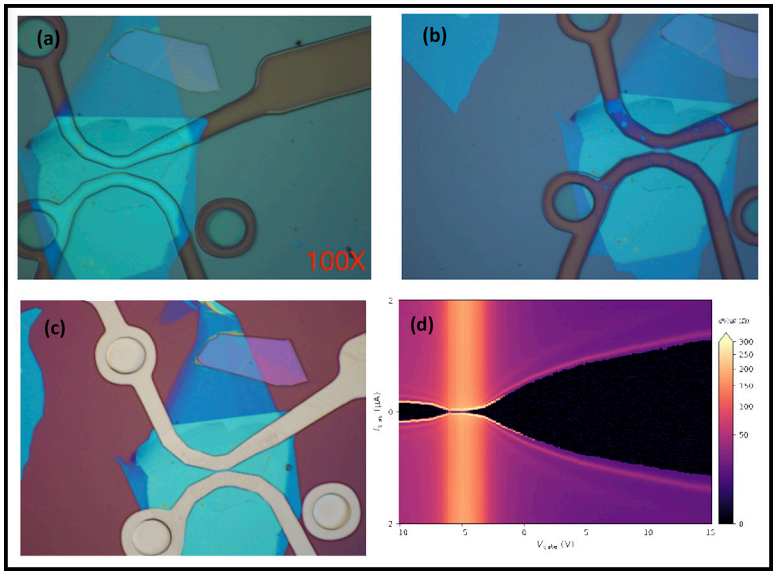

Manufacturing TiO_2 Pillar Arrays and SiN Bullseye Cavities

CNF Project Number: 3008-22
Principal Investigator(s): Professor Pablo A. Postigo
User(s): Christopher (Christer) Everly, Martin Sanchez

Affiliation(s): The Institute of Optics, University of Rochester

Primary Source(s) of Research Funding: UoR Startup

Contact: ppostigo@ur.rochester.edu, ceverly@ur.rochester.edu, msanch23@ur.rochester.edu

Website(s): https://www.postigolab.com

Primary CNF Tools Used: JEOL 6300, Spin Coaters, PT770 RIE, Microscopes, Oxford 82, Oxford 100, Plasma-Therm Tikachi HDP-CVD, Yes EcoClean Asher, Filmetrics systems, Zeiss Ultra SEM

Abstract:

Our group is interested in quantum research on photonic integrated circuit platforms. Two topics we are currently exploring are on-chip lasing, and single-photon emission enhancement with circular Bragg gratings. There have been recent reports of on-chip lasing achieved through bound states in the continuum. The bound states are made possible with an array of dielectric pillars. To study and reproduce these results we manufactured the same arrays at the Cornell NanoScale Facility.

Summary of Research:

This was the first time the user worked at CNF to create a nanostructure so we were mainly concerned with learning how to use the JEOL 6300, and to try a range of dosages to find the best parameters to create the nano pillars. We believe we found a good recipe for the electron beam exposure, but the reactive ion etching timing might need some tuning. Additionally, the quartz substrate we used was exceedingly thin — the vacuum chuck for the spin coater caused non-uniform coating to occur. Regardless, as seen from the images below we successfully created the pillar array.

Additionally, this was the first time the group was trying to manufacture bullseye cavities. Hence dosage tests and anisotropic reactive ion etch times are under study for this fabrication as well. RIE lag has caused an issue in etching smaller but important features in the bullseye cavities. It is still inconclusive as to if this problem will force us to use multiple exposures and etches to maintain the integrity of the smallest physical features.

Conclusions and Future Steps:

With the array of pillars manufactured, the next steps are to optically characterize. If the resonance is where we want it to be, then we proceed with coating the structure in CdZnS to further recreate the paper we are referencing.

For the bullseye cavities, more fabrications will be done to dial in on the best e-beam dosage and etch time. AFM images will be made to determine whether the central hole of the bullseye in future fabrications is up to spec with a single e-beam exposure and etch step, or if multiple exposure and etch steps need to be made to successfully create this bullseye cavity.

References:

[1] Room-Temperature Lasing in Colloidal Nanoplatelets via Mie-Resonant Bound States in the Continuum, Mengfei Wu, Son Tung Ha, Sushant Shendre, Emek G. Durmusoglu, Weon-Kyu Koh, Diego R. Abujetas, José A. Sánchez-Gil, Ramón Paniagua-Domínguez, Hilmi Volkan Demir, and Arseniy I. Kuznetsov; Nano Letters 2020 20 (8), 6005-6011, DOI: 10.1021/acs.nanolett.0c01975.

[2] Enhanced Emission from WSe_2 Monolayers Coupled to Circular Bragg Gratings, Ngoc My Hanh Duong, Zai-Quan Xu, Mehran Kianinia, Rongbin Su, Zhuojun Liu, Sejeong Kim, Carlo Bradac, Toan Trong Tran, Yi Wan, Lain-Jong Li, Alexander Solntsev, Jin Liu, and Igor Aharonovich; ACS Photonics 2018, 3950-3955, DOI: 10.1021/acsphotonics.8b00865.

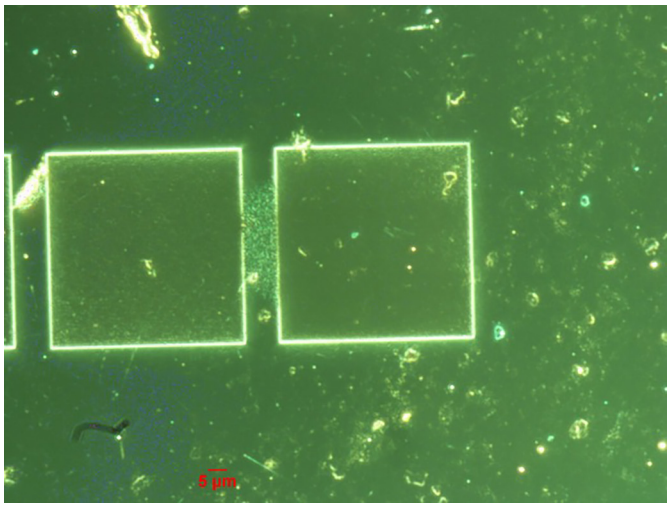

Figure 1: A microscope image of two pillar arrays made at CNF with the JEOL 6300.

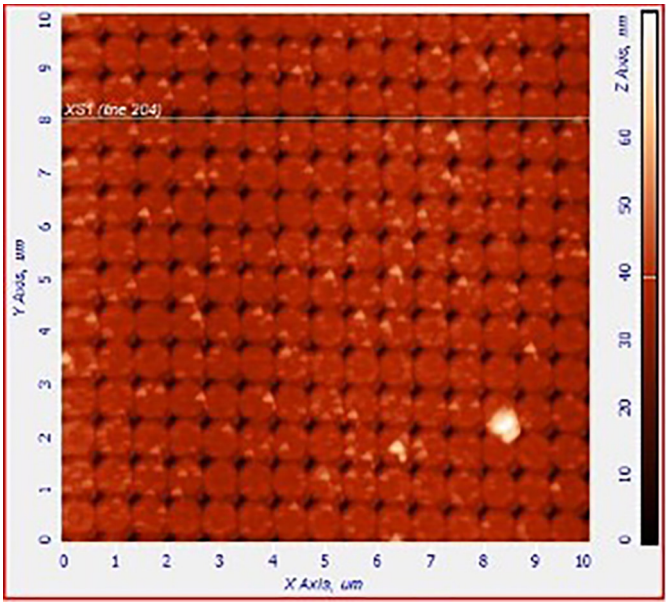

Figure 2: An Atomic Force Microscopy image of the array of pillars.

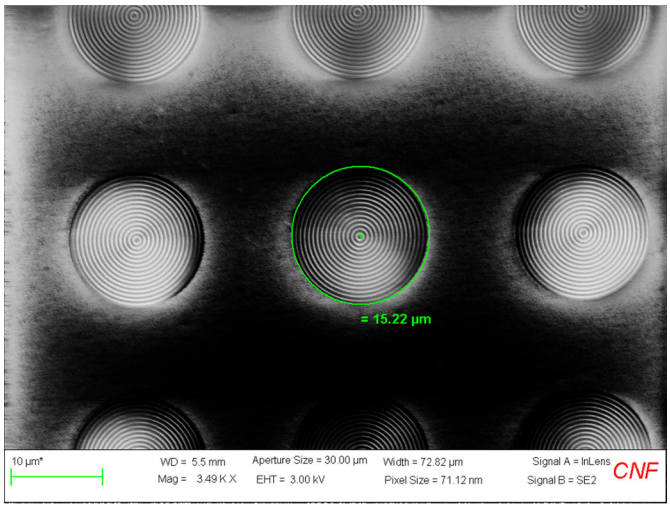

Figure 3: Array of bullseye cavities taken in Zeiss SEM Ultra.

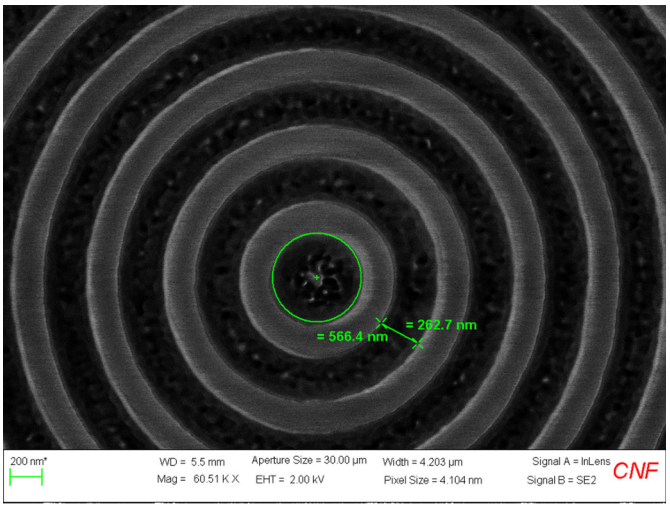

Figure 4: Center of bullseye cavity taken in Zeiss SEM Ultra.

Fabrication of Fluxonium-Like Qubits

CNF Project Number: 3010-22
Principal Investigator(s): Ivan Pechenezhskiy
User(s): Benjamin Byrd, Kesavan Manivannan

Affiliation(s): Department of Physics, Syracuse University

Primary Source(s) of Research Funding: Syracuse University, Army Research Office

Contact: ivpechen@syr.edu, babyrd@syr.edu, kmanivan@syr.edu

Primary CNF Tools Used: ASML DUV Stepper, JEOL 6300, PT770 Plasma Etcher, Heidelberg DWL2000 Mask Writer

Abstract:

In the drive for a scalable qubit-based processor, one of the most important resources is the ratio between qubit lifetime and gate operation time. Superconducting qubits provide a promising avenue for such a processor. Fluxonium qubits are exciting candidates in particular, having larger coherence times than the conventional transmons due to reduced sensitivity to several noise channels. Fluxonium qubits are intrinsically protected against charge noise due to the large inductive chain shunting the two capacitor pads, and protected against flux noise at the two flux sweet spots. Some of these qubits have lifetimes exceeding a millisecond, with gate times on the order of nanoseconds [1]. This project's fluxonium-like qubits are fabricated using an established recipe [2].

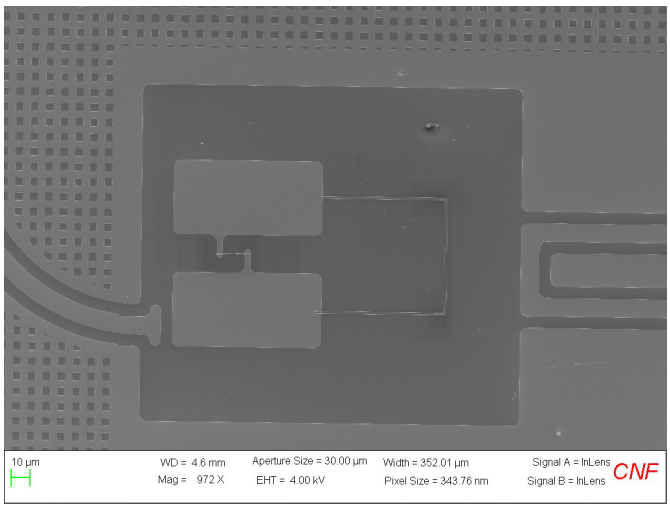

Figure 1: Scanning electron microscopy (SEM) image of one of the fluxonium qubits taken at CNF.

Summary of Research:

A fluxonium qubit is composed of a capacitive element, with a Josephson junction shorting the capacitive element. The key difference between a fluxonium and the more commonly studied transmon qubit is the inclusion of an inductor made of a chain of Josephson junctions, which shorts the two capacitor pads (Figure 1). This forms a closed loop for flux to thread through. This qubit is capacitively coupled to a resonator, whose frequency is shifted based on the state of the fluxonium qubit.

The devices are designed to facilitate direct control of each qubit on chip. For each device, there is one flux line per fluxonium and one charge bias line per transmon. These chips also utilize direct microwave drive lines to the individual qubits. Flux traps are etched across the entire ground plane of the chip, to limit the interaction of stray magnetic vortices with the fluxonium qubits. The resonant frequencies of the co-planar waveguide resonators on the chip are carefully chosen to ensure effective coupling with the qubits and easy measurement with the lab electronics. Test structures are distributed along the chip's edges, allowing for post-fabrication checks on the quality of electron-beam lithography and evaporation.

The fluxonium qubits are fabricated first by depositing a layer of niobium on a silicon wafer at Syracuse University using sputtering. The Heidelberg DWL2000 is used to construct a photomask equipped with various modular components to allow for tuning of circuit parameters after the design is finalized. Each of the chips is fabricated with two fluxonium and two transmon qubits. Frequencies for both of the qubits are targeted to be the same so that the properties of the two different qubit architectures can be compared. They are fabricated simultaneously on the same chip to reduce the factors related to fabrication variability.

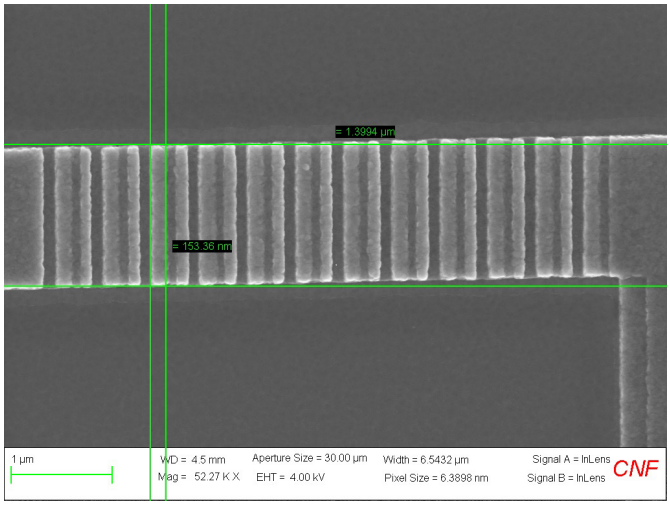

Figure 2: SEM image of a Josephson junction chain, taken at CNF.

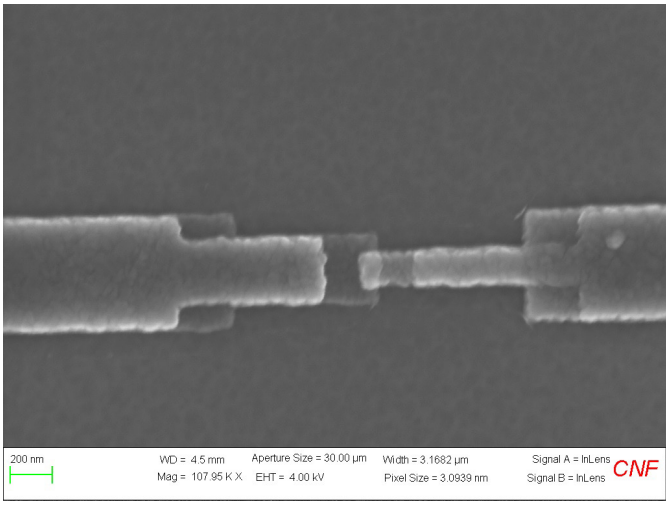

Figure 3: SEM of a single small Josephson junction, taken at CNF.

The base layer pattern (including the readout resonators, capacitor pads for the fluxonium and the transmon qubits, as well as the readout coplanar waveguide) is patterned into this niobium layer with the ASML DUV stepper. The wafer is then developed and cleaned before having the pattern etched into the superconducting niobium with the PT770. To remove oxides that may degrade the qubit performance, an additional HF cleaning step is done, after which the wafer is prepared for electron-beam lithography. After the electron-beam lithography pattern is developed, the device will have bridges formed of the remaining resist, which enables double-angle shadow evaporation for making the Josephson junctions. The lower pads for the Josephson junctions are deposited first, then the junctions are oxidized, and finally, the upper pads are deposited (Figure 2). This is all done with only a single electron-beam lithography.

The technique can be used to form the chain of Josephson junctions that serve a role of an inductor and the singular small junction (Figure 3). This evaporation and the intermediate oxidation are done at Syracuse University.

After the small junctions and the junction chain have been formed, the devices are returned to CNF to be diced. These devices are measured at Syracuse University in a Bluefors dilution refrigerator at temperatures below 10 mK.

The goal is to develop the capability to target specific qubit parameters and to optimize said parameters for a higher energy relaxation T1 and phase coherence T2 times. These devices also will benefit from expanding the range of fabrication techniques used in the fabrication process, potentially further limiting loss and increasing qubit lifetimes.

References:

[1] A. Somoroff, et al. Millisecond Coherence in a Superconducting Qubit. Phys. Rev. Lett., 130, 267001 (2023). https://doi.org/10.1103/PhysRevLett.130.267001.

[2] V. Iaia, et al. Phonon downconversion to suppress correlated errors in superconducting qubits. Nature Communications, 13, 6425 (2022). https://doi.org10.1038/s41467-022-33997-0.

Serpentine Heater Lines

CNF Project Number: 3016-22
Principal Investigator(s): Andrea Pickel
User(s): Benjamin Harrington, Kyle VanDelden, Jay VanDelden

Affiliation(s): Department of Mechanical Engineering, Materials Science Program, University of Rochester; EigenPhase Techologies

Primary Source(s) of Research Funding: National Science Foundation

Contact: apickel@ur.rochester.edu, bharrin9@ur.rochester.edu, kylevandelden@gmail.com, jvd@eigenphase.com
Website(s): https://labsites.rochester.edu/pickel/

Primary CNF Tools Used: Wire bonder, mask writer, ion mill, stepper, evaporator

Abstract:

Testing the performance of new nanoscale thermometry tools requires test structures that produce steep nanoscale temperature gradients. To achieve this outcome, we designed and fabricated Nichrome serpentine heater lines on crystalline quartz substrates that allow for four-point probe electrical measurements. When the serpentine lines are Joule heated, the current density concentrates at the inner corners of the heater lines. This results in a higher temperature rise at the inner corners than the outer corners, a geometric effect known as "current crowding" [1]. The low thermal conductivity of the Nichrome alloy helps maintain the temperature gradient between the inner and outer corners of the serpentines, while the use of the crystalline quartz substrate (factor of ~ 10 higher thermal conductivity than amorphous quartz) maintains the overall temperature rise at a reasonable level.

Summary of Research:

After first making a mask, the serpentine heater lines were then fabricated using a stepper lithography process. Individual chips containing an array of serpentine heater lines were created by dicing the crystalline quartz wafers on which the serpentine lines were fabricated (Figure 1).

Ultrasonic wire bonding was performed on the Westbond 7400A wire bonder at the Cornell NanoScale Facility. The goal was to electrically connect contacts on a printed circuit board (PCB) to the serpentine heater line chip. Over the course of the project, around 50 serpentine heater lines were attached to PCBs through silver epoxy at the University of Rochester (U of R) and brought to Cornell to be wire bonded. For each sample, four 1.25 mil aluminum wedge-to-wedge wire bonds were placed, corresponding to each of the gold contact pads on the PCB leading to the Nichrome pads on the serpentine heater line chip.

Once wire bonded, the heater line/PCB samples were brought back to the U of R to measure the resistance of serpentine heater line section only by means of a four-point probe resistance measurement. The sample was placed atop a hot plate and its resistance was monitored as the temperature increased. A temperature vs. resistance plot with an expected positive linear relationship was generated, and a temperature coefficient of resistance (TCR) value was calculated for the serpentine heater lines (Figure 2). The TCR value will serve as a calibration basis for later experiments, where the heater line will need to be held at a specific temperature via Joule heating.

Conclusions and Future Steps:

Nichrome serpentine heater lines on crystalline quartz substrates were successfully fabricated and the TCR value was calibrated. Major next steps are to measure the temperature rise as a function of the input Joule heating current and to subsequently use the Joule-heated serpentine lines to demonstrate nanoscale temperature mapping.

References:

[1] Q. Weng, et al., "Near-Field Radiative Nanothermal Imaging of Nonuniform Joule Heating in Narrow Metal Wires," Nano Letters 18, 7, 4220-4225 (2018).

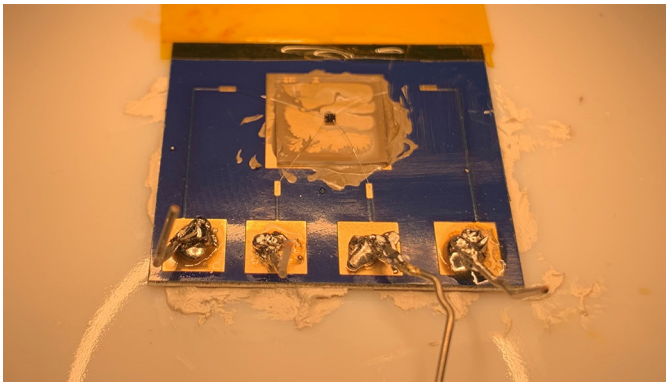

Figure 1: Wire bonded serpentine heater line and PCB sample. Wires soldered onto contact pads of the PCB are used for four-point probe measurements. Wire bonds connect the PCB to the serpentine heater line; in this setup the heater line chip has a single serpentine heater line. The bottom of the PCB is coated with thermal paste and is placed atop a hot plate.

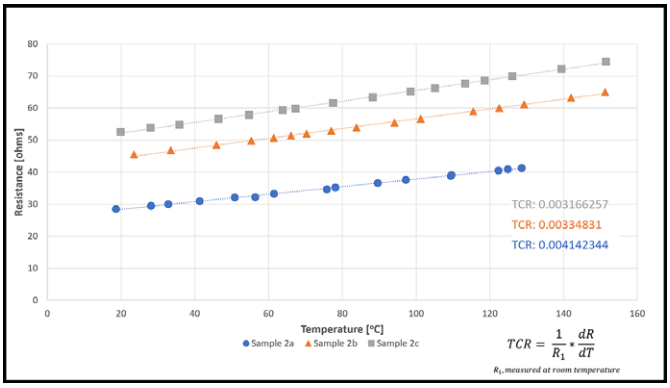

Figure 2: Temperature vs. resistance plot for Nichrome serpentine heater lines. Calculated temperature coefficient of resistance (TCR) values using the formula shown in the figure are also displayed for each respective sample.

Characterization of Fluxonium Qubits

CNF Project Number: 3067-23
Principal investigator(s): Ivan Pechenezhskiy
User(s): Benjamin Byrd, Kesavan Manivannan

Affiliation(s): Syracuse University
Primary CNF Tools Used: Army Research Office
Contact: ivpechen@syr.edu, babyrd@syr.edu, kmanivan@syr.edu
Primary CNF Tools Used: ASML DUV Stepper, JEOL 6300, PT770, Heidelberg Mask Writer - DWL2000

Abstract:

We fabricate and characterize superconducting fluxonium qubits made of nano-scale Josephson junctions as their primary element. Fluxonium qubits are one of the leading candidates for building scalable quantum computing processors owing to their very high (millisecond-long) characteristic times and large anharmonicity [1].

A more rigorous characterization and mitigation of the correlated noise channels affecting this class of qubits is required to further improve the qubit performance to a level where fault-tolerant processors can be built. We aim to study the different extrinsic and intrinsic decoherence mechanisms that couple to this superconducting qubit and attempt to mitigate them.

Summary of Research:

Superconducting quantum systems play a vital role in quantum computing. Superconducting qubits are lithographically defined devices in which the information is stored in quantum degrees of freedom of anharmonic oscillators. Josephson tunnel junctions provide the necessary anharmonicity. A fluxonium qubit has a small Josephson junction shunted by two large capacitor pads and a chain of Josephson junctions acting as a large inductor [2].

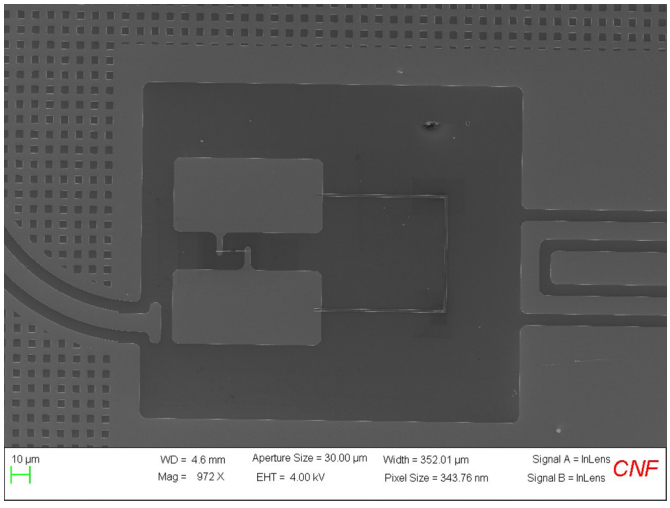

Figure 1: Scanning electron microscopy image of the fluxonium qubit showing the capacitor pad, single Josephson junction and the chain of Josephson junctions.

The flux bias through the formed loop can be tuned to vary the properties of this qubit. When a half-integer superconducting flux quantum threads the loop, the qubit exhibits a very high coherence and large anharmonicity.

The scanning electron microscopy image of our fluxonium qubit fabricated at CNF is displayed in Figure 1. The figure shows the two large niobium capacitor pads that set the capacitive energy scale $E_C/h \sim 1.4$ GHz. The small Josephson junction between the pads determines the Josephson energy $E_J/h \sim 2.3$ GHz. The array of 130 Josephson junctions to the immediate right of the pads is associated with the inductive energy $E_L/h \sim 0.5$ GHz. The capacitor pads are 40 μm × 80 μm in size and are patterned during the photolithography stage. The 90 nm × 100 nm Al-AlO_x-Al small junction and the array junctions, each of which have a dimension of 1.3 μm × 0.1 μm, are fabricated using the electron-beam lithography tool at CNF and electron-beam evaporator at Syracuse University. The Hamiltonian of the qubit can be tuned by modifying the properties of the above elements. The flux bias line can be seen on the right of Figure 1. Each qubit is capacitively coupled to a coplanar waveguide resonator, shown on the left of Figure 1, for dispersive readout of the qubit state.

The fabricated devices are cooled down to less than 10 mK for measurements. Microwave electronics at room temperature is used to manipulate and read out the qubit. Figure 2 shows the data from microwave transmission through a feedline coupled to the readout cavity as a function of flux bias through the loop. This flux-periodic feature is the tell-tale sign of the qubit ring being galvanically closed and the fabricated qubits fully functional. The qubit spectroscopy data in Figure 3 shows the two fundamental transitions, from the ground to the first excited state and from the ground to the second

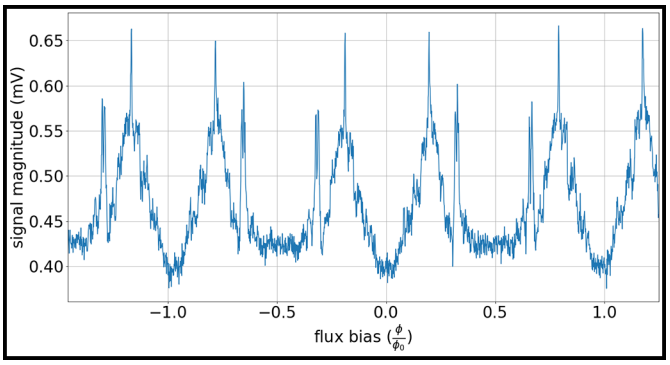

Figure 2: Flux-periodic transmission signal magnitude of the resonator coupled to the fluxonium qubit.

excited state, as a function of the flux through the loop. There is a reasonable agreement between the intended characteristic energy parameters and the ones obtained from fits to the spectrum showing the robustness of the fabrication procedure [3].

In the near future, going beyond the tune-up measurements, we would like to characterize the effect of decoherence due to injected quasiparticles in our fluxonium qubits.

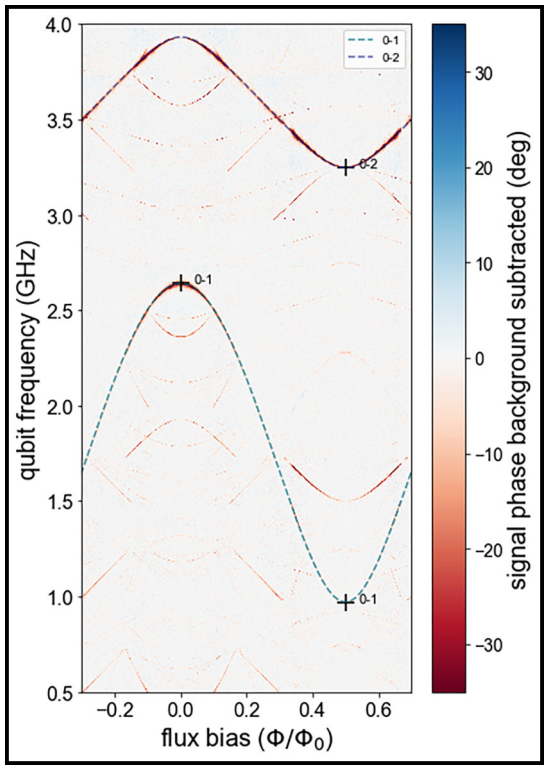

Figure 3: Fluxonium qubit spectrum showing the ground to the first excited and the ground to the second excited transitions.

References:

[1] A. Somoroff, et al. Millisecond Coherence in a Superconducting Qubit. Phys. Rev. Lett., 130, 267001 (2023). https://doi.org/10.1103/PhysRevLett.130.267001.

[2] L. Nguyen, et al. High-Coherence Fluxonium Qubit. Phys. Rev. X, 9, 041041 (2019). https://doi.org/10.1103/PhysRevX.9.041041.

[3] V. Iaia, et al. Phonon downconversion to suppress correlated errors in superconducting qubits. Nature Communications, 13, 6425 (2022). https://doi.org10.1038/s41467-022-33997-0.

Nanoscribe Advanced Patterning Techniques for Two-Photon 2D and 3D Structures

2023 CNF REU Intern: Samantha Averitt
Intern Affiliation: Mechanical Engineering, University of California Berkeley

CNF REU Mentors: Roberto Panepucci, Giovanni Sartorello; Cornell NanoScale Facility Staff, Cornell University

Program & Primary Source of Research Funding: 2023 Cornell NanoScale Science & Technology Facility Research Experiences for Undergraduates (CNF REU) Program via the NSF under Grant No. NNCI-2025233

Contact: saveritt@berkeley.edu, rrp23@cornell.edu, gs664@cornell.edu

Website: https://cnf.cornell.edu/education/reu/2023

Primary CNF Tools Used: Nanoscribe GT2, Zeiss Supra SEM, Glen 1000 Resist Strip

Abstract:

The CNF's Nanoscribe GT2 is a laser lithography system capable of printing three-dimensional structures with a resolution down to 200 nm using two-photon polymerization (2PP). Whereas traditional 2D direct writing (DW) tools require 3D structures to be built up one layer at a time, the Nanoscribe allows for complex 3D geometries to be fabricated with multiple levels in a single process step. Moreover, due to its high resolution, extending this tool to the fabrication of 2D structures provides researchers with enhanced flexibility for their process flows. In this work, we explore the Nanoscribe's capabilities in various configurations, with an emphasis placed on process development for spin-coated resists. An alignment strategy is demonstrated, enabling structures to be printed with overlay accuracy of approximately one micron using pre-existing fiducial markers. By investigating the capabilities of this tool, we also gauge its ability to aid in processes such as lift-off and microfluidic mold fabrication, potentially enabling the realization of devices that would be difficult to create using other methods.

Summary of Research:

To test the resolution capabilities of this tool, oil immersion was used due to oil having a higher index of refraction compared to air, increasing the objective's numerical aperture. Resolution tests were conducted on S1813 and SU-8, using computer-aided design (CAD) with both horizontal and vertical lines of widths ranging from 0.2 to 4 μm. Line widths under 340 nm were observed for the 200 nm nominal CAD on S1813 at a scan speed of 1000 μm/s and a laser power of 10% (Figure 1). Larger line widths of ~ 700 nm were observed for SU-8 at a scan speed of 500 μm/s and a laser power of 60%. We believe this was due to the higher dose required to ensure adhesion between the print and substrate post-development. Focusing was also an issue when working with non-standard materials, as Nanoscribe's automatic interface finding procedure was not possible in certain configurations.

The alignment capabilities of this tool were also investigated. Our proposed alignment strategy consists of two main components: a coordinate transformation followed by offset compensation.

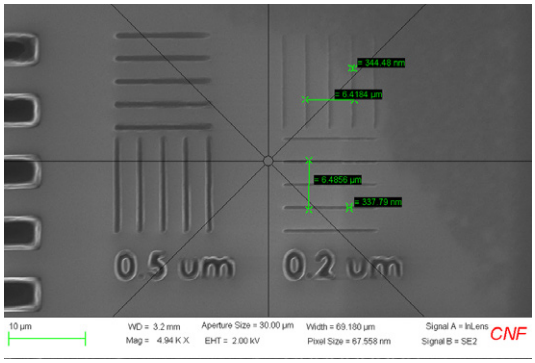

Figure 1: SEM of an S1813 oil immersion resolution test at a 1000 µm/s write speed and 10% laser power.

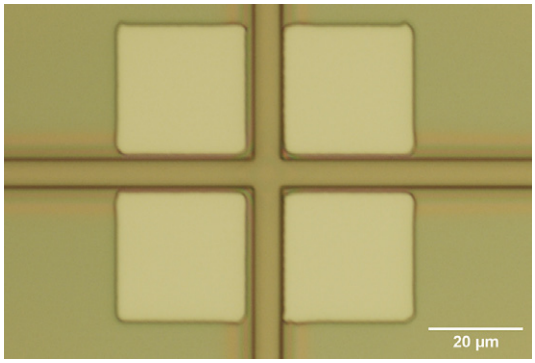

Figure 2: Optical microscopy image of an aligned print conducted using the 10x objective on S1813.

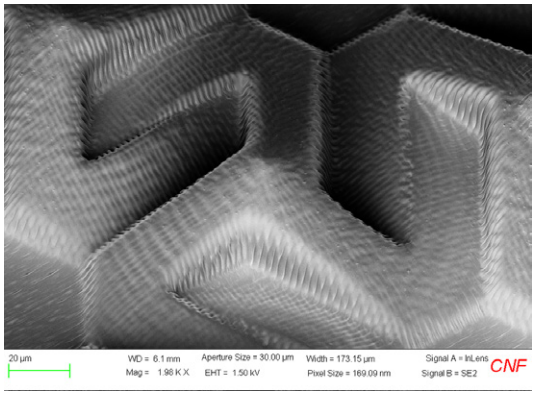

Figure 3: SEM of grayscale print conducted using the 10x objective with IP-Q and slicing distance of 1 µm.

First, a coordinate transformation is performed by the user with alignment to pre-existing marks. This enables stage movement to known locations on the substrate.

Second, offset compensation is required to account for the offset between the camera and laser system. This is done by opening the laser shutter until visible polymerization occurs, manually measuring the observed offset, and adjusting the system's stage position accordingly. It is important to note that this position varies depending on the objective being used. Following this procedure, we were able to demonstrate aligned prints with an accuracy of ~ 1 μm (Figure 2).

After investigating these capabilities, we explored potential applications of the Nanoscribe. Notable difficulties were encountered when exploring the direct fabrication of microfluidic devices on spin-coated resists. Experiments were conducted using both negative (SU-8) and positive (AZ4903) resists. Unfortunately, Nanoscribe's recommended AZ resins are no longer available. Using these resists, we saw incomplete channel development and long print times due to the slow write speeds required for exposure. Moving forward, alternative resins should be explored to address this problem.

We were able to successfully demonstrate the 3D capabilities of this tool through the creation of grayscale structures. Tests were conducted using both the 63x objective with S1827 and the 10x objective with Nanoscribe's IP-Q resin. Using the latter configuration, we observed adhesion issues when printing on bare silicon. This was resolved using plasma etching followed by the addition of a thin SU-8 adhesion layer. The effect of different print parameters was also investigated. We found that increasing the *FindInterfaceAt* value and dose delivered to the resin also helped to improve adhesion. Moreover, by decreasing the slicing distance parameter, we were able to demonstrate the ability of this tool to create 3D structures with relatively smooth surface profiles (Figure 3).

Additionally, we demonstrated the Nanoscribe's ability to be used in lift-off processes. Tests were conducted using the 10x objective on S1813 on LOR, with lift-off successfully occurring following the evaporation of gold and chromium on our sample. This process was performed in conjunction with our aforementioned alignment procedure.

We also conducted aligned prints on ultra-small pieces, approximately 1 mm^2 in dimension. These pieces were secured to a silicon substrate using polymethyl methacrylate (PMMA) before being immersed in IP-Q resin. From here, prints were aligned to the center of pre-existing circles and conducted using the 10x objective.

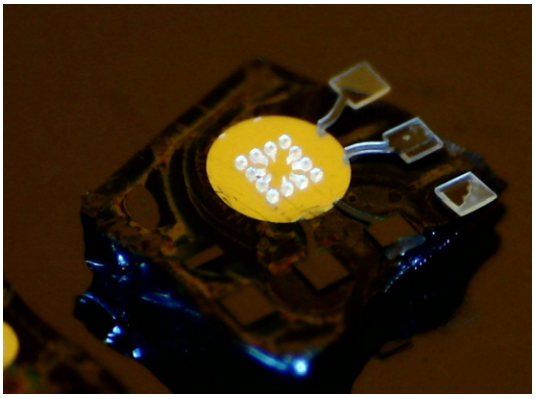

Figure 4: Image of an aligned print conducted using the 10x objective with IP-Q on a ~ 1 mm^2 piece.

The structures printed were 40 μm tall, and show the potential for this tool to create suspended geometries (Figure 4).

Conclusions and Future Steps:

Overall, this work demonstrates that Nanoscribe GT2 is a competitive tool for DW. Although larger than the 200 nm theoretical limit, the resolution results of this work remain non-trivial in showing this tool's capabilities. The linewidths observed are smaller than what is achievable with other DW methods at the CNF and could likely be decreased with additional parameter optimization. Moreover, in combination with its alignment capabilities, this tool has the potential to be used in a variety of applications from grayscale images, to lift-off, to direct fabrication on CMOS chiplets.

More process development is required regarding the Nanoscribe's ability to be used with other spin-coated resists. This, in combination with further parameter optimization, could further push the resolution limit of this tool. Additionally, quantitative characterization of this tool's alignment is still needed.

Acknowledgements:

Special thanks to the Cornell NanoScale Science & Technology Facility Research Experiences for Undergraduates (CNF REU) Program for hosting this internship and to the CNF staff for their support and mentorship. This work was funded by the National Science Foundation via grant no. NNCI-2025233.

References:

[1] NanoGuide Professional Photonic Series. (n.d.). Retrieved June 20, 2023, from https://support.nanoscribe.com/hc/en-gb/categories/201695349

Wafer-Scale Fabrication of Single Domain Magnetic Nanostructures

2023 CNF REU Intern: Naomi Sharlotte Naranjo
Intern Affiliation: Mechanical Engineering, Cornell University

CNF REU Principal Investigator: Professor Itai Cohen; Physics, Cornell University
CNF REU Mentors: Melody Xuan Lim, Zexi Liang; Physics, Cornell University
Program & Primary Source of Research Funding: 2023 Cornell NanoScale Facility Research Experiences for Undergraduates (CNF REU) Program via the National Science Foundation under Grant No. NNCI-2025233
Contact: nsn25@cornell.edu, itai.cohen@cornell.edu, mxl3@cornell.edu, zl467@cornell.edu
Website(s): https://cnf.cornell.edu/education/reu/2023
Primary CNF Tools Used: ASML DUV Stepper, Oxford 82, Gamma Automatic Coat-Develop Tool, SEM, AFM, P7 Profilometer

Abstract:

Single-domain magnets are critical to the development of untethered micromachines. To achieve single-domain behavior, these magnets must have a width of under 100 nanometers (nm). The current fabrication method of these magnets, electron-beam lithography, is both time and cost consuming. To address this, we developed a process to use Deep Ultraviolet (DUV) lithography as a more accessible alternative to the e-beam lithography process. Through precise etching of chromium on quartz photomasks, we can produce phase-shift photomasks with a 180-degree phase-shift, allowing for greater pitch density and depth of focus. Further improvements to the feature width in photoresist can be made by optimizing parameters on the ASML DUV Stepper. Our process successfully created features with a range of widths under the 100 nm threshold. Additionally, we characterized the optimal doses to achieve pitches ranging from 400 to 300 nm and control over the spacing between features.

Summary of Research:

Phase-shift photomasks are fully quartz masks with features etched to a specified depth such that there is a 180-degree phase shift of the light that passes through the etched area. This allows the light intensity to drop to zero at the boundary between the two different depth areas on the mask, leading to two features being defined on the wafer for each feature on the mask, increasing feature density and giving a larger process window.

The phase-shift mask fabrication process involved first using the Heidelberg Mask Writer DWL2000 to write a chrome on quartz mask and then using the CHF_3O_2 oxide etching recipe on the Oxford 82 etcher to etch the quartz on the mask to a desired depth of 248 nm. The etching process consisted of etching the mask for an initial five minutes and using the P7 Profilometer to calculate the chrome and quartz etching rates and remaining etch time. Once the final depth was reached, the chrome was etched off the mask and the final quartz depth was verified using an atomic force microscope (AFM).

Each image on the phase shift mask consisted of vertical alternating etched and unetched lines that were 100 μm long, with pitches ranging from 400 to 800 nm. Within each pitch, there were biases added to the width of the etched area, such that without bias the width of the etched and unetched lines were equal and with a positive bias the width of the etched line is greater than the unetched line while keeping the same pitch. This image was arranged into a 5 × 7 array on the mask, and S1813 photoresist was used to cover alignment marks and other features on the mask while etching one column of the array at a time.

The images were exposed on 4-inch wafers, that were coated with 62 nm of anti-reflective coating (ARC) and 300 nm of DUV210 photoresist using the Gamma Automatic Coat-Develop Tool. On the ASML DUV Stepper, the numerical aperture was set to 0.63, the illumination mode was set to partial coherent with an outer sigma of 0.302 and the focus was -0.1 μm, these parameters were shown to give the best results for phase-shift masks on a simulation software called Prolith. The cell size was set to 10 mm in order to fit multiple cells into a matrix on the wafer, which allowed a range of doses from 6 mJ/cm^2 to 21 mJ/cm^2 to be tested.

Scanning electron microscopy (SEM) was used to analyze the results of the exposures. SEM imaging showed that there was a range of line widths under the 100 nm target and that the line widths decreased as the dose increased (see Figure 1). Two distinct spacings between the lines were also observed, with one spacing being usually larger than the other. The ratio of these spacings was characterized at each of the biases tested on the mask (see Figure 2), which showed that as the unetched area becomes larger than the etched area, the spacing between the lines becomes more equal. This trend supports the hypothesis that the lines are falling onto the area that

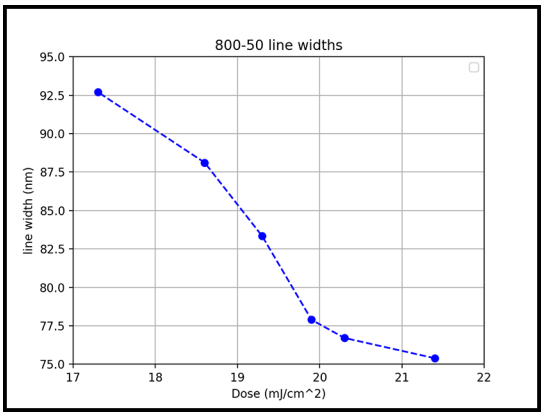

Figure 1: Line width of 800 pitch with a negative 50 bias across various doses.

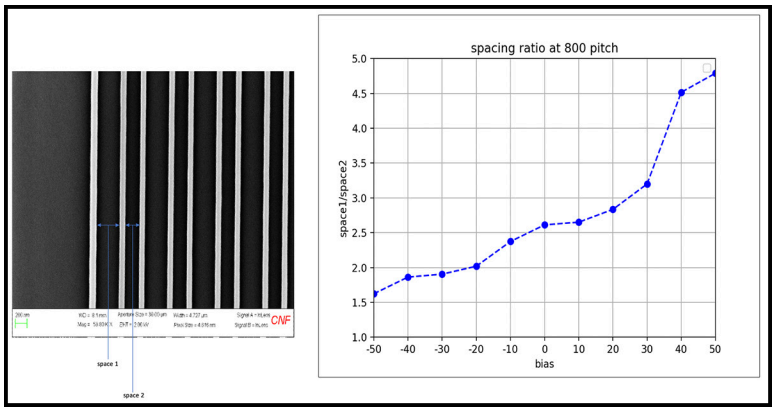

Figure 2: Ratio of line spacings at 800 nm pitch at 18.6 mJ/cm² dose across various biases.

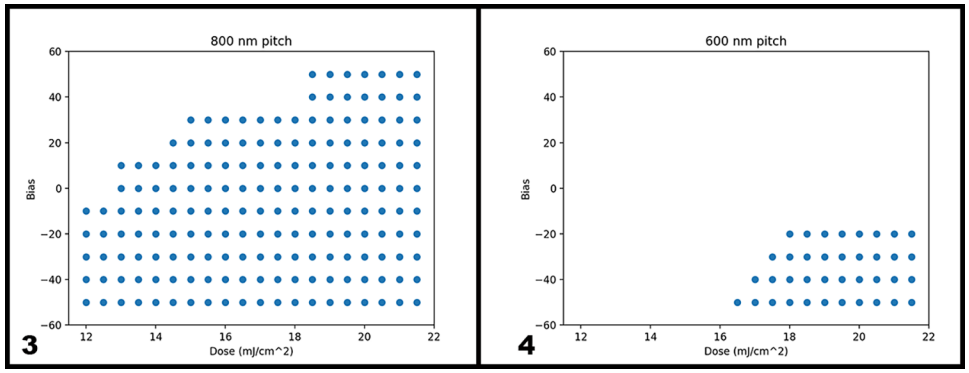

Figure 3, left: Process window for 800 nm pitch. Figure 4, right: Process window for 600 nm pitch.

is unetched on the mask, so the unetched area must be greater than the etched area for the spacing to be uniform. The largest negative bias tested was 50 nm, which lead to a ratio of 1.5, so the ideal negative bias should be greater.

The highest pitch tested was 800 nm on the mask, which translates to 400 nm on the wafer. This pitch had the largest process window (see Figure 3), working at all the doses tested and all the biases. Pitches of 700 nm and 600 nm on the mask were also achieved, but as the pitch decreased, the process window shrunk to higher doses and greater negative biases (see Figure 4). Some pitch doubling was seen at 500 nm, but it was not uniform throughout the length of the lines. However, with a greater negative bias, the photoresist could possibly be fully exposed between the lines making the 500 nm pitch better defined.

Conclusions and Future Steps:

We demonstrated that we could fabricate a phase-shift mask completely at the CNF with an etch depth less than 10 nm away from our target of 248 nm. Using said mask, we achieved features with a range of widths less than 100 nm and were able to control the line width through changes in dose. We also were able to characterize the spacing between the lines and understand how to use bias on our mask to get uniform spacing.

Acknowledgements:

Special thanks to the Cornell NanoScale Facility Research Experiences for Undergraduates (CNF REU) Program for hosting this internship, and to the Cohen Research Group for their support and mentorship. This work was funded by the National Science Foundation via grant no. NNCI-2025233.

Electrical Characterization of Dielectric Films

2023 CNF iREG Intern: Toko Ogata
Intern Affiliation: Chemistry, Graduate School of Chemical Sciences and Engineering, Hokkaido University, Hokkaido, Japan

CNF iREG Principal Investigator: Dr. Lynn Rathbun, Cornell NanoScale Facility (CNF), Cornell University

CNF iREG Mentors: Jeremy Clark, Phil Infante, Aaron Windsor; CNF, Cornell University

Program & Primary Sources of Research Funding: 2023 Cornell NanoScale Facility International Research Experiences for Graduates (CNF iREG) Program via the NSF under Grant No. NNCI-2025233; NNCI/NIMS Graduate Exchange Fellowship Program administered by Coordination Office, Center of Advanced Research Infrastructure for Materials and Nanotechnology of the National Institute for Materials Science - NIMS

Contact: carnation@eis.hokudai.ac.jp, rathbun@cnf.cornell.edu, clark@cnf.cornell.edu, infante@cnf.cornell.edu, windsor@cnf.cornell.edu

Website(s): https://cnf.cornell.edu/education/reu/2023, https://nanonet.mext.go.jp/page/NNCI-prg.html

Primary CNF Tools Used: SC4500 Even-Hour Evaporator, Keithley 4200A - IVCV Testing Station, Arradiance ALD Gemstar-6, MOS Metal Anneal 3 - C1

Abstract:

The characteristics of dielectric thin films have been studied to improve the performance and sizing of semiconductor devices, especially Metal-Oxide-Semiconductor Field Effect Transistors (MOSFETs). The MOSFET switches the current flow by inversion on the semiconductor surface as applied voltage across the MOS capacitor. The MOS capacitor is the heart of the MOSFET, because the operation and characterization are dependent on this inversion. Since the performance of the MOS capacitor is strongly affected by the properties of the oxide film, different dielectric materials and deposition tools are expected to have different C-V curves. We compared the C-V curves of devices using different deposition tools and materials, then discussed which is the best to fabricate MOS capacitors.

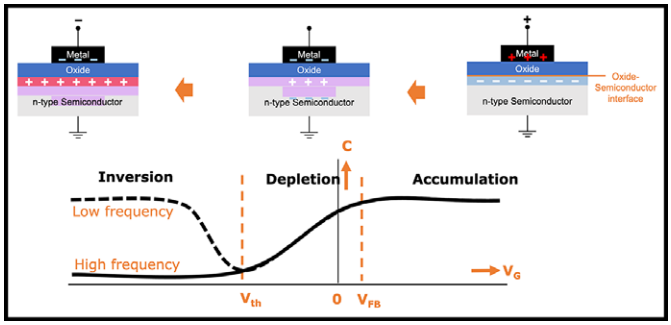

Figure 1: The schematic of the C-V curve for the n-type MOS capacitor at low frequency voltage (dashed), and high frequency voltage (solid) and three regimes: Accumulation regime (right part), Depletion regime (center part), and Inversion regime (left part).

Summary of Research:

The Metal-Oxide-Semiconductor Field Effect Transistor (MOSFET) is a three-terminal device, called Gate, Drain, and Source, used for amplifying or switching electronic signals. When the proper voltage is applied to the gate, the semiconductor surface at the interface of oxide and semiconductor is inverted from n-type to p-type or from p-type to n-type, depending on the semiconductor substrate used. The current flows between source and drain. This Metal-Oxide-Semiconductor structure applied the gate voltage known as MOS Capacitor. The MOS capacitor is the heart of MOSFET.

The capacitance of the MOS capacitor changes by sweeping the gate voltage. The Capacitance-Voltage (C-V) characteristic curve provides some useful information. The C-V curves visualize three regimes of the MOS capacitor: Accumulation, Depletion, and Inversion. The voltages at boundaries of regions are called Flat-band Voltage (V_{FB}) and Threshold Voltage (V_{th}), respectively. V_{FB} is defined as the voltage such that there is zero net charge density in oxide material, and V_{th} as the minimum voltage required to create an inversion layer. These are one of the most important parameters that can be extracted from C-V curves. Since the characteristics of the MOS device is strongly affected by the oxide films, the C-V curve also gives properties of oxide films such as the permittivity. Figure 1 shows the schematic of the C-V curve for the n-type MOS capacitor.

Therefore, we measured the C-V curve for device characterization, and compared the differences in deposition tools and materials, to find which is the best to fabricate MOS capacitors. MOS capacitors, consisting of an aluminum electrode, a dielectric film of various

materials, and a n-type silicon substrate body, were made by a simple process: 20-50 nm silicon dioxide (SiO_2), hafnium oxide (HfO_2), zirconium dioxide (HfO_2), and aluminum oxide (Al_2O_3) films were formed on the n-type silicon wafer, then 200 nm of aluminum was deposited through a shadow mask. Various tools were used to deposit SiO_2 films, including High-Density Plasma Chemical Vapor Deposition (HDP-CVD), e-beam evaporators, and thermal oxidation. For depositing other dielectric films, we used Atomic Layer Deposition (ALD). The fabricated devices were evaluated by measuring and analyzing Capacitance-Voltage (C-V) characteristics at various frequencies. We performed 5% H_2/N_2 anneal to improve the interface trap for getting a better C-V curve. The thickness of oxide films is measured by a variable angle ellipsometer.

First, we compared the normalized C-V curves of the MOS device with SiO_2 film deposited by different tools at various frequencies (Figure 2). The C-V results are different between deposition tools, such as threshold voltage, flat-band voltage, frequency dependence. We observed the sharp transition from accumulation to inversion, so it can be said that evaporator and dry oxidation are great tools for device fabrication.

Next, we compared the normalized C-V curves of the MOS device with different dielectric films at various frequencies (Figure 3, Figure 4). The shape of C-V curves is widely different between materials. Since there is a leakage from Al_2O_3 films, we considered Al_2O3 is a bad dielectric. The C-V curves for SiO_2 and HfO_2 clearly show sharp transitions with small frequency dependence. SiO_2 and HfO_2 are great for MOS capacitors, in addition, ALD is also a great tool for fabrication.

Conclusions and Future Steps:

From the C-V curves, we conclude that e-beam evaporator, dry oxidation, and ALD are great tools for fabrication of the MOS capacitors. SiO_2, HfO_2 are great materials for the MOS capacitor, but Al_2O_3 is a bad dielectric. For the next step, we will consider using other tools, dielectric materials, and gate electrode metals for comparison. To get better results, we will optimize some deposition conditions and measurement parameters including deposition temperature, thickness, and delay time for sweep.

Acknowledgements:

I would like to express my appreciation to my PI Dr. Lynn Rathbun, my mentors Jeremy Clark, Phil Infante, and Aaron Windsor for the advice on experimental design and useful discussion. This work is supported by National Science Foundation under Grant No. NNCI-2025233, National Nanotechnology Coordinated Infrastructure, Cornell NanoScale Science & Technology Facility, Center of Advanced Research Infrastructure for Materials and Nanotechnology of NIMS.

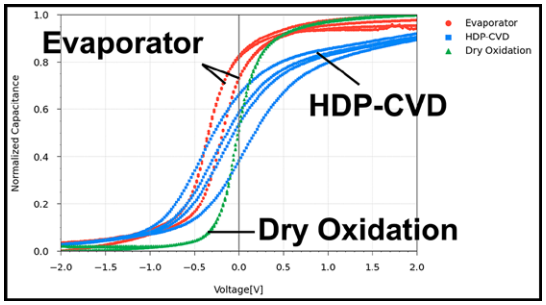

Figure 2: The C-V curves at 10 kHz, 20 kHz, 30 kHz, and 100 kHz for 46.84 nm SiO_2 deposited by the e-beam evaporator (red circle), 42.94 nm SiO_2 deposited by HDP-CVD (blue square), and 19.13 nm SiO_2 formed by dry oxidation (green triangle).

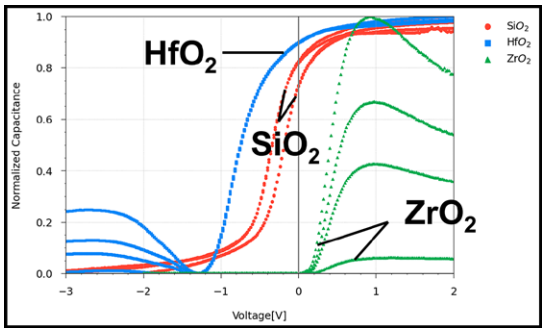

Figure 3: The C-V curves at 10 kHz, 20 kHz, 30 kHz, and 100 kHz for 46.84 nm SiO_2 deposited by the e-beam evaporator (red circle), 44.99 nm HfO_2 deposited by ALD (blue square), and 11.04 nm ZrO_2 deposited by ALD (green triangle).

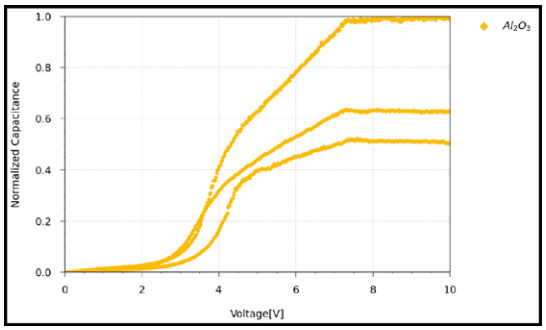

Figure 4: The C-V curves at 10 kHz, 20 kHz, 30 kHz, and 100 kHz for 32.61 nm Al_2O_3 deposited by ALD (yellow diamond).

References:

[1] Houssa, Michel, et al. "Electrical properties of high-κ gate dielectrics: Challenges, current issues, and possible solutions." Materials Science and Engineering: R: Reports 51.4-6 (2006): 37-85.

[2] Wang, Yichun, "Leakage current reduction of MOS capacitor induced by rapid thermal processing" (2010). University of Kentucky Master's Theses 640. https://uknowledge.uky.edu/gradschool_theses/640.

Nanoimprint Process Optimization for PMMA

2023 CNF REU Intern: Amara Taddeo
Intern Affiliation: Chemistry, Allegheny College

2023 CNF REU Mentors: Roberto Ricardo Panepucci, Xinwei Wu; Cornell NanoScale Facility, Cornell University
Program & Primary Source of Research Funding: 2023 Cornell NanoScale Facility Research Experiences for Undergraduates (CNF REU) Program via the National Science Foundation under Grant No. NNCI-2025233
Contact: maratad283@gmail.com, rrp23@cornell.edu, wu@cornell.edu
Website(s): https://cnf.cornell.edu/education/reu/2023, https://www.cnfusers.cornell.edu/node/43
Primary CNF Tools Used: Nanoimprint NX-2500, P7 Profilometer, Oxford 81/82, MVD100, AFM, SEM

Abstract:

Nanoimprint lithography (NIL) has the capabilities of having high resolution, producing features that are sub-10-nm and is also cost-effective compared to lithography techniques with same resolution, such as electron-beam lithography. To achieve such benefits, nanoimprinting parameters must be optimized, such as imprint temperature, pressure, polymer physical properties, residual layer thickness, and etch depth of mask, among others. Within the parameters explored, optimal thermal nanoimprint lithography (T-NIL) guidelines were achieved with polymethyl methacrylate (PMMA), a well-understood electron-beam resist, on Si wafers on the Nanonex NX-2500 with one non-uniform density pattern and a uniform grating pattern. For widest pattern conditions, optimal T-NIL parameters occurred around 250°C with an imprint time of 210 seconds using 50K PMMA, for a 180 nm deep mask.

Summary of Research:

While there are many factors that affect the optimization of nanoimprint lithography, a crucial factor is the temperature of imprint. To achieve an optimal imprint, the polymer needs to be in a viscous state where it can flow completely into the desired pattern being imprinted. For an optimal temperature to achieve such a polymer state, the glass transition temperature, T_g, needs to be taken into consideration [1]. Optimal imprinting begins approximately 70°C to 80°C above T_g so that the polymer is not just in a rubbery state but in a viscous state [1,2]. As for polymethyl methacrylate (PMMA), PMMA has a T_g of approximately 105°C [1]. Therefore, an ideal imprint temperature was determined to be 250°C for a pressure of 200 PSI.

PMMA comes in varying molecular weights such as 950K, 495K, and 50K, each with different polymer chain lengths with 950K PMMA having the longest and 50K PMMA having the shortest. In Figure 1, with an imprint time of 210s, both 50K and 495K PMMA have adequate imprints while 950K PMMA is still not ideal.

UV exposure was considered for enhancement, because when PMMA is irradiated, scissions occur within the polymer chains, reducing the average molecular weight [3]. With polymer chain scissions, the T_g is affected, enhancing nanoimprinting conditions. A wafer with 950K PMMA was flood exposed at λ_{UV} = 220 nm with 12 mW/cm^2 UV followed by an imprint time of 120s, and the results are shown in Figure 1. There is a significant increase in the percent filled compared to the 950K PMMA with no UV exposure imprinted for longer time. Figure 2 exemplifies a typical defect with non-ideal imprinting parameters; PMMA filled in half of the width of the line, not filling completely into the pattern on the mask. Figure 3 shows a scanning electron microscope (SEM) image after Si RIE etching of a PMMA nanoimprinted pattern. The image highlights two problems that must be avoided, specifically, incomplete removal of the residual layer, and complete removal of the PMMA mask during RIE etching. Roughness in the bottom surface was due to incomplete residual layer etching in O_2 plasma of the PMMA, prior to the full SF_6 RIE etch. Complete removal of the PMMA mask due to poor selectivity led to further roughness on the top surface of the structures on the final stages of the Si etch.

A uniform grating pattern with a pitch of 800 nm and trenches with sizes of 541 nm was also explored. Figure 4 is a SEM image of a typical area after optimal nanoimprinting with 200 PSI, 250°C, and for 210s on an 82 nm PMMA coated wafer. While there were large areas that were imprinted fully, some defects were found over some portions of the sample.

Conclusions and Future Steps:

In the parameter space explored in this research, optimal nanoimprinting for non-uniform density patterns for PMMA on Si wafers were determined. These conditions require a temperature of at least 250°C with a pressure of 200 PSI. Print time for 100-400 nm layer thicknesses of 50K PMMA can be 120s for feature sizes from 5 μm

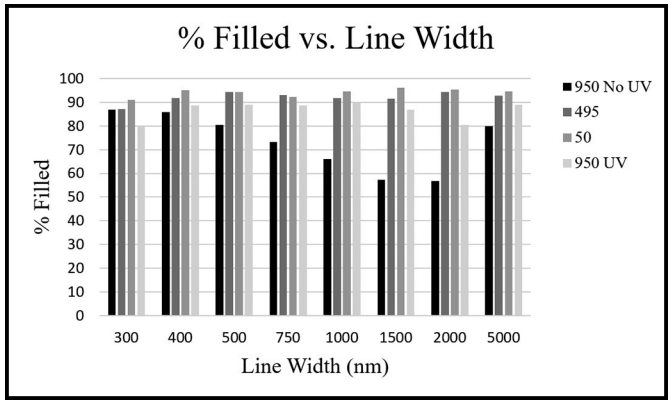

Figure 1: Graph comparing the percent of imprint pattern filled for varying molecular weights of PMMA along with prior UV exposure before imprinting for 950 PMMA for each line width of a non-uniform pattern.

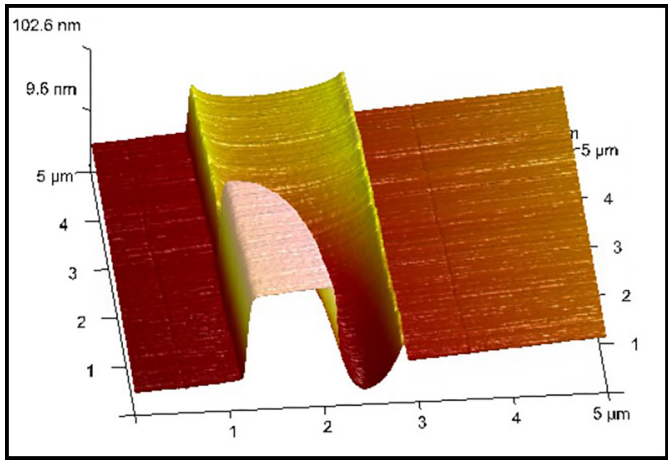

Figure 2: AFM image of a common partially filled line after nanoimprinting when imprinting is done at not optimized parameters.

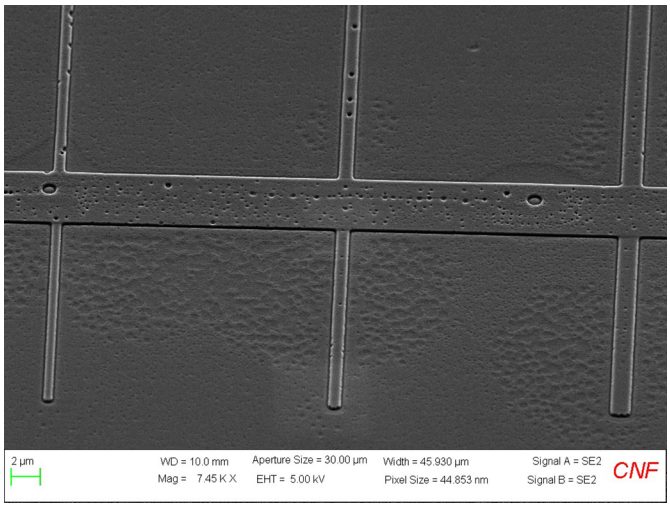

Figure 3: SEM image of after pattern transfer through RIE. Roughness on bottom was due to incomplete residual layer etch.

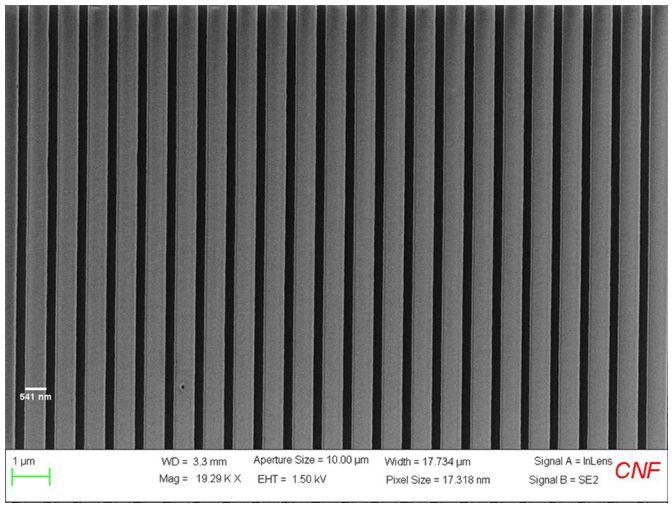

Figure 4: SEM image of a uniform grating pattern after being imprinted with a pitch of 800 nm and feature sizes of 541 nm.

to 300 nm, while 210s is required for 495K PMMA layers. For optimal printing at 950K PMMA, we have determined that 12 mW of UV at $\lambda = 220$ nm for 6s leads to optimal patterning. Uniform printing of the grid pattern was achieved over large areas; however, some areas of the wafer still contained non-uniformities within the pattern. Additional work is required to reproduce large features above 20 μm. We plan to explore printing with 50K PMMA with UV exposure. Furthermore, careful consideration must be given to the depth of pattern transfer during the nanoimprint etch steps, due to PMMA being a poor mask in reactive ion corrosion (RIE).

Acknowledgements:

Special thanks to the Cornell NanoScale Facility Research Experiences for Undergraduates (CNF REU) Program for hosting this internship and to the CNF staff for their support and mentorship. This work was funded by the National Science Foundation via grant no. NNCI-2025233.

References:

[1] L.J. Guo, "Recent progress in nanoimprint technology and its applications," Journal of Physics D: Applied Physics 37(11), (2004).

[2] R.N. Li, F. Chen, C.H. Lam, and O.K.C. Tsui, "Viscosity of PMMA on silica: Epitome of systems with strong polymer-substrate interactions," Macromolecules 46(19), 7889-7893 (2013).

[3] J.O. Choi, "Degradation of poly(methylmethacrylate) by deep ultraviolet, x-ray, electron beam, and proton beam irradiations," Journal of Vacuum Science & Technology B: Microelectronics and Nanometer Structures 6(6), 2286 (1988).

Wafer Scale Piezoelectric Transformers

CNF Project Number: 1121-03
Principal Investigator(s): Prof. Amit Lal
User(s): Meera Vikas Garud

Affiliation(s): Electrical and Computer Engineering, Cornell University
Primary Source(s) of Research Funding: ARPA-E
Contact: amit.lal@cornell.edu, mvg44@cornell.edu
Website(s): https://sonicmems.ece.cornell.edu/
Primary CNF Tools Used: Westbond 7400A Ultrasonic Wire Bonder

Abstract:

Our project aims at developing a wafer scale-wafer mountable piezoelectric transformer for a wafer scale, compact ion accelerator. Miniaturizing conventional magnetic transformers is often a difficult task. However, piezoelectric transformer designs offer a promising alternative by utilizing the vibrational mode shapes of piezoelectric plates to achieve voltage gain. Various modes of vibration, such as shear-transverse, radial, and others, have been explored using different plate geometries. In our research, we aim to tackle the challenge by combining multiple approaches. We design a piezoelectric transformer that utilizes mechanical resonance of the structure, employs multilayer stacking, and incorporates a series electrical connection on the secondary side of the transformer. The device's design is specifically optimized for easy manufacturing and chip-scale assembly onto a PCB board, enhancing its practicality and potential for widespread adoption.

Summary of Research:

We use high Q fused quartz as a substrate and PZT pieces as the piezoelectric material. Figure 1 and Figure 2 illustrate the schematic and photograph of the device stack. The transformer consists of a 200 μm thick PZT layer, a 500 μm thick fused quartz layer, and three PZT pieces connected in series on the secondary side. To manufacture this transformer, we employ the LPKF laser cutter to obtain PZT pieces of the required area, and we use patterned copper tape as the metal contact on both sides of the transformer. We achieve the series connection at the secondary side PZT pieces using wire-bonds. The aluminum wire of the wire bonder is compatible with the sintered nickel metal layer on the PZT pieces. The wire bonds aid in electrical connections without shifting the resonance frequency due to the mass loading effect on the PZT pieces.

Conclusions and Future Steps:

The prototype gives promising results. We achieve a voltage gain of 6 at 8 MHz from a very thin (<1mm) device. To avoid effects of a non-uniform adhesion between PZT pieces and the copper tape on the frequency response, we propose the use of indium plating and flip-chip bonding to have better process control — for which Pico MA FinePlacer FlipChip Bonder would be a useful tool at CNF, and process flow would be modified appropriately. This will also aid in precise alignment of secondary side small PZT pieces with respect to the primary side larger PZT actuator.

References:

[1] Y. Hou et al., "Vertically Stacked Piezoelectric Transformer for High Frequency Power Amplifier," 2023 IEEE Applied Power Electronics Conference and Exposition (APEC), Orlando, FL, USA, 2023, pp. 392-396.

[2] M. Garud, Y. Hou, A. Lal, K. Afridi, "Piezoelectric Transformer using bulk PZT & Fused Quartz for RF Ion Accelerators," in 2023 IEEE International Ultrasonics Symposium (IUS), 2023.

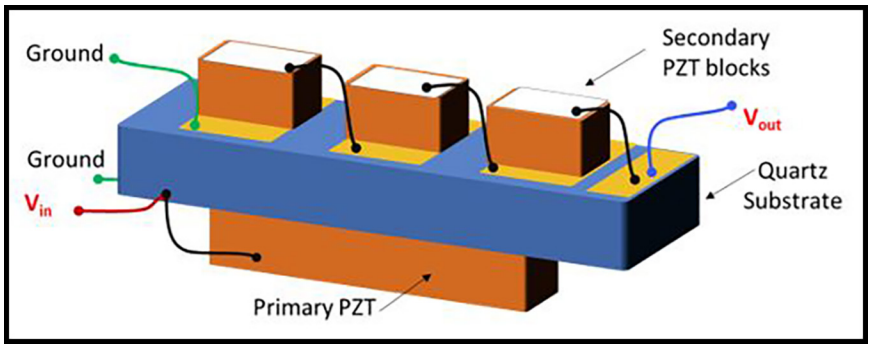

Figure 1: Schematic of the piezoelectric transformer architecture.

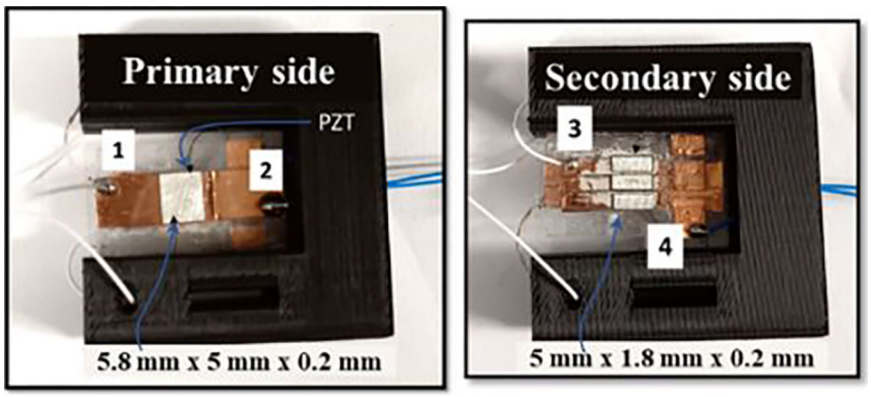

Figure 2: Photograph of a prototype of the transformer mounted on a 3D printed support structure.

Exploring the Relevance of Mucin-Induced Extracellular Vesicles in Therapeutics and Cancer

CNF Project Number: 2272-14
Principal Investigator(s): Dr. Matthew Paszek
User(s): Erik Chow

Affiliation(s): Department of Biomedical Engineering, Cornell University
Primary Source(s) of Research Funding: National Science Foundation Graduate Research Fellowship
Contact: paszek@cornell.edu, ec829@cornell.edu
Primary CNF Tools Used: Malvern NS300 Nanosight

Abstract:

Extracellular vesicles (EVs) have garnered increasing biomedical research focus due to their ability to transport DNA, RNA, and proteins. In a therapeutic context, EVs represent inherently biocompatible vessels for targeted delivery. However, in a disease context such as cancer, EVs become an avenue for disease pathogenesis and progression. In either context, the significance of the glycocalyx in EV biogenesis and function is largely unexplored, and the capacity to effect EV production and properties through rational manipulation of the glycocalyx remains poorly understood. We have previously demonstrated that overexpressing the mucin glycoprotein MUC1 in the glycocalyx leads to a dramatic increase in the production of EVs [1]. Here we summarize our recent findings characterizing the physical properties of these mucin-induced EVs (MUC-EVs).

Summary of Research:

Extracellular vesicles (EVs) have quickly gained traction in numerous areas of biomedical engineering research — including disease pathogenesis and drug delivery, among others — due to their ability to transport DNA, RNA, and proteins. The glycocalyx is a polymer meshwork of proteins, nucleic acids, and glycans which dictates numerous intercellular interactions. However, the role of the glycocalyx in regulating intercellular communication by way of EVs remains poorly understood. It has been previously shown that engineering the glycocalyx via the overexpression of mucin can result in membrane morphologies which are favorable for the formation of EVs [1]. This report summarizes research from the last year characterizing the effects of MUC1 overexpression on EV properties.

MCF10A cells were genetically engineered to overexpress a tetracycline-inducible MUC1-construct. A single clone was then expanded and used as a workhorse cell line for this research, hereafter referred to as MCF10A-1E7 cells. To induce MUC1 overexpression, MCF10A-1E7 cells were treated with 1 μg/mL doxycycline (Dox) for 24 h. Uninduced MCF10A.1E7 cells were used as a negative control. Subsequently, the cells were switched to serum-free media and cultured at 37°C, 5% CO_2 for 15 h to 18 h. EV-containing media was harvested, and the EVs were isolated by PEG-enrichment [2]. EV mucin coatings were optionally removed by treatment with stcE mucinase [3], and EV sizes and concentrations were measured by nanoparticle tracking analysis (NTA) using the Malvern NS300 Nanosight.

Figure 1 shows that mucin-induced EVs (MUC-EVs) are themselves coated in MUC1. Treatment of mucin-induced EVs with StcE mucinase resulted in an overall decrease in EV size consistent with the removal of MUC1 from the EV surface [4]. The stability of MUC-EVs stored at 4°C was evaluated by repeatedly recording NTA measurements of MUC-EV samples with or without mucinase treatment over the span of seven days. Non-mucinase-treated MUC-EV stability was dramatically improved over MUC-EVs which had their MUC1 coatings cleaved by StcE mucinase, as shown in Figure 2, with only mucinase-treated EVs decaying to 50% of their original concentration within seven days. This suggests that MUC1 overexpression enhances EV stability through the generation of EVs with MUC1 surface coatings.

Recognizing the MUC1 overexpression is a hallmark of numerous solid-tumor cancers, EV production was analyzed from KPL-1, a MUC1-overexpressing breast cancer cell line. A MUC1 knockdown cell line (KPL-1 MUC1KD) was generated by lentiviral delivery of small hairpin RNA (shRNA) with reduced MUC1 expression validated by flow cytometry shown in Figure 3. EVs were harvested from wild-type KPL-1 and KPL-1 MUC1KD using the same method as described above. Figure 4 demonstrates that MUC1 knockdown dramatically attenuated the release of EVs from KPL-1 cells.

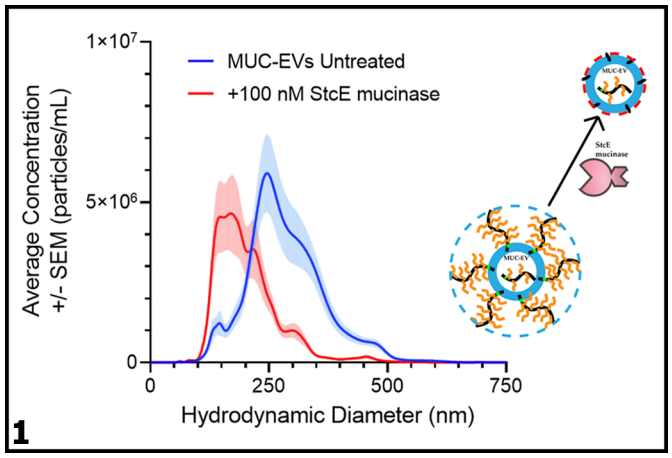

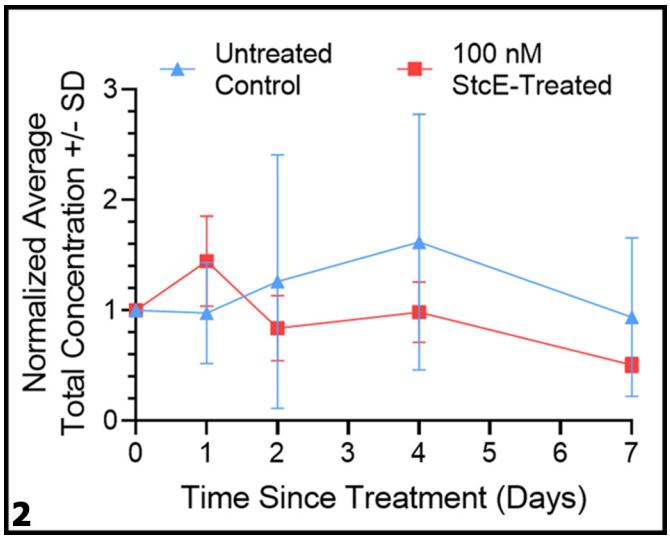

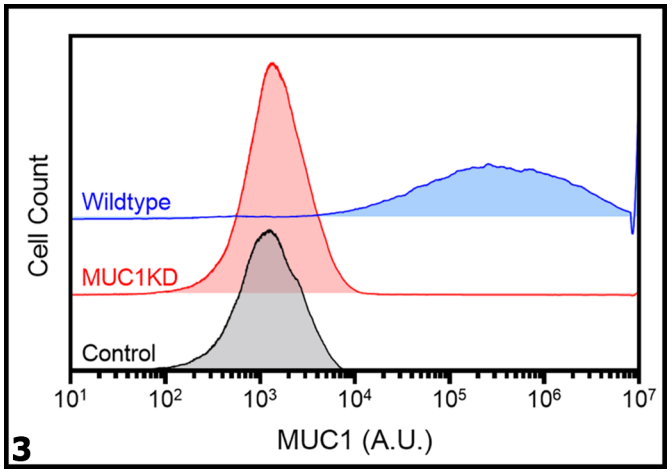

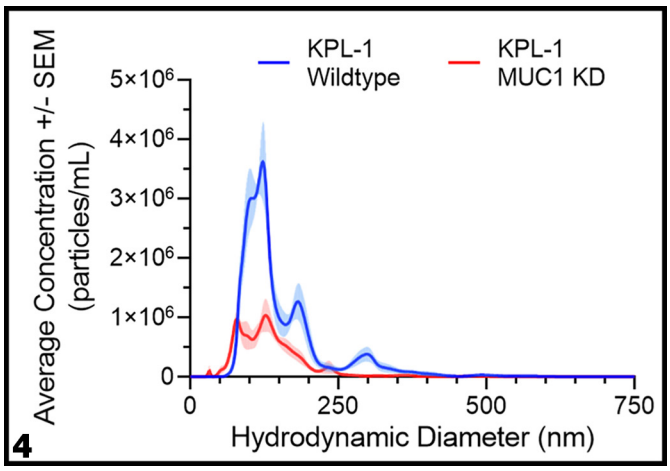

Figure 1: Induced biogenesis of MUC1-coated EVs. *Size distributions of EVs from MCF10A.1E7 cells before and after 100 nM StcE mucinase treatment measured by NTA. Plotted are the average particle concentrations +/-SEM from three independent experiments.*
Figure 2: MUC1 coatings improve EV stability. *Total particle concentrations of EVs from MCF10A-1E7 measured by NTA. EVs were either untreated (Control) or treated with 100 nM stcE mucinase. Plotted are the average total particle concentrations +/-SD from three independent experiments as a percentage of the concentration at Day 0. Dotted line represents 50% EV decay.* **Figure 3: Validation of MUC1 knockdown in engineered KPL-1 cells.** *Wildtype KPL-1 and KPL-1 MUC1KD cells were fixed with 4% PFA for 15 min at room temperature, incubated with mouse anti-MUC1 (HPMV) primary antibody for 30 min at room temperature, and finally incubated with goat anti-mouse IgG secondary antibody conjugated with AlexaFluor™ 647 for 30 min at room temperature. Fluorescence histograms shown were acquired using an Attune™ NxT flow cytometer. KPL-1 wildtype cells fixed and stained only with secondary antibody were used as a negative control.*
Figure 4: MUC1 knockdown attenuates release of EVs from KPL-1 breast cancer cell line. *Size distributions of EVs from wildtype KPL-1 and KPL-1 MUC1KD measured by NTA. Plotted are the average particle concentrations +/-SEM from five technical replicates.*

Conclusions and Future Steps:

Altogether, these data demonstrate that EV properties can be dramatically impacted by the glycocalyx. Overexpression of MUC1 acts as a driver of EV release, and these EVs may be imparted with mucin coatings which improve stability and could enhance their role as long-range delivery vehicles of therapeutic or oncogenic agents. Further studies are needed to characterize MUC-EV cargoes and to explore the applications of engineered EV mucin coatings.

References:

[1] Shurer, C. R., et al. (2019). Physical Principles of Membrane Shape Regulation by the Glycocalyx. Cell, 177(7), 1757-1770. https://doi.org/10.1016/j.cell.2019.04.017.

[2] Rider, M., et al. (2016). ExtraPEG: A Polyethylene Glycol-Based Method for Enrichment of Extracellular Vesicles. Sci Rep 6, 23978. https://doi.org/10.1038/srep23978.

[3] Malaker, S.A., et al. (2019). The mucin-selective protease StcE enables molecular and functional analysis of human cancer-associated mucins. PNAS, 116(15), 7278-7287. https://doi.org/10.1073/pnas.1813020116.

[4] Park, S., et al. (2022). Mucins form a barrier against immune cell attack. bioRxiv. https://doi.org/10.1101/2022.01.28.478211.

Fabrication and Characterization Support for CCMR

CNF Project Number: 2974-21
Principal Investigator(s): Jonathan Shu
User(s): Philip Carubia

Affiliation(s): Cornell Center for Materials Research (CCMR), Cornell University

Primary Source(s) of Research Funding: National Science Foundation

Contact: jbs24@cornell.edu, pmc228@cornell.edu
Website: www.ccmr.cornell.edu

Primary CNF Tools Used: Universal Laser Systems VersaLaser VLS3.50

Abstract:

The Cornell NanoScale Facility (CNF) is accessed for use of the Universal Laser Systems VersaLaser VLS3.50, and laser cutting 20 mm, 25 mm, and 40 mm discs from PSA backed grinding papers to be used with the DHR3 shear rheometer located in the Cornell Center for Materials Research (CCMR).

Summary of Research:

Project 2974-21 was established for facilities staff from the Cornell Center for Materials Research (CCMR) to access basic instrumentation within the Cornell NanoScale Facility (CNF) for purposes of sample preparation and fabrication of accessories for CCMR instrumentation. The initial project proposal was started to gain access to the Universal Laser Systems VersaLaser VLS3.50 by the bard materials facility for cutting 20 mm, 25 mm, and 40 mm discs from PSA backed grinding papers to be used with our DHR3 shear Rheometer. These discs are used to increase the friction between stiffer samples and the instrument to reduce artifacts related to sample slippage.

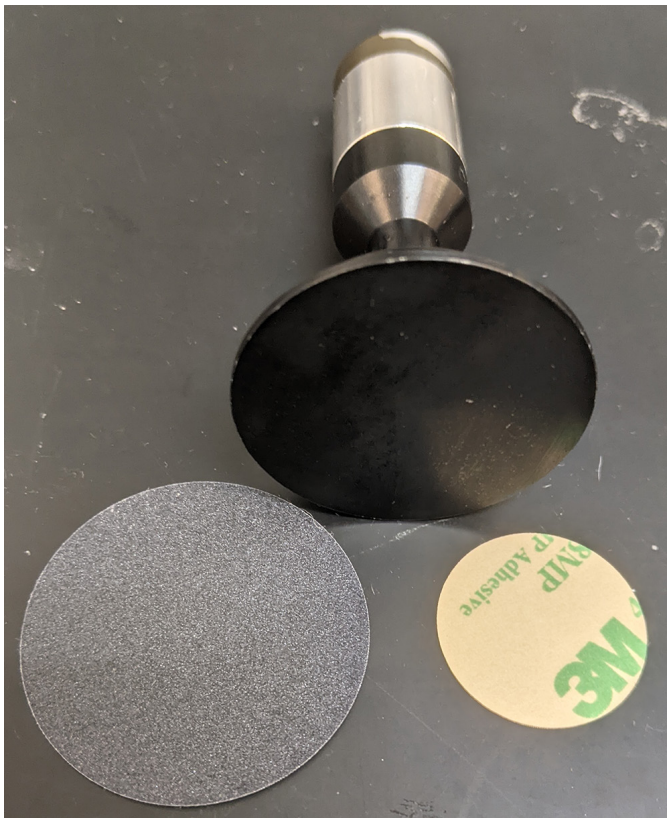

Figure 1: 40 mm upper parallel plate geometry with 40 mm disc front and 25 mm disc back.

Conclusions and Future Steps:

Access to this laser cutter has allowed us to test tougher hydrogels and viscoelastic materials at higher strains than previously available. It is likely that we will be using the Universal Laser Systems VersaLaser VLS3.50 in the future as we use up our existing stock.

Fabrication and RF Evaluations of 5G Antennas on Flexible Substrates

CNF Project Number: 3038-22
Principal Investigator(s): Mark D. Poliks
User(s): Dylan Richmond

Affiliation(s): Materials Science and Engineering, Binghamton University

Primary Source(s) of Research Funding: SUNY Research Foundation

Contact: mpoliks@binghamton.edu, drichmo2@binghamton.edu

Primary CNF Tools Used: Electron beam evaporator (odd & even hour), Heidelberg Mask Writer - DWL2000, DISCO dicing saw

Abstract:

Internet-of-things (IoT) implementations are becoming increasingly popular as real-time sensing and edge computing aim to improve efficiency, safety, and wellness. To enable communication among IoT devices, such as self-driving cars, mobile, and wearable devices, they must be networked and are often reliant on rapid signal transmission and processing. Flexible glass and flexible ceramic have emerged as two primary candidates for the fabrication of high-quality roll-to-roll (R2R) antennas at low cost. We have previously demonstrated a fully additive technique for fabricating double-sided 5G Vivaldi antennas using aluminum on flexible glass [1]. This work continues and expands the scope of substrates, metallizations, and RF devices to develop wafer-level processes that can be ported to R2R. Herein, we demonstrate fabrication of double-sided 5G mm-wave RF devices on flexible glass and ceramic operating at 28 and 39 GHz. Devices are designed and simulated using ANSYS high-frequency structure simulator (HFSS). Validation of the designs is conducted by measuring the return loss and 3D radiation patterns using a Rohde and Schwarz ZNB-40 Vector Network Analyzer (VNA) and comparing operational performance to simulated results. While a R2R manufacturing process is developed in tandem, the wafer scale prototypes have been made using standard materials, processes, and facilities to allow a facile translation to R2R.

Summary of Research:

RF devices were fabricated on flexible glass and ceramic wafers using both conventional photolithography and depositions with shadow masks to define features. First, metals were evaporated onto both sides of the wafer substrates using the electron beam evaporators available in the CNF. Blank photomasks were purchased from the CNF store and designs were exposed using the direct-write expose tool to define mask patterns. Photolithography was performed at Binghamton University's clean room on the wafers metallized at the CNF. Once metal patterns were defined onto the wafer, a subsequent via filling process was done to make electrical connections from one side of the wafer to the other. Wafers were then coated in a dry film photoresist and brought back to the CNF for dicing. The DISCO dicing saw was used (with the all-purpose blade) to singulate the devices from the wafer. Finally, devices were evaluated for their RF performance using a vector network analyzer to obtain S-parameters and radiation patterns in an anechoic chamber.

Conclusions and Future Steps:

This work was meant to prototype and evaluate processes that can be used to fabricate these devices on webs of flexible materials on a larger scale, roll-to-roll (R2R) manufacturing level. The initial trails of fabricating these devices were successful in that the devices operated as expected. The next steps consist of testing the compatibility of these webs of flexible materials with our tool set at Binghamton University and begin to carry out preliminary experiments on the R2R platform towards high-volume manufacturing these devices. The final step will eventually be the manufacturing of these devices.

References:

[1] M. D. Poliks, et al., "Transparent antennas for wireless systems based on patterned indium tin oxide and flexible glass," in 2017 IEEE 67th Electronic Components and Technology Conference (ECTC), 2017, pp. 1443-1448.

[2] J. P. Lombardi, et al., "Copper transparent antennas on flexible glass by subtractive and semi-additive fabrication for automotive applications," in 2018 IEEE 68th Electronic Components and Technology Conference (ECTC), 2018, pp. 2107-2115.

[3] D. Richmond, et al. "Additive Fabrication of Aluminum Antennas on Flexible Glass," New York State Nanotechnology Network (NNN) Symposium, May 2022.

[4] D. Richmond, et al. "Fabrication and RF evaluations of 5G Antennas on Flexible Substrates," New York State Nanotechnology Network (NNN) Symposium, April 2023.

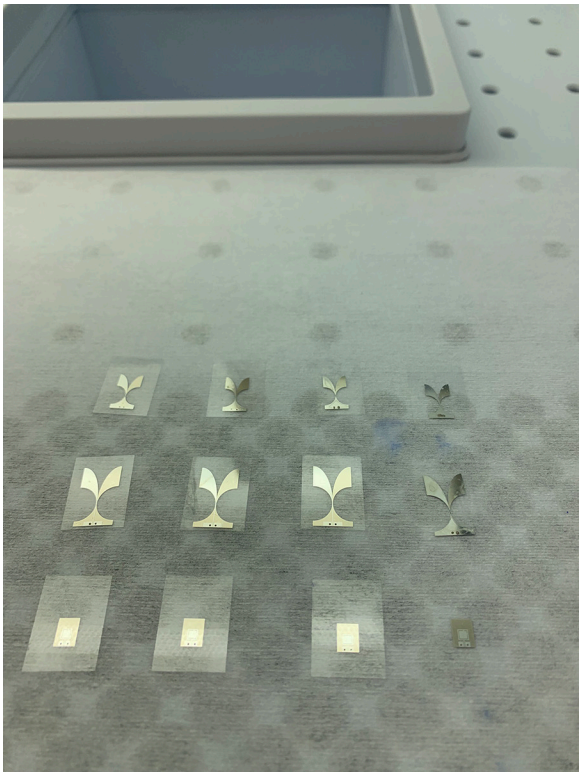

Figure 1: RF devices on 100 µm flexible glass, diced using DISCO dicing saw.

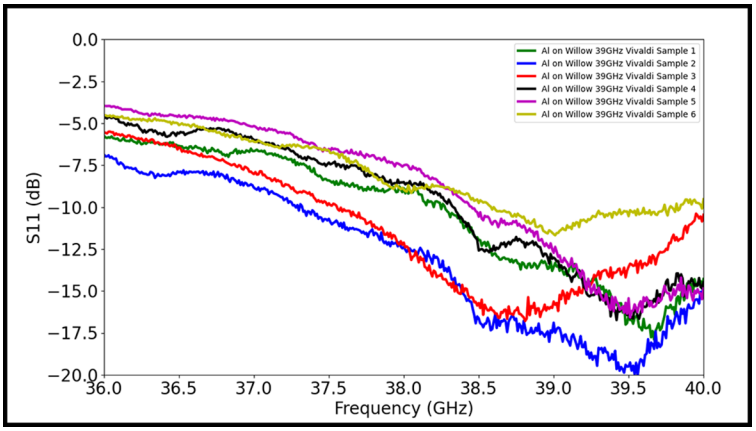

Figure 2: Return loss (S11) of Vivaldi antennas on 100 µm flexible glass.

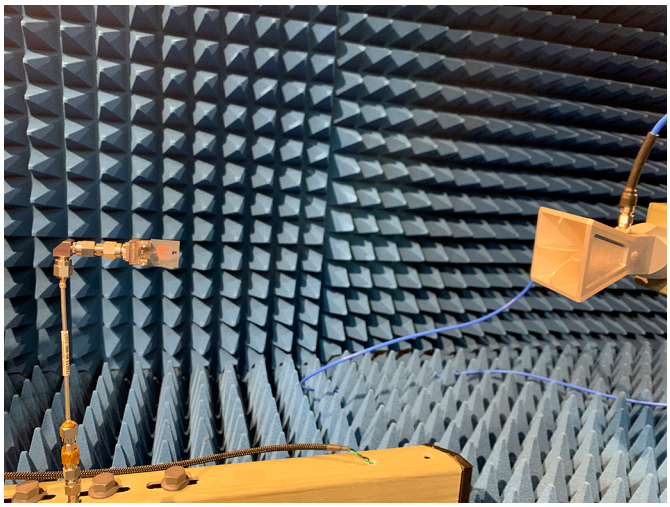

Figure 3: Anechoic chamber radiation measurement setup.

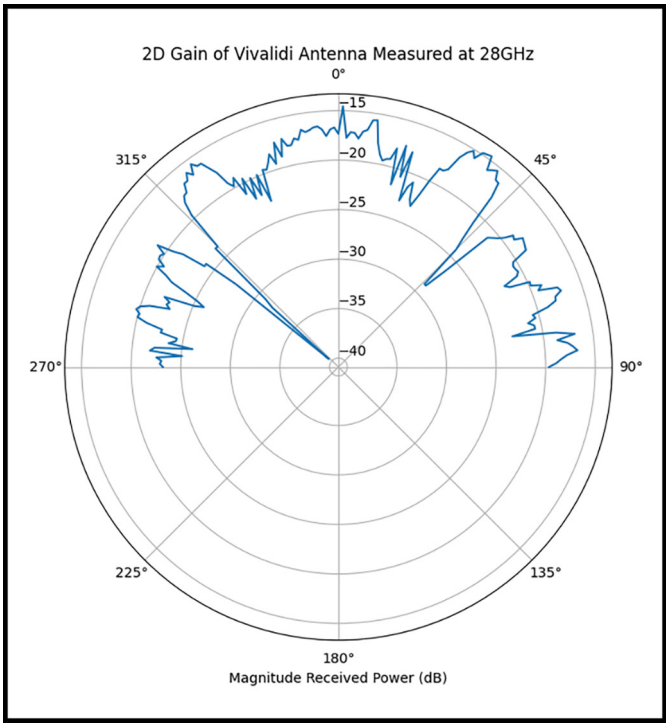

Figure 4: 2D gain of Vivaldi antenna on 40 µm flexible ceramic measured at 28 GHz.

Wolfspeed Development of T-Gate Structure by Electron Beam Lithography

CNF Project Number: 3073-23
Principal Investigator(s): Evan Jones
User(s): Evan Jones, Jim Tajadod

Affiliation(s): Wolfspeed, Inc.

Primary Source(s) of Research Funding: Internal Research and Development

Contact: Evan.Jones@wolfspeed.com, Jim.Tajadod@wolfspeed.com

Primary CNF Tools Used: JEOL 9500

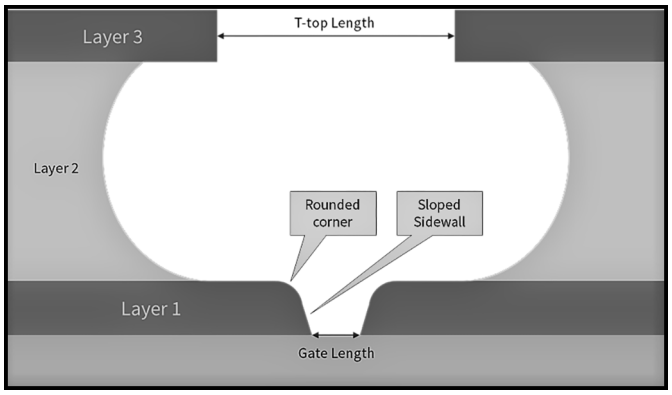

Figure 1: Schematic of target cross section.

Abstract:

Wolfspeed aims to add electron-beam lithography (EBL) processes to our toolset to improve our competitive position in the RF electronics markets.

Summary of Research:

Near term goals to be accomplished at Cornell NanoScale Facility (CNF) over a time range of 12 to 24 months include gain experience in EBL, identify baseline functional process for transfer into NC Fabrication upon toolset installation, and identify EBL toolset and facility specifications based on development work. Prototype demonstration of fully functional "T-Gate" HEMT 90 nm gate length with 30 nm overlay on 100 mm wafer processing. Long term goals to be accomplished beyond work at CNF include fully outfit EBL toolset, transfer process knowledge into NC Fab, and fully staff EBL process organization. A schematic of the target "T-Gate" profile is shown in Figure 1.

Conclusions and Future Steps:

Work was initiated in the summer of 2023.

References:

[1] Chen, Y., et al. "T-Gate Fabrication Using a ZEP520A/UVIII Bilayer." Microelectronic Engineering, vol. 57-58, 2001, pp. 939-943., https://doi.org/10.1016/s0167-9317(01)00475-0.

[2] Kim, Tae-Woo, et al. "Effect of a Two-Step Recess Process Using Atomic Layer Etching on the Performance of $In_{0.52}Al_{0.48}As/In_{0.53}Ga_{0.47}As$ P-HEMTs." IEEE Electron Device Letters, vol. 28, no. 12, 2007, pp. 1086-1088., https://doi.org/10.1109/led.2007.910278.

[3] Ocola, Leonidas E., and Aaron Stein. "From Microchannels to Nanochannels in a Bilayer Resist." Nanofabrication: Technologies, Devices, and Applications, 2005, https://doi.org/10.1117/12.572068.

[4] Zhong, Yinghui, et al. "T.Gate Fabrication of Inp.Based HEMTs Using PMGI/ZEP520A/PMGI/ZEP520A Stacked Resist." Chinese Journal of Electronics, vol. 25, no. 3, 2016, pp. 448-452., https://doi.org/10.1049/cje.2016.05.009.

[5] Zhu, Mingsai, et al. "Nanofabrication of T Shape Gates for High Electron Mobility Transistors in Microwaves and THz Waves, a Review." Micro and Nano Engineering, vol. 13, 2021, p. 100091., https://doi.org/10.1016/j.mne.2021.100091.

[6] Fitch, Walker, et al. "Implementation of High-Power-Density X-Band AlGaN/GaN High Electron Mobility Transistors in a Millimeter-Wave Monolithic Microwave Integrated Circuit Process" IEEE Electron Device Letters, VoL. 36, No. 10, October 2015.

2022-2023 CNF Research Accomplishments

INDEX

Reports by CNF Project Number

Reports by CNF Principal Investigators & Users

A

B

C

D

E

F

G

H

I

J

K

L

M

N

O

P

P
continued

R

S

T

V

W

X

Y

Z

The 2022-2023 CNF Research Accomplishments are online in full color @ http://cnf.cornell.edu/publications/research_accomplishments

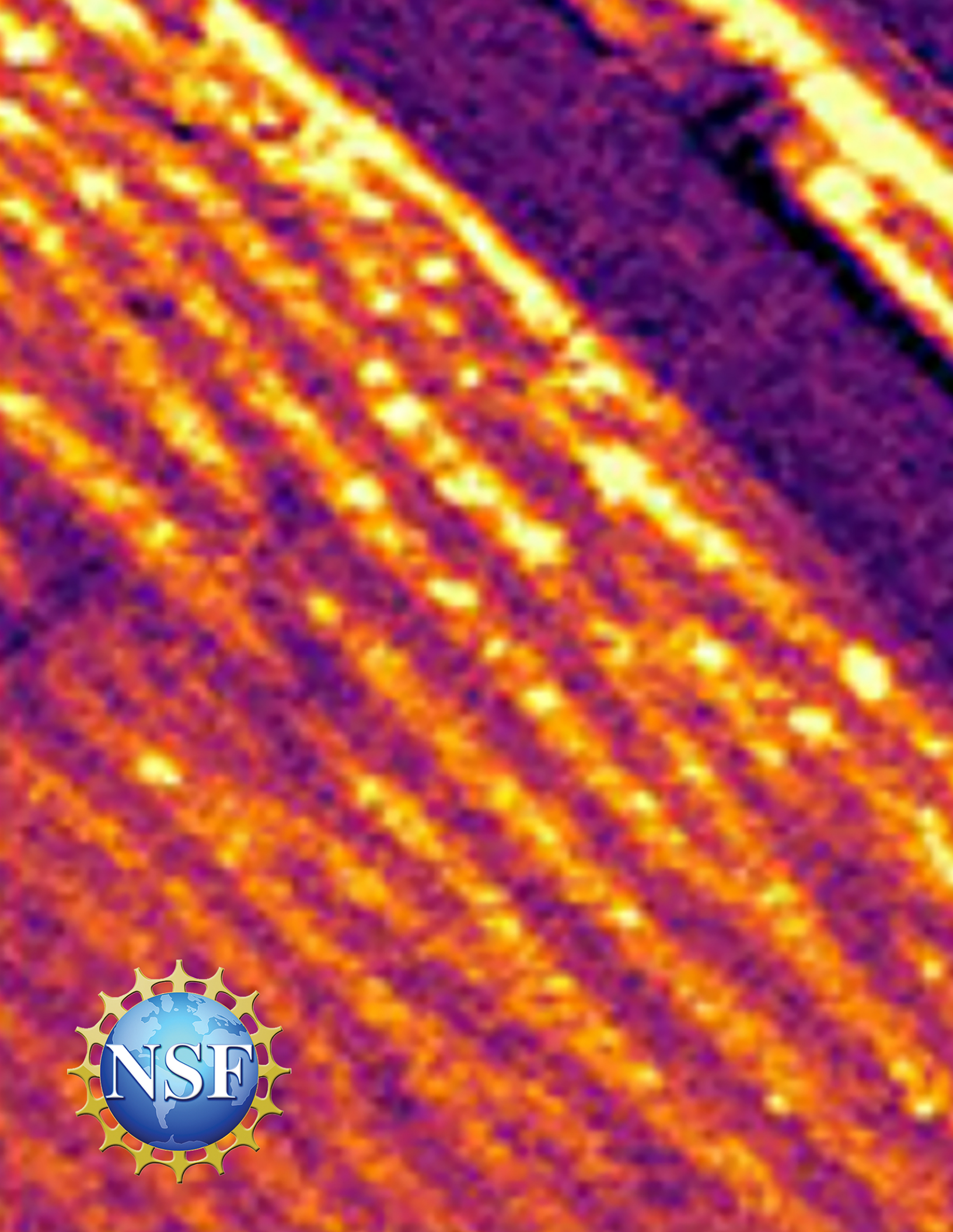
NSF